VOLUME 37 DECEMBER 1959 NUMBER 12

Canadian Journal of Physics

Editor: H. E. DUCKWORTH

Associate Editors:

L. G. ELLIOTT, *Atomic Energy of Canada, Ltd., Chalk River*
J. S. FOSTER, *McGill University*
G. HERZBERG, *National Research Council of Canada*
L. LEPRINCE-RINGUET, *Ecole Polytechnique, Paris*
B. W. SARGENT, *Queen's University*
G. M. VOLKOFF, *University of British Columbia*
W. H. WATSON, *University of Toronto*
G. A. WOONTON, *McGill University*

Published by THE NATIONAL RESEARCH COUNCIL

OTTAWA CANADA

CANADIAN JOURNAL OF PHYSICS

Under the authority of the Chairman of the Committee of the Privy Council on Scientific and Industrial Research, the National Research Council issues THE CANADIAN JOURNAL OF PHYSICS and five other journals devoted to the publication, in English or French, of the results of original scientific research. Matters of general policy concerning these journals are the responsibility of a joint Editorial Board consisting of: members representing the National Research Council of Canada; the Editors of the Journals; and members representing the Royal Society of Canada and four other scientific societies.

EDITORIAL BOARD

Representatives of the National Research Council

I. McT. Cowan, *University of British Columbia*
A. Gauthier, *University of Montreal*
H. G. Thode (Chairman), *McMaster University*
D. L. Thomson, *McGill University*

Editors of the Journals

D. L. Bailey, *University of Toronto*
T. W. M. Cameron, *Macdonald College*
H. E. Duckworth, *McMaster University*
Léo Marion, *National Research Council*
J. F. Morgan, *Department of National Health and Welfare, Ottawa*
R. G. E. Murray, *University of Western Ontario*
J. A. F. Stevenson, *University of Western Ontario*

Representatives of Societies

D. L. Bailey, *University of Toronto*
Royal Society of Canada
T. W. M. Cameron, *Macdonald College*
Royal Society of Canada
H. E. Duckworth, *McMaster University*
Royal Society of Canada
Canadian Association of Physicists
P. R. Gendron, *University of Ottawa*
Chemical Institute of Canada
J. F. Morgan, *Department of National Health and Welfare, Ottawa*
Canadian Biochemical Society
R. G. E. Murray, *University of Western Ontario*
Canadian Society of Microbiologists
J. A. F. Stevenson, *University of Western Ontario*
Canadian Physiological Society
T. Thorvaldson, *University of Saskatchewan*
Royal Society of Canada

Ex officio

Léo Marion (Editor-in-Chief), *National Research Council*
J. B. Marshall (Administration and Awards), *National Research Council*

Manuscripts for publication should be submitted to Dr. H. E. Duckworth, Editor, Canadian Journal of Physics, Hamilton College, McMaster University, Hamilton, Ontario.
For instructions on preparation of copy, see **NOTES TO CONTRIBUTORS** (back cover).

Proof, correspondence concerning proof, and orders for reprints should be sent to the Manager, Editorial Office (Research Journals), Division of Administration and Awards, National Research Council, Ottawa 2, Canada.

Subscriptions, renewals, requests for single or back numbers, and all remittances should be sent to Division of Administration and Awards, National Research Council, Ottawa 2, Canada. Remittances should be made payable to the Receiver General of Canada, credit National Research Council.

The journals published, frequency of publication, and prices are:

Canadian Journal of Biochemistry and Physiology	Monthly	$9.00 a year
Canadian Journal of Botany	Bimonthly	$6.00 a year
Canadian Journal of Chemistry	Monthly	$12.00 a year
Canadian Journal of Microbiology	Bimonthly	$6.00 a year
Canadian Journal of Physics	Monthly	$9.00 a year
Canadian Journal of Zoology	Bimonthly	$5.00 a year

The price of regular single numbers of all journals is $2.00.

Canadian Journal of Physics

Issued by THE NATIONAL RESEARCH COUNCIL OF CANADA

VOLUME 37 DECEMBER 1959 NUMBER 12

A THERMISTOR HYPSOMETER[1]

W. R. BLACKMORE

ABSTRACT

A thermistor hypsometer used as a sensitive, recording, gas-pressure measuring device is described. It is shown that the limitation on this device is the noise introduced by the pressure fluctuations over the surface of the boiling liquid. These fluctuations are about $\pm(5-10)$ μ(microns) Hg peak-to-peak. When a pressure measurement is averaged over a moderately short period of time it may be estimated to ± 1 μHg.

INTRODUCTION

A survey of the literature of gas-pressure measuring devices shows that many transducers based on different principles have been used for this frequently occurring task. The devices which have been used range from simple mercury, oil, or water columns to sensitive diaphragms or bellows (Jutras *et al.* 1959; National Bureau of Standards 1953; Sancier *et al.* 1956; Lion 1956), the motion of which alters an electrical characteristic such as capacitance or inductance in an associated circuit. Unfortunately, the simplest sensitive manometers, such as tilting or bubble manometers (Eichhorn *et al.* 1958; Chattock–Fry; Hindley 1947) rarely yield a record but must be read by eye. On the other hand, the sensitive electromechanical devices usually require machine shop time if constructed in the laboratory or, if purchased, may be very expensive (Consolidated Engineering Corp. 1947).

The principle of the hypsometer is not new. About 1860 E. Whymper reputedly carried a teakettle and a thermometer up Mont Blanc in the Alps and established that the boiling point of pure liquid varies with the atmospheric pressure. When this fact is combined with the high sensitivity of the modern thermistor to temperature changes, then a sensitive absolute or differential pressure transducer is obviously available. Fundamentally all that is required for a thermistor hypsometer is a Wheatstone bridge and some elementary glassware normally readily available in the laboratory.

APPARATUS

(*a*) *Thermistors*

The thermistors employed have been glass-encased beads (types 32A1, 32A11, 51A1, and 51A11) from Victory Engineering Corporation (Springfield

[1]Manuscript received July 23, 1959.
Contribution from the Central Research Laboratory, Canadian Industries Limited, McMasterville, Que.

Road, Union, New Jersey). These thermistors are normally calibrated following the procedure described earlier (Blackmore, Part I, 1959) before being used in a hypsometer.

(*b*) *Electrical Circuitry*

The actual measurement of the thermistor resistance in the hypsometer is made with a Wheatstone bridge (type 3352) manufactured by the Tinsley Co. (Smiths Falls, Ontario). The "battery" and "galvanometer" bridge connections have been interchanged so that the bridge current is equally divided between the thermistor and the variable arm. The ratio arms are variable and are normally chosen so that the bridge may approximate an "equal-arm" bridge. The microvolt d-c. amplifier used to detect the unbalance voltage from this Wheatstone bridge is usually a Leeds–Northrup Model 9835-B, which at maximum sensitivity has a full-scale deflection for 50 microvolts. The amplifier output is fed into a Brown Electronik potentiometer recorder (Minneapolis-Honeywell), 10 millivolts full scale. The Wheatstone bridge supply is normally a 6-volt lead–acid storage battery. This is in series with a Heathkit (Heath Company) decade resistance box used as a current-limiting device. An ammeter is included so that the bridge current may be measured at all times.

(*c*) *Glassware*

The first apparatus tried is shown in Fig. 1. The boiler was a 2-liter flask fitted with a "Glass-Col" heating mantle. Boiling chips were used to promote

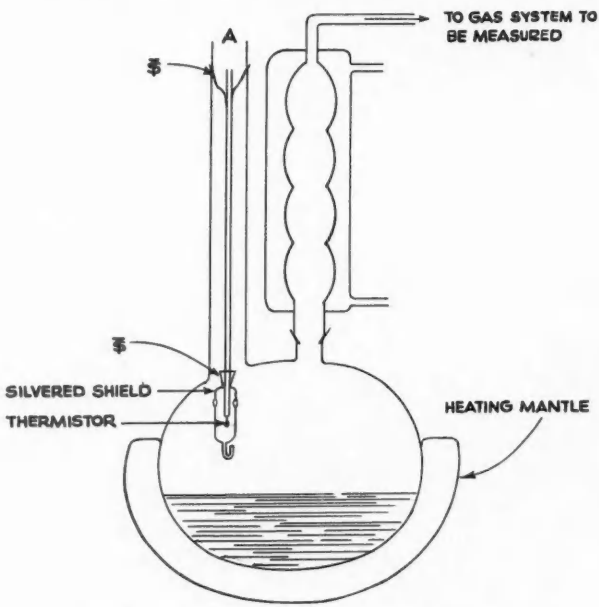

FIG. 1. First thermistor hypsometer apparatus.

boiling. The reflux condenser and the thermistor holder (A) were fitted using standard-taper joints. The thermistor itself (a 51A11 V.E. Co.) was sealed into a glass tube with Araldite (Canadian Bronze Powder Works Ltd.) cement. The thermistor was surrounded by a silvered-glass shield which was pierced by several large-diameter holes. These allowed any pressure changes in the vapor to act on the thermistor immediately. The shield was used to protect the thermistor from radiation from the heater.

The second piece of apparatus (Fig. 2) was an improvement over the first in that boiling proceeded more quietly and hence the background noise was

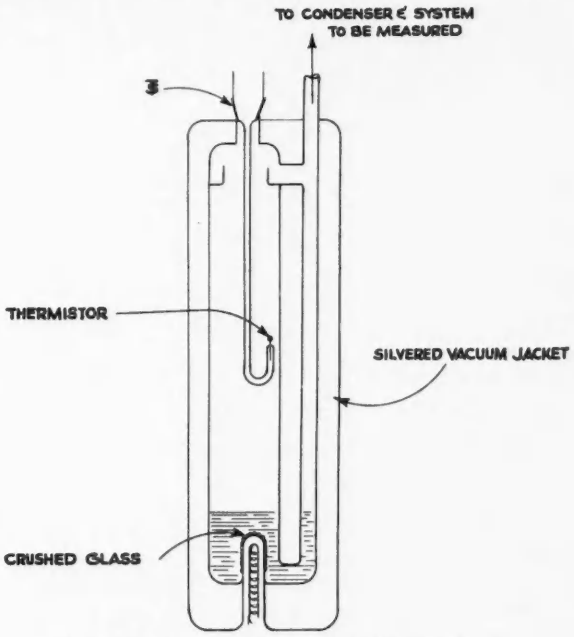

FIG. 2. Improved thermistor hypsometer apparatus.

less. The thermistor was held in position with the sensitive tip uppermost so that large drops of liquid could not form on (and then drop off) the thermistor bead. Each time this did happen with the apparatus shown in Fig. 1, there was a spurious change in the recorded pressure.

Another modification was to dispense with the silvered shield around the thermistor. This could be done safely, in our case, since we only wished to measure pressure changes throughout the day. Under these conditions the true absolute pressure was not required. Hence, any radiation from the boiler heater affecting the thermistor could be treated as constant and ignored.

One other piece of apparatus was then investigated as a potential hypsometer. This had been built during the study of ebulliometers (Blackmore, Part IV, 1959) carried out at Canadian Industries Limited, Central Research Laboratory, and is shown in Fig. 3.

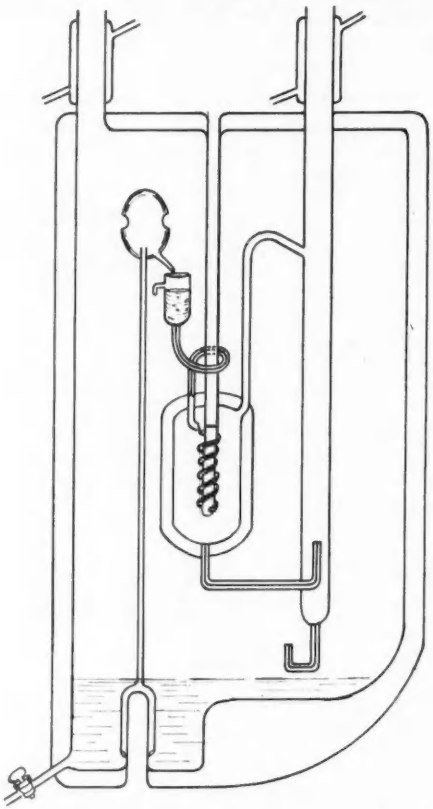

FIG. 3. Half-ebulliometer used as a thermistor hypsometer.

CALIBRATION

The pressure calibration may be performed very simply with the apparatus arranged as in Fig. 4. With the reference tank at some constant pressure, the pressure in the surge tank may be set at different values and the pressure difference measured to ± 0.1 mm of manometer fluid with a magnifying eyepiece or a cathetometer. At the same time the change in resistance of the thermistor produced by this change in pressure may be measured.

It is found (Adey 1957) that the relationship between thermistor resistance and temperature is quite accurately represented over a range of a few degrees by

$$R = R_0 e^{B/T} \tag{1}$$

where R is the thermistor resistance at temperature T °K, R_0 is the thermistor resistance at some reference temperature, and B is a constant, equal to about 3500° K for many thermistors.

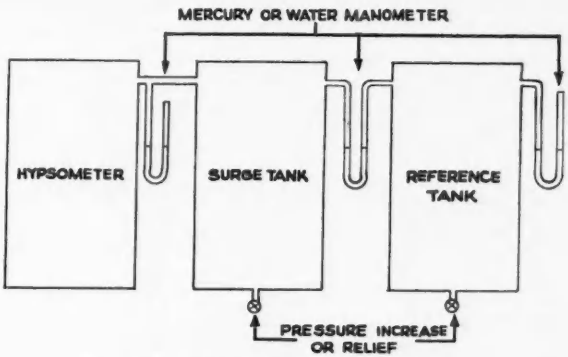

FIG. 4. Block diagram of pressure system.

Similarly the relationship between the vapor pressure of a pure liquid and its boiling point may be written

$$p = p_0 e^{-L_v/R_g T}, \tag{2}$$

where p is the vapor pressure at the temperature T °K, p_0 is the vapor pressure at some reference temperature, L_v is the molar heat of vaporization, and R_g is the gas constant.

By differentiating equations (1) and (2) and substituting we obtain

$$dR = (-B.R_g/L_v) \times (dp/p) \times R \tag{3}$$

as the change in thermistor resistance produced by a change in pressure on the vapor. As a typical case, let us assume that water is being used in the hypsometer for which $L_v = 9712$ cal/mole, $R_g = 2$ cal/mole-degree, $B = 3500°$ K for many thermistors, and $R = 5000\ \Omega$ for a 51A1 V.E. Co. thermistor at 100° C. Hence, for a change of 1 μ Hg at an atmospheric pressure of 760 mm Hg the change in resistance of the thermistor is 0.005 Ω.

In the normal course of events when small pressure fluctuations are being measured about some average value of the pressure, p, then both B and L_v may be treated as constants. However, when a different range of pressures, p, is being considered, then it is necessary to recalibrate since B, L_v, and R will have changed. This problem is not a serious one and may in any event be avoided if the thermistor resistance has been calibrated against temperature (Blackmore, Part I, 1959). For then, working with a liquid such as water for which the boiling point is accurately known over a large range of pressures, the information required for equations (1) and (2) above is available and hence (3) may be calculated.

RESULTS

The first measurements to be discussed are those made with the apparatus shown in Fig. 2. The changes in the output voltage from the Wheatstone bridge (as a recorder pen shift in chart divisions; Brown chart No. 5221, 200

divisions full scale) are shown in Table I as a function of the changes in pressure acting on the vapor over the boiling water.

TABLE I

Typical cumulative pressure change versus the associated cumulative recorder pen shift

$\Sigma\Delta p$, mm H_2O	$\Sigma\Delta S$, chart divisions	$\Sigma\Delta S/\Sigma\Delta p$, div/mm H_2O
13	156	12.0
28	339	12.1
38	469	12.3
48	599	12.5
58	723	12.5
69	857	12.4
81	1005	12.4
92	1133	12.3

The peak-to-peak noise actually measured in the trace was ± 2 divisions. This is equivalent to $\pm 1/6$ mm H_2O which, in turn, is about ± 12 μ Hg. However, it is easily possible to estimate the average value of the recorder trace within $\pm 1/10$ of the peak-to-peak noise. Hence, the average pressure may be estimated to ± 1 μ Hg. To increase the precision still further, it would be necessary to reduce the magnitude of the pressure fluctuations over the surface of the boiling liquid.

Since substituting a wire wound resistor of the same resistance for the thermistor produced a flat trace on the recorder, at the same amplifier gain and bridge current, the noise measured must truly be present as pressure fluctuations over the surface of the boiling liquid. The possibility that the noise is produced by the electrical current flowing through the thermistor must be discarded as is shown by the results described in Blackmore, Part III.

Interspersed with the measurements, reported in Table I, others were being made to record the bridge sensitivity at this amplifier gain and bridge current. This was done by changing the variable arm of the Wheatstone bridge by a known number of ohms and recording the attendant change in the recorder pen position (Table II).

TABLE II

Bridge sensitivity

$\Sigma\Delta R$, Ω	$\Sigma\Delta S$, chart divisions	$\Sigma\Delta S/\Sigma\Delta R$, div/$\Omega$
5	166	33.2
9	297	33.0
13	430	33.1
17	563	33.1

As a rough check on these results, we may calculate the order of magnitude

of sensitivity to be expected. At 100° C a change of 1 m° C in the boiling point would produce a change of 153 mΩ in the thermistor resistance. For water at 760 mm Hg and 100.000° C a change of 1 mm Hg produces a change of 37 m° C in the boiling point. Hence, a 153-mΩ resistance change is equivalent to a change in pressure of 0.368 mm H_2O. Now, as shown in Table II, a change of 1 Ω in the variable arm of the Wheatstone bridge produced a shift of 33 recorder divisions. Hence, one would expect a shift of 13.7 div/mm H_2O. The average measured value from Table I is 12.3 div/mm H_2O.

In an attempt to reduce the noise introduced by the boiling process, the apparatus shown in Fig. 3 was investigated. The results are given in Table III.

TABLE III

Typical cumulative pressure change versus the associated cumulative recorder pen shift

$\Sigma\Delta p$, mm H_2O	$\Sigma\Delta S$, chart divisions	$\Sigma\Delta S/\Sigma\Delta p$, div/mm H_2O
12	134	11.1
29	312	10.8
41	474	11.6
55	640	11.6
72	816	11.3

The bridge sensitivity was also measured with the results shown in Table IV.

TABLE IV

Bridge sensitivity

$\Sigma\Delta R$	$\Sigma\Delta S$, chart divisions	$\Sigma\Delta S/\Sigma\Delta R$, div/Ω
7	228	30.7
13	418	31.1
18	580	31.0
23	741	31.0

The peak-to-peak trace noise was about half what it had been, i.e., it now was about ±6 μ Hg.

Since the time constant of this apparatus cannot be smaller than that of a bare 51A11 thermistor, we may expect that some of the improvement in the trace noise may simply be that the thermistor may now not respond so quickly.

The last experiments were performed using pure toluene as the boiling fluid. The apparatus used is shown in Fig. 3. The results are given in Table V.

The bridge sensitivity that day is given in Table VI. This is higher than the previous values because the bridge current was increased to 1.1 milliamperes.

The noise level was about ±1 division peak-to-peak, i.e., ±5 μ Hg.

TABLE V

Typical cumulative pressure change versus the associated cumulative recorder pen shift

$\Sigma\Delta p$, mm H_2O	$\Sigma\Delta S$, chart divisions	$\Sigma\Delta S/\Sigma\Delta p$, div/mm H_2O
12	170	14.2
24	350	14.6
34	507	14.9
43	635	14.8
52	779	15.0
63	929	14.8
72	1070	14.9
80	1220	15.3

TABLE VI

Bridge sensitivity

$\Sigma\Delta R$, Ω	$\Sigma\Delta S$, chart divisions	$\Sigma\Delta S/\Sigma\Delta R$, div/Ω
3	141	47.0
6	281	46.8
9	420	46.7
12	558	46.5
16	742	46.4

CONCLUSIONS

The limitation to this technique of pressure measurement is the pressure fluctuations produced by the surges of the boiling liquid. These are normally in the $\pm(5\text{–}10)$ μ Hg range (peak-to-peak) and hence an estimate of a shift in the average may usually be made to ± 1 μ Hg.

ACKNOWLEDGMENT

The author wishes to acknowledge the assistance of Christopher Sealy and Roland Richard, by whom the experimental work was performed.

REFERENCES

ADEY, A. W. 1957. Radio Physics Laboratory, Project Report No. 22-1-2 (Defence Research Telecommunications Establishment, Ottawa).
BLACKMORE, W. R. 1959. Can. J. Chem. **37**, 1508.
——— 1959. Rev. Sci. Instr. (submitted).
——— 1959. Can. J. Phys. **37**, 1365.
CANADIAN BRONZE POWDER WORKS LTD., Valleyfield, Quebec.
CHATTOCK–FRY TILTING MANOMETER. C. F. Cassela and Co. Ltd., Regent House, Fitzroy Square, London.
CONSOLIDATED ENGINEERING CORPORATION, Pasadena, California. The Electromanometer, Bulletin 1547.
EICHHORN, R. and IRVINE, T. F. 1958. Rev. Sci. Instr. **29**, 23.
HEATH COMPANY, Benton Harbor, Michigan, U.S.A.
HINDLEY, H. R. 1947. J. Sci. Instr. **24**, 295.
JUTRAS, J. R., LEGER, E. G., and OUELLET, C. 1956. Can. J. Technol. **34**, 29.
LION, K. S. 1956. Rev. Sci. Instr. **27**, 23.
MINNEAPOLIS-HONEYWELL, VanderHoof Avenue and Brentcliffe Road, Leaside, Toronto, Ontario.
NATIONAL BUREAU OF STANDARDS. 1953. Tech. News Bull. **37**, 140.
SANCIER, K. M. and RICHESON, W. 1956. Rev. Sci. Instr. **27**, 134.

ON THE POSSIBLE EXISTENCE OF A DERIVATIVE COUPLING IN QUANTUM ELECTRODYNAMICS[1]

F. A. KAEMPFFER

ABSTRACT

Within the framework of quantum electrodynamics there exists the possibility of a derivative coupling between source and photon field, referred to as $e\Lambda$-charge, which has no classical analogue. For calculations the usual graph technique can be used, provided the factor $e\gamma_\mu$ contributed by each vertex in a conventional graph is replaced by $ie\Lambda k_\mu$, where Λ is a length characteristic of the new interaction. Using as cutoff the nucleon mass M one finds for a bare source of electronic mass m the self-energy in second order to be $\Delta m/m \approx 200$, if $\Lambda^{-1} \approx 60M$. It is argued that the large mass difference between muon and electron may be due to this effect, assuming muon and electron to differ only in that the muon has $e\Lambda$-charge whereas the electron has not. An estimate is made of the muon–muon scattering cross section caused by the presence of $e\Lambda$-charge on the muon, and it is found that the existence of this derivative coupling may have escaped observation.

Quantum electrodynamics is unique among all other quantum field theories, which purport to describe elementary particles and their interactions, in that the form of the interaction coupling electric charges to the photon field was never in doubt. At the time of inception of quantum electrodynamics empirical knowledge of electromagnetic interactions was sufficiently advanced to make the choice of the corresponding interaction term in the Lagrangian unique. Only a vector coupling, linear in the field variables A_μ, and free of derivatives of A_μ, namely

$$L = ej_\mu A_\mu \tag{1}$$

where ej_μ is the fourvector of electric current, can give rise to a description in agreement with experiment.

The belief that the photon possesses no other interaction with electric charges has been canonized by Gell-Mann (1956) in the so-called principle of minimal electromagnetic interaction. This principle is sufficient to avoid situations in which electromagnetic interactions other than (1) may lead to nonconservation of strangeness.

Strong and weak interactions, on the other hand, were so little explored experimentally, in the early days of quantum field theory, that a wide variety of possible interaction Lagrangians had to be considered, always assuming theories modelled on quantum electrodynamics to be adequate descriptions of these other interactions, in the hope a detailed investigation of all their consequences might eventually lead, by crucial experiments, to a narrowing down of the various possible interaction terms to some unique form. This aim has only partially been accomplished.

[1]Manuscript received August 24, 1959.
Contribution from the Department of Physics, The University of British Columbia, Vancouver 8, B.C.

Although, for example, at low nucleon energy in the strong nucleon pion interaction the pseudovector coupling can be made to fit experiment as well as the pseudoscalar coupling (see Hamilton 1959), the latter is favored because renormalization procedures can be applied to it, in contrast to the nonrenormalizable pseudovector coupling. However, renormalizability as a criterion for choosing the right interaction has lost ground recently when the weak interactions were found to be describable in terms of the nonrenormalizable four fermion V–A point interaction. A sensible position to take is then to treat all infinite quantities appearing in the course of a calculation as revealing some physical reality whose effect can be estimated by use of the same cutoff λ, which gives, for example, the correct mass difference between neutron and proton (Feynman and Speisman 1954), namely $\lambda \approx M$ where M is the nucleon mass.

This raises again the question what is the justification for not taking into consideration derivative couplings, which are not renormalizable, at least not in the usual way (Arnowitt and Deser 1955). As is well known, there are two famous cases of derivative coupling, invoked in phenomenological theories of the anomalous magnetic moment of the nucleon and of the decay of the neutral pion into two photons. It is generally believed, however, that the corresponding interaction terms involving the electromagnetic field tensor $F_{\mu\nu}$ are not fundamental, and that their effect should in principle be contained in a correct theory of strong interactions in conjunction with conventional quantum electrodynamics (Wick 1935; Steinberger 1949).

It seems to have been overlooked, strangely enough, that within the framework of quantum electrodynamics there exists the possibility of a derivative coupling which has no classical analogue. The interaction in question can be obtained by adding to the Lagrangian the term

$$L' = -e\Lambda\rho\frac{\partial A_\mu}{\partial x_\mu} \tag{2}$$

where ρ is the source density and Λ a characteristic length. The electric charge e has been extracted as a factor to facilitate comparison with the interaction (1). For a spinor field one would have to take, in the notation of Källen (1958),

$$\rho = \tfrac{1}{2}[\bar{\psi}(x), \psi(x)]. \tag{3}$$

As is readily seen, adopting interaction (2) instead of (1) means replacing all factors $e\gamma_\mu$, contributed by each vertex in every graph describing some process according to the usual technique (Feynman 1949), by $ie\Lambda k_\mu$.

If one favors a point of view recently expressed by Landau (1959), who prefers direct study of graphs without reference to any classical quantities like Lagrangians etc., one could say the purpose of the present work is to study consequences of a hypothesis laid down in the above prescription for the evaluation of graphs, without the encumbrance imposed by a Hamiltonian and perturbation theory.

On first sight one might think an interaction of type (2) cannot give rise to

any physical effects because of the Lorentz condition. However, in quantum electrodynamics this condition does not hold as an operator identity, because only the expectation value of $\partial A_\mu/\partial x_\mu$ is required to vanish, and to this end it is sufficient to let all free photon states $|\phi>$ satisfy (Gupta 1950)

$$\left(\frac{\partial A_\mu}{\partial x_\mu}\right)^{(+)} |\phi> = 0. \tag{4}$$

Consequently only those free photon states need be considered in which only transverse photons are present, because condition (4) guarantees any admixture of longitudinal and scalar photons to be of such a form that their contribution to the energy of the system will vanish. The situation changes in presence of any interaction which may generate transitions to and from intermediate states with longitudinal and scalar photons present, giving rise to effects of second and higher order. Thus the well-known Coulomb interaction between e-charges is mediated by longitudinal and scalar photons in accordance with (1). Similarly, the interaction (2) may give rise to effects of second and higher order.

As a first example, consider the self-energy integral (see Feynman 1949) belonging to a Dirac particle of bare electronic mass m, coupled to the photon field by e-charge,

$$\frac{e^2}{\pi i}\int_F \gamma_\mu(\mathbf{p}-\mathbf{k}-m)^{-1}\gamma_\mu \mathbf{k}^{-2}C(\mathbf{k}^2)d^4k. \tag{5}$$

If the same particle possesses $e\Lambda$-charge only, the corresponding graph contributes according to the prescription the integral

$$-\frac{e^2\Lambda^2}{\pi i}\int_F \frac{C(\mathbf{k}^2)d^4k}{\mathbf{p}-\mathbf{k}-m}. \tag{6}$$

As cutoff function one needs here

$$C(\mathbf{k}^2) = \frac{\lambda^4}{(\mathbf{k}^2-\lambda^2)^2}. \tag{7}$$

Evaluation of the integral (6) is straightforward by the standard method. Replacing in the result $\mathbf{p}$ by m one obtains the self-energy

$$\Delta m = \frac{e^2\Lambda^2\pi m^3\alpha^4}{2}\left\{1-(\alpha^2-3)\ln\alpha + \tfrac{1}{2}(\alpha^2-1)\sqrt{1-(4/\alpha^2)}\ln\left[\frac{1+\sqrt{1-(4/\alpha^2)}}{1-\sqrt{1-(4/\alpha^2)}}\right]\right\} \tag{8}$$

where

$$\alpha = \lambda/m. \tag{9}$$

For $\alpha \gg 1$ one has approximately

$$\frac{\Delta m}{m} \approx \pi e^2\Lambda^2 m^2\alpha^4 \ln\alpha. \tag{10}$$

Now suppose one takes as usual $\alpha \approx 2\times10^3$, corresponding to a cutoff parameter λ of about nucleon mass M, and writes $\Lambda^{-1} = \beta M$, then

$$\frac{\Delta m}{m} \approx \beta^{-2}\times0.7\times10^6. \tag{11}$$

This large numerical value for $\Delta m/m$ tempts one to make the hypothesis that the muon is a particle which possesses $e\Lambda$-charge, in contrast to the electron which does not, and to account for the large mass difference between muon and electron as a self-energy effect (11), both muon and electron having the same bare mass m. Numerically one finds $\Delta m/m \approx 200$ can be obtained if $\beta \approx 60$.

Existence of $e\Lambda$-charge on the muon must give rise to muon–muon scattering in complete analogy to the Møller scattering caused by e-charge. Replacing in the well-known expression (see Jauch and Rohrlich 1955) according to the prescription $e\gamma_\mu$ by $ie\Lambda k_\mu$, one finds immediately for the differential cross section in the center of mass system

$$d\sigma = \left(\frac{e^2\Lambda^2}{m}\right)^2 m^4(A+B-2C)\frac{d\Omega}{\gamma^2}; \qquad \gamma^2 = (1-v^2)^{-1} \tag{12}$$

with

$$\begin{cases} A = 4\tfrac{1}{4}\, Tr[\Lambda_-(p_1)\,\Lambda_-(p_1')]\,\tfrac{1}{4}\, Tr[\Lambda_-(p_2)\,\Lambda_-(p_2')], \\ B = 4\tfrac{1}{4}\, Tr[\Lambda_-(p_1)\,\Lambda_-(p_2')]\,\tfrac{1}{4}\, Tr[\Lambda_-(p_2)\,\Lambda_-(p_1')], \\ C = \tfrac{1}{4}\, Tr[\Lambda_-(p_1)\,\Lambda_-(p_1')\,\Lambda_-(p_2)\,\Lambda_-(p_2')], \end{cases} \tag{13}$$

where $\Lambda_-(p)$ is the usual projection operator and p_1, p_2 and p_1', p_2' are initial and final momenta respectively. Evaluation of the traces (13) is again straightforward by the standard method, yielding

$$d\sigma = \left(\frac{e^2\Lambda^2}{m}\right)^2 \frac{m^4 d\Omega}{2}\left[\frac{\gamma^2}{2} - 1 + \frac{3}{2\gamma^2} + \tfrac{1}{2}\,\frac{(\gamma^2-1)^2}{\gamma^2}\cos^2\theta\right], \tag{14}$$

from which one obtains by integration over all scattering angles θ the total cross section, which is in the nonrelativistic limit $\gamma \to 1$

$$\sigma_{\text{nonrel.}} = \frac{8\pi}{3}\left(\frac{e^2\Lambda^2}{m}\right)^2 m^4. \tag{15}$$

It stands to reason that for a numerical estimate of σ one should in (15) replace m by the dressed mass m_μ of the muon, thus taking into account, rather summarily, radiation corrections which may possibly be very large on account of the large value of $\Delta m/m$ in this case, but which are difficult to evaluate exactly. As a crude order of magnitude estimate of the muon–muon scattering cross section at nonrelativistic energies one has then

$$\sigma = \frac{8\pi}{3} r_0^2\left(\frac{m_\mu m}{\beta^2 M^2}\right)^2 \approx \frac{4\pi}{3} r_0^2\times10^{-15} \tag{16}$$

where r_0 stands for the classical electron radius e^2/m.

This exceedingly small value strengthens one's suspicion that the existence of $e\Lambda$-charge may so far have escaped experimental detection. The only other second-order process to which $e\Lambda$-charge may conceivably contribute a detectable effect is the $e\Lambda$-charge radiation correction to ordinary e-charge Coulomb scattering of the muon. A preliminary survey of this problem indicates the main contribution comes in this case from the vertex part integral which has here the form

$$\Lambda_\mu(p', p) = -\frac{e^2\Lambda^2}{\pi i}\int_F (\mathbf{p}'-\mathbf{k}-m)^{-1}\gamma_\mu(\mathbf{p}-\mathbf{k}-m)^{-1}C(\mathbf{k}^2)d^4k. \tag{17}$$

The necessary calculations are laborious and are reserved for a later occasion.

It should finally be noted that no contribution can arise from graphs containing an odd number of $e\Lambda$-vertices. Matrix elements describing the exchange of a photon between an e-vertex and an $e\Lambda$-vertex vanish identically, because they always contain an integral of the form

$$\int_F \bar{u}(p_1')u(p_1)\bar{u}(p_2')\mathbf{k}u(p_2)\delta(p_1-p_1'-k)\delta(p_2-p_2'+k)\frac{d^4k}{\mathbf{k}^2}, \tag{18}$$

giving rise to a factor

$$\bar{u}(p_2')(\mathbf{p}_2'-\mathbf{p}_2)u(p_2) = \bar{u}(p_2')(m-m)u(p_2) = 0. \tag{19}$$

Similarly, direct scattering of an $e\Lambda$-charge by a fixed external field A_μ cannot occur since the corresponding matrix element

$$\langle p'|M|p\rangle = \text{const.}\ \langle p'|k_\mu A_\mu|p\rangle \tag{20}$$

contains the expectation value of the Lorentz operator $k_\mu A_\mu$ between free photon states and thus vanishes identically.

ACKNOWLEDGMENT

J. R. H. Dempster of the U.B.C. Computing Centre has contributed to this work encouragement and helpful criticism.

REFERENCES

ARNOWITT, R. and DESER, S. 1955. Phys. Rev. **100**, 349.
FEYNMAN, R. P. 1949. Phys. Rev. **76**, 769.
FEYNMAN, R. P. and SPEISMAN, G. 1954. Phys. Rev. **94**, 500.
GELL-MANN, M. 1956. Nuovo cimento, Suppl. **4**, 848.
GUPTA, S. N. 1950. Proc. Phys. Soc. A, **63**, 681.
HAMILTON, J. 1959. The theory of elementary particles (Oxford University Press).
JAUCH, J. M. and ROHRLICH, F. 1955. The theory of photons and electrons (Cambridge, Mass.).
KÄLLEN, G. 1958. Encyclopedia of physics, Vol. V (1) (Springer-Verlag, Berlin).
LANDAU, L. D. 1959. On analytic properties of vertex parts in quantum field theory (Preprint).
STEINBERGER, J. 1949. Phys. Rev. **76**, 1180.
WICK, G. C. 1935. Accad. Lincei, Atti, **21**, 170.

THE PHOTODISINTEGRATION OF MANGANESE AND RHODIUM[1]

R. W. PARSONS[2]

ABSTRACT

The cross section for the production of photoneutrons from Mn^{55} and Rh^{103} has been found by irradiating these elements in the X-ray beam of a 24-Mev betatron. For Mn^{55}, the giant resonance shows two distinct peaks and the intrinsic quadrupole moment is estimated to be 0.73 ± 0.14 barn; for Rh^{103}, two peaks cannot be resolved, but the shape of the giant resonance curve is consistent with an intrinsic quadrupole moment of approximately 2.1 barns.

The splitting of the giant resonance in the photon absorption cross section for non-spherical nuclei as predicted by Okamoto (1958) and Danos (1958) has been verified experimentally by measuring the photoneutron cross sections of tantalum (Fuller and Weiss 1958; Spicer *et al.* 1958; Parsons and Katz 1959) and of terbium (Fuller and Weiss 1958). Estimates of the intrinsic quadrupole moments of these nuclei based on the magnitude of the splitting are in good agreement with values obtained by other methods. Other evidence for splitting was sought by Fuller and Hayward (1958); they measured the cross section for the elastic scattering of photons by tantalum, and although their measurements were not conclusive they were consistent with a splitting of the giant resonance in the photon absorption cross section.

Spicer (1958) has pointed out that the splitting should be observable for nuclei with atomic numbers between 9 and 30; in this region quite large deviations from sphericity occur although the intrinsic quadrupole moments, which depend on the atomic numbers and masses as well as the eccentricities, are fairly small. He considered published data for F^{19}, Mg^{25}, Si^{29}, V^{51}, and Cu^{63}, and showed that this could be interpreted on a split resonance hypothesis, and also estimated the magnitude of the splitting to be expected for five other nuclei in this region for which good experimental data was not available.

The purpose of the present paper is to report measurements of the photoneutron cross sections of one element in the $9 \leqslant Z \leqslant 30$ region, Mn^{55}, and also of Rh^{103}.

Specimens were irradiated in the X-ray beam of the University of Saskatchewan betatron and the emitted photoneutrons were detected using BF_3 counters; the experimental procedure was identical with that used for tantalum by Parsons and Katz (1959). The manganese was in the form of a powder, of purity in excess of 99.9%, and presented a thickness to the X-ray beam of 5.68 g cm^{-2}; the rhodium consisted of a stack of foils, of total thickness 3.75 g cm^{-2}, whose purity exceeded 99.5%. In each case the photoneutron yield

[1]Manuscript received August 20, 1959.
Contribution from the Physics Department, University of Saskatchewan, Saskatoon, Saskatchewan.
[2]National Research Council Postdoctorate Fellow. Present address: Physics Department, University of Queensland, Brisbane, Australia.

was measured at intervals of 0.2 Mev from the (γ,n) threshold to 24 Mev, approximately 40,000 counts being registered at all points except those near threshold. The dose was monitored with an aluminum-walled ionization chamber which was subsequently calibrated against a Victoreen thimble in an 8-cm lucite block. The scale of the yield curves was determined by comparing the yields at 22 Mev from manganese and rhodium with that from copper at the same energy; the latter was assumed to be 2.71×10^8 neutrons per mole per 100 roentgens.

The yield curves are shown in Fig. 1. They were smoothed by the same procedure as that adopted by Parsons and Katz (1959) for tantalum and the smoothed curves were analyzed by the inverted matrix method of Penfold and Leiss (1958), using a bin width of 0.5 Mev. The resulting values of $\sigma_1+2\sigma_2$, where σ_1 is the (γ,n) cross section and σ_2 the $(\gamma,2n)$ cross section, are shown in Figs. 2 and 3.

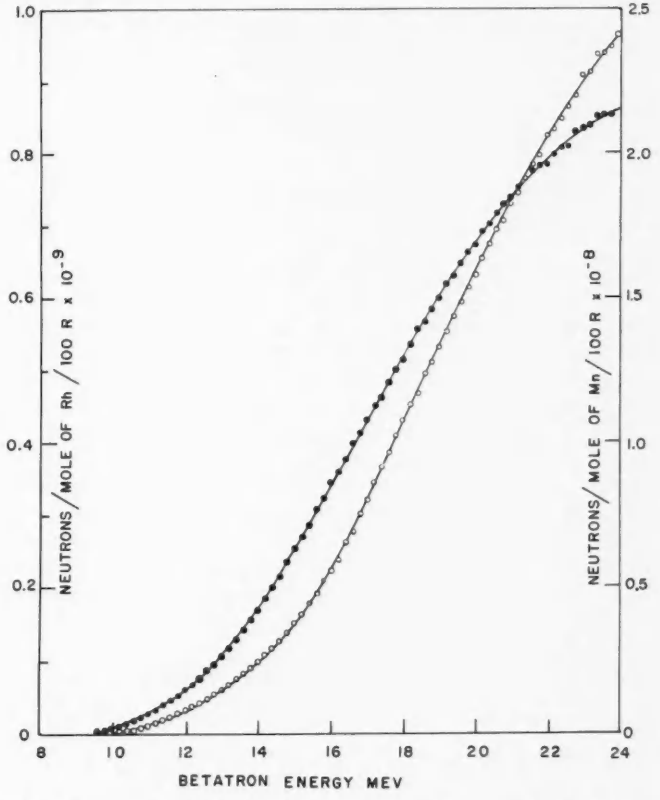

FIG. 1. Photoneutron yield versus betatron energy. ○ manganese; ● rhodium.

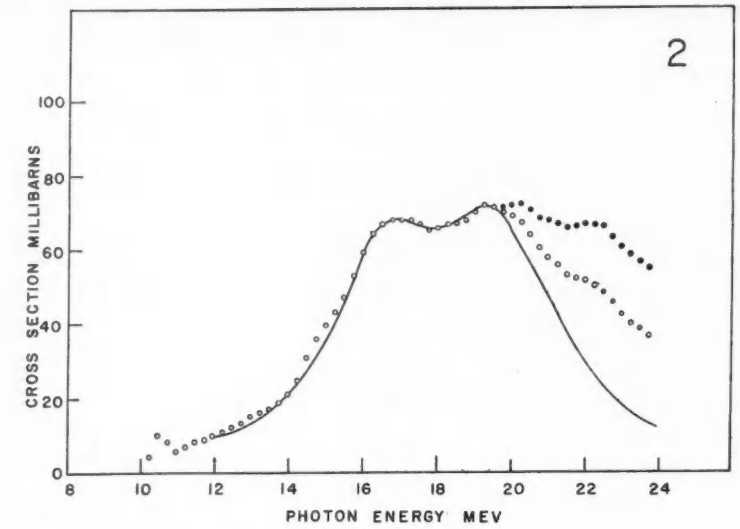

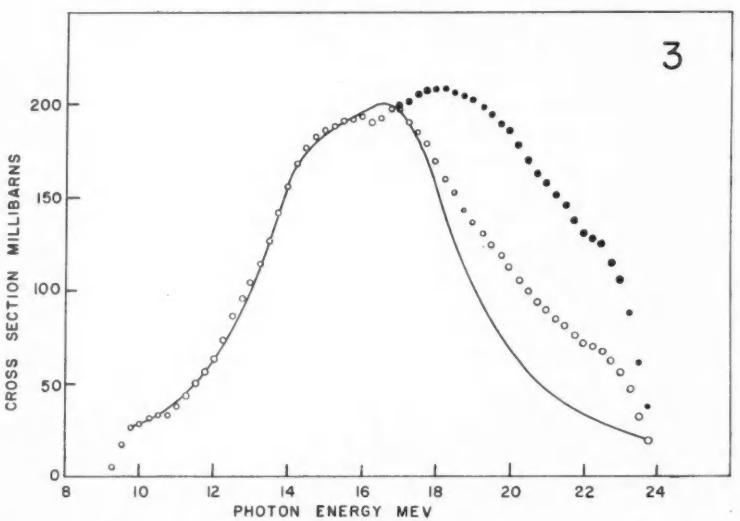

FIG. 2. $\sigma_1+\sigma_2$ (○) and $\sigma_1+2\sigma_2$ (●) for manganese versus photon energy. The full curve is compounded of two resonance curves whose parameters are given in the text.

FIG. 3. $\sigma_1+\sigma_2$ (○) and $\sigma_1+2\sigma_2$ (●) for rhodium versus photon energy. The full curve is compounded of two resonance curves whose parameters are given in the text.

Values of $\sigma_1+\sigma_2$ are also shown. They were found by using a neutron multiplicity correction based on the calculations of Blatt and Weisskopf (1952); in these calculations the temperature Θ of the intermediate nucleus

was assumed to be related to the photon energy E and the (γ,n) threshold energy B_n by the equation $\Theta = \sqrt{\{a/(E-B_n)\}}$ where a is given in terms of the mass number A by $a = 0.07(A-30)$ Mev^{-1} (Feld *et al.* 1951). The $(\gamma,2n)$ threshold of manganese was found from the mass data of Wapstra (1955) to be 19.2 Mev; that of rhodium was found to be 16.8 Mev from the mass tables of Cameron (1957).

It is seen from Fig. 2 that, in the case of manganese, $\sigma_1+\sigma_2$ shows peaks at 19.5 ± 0.25 and 16.75 ± 0.25 Mev. The photon absorption cross section must also include a contribution for photoproton emission, since the (γ,p) threshold is found from mass data (Wapstra 1955) to be 8.2 Mev. If, in the absence of experimental data, it is assumed that this shows maxima at the same energies as $\sigma_1+\sigma_2$, the photon absorption cross section would also show maxima at these energies. From the Danos (1958) theory, the intrinsic quadrupole moment should therefore be 0.73 ± 0.14 barn. This is rather smaller than the value 1.26 ± 0.4 barns found from the Coulomb excitation experiments of Mark *et al.* (1955). The smooth curve in Fig. 2 is the sum of two optical dispersion curves,

$$\sigma = \frac{\sigma_a}{1+\{(E-E_1)/\Gamma_1/2\}^2} + \frac{\sigma_b}{1+\{(E-E_2)/\Gamma_2/2\}^2},$$

where $\sigma_a = 45.9$ mb, $\sigma_b = 62.7$ mb, $E_1 = 16.5$ Mev, $E_2 = 19.5$ Mev, $\Gamma_1 = 3.0$ Mev, and $\Gamma_2 = 4.5$ Mev. A combination of curves of this type was found to fit the experimental data of Parsons and Katz (1959) for tantalum very well up to the second peak of the giant resonance.

The data for rhodium is shown in Fig. 3. This shows a broad resonance which is consistent with the Danos theory, for as shown by the full curve, it is fitted fairly well by the sum of two optical dispersion curves with the following parameters: $\sigma_a = 104$ mb, $\sigma_b = 164$ mb, $E_1 = 14.5$ Mev, $E_2 = 17$ Mev, $\Gamma_1 = 3.4$ Mev, and $\Gamma_2 = 4.5$ Mev. These values of E_1 and E_2 correspond, on the Danos theory, to an intrinsic quadrupole moment of 2.1 barns, which is close to the value 2.2 barns deduced from Coulomb excitation by Heydenburg and Temmer (1954). Several attempts were made to find pairs of resonance curves which fit the data up to 24 Mev, but for neither rhodium nor manganese was this attempt successful. The large high-energy tail of the curves may be due in part to direct interactions or it may be that the multiplicity correction is insufficient; however, it should be remembered that for both manganese and rhodium the (γ,p) thresholds are well below the (γ,n) thresholds, and so competition from (γ,p) reactions may depress the (γ,n) cross sections on the low-energy side of the giant resonance more than on the high-energy side. Resonance curves which fit the data up to the giant resonance might be expected to deviate thereafter.

The author is indebted to Dr. L. Katz for his constant interest and encouragement and to the National Research Council of Canada for a Postdoctoral Fellowship.

REFERENCES

BLATT, J. M. and WEISSKOPF, V. F. 1952. Theoretical nuclear physics (John Wiley & Sons, Inc., New York), p. 379.
CAMERON, A. G. W. 1957. Atomic Energy of Canada Limited, Report CRP-690, AECL No. 433.
DANOS, M. 1958. Nuclear Phys. **5**, 23.
FELD, B. T., FESHBACK, H., GOLDBERGER, M. L., GOLDSTEIN, H., and WEISSKOPF, V. F. 1951. Final Report of the Fast Neutron Project, NYP-636 (Technical Services, Oak Ridge, Tenn.).
FULLER, E. G. and HAYWARD, E. 1958. Phys. Rev. Letters, **1**, 465.
FULLER, E. G. and WEISS, M. S. 1958. Nat. Bur. Standards, Report 5687.
HEYDENBURG, N. P. and TEMMER, G. M. 1954. Phys. Rev. **95**, 861.
MARK, H., MCCLELLAND, C., and GOODMAN, E. 1955. Phys. Rev. **98**, 1245.
OKAMOTO, K. 1958. Phys. Rev. **110**, 143.
PARSONS, R. W. and KATZ, L. 1959. Can. J. Phys. **37**, 809.
PENFOLD, A. S. and LEISS, J. E. 1958. Analysis of photo cross sections (Physics Research Laboratory, University of Illinois, Chicago, Illinois).
SPICER, B. M. 1958. Australian J. Phys. **11**, 490.
SPICER, B. M., THIES, H. H., BAGLIN, J. E., and ALLUM, F. R. 1958. Australian J. Phys. **11**, 298.
WAPSTRA, A. H. 1955. Physica, **21**, 385.

SURFACE WAVE PROPAGATION OVER A SAND-COVERED CONDUCTING PLANE[1]

A. G. Mungall and D. Morris

ABSTRACT

The velocity of surface waves propagated over a sand-covered metal plane has been investigated experimentally as a function of the depth of the sand. Measurements were made at a frequency of approximately 9000 Mc/sec, using a phase comparison system. A periodic variation of surface wave velocity with sand depth was found, as predicted theoretically. The possible application of the results to effects found in precise microwave distance measuring techniques is discussed.

The problem of the trapping of electromagnetic waves to a plane metal surface coated with a thin layer of low loss dielectric has a simple approximate solution. This problem has been investigated thoroughly both experimentally and theoretically (Atwood 1951; Barlow and Cullen 1953). If the thickness of the dielectric is increased so that it becomes appreciable compared to a wavelength of the propagated wave, the general solution becomes more complicated and the simple approximation for thin layers is not valid. However, if the dielectric is assumed to have zero loss and the metal surface infinite conductivity, a fairly simple solution is obtainable (Brown 1953; Rich 1955).

The case of a thick dielectric layer is of little practical importance from the point of view of using it as a transmission line. However, it may well be applicable in explaining some of the errors encountered in precise microwave distance measuring techniques. In these applications it is important that the velocity of propagation be known to a few parts per million over the distance to be measured. If surface wave propagation takes place over any part of the path, then it is difficult to ascertain the correct value for the average velocity between the measuring stations. In this case, the accuracy of the measurements will deteriorate. This paper will show that such surface wave propagation can occur with layers of dry sandy soil underlain by plane metallic conductors.

THEORETICAL

The problem of propagation over a dielectric-coated plane conducting sheet may be considered in the following manner. For the co-ordinate system shown in Fig. 1, the fields in medium 3 (air), characterizing surface wave propagation in the x direction, for both TM and TE modes are as follows:

[1]Manuscript received August 12, 1959.
Contribution from the Division of Applied Physics, National Research Council, Ottawa, Canada.
Issued as N.R.C. No. 5404.

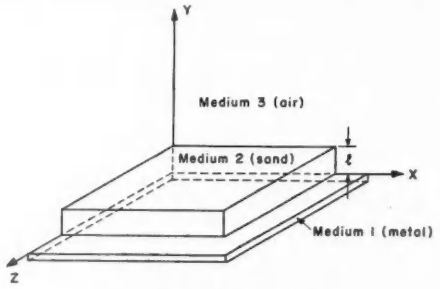

FIG. 1. Co-ordinate system.

$$
\begin{array}{lll}
 & TM & TE \\
 & H_{z_3} = Ae^{j\omega t-\gamma x-\gamma_3 y} & E_{z_3} = Ae^{j\omega t-\gamma x-\gamma_3 y} \\
(1) & E_{x_3} = \dfrac{-A\gamma_3}{j\omega\epsilon_0}\, e^{j\omega t-\gamma x-\gamma_3 y} & H_{x_3} = \dfrac{A\gamma_3}{j\omega\mu_0}\, e^{j\omega t-\gamma x-\gamma_3 y} \\
 & E_{y_3} = \dfrac{A\gamma}{j\omega\epsilon_0}\, e^{j\omega t-\gamma x-\gamma_3 y} & H_{y_3} = -\dfrac{A\gamma}{j\omega\mu_0}\, e^{j\omega t-\gamma x-\gamma_3 y}
\end{array}
$$

where ω is the angular frequency, ϵ_0 is the permittivity of free space, and γ and γ_3 are propagation constants. The magnetic permeabilities of the three media are assumed to be that of free space, μ_0.

The velocity of propagation of the surface wave is given by the value of γ, which can be determined by solution of each set of the following equations:

$$
\left.
\begin{array}{ll}
(2) & \gamma^2+\gamma_1^2 = -\dfrac{\omega^2}{c^2}\,\kappa_1^*, \\
(3) & \gamma^2+\gamma_2^2 = -\dfrac{\omega^2}{c^2}\,\kappa_2^*, \\
(4) & \gamma^2+\gamma_3^2 = -\dfrac{\omega^2}{c^2};
\end{array}
\right\} \quad TM \text{ and } TE
$$

$$
(5a) \qquad TM\text{:}\quad \tanh\gamma_2 l = -\kappa_2^*\,\gamma_2\left[\frac{\gamma_1+\kappa_1^*\gamma_3}{\kappa_1^*\gamma_2^2+\kappa_2^{*2}\gamma_1\gamma_3}\right];
$$

$$
(5b) \qquad TE\text{:}\quad \tanh\gamma_2 l = -\gamma_2\left[\frac{\gamma_1+\gamma_3}{\gamma_2^2+\gamma_1\gamma_3}\right].
$$

In these equations,

$$\kappa_1^* = \kappa_1'-j\kappa_1''$$

and

$$\kappa_2^* = \kappa_2'-j\kappa_2''$$

are the complex dielectric constants of media 1 and 2, l is the thickness of

the dielectric coating, medium 2, and γ_1, γ_2, γ_3 are the propagation constants in the y direction for media 1, 2, 3 respectively.

These equations can be solved fairly simply for the case in question: that of a thick, loss-free dielectric layer on a perfectly conducting plane sheet. In this case, κ_2^* becomes real, and equations 5 and 3 become

$$TM: \quad \beta_2 \tan \beta_2 l = \kappa_2' \left[\frac{\omega^2}{c^2} (\kappa_2' - 1) - \beta_2^2 \right]^{1/2},$$

$$TE: \quad \beta_2 \cot \beta_2 l = - \left[\frac{\omega^2}{c^2} (\kappa_2' - 1) - \beta_2^2 \right]^{1/2},$$

$$v = \left[\frac{\omega^2}{c^2} \kappa_2' - \beta_2^2 \right]^{-1/2},$$

where v is the surface wave velocity and $\gamma_2 = j\beta_2$.

Numerical solutions for both *TM* and *TE* modes have been carried out for a dielectric layer up to several wavelengths in thickness, with a dielectric constant of 3.0. The characteristics of such solutions, discussed by Brown (1953) and Rich (1955), are interesting; the velocity of the trapped wave varies periodically with the thickness of the dielectric layer between limits defined by velocity in free space and that within an infinite volume of the dielectric. These results are shown in comparison with experimental data in Fig. 7.

EXPERIMENTAL

1. *Technique*

Experimental equipment, operating near 9000 Mc/sec, was devised to measure surface wave velocity over a path length up to 240 cm. The essential part of this was a phase comparison system similar to that used by Straiton and Tolbert (1948), a block diagram of which is shown in Fig. 2.

The power output from the transmitter is split between two channels: one consisting of a surface wave guiding structure placed between transmitting and receiving antennas, and the other a comparison path containing a phase shifter. The surface wave and comparison signals are mixed with the same local oscillator signal in mixers 1 and 2, and the two 10-Mc/sec output signals enter identical amplifiers. The amplifier outputs then drive the X and Y plates of an oscilloscope, producing a lissajous pattern. It can be shown that any change in the relative phase of the microwave signals entering the mixers at 9000 Mc/sec is directly converted to the same relative phase in the 10-Mc/sec amplifier output signals. Consequently, a phase change in the surface wave path alters the shape of the oscilloscope pattern. If this pattern is returned to its former shape by alteration of the microwave phase shifter, then the change indicated by the phase shifter is the same as that which occurred over the surface wave path.

In practice, the surface wave guiding structure is placed between the transmitting and receiving antennas. Part of this structure is then covered by metal sheets, part being left uncovered. Propagation at free-space velocity

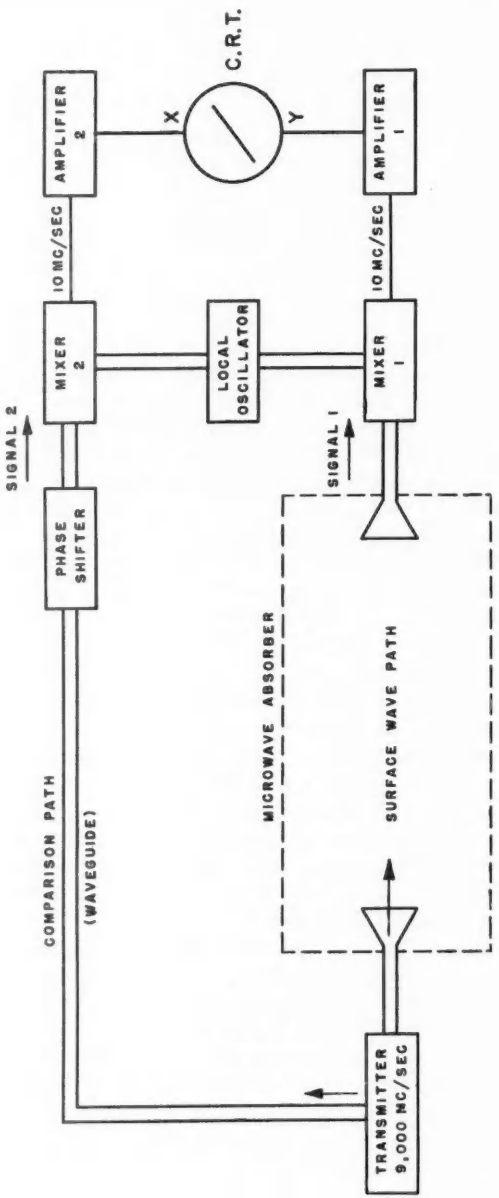

FIG. 2. Phase comparison system.

occurs over the metal sheets, and in general, a mixture of free-space waves and surface waves propagate over the guiding structure. For efficient guiding structures it appears that most of the power propagated over the metal sheets continues across the boundary and travels as a surface wave over the guiding structure to the receiver.

The surface wave velocity is easily deduced from the variation in phase of the received signal as the proportion of free-space and surface wave path is varied, their sum (i.e. the distance between transmitter and receiver) remaining constant. If the guiding structure does not propagate a surface wave, the variation in phase over path changes up to 110 cm does not exceed 2 or 3 degrees. If a very strong surface wave is propagated, monotonic changes of several thousand degrees over this path change can occur. Such large changes are measured in small increments of perhaps 30 degrees to avoid ambiguities in the phase.

2. Results

Measurements of the surface wave velocity by the technique outlined above were made for a large number of different depths of dry sand covering a flat aluminum sheet. Both transmitting and receiving antennas consisted of horns flared in the H plane only. These were oriented so that the electric vector was perpendicular to the sand surface, in order to excite only the TM mode, and were placed at the sand surface. The dry sand had a dielectric constant of 3.0 and a loss tangent of 0.001 at the frequency used, 8700 Mc/sec. Figure 3, for 2.8-cm sand depth, indicates a typical change of phase in the case of a surface wave whose amplitude greatly exceeds that of the accompanying free space wave. A change in phase of about 10 degrees per centimeter path change occurs. This indicates a surface wave velocity approximately 0.91 of c, the free-space velocity. Also apparent in this figure is a periodic oscillation of the phase about the average slope of the graph. This can be interpreted as the effect of interference between the surface wave and the accompanying free-space wave.

In Fig. 4 appear data for a 3-cm depth of sand which indicate both a monotonic change of phase and also a periodic one. This indicates that over part A of the graph, the free-space wave predominates, while over part B, the surface wave predominates. It will be noted that one period of oscillation of the phase in part A corresponds to a 360-degree change of phase in part B.

In the next two figures are shown completely periodic phase variations with no indication of a monotonic change. In Fig. 5, for a 3.2-cm depth of sand, the relatively large amplitude of the phase excursion indicates a surface wave with an amplitude less than, but still appreciable compared with, that of the free-space wave. In Fig. 6 for a 1-cm sand depth, the phase excursion is much smaller, and of very short period, indicating a weak surface wave with a velocity very different from that of free space, actually approximately $0.64c$. Also apparent in this figure is the existence of a second, much longer periodicity. This is not explicable on the basis of the theory outlined earlier as a second mode of propagation, even for a TE mode, since the velocity does not correspond to any of the theoretically allowable values for the particular depth of sand.

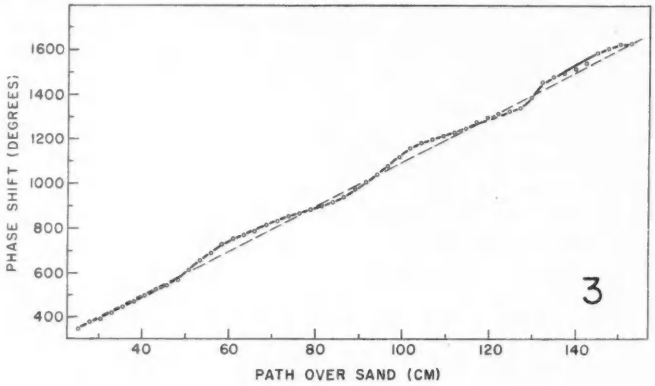

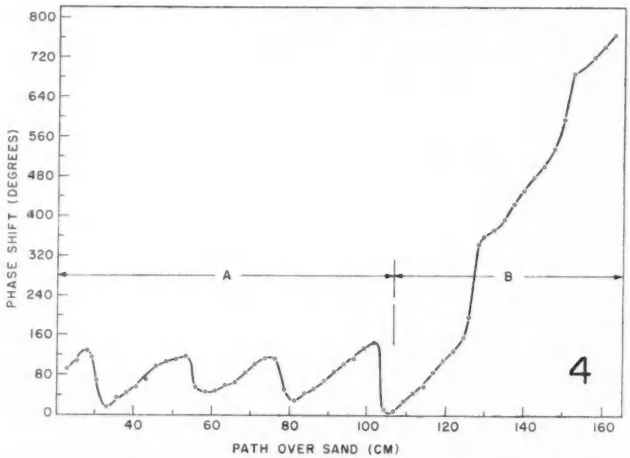

FIG. 3. Phase change for a surface wave with much greater amplitude than accompanying free-space wave.

FIG. 4. Phase change for a surface wave with amplitude slightly less than the free-space wave amplitude (part A), and slightly greater (part B).

In Fig. 7 the ratios of the velocities of surface and free-space waves, v/c, deduced from the experimental data are shown in relation to the values computed from the theory outlined earlier for the case of a loss-free dielectric with dielectric constant 3. The experimental points denoted by circles indicate surface waves with amplitudes greater than the free-space waves; the triangles indicate those with amplitudes less than the free-space waves. From the distribution of these points it can be seen that the strongest surface waves were excited when the velocity did not differ too much from c. Surface waves with velocities approaching the lower limit, defined by $c/\sqrt{\kappa_2'}$, were very weak, and for certain sand depths, it was not possible to detect any surface wave.

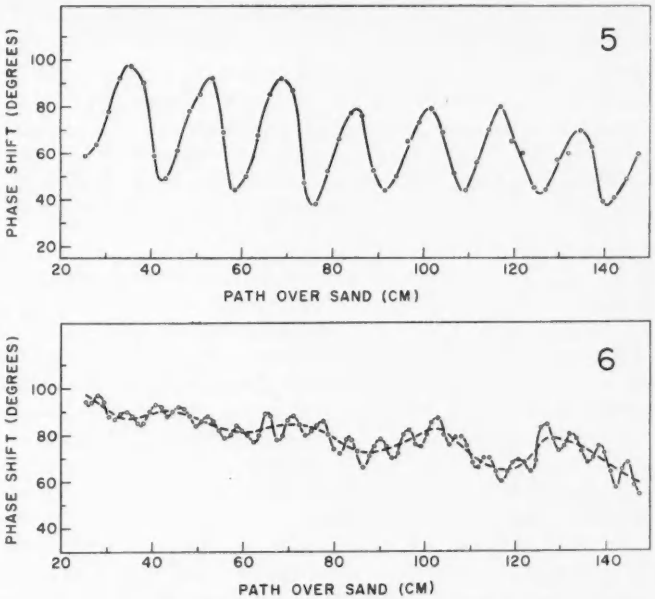

FIG. 5. Phase change for a surface wave with amplitude less than free-space wave.
FIG. 6. Phase change for surface wave amplitude very small compared with free-space wave.

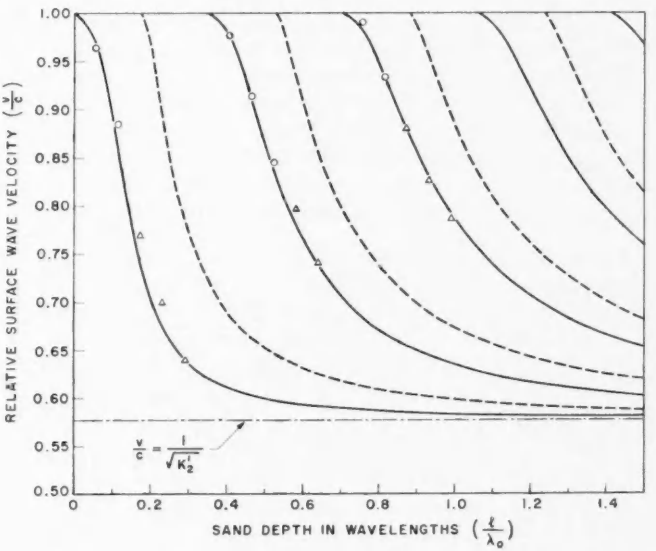

FIG. 7. Comparison of experimental and theoretical surface wave velocities as a function of sand depth. Experimental points for $\lambda_0 = 3.43$ cm. *TM* modes ———, *TE* modes – – –.

The agreement between the experimental data and the theory is satisfactory, considering the unavoidable difficulties in obtaining sand layers of uniform depths. While the theory indicates that for certain sand depths two or more modes with different velocities might propagate simultaneously, it was found experimentally that the mode having a phase velocity closest to c was excited. However, a number of phase curves measured exhibited weak secondary periodicities, indicating the possibility of simultaneous secondary *TM* or *TE* mode propagation, but these were not in agreement with theory.

3. Application to Radio Distance Measurement

There are cases where precise microwave distance measurements are made in areas where metallic conductors exist within a few inches or feet of the surface of the ground. If these are approximately plane, and the surface soil is sufficiently dry, it is possible to propagate a relatively strong surface wave. From Fig. 7, such a surface wave could be propagated with a velocity 10% less than c. If such propagation took place over even a 20-ft section of a 5000-ft survey line, an error of 2 ft or 1 part in 2500 would result.

In the case of the Tellurometer, an instrument recently developed for the precise measurement of distances up to 30 miles, even weak surface wave propagation could cause disturbing effects where the microwave beam travels near to the ground. With this instrument, the effects of ground reflection paths on the measurement are eliminated by varying the carrier frequency (Wadley 1958). This results in a periodic variation of the transit time between the measuring stations as a function of the carrier frequency, provided that the difference in path between direct and reflected beams is at least 10 wavelengths (100 cm). It can be shown that so long as the ratio of the amplitudes of the direct and reflected waves remains constant throughout the frequency variation, the average of this periodic curve gives the true transit time. For surface wave propagation, both the amplitude and velocity of propagation are functions of the frequency (Fig. 7). Consequently, in cases where surface wave propagation causes the variation of transit time, this method of averaging cannot be expected to yield correct results. Variations of transit time between stations not explicable by ground reflections have been measured and it is possible that these are due to some form of surface wave propagation.

REFERENCES

ATWOOD, S. S. 1951. J. Appl. Phys. **22**, 504.
BARLOW, H. M. and CULLEN, A. L. 1953. Proc. Inst. Elec. Engrs. (London), III, **100**, 329.
BROWN, J. 1953. Proc. Inst. Elec. Engrs. (London), III, **100**, 363.
RICH, G. J. 1955. Proc. Inst. Elec. Engrs. (London), B, **102**, 237.
STRAITON, A. W. and TOLBERT, C. W. 1948. J. Franklin Inst. **246**, 13.
WADLEY, T. L. 1958. Trans. S. African Inst. Elec. Engrs. **49**, 143.

FINE STRUCTURE IN THE $O^{16}(\gamma,n)O^{15}$ YIELD CURVE[1]

H. KING[2] AND L. KATZ

ABSTRACT

Fine structure in the $O^{16}(\gamma,n)O^{15}$ yield curve near threshold was examined using improved experimental techniques. Breaks were observed at threshold, 15.85, 16.14, 16.45, 16.74, 16.88, 17.05, 17.15, and 17.21 Mev. These energies are established to within ±0.04 Mev. The integrated photon absorption cross section in these breaks resulting in (γ,n) reactions was found to be 0.47±0.11 Mev-mb. Our results are in good agreement with the measurements of other workers.

INTRODUCTION

Previous studies (Katz *et al.* 1954; Penfold and Spicer 1955) revealed discontinuities or "breaks" in the residual 2.1-minute β^+ activity of O^{15} following the $O^{16}(\gamma,n)O^{15}$ reaction when this is measured as a function of peak bremsstrahlung energy. These breaks are attributed to resonance in the photon absorption cross section.

The present work reports detection of these discontinuities by a method of improved sensitivity in an energy region near threshold and compares our results with those of other investigators. As a result of improved betatron energy calibration techniques, good agreement is found among the different measurements and indicates that this scale can now be established at least up to 19 Mev with an accuracy of better than 40 kev.

EXPERIMENTAL TECHNIQUE—ACTIVATION NEAR THRESHOLD

(*i*) *Samples*

The experiments of Katz *et al.* (1954) and of Penfold and Spicer (1955) were performed with oxygen samples made by subjecting boric acid powder to high pressure. After irradiation the residual activity of a sample was measured with one or more Geiger–Mueller counters. While these samples are quite satisfactory at higher energies, the low-induced activity near threshold severely limits the statistical accuracy with which measurements can be made. The major difficulty in improving the counting rate is self-absorption within the sample.

To obtain a higher counting rate for a given dose, liquid scintillators containing oxygen were used. The scintillator samples were irradiated in the betatron X-ray beam, then placed in contact with a photomultiplier where the induced activity was registered. Thus all the betas stopped in the scintillating liquid are counted and only those which escaped from the surface were lost. This method had been previously used by Cohen and McElhinney (1956) to detect the $C^{12}(\gamma, n)C^{11}$ reaction.

[1]Manuscript received June 22, 1959.
Contribution from the Department of Physics, University of Saskatchewan, Saskatoon, Saskatchewan.
[2]Department of Physics, McMaster University, Hamilton, Ontario.

The scintillating material which we used was a mixture of *p*-terphenyl in *p*-dioxane to a concentration of 10 g per liter (Prescott 1956). This liquid was sealed in glass bottles to form a uniform set of samples which could be handled easily. The two types of bottles used are shown in Fig. 1.

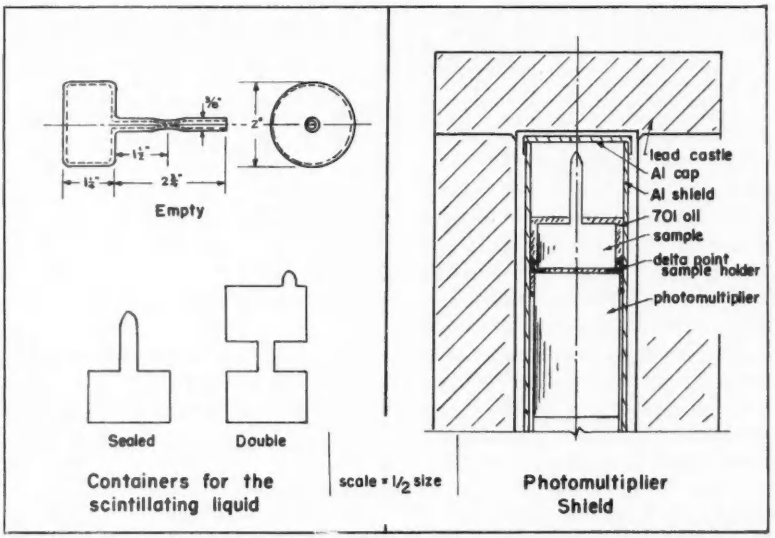

FIG. 1. Glass containers used to hold liquid scintillator and experimental arrangement to count the β^+ activity resulting from the $O^{16}(\gamma,n)O^{15}$ reaction in the scintillator liquid.

(*ii*) *Counting Apparatus*

After irradiation the activity in a sample was measured by placing it in optical contact with the photocathode of a 6342 photomultiplier tube. The tube was in a vertical position, with an aluminum cylinder sealed to it by O-rings and projecting above the photocathode to form a well. This well was partly filled with Dow Corning No. 701 silicone fluid and the samples to be counted were immersed in it. A retaining ring between the sample and photocathode served both to center the sample and to hold it a fixed distance (~1/16 in.) above the tube face (Fig. 1).

The counting system consisted of a commercial single-channel pulse height analyzer and counter. The counting rate was such that 200,000 or more counts were recorded in 5 minutes when the betatron was operating at 17.4 Mev.

(*iii*) *Experimental Setup*

The three experimental setups used are shown in Fig. 2.

(*a*) The normal setup was to place the samples between the betatron pole pieces about 27 cm from the X-ray target.

(*b*) For threshold measurements the "hour glass" shaped samples were

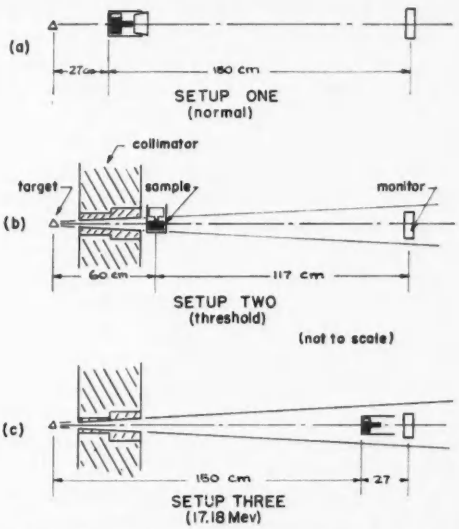

FIG. 2. Experimental arrangement during irradiation. For irradiations very close to threshold arrangement (*b*) was used with the special-shaped containers since at these energies there is very little O^{15} activity and the background from the irradiated glass is troublesome. The liquid was therefore irradiated in one half of the container and counted in the other half.

placed 60 cm from the X-ray target. The beam was collimated by 23 cm of lead to just strike the lower half of the bottle and the liquid it contained.

The samples were inverted when counting. By this method any activity induced in the glass (mainly in the silicon and only detectable near threshold) was almost completely kept from being counted.

(*c*) In the region near 17.18 Mev Penfold and Spicer (1955) had detected two very closely spaced levels. These can be resolved only by moving the sample back from the target to minimize thick target effects by subtending a smaller angle. This procedure effectively increases the number of photons in the high-energy tip of the bremsstrahlung spectrum. It was possible in this setup to move the sample 150 cm from the target and still obtain better than 1% counting statistics.

(*iv*) *Betatron Energy Calibration*

The energy scale of our betatron is usually established by calibration against the thresholds for a number of (γ,n) reactions. However, for internal consistency in this work, we adopted a different procedure due to the nature of our energy-controlling circuit. Our calibration equations can be written (Katz 1959)

$$I = ap+b$$

where I is the integrator helipot setting, p the electron momentum just prior to striking of the X-ray target, and a and b are constants.

Now in this equation a is directly related to the stability of our 100-volt reference supply, which is monitored against a standard cell and is kept fixed to 1 part in 10^4. But b depends on a number of variables, such as heater potentials in the circuit tubes, and may change slightly from day to day.

The procedure adopted was to check on the value of a by measuring the D^2 and C^{12} thresholds, but to fix the energy scale during each experiment relative to a level reported by Penfold and Spicer (1955) at 17.15 Mev.

On this basis our oxygen threshold measured on four separate occasions fell at 15.58±.06, 15.54±.06, 15.55±.06, and 15.56±.06: an average value of 15.56±.06. The quoted accuracy was determined by an estimate of the accuracy of our energy scale and the precision to which the threshold could be located, not the internal consistency of our data.

At the time of these measurements (1956–57) the accepted threshold for the $O^{16}(\gamma,n)O^{15}$ reaction was 15.59+.007 Mev (Mattauch *et al.* 1956) and thus we felt there was good internal consistency between our energy scale and the measured threshold position. The levels so found were reported at the 1958 Washington Photonuclear Conference and were in good agreement with the levels given by Penfold and Spicer (1955).

The recent change in the value of the (γ,n) threshold in O^{16} to 15.655+.007 Mev (Bendel *et al.* 1958) requires a re-examination of our previous quoted energies. The companion paper by Katz (1959) shows the "17.15" level to be really at 17.18±0.04 Mev. Recent precise measurements in our laboratory have confirmed this value. Accepting our value of 17.18 Mev requires that we add 0.03 Mev to our previously quoted level positions. The observed average oxygen threshold is now 15.59±0.06 Mev, which is just within experimental error of the new threshold energy of 15.65 Mev.

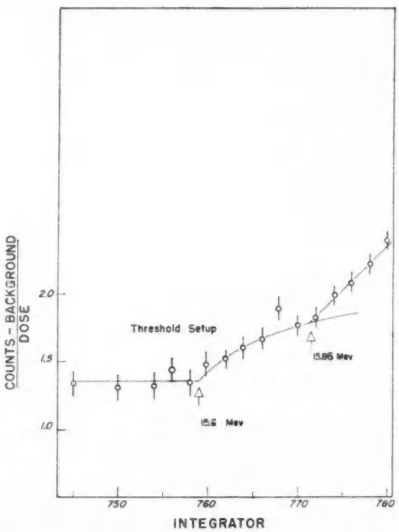

FIG. 3. Yield of O^{15} near threshold measured in recorded counts less the background per irradiation dose. The energy scale has been shifted 0.03 Mev as explained in the text.

RESULTS

In Fig. 3 we show one of the measurements near threshold taken in steps of 40 kev or less. The energy scale in this diagram has been corrected to make the "17.15" level fall at 17.18 Mev as outlined above. Each break

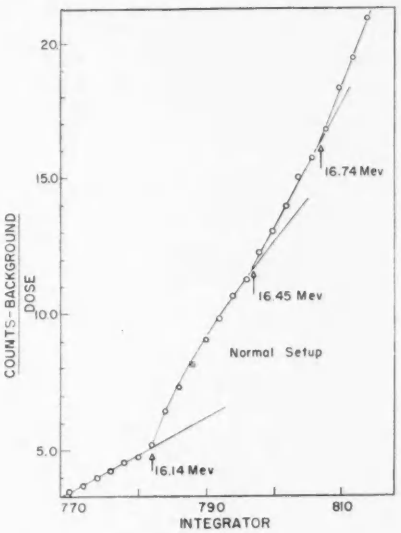

FIG. 4. Breaks in the $O^{16}(\gamma,n)O^{15}$ yield curve between 16.0 and 16.85 Mev.

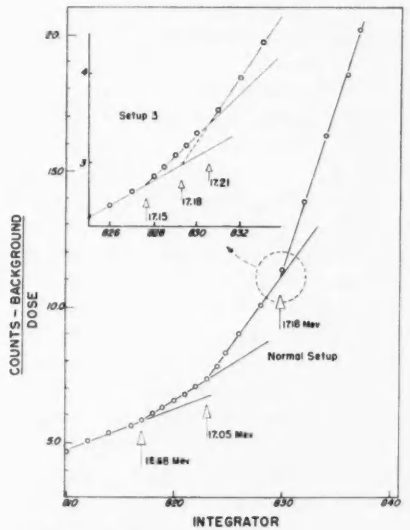

FIG. 5. Breaks in the $O^{16}(\gamma,n)O^{15}$ yield curve between 16.75 and 17.5 Mev. The curve was taken with the setup (*a*) illustrated in Fig. 2. Insert shows how the 17.18 Mev is resolved into two levels when setup (*c*) is used.

was measured at least three times, and averaging the results at each energy gave the curves shown in Figs. 4 and 5. Again the energy scale has been corrected by 0.03 Mev. The results of these measurements are collected in Table I and compared with those found by other workers. All values of the "break" positions found in this work are estimated to be established to within ±0.04 Mev.

TABLE I

Position of the breaks in the oxygen (γ,n) yield curve, their relative strengths, and comparison with other measurements

Present work		Bendel *et al.* (1958), $O^{16}(\gamma,n)O^{15}$	Geller and Muirhead (1958), $O^{16}(\gamma,n)O^{15}$	Jones *et al.* (1958), $N^{15}(p,n)O^{15}$
Break position, Mev	$G\int\sigma_i dE$, Mev-mb			
15.59±0.06			15.79±0.025	
15.85±0.04	0.001	15.94±0.05	16.08	
16.14±0.04	0.022	16.18±0.02	16.26	16.21 (1^+) 16.3 (0^-)
16.45±0.04	0.006		Not explored	
16.74±0.04	0.031		16.97	
16.88±0.04	0.034		17.07	~17.0
17.05±0.04	0.130		17.19	17.13
17.15±0.04 *	0.125		17.33	
17.21±0.04 *	0.125			17.29

$\sum_i G\int\sigma_i dE = 0.47\pm0.11$

*Our 17.18-Mev break is the average of these two levels.

The insert in Fig. 5 shows how the level at 17.18 Mev can be resolved into two levels by moving the samples away from the target as outlined in setup (*c*). It should be noted that except for the region between 16.2 and 16.5 Mev, the data defining the activation curves can be fitted by a series of straight lines between the breaks.

The integrated cross sections corresponding to the photon absorption levels which give rise to these breaks can be calculated from the formula (Katz *et al.* 1954)

$$G\int_{E_i}^{E}\sigma_i\,dE = \frac{\Delta\alpha(E_0)}{0.602P(E_i,E_0)},$$

where σ_i is the photon absorption cross section in the level giving rise to the ith break, G is the fraction of photons absorbed into the ith level which give rise to (γ,n) reactions, $P(E_i,E_0)$ is the number of photons of energy E_i per square centimeter per roentgen in the bremsstrahlung spectrum of maximum energy E_0, and $\Delta\alpha(E_0)$ represents the contribution to the yield curve at energy $E_0 > E_i$ by photon absorption into the ith level; it is measured in reactions per mole of sample per roentgen of radiation. Its absolute value was found by taking the yield of the $O^{16}(\gamma,n)O^{15}$ reaction at 22.0 Mev to be $(1.3\pm0.3)\times10^7$ neutrons/100 r mole (Katz, Lindenberger, and King 1959). Penfold and Spicer (1955) have shown that σ_i has its maximum value

at $\sim(E_t+\Gamma)$, where Γ is the level width. Since this is certainly less than 0.5 Mev we have taken $E_0 = E_t+\frac{1}{2}$ Mev and calculated the values of the integrated cross section for each of the levels. These are also collected in the table. The sum of the integrated cross sections over these levels

$$\sum G\int\sigma_t\,dE \text{ is } 0.47\pm0.11 \text{ Mev-mb.}$$

Carrying out an analysis by the photon difference method from threshold to 17.3 Mev we find

$$\int_0^{17.3}\sigma_{\gamma n}\,dE = 0.5\pm0.1 \text{ Mev-mb.}$$

This would seem to indicate that the levels account for most if not all the photon absorption cross section giving rise to (γ,n) reaction in O^{16} to this energy. The errors quoted are our best estimates of the absolute accuracy; their relative accuracy is probably twice as good.

DISCUSSION

The agreement between the measured positions of the breaks among the different researches listed in Table I is seen to be quite good. The first strong break above threshold, as shown in the table, was measured on four separate occasions at 16.14, 16.16, 16.11, and 16.16, giving an average value of 16.14 $\pm$0.04 Mev. This is to be compared with a narrow level found by Jones *et al.* (1958), at 16.21 Mev of 24-kev width. Penfold and Spicer (1955) have estimated that the break in the yield curve falls about one level width below the resonance energy, thus these results are in fair agreement.

Since the oxygen threshold is very difficult to establish, and breaks in the yield curve far above the threshold are not so readily identified, we would recommend that the break in the yield curve at 16.14$\pm$0.04 Mev be used for energy-scale calibration.

The wide level found by Jones *et al.* (1958) at 16.3 Mev is shown by them to have a spin and parity of 0^-. This cannot be reached by photon absorption into the O^{16} ground state (0^+) and has not been observed in our work. Two breaks found by us at 16.45+.04 and 16.74+.04 Mev were not observed by them, though if the published breaks of Penfold and Spicer (1955) are corrected to move their "17.15"-Mev break to 17.18 Mev two levels found by them have energies of 16.50 and 16.78 Mev. If the levels found by Geller and Muirhead (1958) are matched against ours as indicated in the table, then they are on the average at about 0.17-Mev higher energy.

Each of the two workers mentioned in the table (Bendel *et al.* 1958; Geller and Muirhead 1958) felt he was not able to observe the true $O^{16}(\gamma,n)O^{15}$ threshold, but found instead an experiment threshold where the reaction yield could be detected above background.* In each case this was some 0.1

*The Geller and Muirhead "16.08-Mev" break (as shown in the table) is 0.18 Mev above the mean position for this break as found by Bendel *et al.* and in the present work. Similarly their "16.26-Mev" break is 0.10 Mev higher. This may indicate that their energy scale is on the average $\sim$0.14 Mev high. Applying this correction to their threshold value places it at 15.65 Mev in excellent agreement with the mass data value.

to 0.15 Mev above the position on their energy scale where the true threshold was expected. Using an improved detection technique we were able to locate this threshold at the expected energy on our energy scale as established by other thresholds. Thus we conclude that with sufficient sensitivity the reaction $O^{16}(\gamma,n)O^{15}$ can in fact be detected at the true threshold energy.

REFERENCES

BENDEL, L. B., MCELHINNEY, J., and TOBIN, R. A. 1958. Phys. Rev. **111**, 1297.

COHEN, L. and MCELHINNEY, J. 1956. Rev. Sci. Instr. **27**, 7731.

GELLER, K. N. and MUIRHEAD, E. G. 1958. Precision energy measurements with a 25-Mev betatron (University of Penn. Report).

——— 1959. Bull. Am. Phys. Soc. Ser. II, **4**, 32.

JONES, K. W., LIDOFSKY, L. J., and WEIL, J. L. 1958. Phys. Rev. **112**, 1252.

KATZ, L., LINDENBERGER, H., and KING, H. 1959. Can. J. Phys. (to be published).

KATZ, L. 1959. Can. J. Phys. (this issue).

KATZ, L., HASLAM, R. N. H., HORSLEY, R. J., CAMERON, A. G. W., and MONTALBETTI, R. 1954. Phys. Rev. **95**, 464.

MATTAUCH, J., WALDMANN, L., BIERI, R., and EVELING, F. 1956. Ann. Rev. Nuclear Sci. **6**, 179.

PENFOLD, A. S. and SPICER, B. M. 1955. Phys. Rev. **100**, 1377.

PRESCOTT, J. R. 1956. J. Sci. Instr. **33**, 126.

EBULLIOMETRY AND THE DETERMINATION OF THE MOLECULAR WEIGHTS OF POLYMERS

PART III. CONSIDERATIONS ON THERMISTOR WHEATSTONE BRIDGES[1]

W. R. BLACKMORE

ABSTRACT

It is shown that a d-c. thermistor Wheatstone bridge may be used in ebulliometry to measure the small temperature differences which are observed between the boiling points of polymer solutions and the pure solvent. A relationship is derived between the thermistor bridge unbalance voltage and the solute molecular weight, which it is desired to measure. It is shown that a bridge composed of suitably matched thermistors may be made independent of the gross changes in boiling point of both solution and solvent produced by changes in atmospheric pressure. The possibility of the current flowing through the thermistors disturbing the measurements is discussed and *in situ* measurements of thermistor dissipation and time constants are given. The sensitivity attainable with various thermistor bridges and modern amplifiers at full gain is calculated and shown to be much greater than may be employed with the usual type of ebulliometer. The reason for this is the relatively large background noise (random temperature fluctuations) produced in the ebulliometer by the boiling process itself.

INTRODUCTION

Ebulliometry is the measurement of the elevation of the boiling point of a solution compared with that of the pure solvent at the same pressure. This elevation is inversely proportional to the molecular weight of the solute, and it is this latter quantity which it is desired to measure. Because of the inverse proportionality and the fact of working with polymers of high molecular weight, it is necessary to detect very small boiling-point elevations. There are two transducers with sufficient sensitivity to be used with polymer solutions. These are thermocouples (Saxton and Smith 1932; Plake 1935; Ray 1952; Smith 1956) and thermistors (Muller and Stolten 1953; Dimbat and Stross 1957; Lehrle and Majury 1958; Blackmore 1959*a*, *b*). An excellent discussion of both detector systems is given by Smith, Jones, and Chasmar (1957).

There are only two ways to use thermistors in ebulliometry. The more obvious way is to use a single thermistor as a platinum resistance thermometer is used. However, there are several serious objections to this method. Possibly the most serious is that the resistance of a calibrated thermistor may drift with its age and thermal history (Adey 1957). The better method of using thermistors is to obtain a matched pair and measure the boiling-point elevation differentially. In practice, the matched thermistors are used as separate arms in a Wheatstone bridge circuit. One thermistor is maintained at the boiling point of the solvent while the other measures the boiling point of the solution. Because their individual surroundings are at slightly different temperatures, the resistances of the thermistors differ. Hence an unbalance voltage appears at the bridge output terminals. The voltage is first amplified

[1]Manuscript received June 15, 1959.
Contribution from Canadian Industries Limited, Central Research Laboratory, McMasterville, Que.

and then displayed on a recorder. The changes in the unbalance voltage produced by successive additions of polymer pellets to the solution are dependent on the solute concentration and the solute molecular weight. This latter quantity is the object of the measurements and is determined by adding known weights of polymer to known amounts of solvent and using the changes in unbalance voltage from the bridge as measures of the boiling-point elevations.

The Wheatstone Bridge Unbalance Voltage

We begin by assuming the resistance of each arm (Fig. 1) is R, except for R_1 which has resistance of $R+\Delta R$, while $R_5 = bR$ and $R_6 = aR$. Under these conditions the unbalance voltage e_5, derived from the equations given by Harris (1952, pp. 688–689) is

$$(1) \qquad e_5 = E \cdot \frac{\Delta R}{R} \cdot \frac{b}{4(1+a)(1+b)+[3+2(a+b)+ab](\Delta R/R)} .$$

From a consideration of this equation (or from Harris 1952, pp. 692–695), it can be shown that e_5 is greatest when "a" is least. Furthermore, assuming $a = R_6/R$ is negligible, then the maximum e_5 is obtained for a detector with infinite input impedance. However, if a detector which is fundamentally power-sensitive is being used (e.g. a galvanometer) then the maximum sensitivity is achieved when the impedances of the bridge and detector are matched. The bridge for which equation (1) has been derived is an equal-arm bridge because this is the most sensitive arrangement (Harris 1952, p. 695) for any given proportional unbalance ($\Delta R/R$) and supply voltage E.

The Relation Between a d-c. Thermistor Wheatstone Bridge Unbalance Voltage, Solute Molecular Weight, and Concentration

For the sake of this discussion we will assume that the current limiting resistance R_6 (Fig. 1) is zero, and that the unbalance voltage detector has

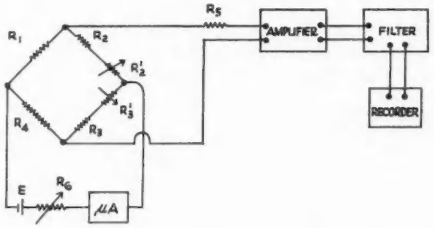

FIG. 1. R_1, R_4 thermistors; R_2, R_3 fixed wire-wound resistors; R'_2, R'_3 variable wire-wound resistance decades; R_5 detector resistance; R_6 current limiting variable resistor.

infinite impedance (e.g. a potentiometer). Hence equation (1) simplifies considerably to become

$$(2) \qquad e_5 = \frac{E}{4} \cdot \frac{\Delta R}{R} = \frac{i_b \cdot \Delta R}{4}$$

where i_b is the bridge current, and $(\Delta R/R)$ is assumed to be small (1% or less). Now for an ideal solution (or any solution at infinite dilution) the boiling-point elevation (Glasstone 1946, p. 635) is given by

$$\Delta T = \frac{R_g T^2 \cdot N_2}{L_g} \tag{3}$$

where R_g is the gas constant, L_g the latent heat of vaporization of the solvent, T the boiling point in degrees Kelvin, and N_2 the mole fraction of solute present in the solution. The equation relating the resistance of a thermistor to its temperature is

$$R = R_0 e^{B/T} \tag{4}$$

where R_0 is a constant, interpreted as a resistance at some reference temperature, B is a constant typical of the thermistor material, and T the temperature in degrees Kelvin. Now if we consider two matched thermistors (by which is meant that their R_0 and B values are identical) at temperatures T and $T+\Delta T$ then their resistances will differ by an amount

$$\Delta R = \frac{-B}{T^2} \cdot R \cdot \Delta T. \tag{5}$$

Hence, by combining (5), (3), and (2) we obtain an expression for the unbalance voltage from a thermistor bridge as a function of the solute mole fraction

$$e_5 = i_b \left(\frac{B \cdot R_g}{4 \cdot L_g} \right) \cdot R \cdot N_2. \tag{6}$$

The mole fraction of solute $N_2 = n_2/(n_1+n_2)$ where n_1 is the number of moles of solvent, and since in a dilute solution $n_1 \cong (n_1+n_2)$ while $n_2 = w_2/M_2$ where w_2 and M_2 are the weight and molecular weight of solute, respectively, therefore

$$e_5 = K \cdot i_b \cdot R \cdot \frac{M_1}{w_1} \cdot \frac{w_2}{M_2} \tag{7}$$

where $K = B \cdot R_g / 4L_g$. The changes in e_5 resulting from changes in w_2 are obtained by differentiating this equation to obtain de_5/dw_2. When the second component is a polymer, then M_2 is identical with M_n, the number average molecular weight (Hildebrand 1950). Strictly speaking equation (3) does not accurately represent the boiling-point elevation obtained with a polymer solution. For these a more appropriate form may be developed from an equation proposed by Huggins (1943) and used by Smith (1956). Equation (3) of Smith's paper is

$$\frac{\Delta T}{c_2} = \frac{R_g \cdot T^2 \cdot \bar{V}_1}{L_g} \cdot \frac{1}{M_2} + \frac{R_g T^2}{L_g d_2^2} (1/2 - \mu) c_2$$

where $c_2 = w_2/V_1$ is the polymer concentration in grams per cubic centimeter, $\bar{V}_1$ the partial molar volume of solvent, d_2 the polymer density, and μ is

Huggins' constant, providing a measure of polymer–solvent interaction. Combining equations (2) and (5) and substituting in Smith's equation (3) leads to an expression which when differentiated is

$$\frac{de_5}{dw_2} = 2K \cdot R \cdot i_b \left[\frac{V_1 \bar{V}_1}{M_n} + \frac{2}{d_2^2} (1/2 - \mu) w_2 \right]. \tag{8}$$

In actual practice, a series of recorder shifts Δs_j which are measures of de_5 and which are proportional to the boiling-point elevations produced by polymer pellets of weight, w_j, added to a constant volume of solvent, are plotted either as $\Sigma\Delta s$ vs. Σw corresponding to the simple case used in the derivation from equation (3) or as $(\Sigma\Delta s/\Sigma w)$ vs. Σw, which is dictated by equation (8). The actual magnitude of these temperature changes may be calculated if calibrated thermistors are employed or a standard material of known molecular weight may be used to calibrate the apparatus and permit a calculation of M_n directly and simply.

Thermistor Bridge Output Voltage as Affected by Atmospheric Pressure Changes

Suppose first that we consider the two-thermistor bridge in Fig. 1. At balance $(R_1/R_4) = (R_2/R_3)$ and if $R_1 = R_1^0 e^{B/T}$ while $R_4 = R_4^0 e^{B/T}$ then obviously the ratio R_1/R_4 is identical with R_1^0/R_4^0, which ratio is a constant independent of boiling temperature changes. Hence, the balance is unaffected by changes in atmospheric pressure. Even when the bridge is slightly off-balance the effect of a pressure change may be proved to be negligible as follows: equation (5) is substituted into equation (2) and the result differentiated treating both ΔT and T as functions of pressure. When the result of these operations is divided by e_5 to express the change on a relative basis and the data given by Washburn (1919) for benzene solutions is applied, we have

$$\frac{1}{e_5} \cdot \frac{de_5}{dp} = 0.05\% \text{ per mm Hg.}$$

Therefore for all practical purposes the output from a matched thermistor bridge is independent of pressure, even when the bridge is slightly off-balance.

Now, however, we must examine real thermistor bridges. The first point to be made is that the decade box (R_2' or R_3' in Fig. 1) used to keep the bridge near balance should not be in series in one thermistor arm. For then the value of the ratio of the thermistor arms is no longer constant with a change in atmospheric pressure. Furthermore, it has been assumed that the thermistor slopes are matched. Suppose, however, that R_1 and R_4 the thermistors in the bridge are mismatched and do not have the same B values, then

$$\frac{R_1}{R_4} = \frac{R_2}{R_3} = \frac{R_1^0 e^{B_1/T}}{R_4^0 e^{B_4/T}} = e^{\Delta B/T} \tag{9}$$

if we assume $R_0^1 = R_4^0$ and $\Delta B = B_1 - B_4$. Thus the bridge balance is sensitive to changes in atmospheric pressure and the sensitivity is greater the greater the difference in B.

Considerations on the Choice of a Suitable Bridge Current

In general, each thermistor will be at a temperature greater than that of its surroundings because of the electrical power developed in it. The difference

in temperature between either thermistor and its particular ambient temperature will be referred to as the "thermistor float." The first question which arises is whether the fluctuations in temperature in the liquid spiralling down either thermistor well are attenuated by the magnitude of the thermistor float.

To answer this question we may write the differential equation relating the thermistor temperature, T, to the ambient temperature, T_a, as

$$W-G(T-T_a) = C\frac{d}{dt}(T-T_0) \tag{10}$$

where W is the rate of heat flow into the thermistor produced by the electrical current flowing through it, while T_0 is the temperature of the thermistor at time $t = 0$. The symbols G and C refer to the thermal conductance and thermal capacitance of the sheath separating the thermistor bead from the flowing liquid. Now we wish to know the amplitude and phase lag in the temperature as measured by the thermistor when T_a oscillates about some mean value and particularly whether the magnitude of the thermistor float alters either of these quantities. If we let $T_a = T_m+X_0 \sin \omega t$ and $L = RC = C/G$ where R is here the thermal resistance of the sheath, then the solution to equation (10) is

$$T-T_m = WR+\left[(T_0-T_m)+\frac{LX_0\omega}{1+\omega^2L^2}-\frac{LW}{C}\right]e^{-t/L}+\frac{X_0}{(1+\omega^2L^2)^{1/2}} \times \sin(\omega t-\tan^{-1}\omega L). \tag{11}$$

This shows quite explicitly that the thermal resistance and capacitance of the sheath are the only two physical factors involved in the attenuation. Thus the first term on the right-hand side is a constant governed by the power developed in the thermistor and the thermal resistance encountered by this heat in being dissipated. The second term is a transient and dies out as soon as t becomes large compared to L, while the last term is the measured oscillation of the ambient temperature, the amplitude being reduced by the factor $1/(1+\omega^2L^2)^{1/2}$ with the phase lag $\tan^{-1}\omega L$. Thus a thermistor is able to follow oscillations in the ambient temperature more closely as both the time constant L of the thermistor assembly is small and the frequency $f = (\omega/2\pi)$ of the oscillations is low. Although this solution to the equation apparently allows as great a thermistor current as may be desired, there are reasons for maintaining only moderate currents. Among these are (*a*) for a large thermistor float (e.g. say 100° C) then the differential equation (10) would require modification to include a term correcting for radiation from the thermistor and (*b*) "current noise" (Bell 1955) in the thermistor might become significant.

DISSIPATION CONSTANTS

The following technique was employed to measure the dissipation constants of the thermistors in the thermistor well in the small ebulliometer (Blackmore 1959*a*). With the ebulliometer operating with pure solvent, the resistance of either thermistor was measured individually with the Tinsley Wheatstone bridge, and the Leeds and Northrup amplifier feeding a 10-mv full-scale

Brown Electronik potentiometer recorder. The pressure in the ebulliometer and surge tank was held constant so that the ambient temperature at the thermistor well was constant to better than ±.01° C. Then with the resistance of the thermistor at the lowest current chosen as the arbitrary zero, the current was increased to successively higher values and the change in thermistor resistance measured. A plot of ΔR vs. I^2R was then made. The slope of this line gave the number of ohms by which the thermistor resistance changed per milliwatt of power developed. Then since the thermistor was calibrated so that the resistance vs. temperature equation was known the dissipation constant was calculated in mw/°C. (Typical data are given in Table I.)

TABLE I

Dissipation constant data for upper thermistor

R, Ω	ΔR, Ω	Thermistor current, ma	I^2R, mw
4442.5	0	.05	.011
4439.1	3.4	.10	.044
4435.8	6.7	.15	.100
4432.1	10.4	.20	.177
4427.2	15.3	.25	.277
4421.1	21.4	.30	.398
4413.8	28.7	.35	.541
4406.5	36.0	.40	.705
4398.1	44.4	.45	.891
4386.3	56.2	.50	1.097

The slope of ΔR vs. I^2R is -49.5 Ω/mw and from the calibration for this thermistor dR/dT at a temperature of 110° C is -135.9 Ω/°C; therefore the dissipation constant is 2.75 mw/° C. The same technique was then used to measure the dissipation constant of the lower thermistor in the thermistor well with the pump operating. Several series of measurements were made with the pump operating at different rates for each series. Finally the dissipation constant was measured with foam being pumped over the thermistor well. No significant differences in dissipation constant under these conditions were found. The conclusion is that the glass in which the thermistor bead is encased largely determines the dissipation constant of the assembly. The dissipation constant actually measured for the lower thermistor was 2.95 mw/°C.

TIME CONSTANTS

The time required for the dissolution of a pellet added to boiling solvent or solution in the ebulliometer is in the range of seconds for very low molecular weight material, such as benzil, to perhaps 10 or more minutes for a fairly high molecular weight polymer. The time constant of the Tinsley Wheatstone bridge, Liston–Becker amplifier, and the Brown recorder ($\frac{1}{4}$ sec f.s. ±5 mv) was measured first by finding the amount of time required for the recorder pen to follow a resistance change in the variable arm of the Tinsley bridge. The time constant is given by the relation $\tau = t_{0.5}/\ln 2$, where $t_{0.5}$ is the

time required for the recorder pen to travel half the distance from its original to its final position. The bridge-amplifier time constant was 2.88 seconds.

The thermistor time constant was measured by suddenly switching the bridge current to a new value (e.g. from 500 μa $\rightarrow$ 1250 μa). This greater current forced the thermistor to float at a new temperature above ambient and effectively provided a measure of the time required for the thermistor to reach the new temperature level. Both the upper and lower thermistors were found to have time constants of 3.84 seconds. This proved that the thermistors were fast enough to follow the dissolution of most pellets added to the ebulliometer.

The Effect of Bridge Current Fluctuations

One possible effect of a bridge current fluctuation (di_b) on the unbalance voltage, e_5, from the bridge might be through a change in the thermistor float (ΔT), produced by the different power being developed in it. It is, however, possible to derive equation (12),

$$\frac{de_5}{e_5} = \frac{di_b}{i_b}\left[1-2B\left(\frac{\Delta T}{T^2}\right)\right], \tag{12}$$

which shows that the relative change in the unbalance voltage is equal to the relative fluctuation in the bridge current, since the bracketted expression is approximately equal to unity: $2B/T^2 \approx 0.05\ \text{deg}^{-1}$ for toluene at the boiling point and ΔT is certainly less than 1° C. Also for a Wheatstone bridge such as this it is easy to show that the relative fluctuation in the bridge current must be equal to the relative fluctuation in the bridge supply, a 2-volt lead–acid battery. But from Benson *et al.* (1950) we have $dE/E = 5\times10^{-5}$ per hour on open circuit and as the bridge current is so low hence $de_5/e_5 = 5\times10^{-5}$ as the relative change in e_5 per hour of operation. This drift is too small to be measured.

Choice of Amplifier, Frequency Response, and Filter Network

The microvolt d-c. chopper amplifiers which have been employed at C-I-L are the Liston–Becker Model 14 breaker amplifier and the Leeds–Northrup Model 9835. The Liston–Becker is the more sensitive of the two, and the sensitivity changes with the source impedance (Table II). With any Liston–

TABLE II

Input voltage required by different Liston–Becker amplifiers to produce identical outputs

Input impedance	Input voltage, μv
100 kΩ	10
10 kΩ	3
1 kΩ	0.6
20 Ω	0.1

Becker amplifier the noise level is about twice Johnson noise (Johnson 1928). For instance, a signal of 0.1 μv may be measured to $\pm1\%$ with the 20-Ω

amplifier. The Leeds–Northrup is not recommended for use with source impedances exceeding 10 kΩ. With no attenuation, full scale is 50 μv and the accuracy ±1%. The response times of the two amplifiers are about the same; both accept only low-frequency signals.

Attainable Sensitivity

In this section we wish to establish the magnitude of the unbalance voltage which might be obtained from equal-arm two-thermistor bridges with thermistors of different resistances (e.g. arms of 100 Ω, 1000 Ω, or 10 kΩ) and with different bridge currents when given a known temperature difference between the arms. The entries in Table III were computed using $e_s = i_b \cdot \Delta R/8$

TABLE III

The unbalance voltage from thermistor bridges with various bridge currents and thermistor resistances assuming a 1-degree difference in temperature between the thermistors

R, Ω	i, μa	P, mw	T, m°C	e_s, μv/°C
10,000	10	0.001	0.33	750
	100	0.1	33.0	7,500
	1,000	10.0	3,300.0	75,000
1,000	10	0.0001	0.033	75
	100	0.01	3.3	750
	1,000	1.0	330.0	7,500
100	10	0.00001	0.0033	7.5
	100	0.001	0.33	75.
	1,000	0.1	33.0	750.

NOTE: R is the thermistor resistance at the operating temperature, i is the thermistor current, P is the power developed in the thermistor, ΔT is the thermistor float above ambient temperature, e_s is the bridge output voltage per degree centigrade difference in temperature between the thermistor arms.

which is the approximation to equation (1) when it is assumed that the amplifier impedance is matched to the equivalent bridge resistance. The thermistor dissipation constant used was 3.0 mw/°C. Thermistors of the "bead-in-glass-probe" type (Victory Engineering Corporation) have been assumed to be used and their temperature coefficient of resistance has been taken as 3%. Now Table III apparently argues strongly in favor of a high-resistance, low-current bridge. However, suppose we use Tables II and III, to compare high resistance – low current bridges with high current – low resistance bridges, each feeding a matched impedance amplifier with the same power being developed in the thermistors. The result is that there is very little advantage, if any, to a high-resistance bridge over a high-current bridge.

If we consider the 100-Ω bridge at a thermistor current of 1.0 ma then a 133-μ°C difference in temperature between the arms produces a signal of 0.1 μv and with the 20-Ω amplifier the gain may be set so that 0.1 μv is a full-scale deflection on a Brown potentiometer recorder. Obviously this is well beyond the sensitivity which may be employed with a standard ebulliometer. For then the background noise is about ±(100 → 150) μ° C (Blackmore 1959*b*), or in other words ± a full-scale deflection.

CONCLUSION

The principal conclusion to be drawn from this study is that thermistor bridges and modern high-gain amplifiers offer greater sensitivity than may be employed in most ebulliometers. The principal problem in ebulliometry is to develop an apparatus in which the random temperature fluctuations produced in the boiling process are reduced in magnitude.

ACKNOWLEDGMENT

The author wishes to thank Mr. H. H. Wood for his frequent and valuable advice concerning the electrical equipment used in these investigations.

REFERENCES

ADEY, A. W. 1957. Radio Physics Laboratory, Project Report No. 22-1-2, Defence Research Telecommunications Establishment, Ottawa, Ontario.
BELL, D. A. 1955. Brit. J. Appl. Physics, **6**, 284.
BENSON, F. A. and HARRISON, D. 1950. J. Sci. Instr. **27**, 315.
BLACKMORE, W. R. 1959*a*. Can. J. Chem. **37**, 1508.
——— 1959*b*. Can. J. Chem. **37**, 1517.
DIMBAT, M., and STROSS, F. H. 1957. Anal. Chem. **29**, 1517.
GLASSTONE, S. 1946. Textbook of physical chemistry, 2nd ed. (D. Van Nostrand Company, Inc., New York).
HARRIS, F. K. 1952. Electrical measurements (John Wiley & Sons, Inc., New York).
HILDEBRAND, J. 1950. Solubility of non-electrolytes, 3rd ed. (Reinhold Publishing Corp., New York).
HUGGINS, M. L. 1943. Ind. Eng. Chem. **35**, 216.
JOHNSON, J. B. 1928. Phys. Rev. **32**, 97.
LEHRLE, R. S. and MAJURY, T. G. 1958. J. Polymer Sci. **29**, 219.
LISTON–BECKER INSTRUMENT COMPANY, INC., Stamford, Connecticut.
MULLER, R. H. and STOLTEN, H. J. 1953. Anal. Chem. **25**, 1103.
PLAKE, E. 1935. Z. phys. Chem. A, **172**, 105.
RAY, N. H. 1952. Trans. Faraday Soc. **48**, 809.
SAXTON, B. and SMITH, R. P. 1932. J. Am. Chem. Soc. **54**, 2626.
SMITH, H. 1956. Trans. Faraday Soc. **52**, 402.
SMITH, R. A., JONES, F. E., and CHASMAR, R. P. 1957. The detection and measurement of infrared radiation (The Clarendon Press, Oxford).
VICTORY ENGINEERING CORPORATION, Springfield Road, Union , N.J.
WASHBURN, E. W. and READ, J. W. 1919. J. Am. Chem. Soc. **41**, 729.

LUMINESCENCE AND CONDUCTIVITY INDUCED BY FIELD IONIZATION OF TRAPS[1]

RUDOLPH R. HAERING[2]

ABSTRACT

When a photoconductor is illuminated at low temperatures, trapping states may be populated by electrons. If the light is then removed and an electric field is applied to the sample, these traps may be emptied by field ionization. For an electric field which increases linearly with time, the conductivity and the luminescent brightness display a sharp maximum at some field strength. It is shown that this maximum may be used to obtain the trap energy. The analysis of such field-ionization-induced maxima is very similar to the analysis of glow curves in thermoluminescence.

1. INTRODUCTION

When a photoconductor is illuminated, electrons in the valence band and in bound states are excited to the conduction band. Once in the conduction band, these electrons may recombine with holes either directly or at recombination centers. Alternatively, these electrons may become trapped. A trapping state is simply a bound state at which recombination is improbable. If the above-mentioned illumination is carried out at low temperatures, it is possible to obtain a nonequilibrium electron distribution in which shallow traps are filled with electrons while deeper-lying recombination centers are empty. The reason for the stability of such an "inverted" electron distribution is simply that an electron, once trapped, can only recombine if it is first ejected from the trap into the conduction band. At low temperatures such ejection is improbable even for a shallow trap and hence the inverted distribution is metastable. An estimate of the half-life of this metastable state is clearly the ejection time for the trap in question,

$$\tau_{\text{eject}} = \frac{1}{N_c S v} \exp\left[+\frac{\epsilon_1}{kT}\right].$$

In this relation, ϵ_1 is the trap depth, N_c is the density of thermally available states in the conduction band, v is the thermal velocity of a carrier, and S is the capture cross section of the trap for capture of an electron. At 30° K, one obtains for a trap with $\epsilon_1 = 0.1$ ev and $S = 10^{-15}$ cm^2:

$$\tau_{\text{eject}} \sim 1 \text{ year}.$$

Even at somewhat higher temperatures, our inverted distribution has a half-life of the order of hours.

It is possible to assist the escape of electrons from traps in at least two ways. The most obvious method is to heat the sample. As the temperature is increased

[1]Manuscript received August 20, 1959.
Contribution from the International Business Machines Corporation Research Laboratory, Poughkeepsie, New York.
[2]Permanent address: Department of Physics, McMaster University, Hamilton, Ontario.

the probability of escape increases. On the other hand, the number of electrons which remain trapped decreases. For this reason, if either the conductivity or the light emission associated with carrier recombination is measured as a function of temperature during the warm-up, maxima characteristic of the traps in question are observed. The analysis of such "glow curves" is well-known (Klick and Schulman 1957; Bube 1957; Haering and Adams 1959).

Trapping states may also be emptied by the application of an electric field to the sample. Experiments of this type have been performed by Mattler and Curie (1950), by Boer, Kümmel, and Rompe (1952), and by Boer and Kümmel (1954). These experiments were performed at moderately high temperatures (−150° C). At these temperatures the probability of thermal ejection still exceeds the probability of field ionization for a typical trap. A true field-stimulated maximum cannot be expected unless the reverse is true. In the following theory it will be assumed that this is the case, which implies that the sample is at a very low temperature ($T \lesssim 30°$ K).

It is convenient to use a field which increases linearly with time in order to stress the analogy with thermal glow curves. If the conductivity or the light emission is then measured as a function of electric field, peaks similar to those observed in glow curves will be seen. In this paper we present the theory applicable to such an experiment and show how one may use the results to obtain the trap depth.

2. THEORY OF FIELD-INDUCED GLOW

The probability per unit time that an electron bound to a trap of ionization energy ϵ_1 is field ionized by an electric field E may be calculated using the WKB approximation and is given by

$$P(E) = \alpha_n(\epsilon_1)E^n \exp\left[-\frac{\beta(\epsilon_1)}{E}\right]. \tag{2.1}$$

The pre-exponential factor $\alpha_n E^n$ depends somewhat on the model chosen for the trap (Piper and Williams 1958). For example, a square well yields:

$$P(E) = 2\times10^7 \epsilon_1^{1/2}\left(\frac{m^*}{m}\right)^{1/2} E \exp\left[-\frac{7\times10^7 (m^*/m)^{1/2}\epsilon_1^{3/2}}{E}\right]. \tag{2.2a}$$

On the other hand, for a coulombic center one obtains

$$P(E) = 3.4\times10^{12}\left(\frac{m^*}{m}\right)^{-1/8} \epsilon_1^{5/8} E^{1/4} \exp\left[-\frac{7\times10^7 (m^*/m)^{1/2}\epsilon_1^{3/2}}{E}\right]. \tag{2.2b}$$

In equations (2.2*a*) and (2.2*b*) the electric field is to be measured in volts per centimeter and the ionization energy ϵ_1 is to be expressed in electron volts; m^* is the effective mass of a carrier in the conduction band. The theory we present below is not sensitive to the form of the pre-exponential factor $\alpha_n E^n$; if it were, one could not obtain reliable trap energies by this method.

We are now in a position to write down the rate equations governing the ejection of electrons from the traps. We shall assume that the recombination of carriers may be described by a recombination lifetime τ.[3] Furthermore, we

[3] A discussion of this point is contained in Haering and Adams (1959).

shall ignore the effect of retrapping for the moment. Later, we will see that the inclusion of retrapping does not alter our conclusions appreciably.

The rate equations are:

$$\frac{dn_1}{dt} = -n_1 P(E), \tag{2.3a}$$

$$\frac{dn_c}{dt} = -\frac{n_c}{\tau} - \frac{dn_1}{dt}. \tag{2.3b}$$

In equations (2.3*a*) and (2.3*b*), n_1 and n_c are the densities of trapped and conduction electrons respectively. We now assume that the electric field E is a linear function of time.

$$E = bt. \tag{2.4}$$

Clearly, the solution of (2.3*a*) is then

$$n_1 = n_0 \exp\left[-\frac{1}{b}\int_0^E P(E')dE'\right] \tag{2.5}$$

where n_0 is the initial density of trapped electrons. Similarly, equation (2.3*b*) yields

$$n_c = -\int_0^E dE' \frac{dn_1}{dE'} \exp\left[\frac{E'-E}{b\tau}\right] \simeq -b\tau \frac{dn_1}{dE}. \tag{2.6}$$

The approximation adopted in equation (2.6) involves averaging dn_1/dE over a range of fields $\Delta E \sim b\tau$. For a typical sweep rates ($b \gtrsim 10^2$ volts/cm sec) and a typical recombination lifetimes ($\tau \lesssim 10^{-3}$ sec), this is an excellent approximation. Hence using (2.5) and (2.6) we find

$$n_c(E) \simeq n_0 \tau P(E) \exp\left[-\frac{1}{b}\int_0^E P(E')dE'\right]. \tag{2.7}$$

The conductivity or the luminescent brightness will show a maximum when $n_c(E)$ is a maximum. Differentiating $\ln(n_c)$ and putting $d/dE \ln(n_c) = 0$, we obtain

$$\left.\frac{d \ln P}{dE}\right|_{E=E_m} = \frac{1}{b} P(E_m). \tag{2.8}$$

In differentiating $\ln P$ we need not differentiate the slowly varying pre-exponential factor. We then obtain

$$\frac{\beta}{E_m^2} = \frac{1}{b} P(E_m). \tag{2.9}$$

Using (2.1), this may be written

$$x^{n+2} e^x = \frac{\alpha_n \beta^{n+1}}{b} \tag{2.10}$$

where $x = \beta/E_m$. The right-hand side of (2.10) is readily evaluated for a square well or for a coulombic center. One finds

$$x^3 e^x = 9.8\times10^{22}\frac{(m^*/m)^{1/2}\epsilon_1^{5/2}}{b} \quad \text{(square well)}, \tag{2.11a}$$

$$x^{2.25} e^x = 2.2\times10^{22}\frac{(m^*/m)^{1/2}\epsilon_1^{5/2}}{b} \quad \text{(coulombic well)}. \tag{2.11b}$$

The values of x which satisfy (2.11a) and (2.11b) for a typical trap are very nearly equal. For instance, for $\epsilon_1 = 0.25$ ev, $m^*/m = 1$, and $b = 10^4$ volts/cm sec, we find $x \sim 30.1$ from (2.11a), while (2.11b) yields $x \sim 31.0$. We may conclude that the position of the maximum is not sensitive to the nature of the traps, and that if trapping energies are calculated from such maxima, these can be trusted to about 5% in a representative case.

Using the relation

$$\beta = 7\times10^7\left(\frac{m^*}{m}\right)^{1/2}\epsilon_1^{3/2} \tag{2.12}$$

equations (2.11a) and (2.11b) may be rewritten. We find

$$x^{4/3} e^x = 8.2\times10^9\frac{(m/m^*)^{1/3}E_m^{5/3}}{b} \quad \text{(square well)}, \tag{2.13a}$$

$$x^{7/12} e^x = 1.9\times10^9\frac{(m/m^*)^{1/3}E_m^{5/3}}{b} \quad \text{(coulombic well)}. \tag{2.13b}$$

If the effective mass is assumed known and E_m and b are measured, the trap energy ϵ_1 may be calculated from (2.13). The trap energy can also be obtained from any of the modes of analysis used in thermoluminescence (Klick and Schulman 1957; Bube 1957; Haering and Adams 1959). For instance, the method of Booth (1954) applied to the present problem yields

$$\beta = \frac{E_{m1}E_{m2}}{E_{m2}-E_{m1}}\left\{\ln\left(\frac{b_2}{b_1}\right)+3\ln\left(\frac{E_{m1}}{E_{m2}}\right)\right\} \quad \text{(square well)}, \tag{2.14a}$$

$$\beta = \frac{E_{m1}E_{m2}}{E_{m2}-E_{m1}}\left\{\ln\left(\frac{b_2}{b_1}\right)+2.25\ln\left(\frac{E_{m1}}{E_{m2}}\right)\right\} \quad \text{(coulombic well)}. \tag{2.14b}$$

In equations (2.14a) and (2.14b), E_{m1} is the electric field at which the maximum occurs when the sweep rate is b_1.

Effect of Retrapping

Equations (2.3a) and (2.3b) ignore the possibility that an electron, once liberated by field ionization, may be retrapped. We may readily include the effect of retrapping if we ignore the Pauli principle for the trapped electrons. In this case, retrapping may be described by a retrapping time

$$\tau_t = \frac{1}{N_t S v}$$

where N_t is the trap concentration, S is the cross section for electron capture, and v is the carrier velocity. Equations (2.3a) and (2.3b) now become

$$\frac{dn_1}{dt} = -n_1 P(E)+\frac{n_c}{\tau_t}, \tag{2.15a}$$

$$\frac{dn_c}{dt} = -\frac{n_c}{\tau} - \frac{dn_t}{dt}. \tag{2.15b}$$

Using (2.7) we readily find

$$n_c(E) \sim n_0 \frac{\tau\tau_t}{\tau+\tau_t} P(E) \exp\left[-\frac{1}{b}\int_0^E P(E')dE'\right]. \tag{2.16}$$

Comparing this result with equation (2.7) we see that to this approximation the effect of retrapping is simply to introduce an effective recombination lifetime

$$\frac{1}{\tau_{\text{eff}}} = \frac{1}{\tau} + \frac{1}{\tau_t}.$$

This change does not affect our earlier analysis.

3. DISCUSSION

There are a number of factors which limit the applicability of this method of measuring trap energies. The most important of these are:

1. The maximum electric field which can be applied to the sample. In what follows we shall assume (somewhat arbitrarily) that this field is 5×10^5 volts/cm.

2. The slowest sweep rate which is experimentally convenient. We shall assume that this rate is 140 volts/cm sec, which corresponds to turning the above field on in about one hour.

3. The smallest conductivity (or brightness) which can be measured. In the following estimate we confine our attention to a conductivity peak. We shall assume that a carrier concentration of 10^5 leads to a measurable conductivity. (With a mobility of 100 cm^2/volts sec this implies that a resistivity of 10^{12} ohms cm can be measured.)

4. The extent to which the traps can be initially populated. We shall assume that the initial trapped electron concentration, n_0, is 10^{15} cm^{-3}.

5. The magnitude of the recombination lifetime τ. We shall assume a representative value of 10^{-7} sec.

Using equation (2.13) and the limiting values for E_m and b given by conditions (1) and (2), one readily finds that the deepest trap which can be field ionized with this choice of parameters has an ionization energy of 0.4 ev. One might be tempted to decrease the sweep rate b even further, in order that deeper traps might be observed in the range of experimentally available fields. However, a decrease of b results in a corresponding decrease of the peak conductivity. For this reason, one cannot make b arbitrarily small. Let us investigate this point further.

The peak conductivity $\sigma(E_m)$ is readily evaluated from (2.7) and (2.10). One finds (Haering and Adams 1959)

$$\sigma(E_m) = n_c(E_m)q\mu = 0.37 n_0 q\mu\tau P(E_m). \tag{3.1}$$

In equation (3.1), q is the electron charge and μ is the carrier mobility. It has been assumed that $x = \beta/E_m \gg 1$. Using $n_0 = 10^{15}$ cm^{-3}, $\tau = 10^{-7}$ sec in equation (3.1), condition (3) requires that

$$P(E_m) \gtrsim 3\times10^{-3}\ \text{sec}^{-1}. \tag{3.2}$$

It is readily verified that in the above example this condition is satisfied. In fact, one obtains

$$P(E_m) \simeq 10^{-2}\ \text{sec}^{-1}.$$

In the present example a somewhat slower sweep rate could therefore be tolerated. Hence traps with ionization energies slightly larger than 0.4 ev could still be observed. For a given sweep rate, there exists a simple approximate relation between the trap energy and the field at which the maximum occurs. For the sweep rate used in the above example, one obtains

$$\epsilon_1 \sim \left(\frac{E_m}{2\times 10^6}\right)^{2/3}.$$

In some cases, conditions will be somewhat more favorable than those envisaged in the above example. For instance, if one is dealing with a large trap concentration or with a long recombination lifetime, the condition represented by equation (3.2) will be markedly less stringent. In such a case the use of slower sweep rates will enable one to observe slightly deeper traps.

The author would like to thank Drs. E. N. Adams, D. C. Mattis, and F. F. Morehead for helpful discussions.

REFERENCES

Boer, K. W., Kümmel, U., and Rompe, R. 1952. Z. phys. Chem. **200**, 180.
Boer, K. W. and Kümmel, U. 1954. Ann. Physik, **14**, 341.
Booth, A. H. 1954. Can. J. Chem. **32**, 214.
Bube, R. H. 1957. Phys. Rev. **106**, 703.
Haering, R. R. and Adams, E. N. 1959. Phys. Rev. (to be published).
Klick, C. C. and Schulman, J. H. 1957. Solid state physics, Vol. 5 (Academic Press, Inc., New York), p. 165.
Mattler, J. and Curie, D. 1950. Compt. rend. acad. sci. Paris, **230**, 2086.
Piper, W. W. and Williams, F. E. 1958. Solid state physics, Vol. 6 (Academic Press, Inc., New York), p. 118.

SPECTRAL DISTRIBUTION OF BREMSSTRAHLUNG FROM AN IONIZED GAS[1]

MAHENDRA SINGH SODHA

ABSTRACT

Using Heitler's and Sommerfeld's cross section the spectral distribution of bremsstrahlung from an ionized gas has been calculated, neglecting self-absorption and stimulated emission. These results can be used to calculate the spectral distribution of bremsstrahlung from a mass of ionized gas, considering self-absorption and stimulated emission if one utilizes the expression obtained by Allen and Hindmarsh.

INTRODUCTION

Cillie (1932) has given a classical treatment of the continuous spectrum of bremsstrahlung in an ionized gas. His calculation is an indirect one and makes use of thermodynamic equilibrium between radiation and matter. He arrived at expressions for spectral distribution of and total energy radiated by bremsstrahlung. In his treatment Cillie (1932) neglected self-absorption and stimulated emission. These processes were incorporated in the treatment of Allen and Hindmarsh (1955), who investigated spectral distribution of bremsstrahlung from a mass of ionized gas, using Cillie's result.

Heitler (1944) has given a wave mechanical treatment for the production of bremsstrahlung by collision between electrons and positive ions, using Born approximation. He calculated the cross section for a collision between a positive ion and an electron of given energy E, which emits a photon of energy ϵ in the process. Sommerfeld (1931) extended Heitler's treatment to give cross section, when Born approximation is no longer valid. These cross sections have been used by Thompson (1957) to calculate the total energy radiated per unit volume by an ionized gas, taking into account the velocity distribution of electrons.

In this communication the author has used the cross sections of Heitler (1944) and Sommerfeld (1931) to calculate the spectral distribution of bremsstrahlung per unit volume, neglecting self-absorption and stimulated emission. Spectral distribution of energy radiated by a mass of ionized gas, enclosed between two infinite planes has also been considered, taking into account self-absorption and stimulated emission.

SPECTRAL DISTRIBUTION OF BREMSSTRAHLUNG

The cross section of collision between a positive ion of charge Ze and an electron of energy E, emitting a photon of energy $\epsilon = h\nu$ in the process is given by (Heitler 1944; Sommerfeld 1931)

[1]Manuscript received May 1, 1959.
Contribution from the Armour Research Foundation of the Illinois Institute of Technology, Chicago, Illinois. Work supported by Rome Air Development Center and Air Research Development Command.

$$\phi(E,\epsilon)d\left(\frac{\epsilon}{E}\right)=\frac{A''}{\epsilon}\ln\left\{\frac{(\sqrt{E}+\sqrt{E-\epsilon})}{\sqrt{\epsilon}}\right\}^2 f d\left(\frac{\epsilon}{E}\right) \tag{1}$$

where

$$A''=\frac{8}{3}\frac{Z^2e^6}{\hbar mc^3};$$

f is a factor due to nonvalidity of Born approximation and given by

$$f=\frac{(2\pi\xi)(2\pi\xi_0)}{\{1-\exp(-2\pi\xi)\}\{\exp(2\pi\xi_0)-1\}}$$

where

$$\xi_0=\frac{e^2}{\hbar}\cdot\frac{1}{v}=\frac{e^2}{\hbar}\left(\frac{m}{2E}\right)^{1/2}=\frac{e^2}{\hbar}\left(\frac{m}{2kT}\right)^{1/2}b^{-1/2}(x+1)^{-1/2},$$

$$\xi=\frac{e^2}{\hbar}\cdot\frac{1}{v'}=\frac{e^2}{\hbar}\left\{\frac{m}{2(E-\epsilon)}\right\}^{1/2}=\frac{e^2}{\hbar}\left(\frac{m}{2kT}\right)^{1/2}b^{-1/2}x^{-1/2};$$

m is the mass of electron,

v and v' are the velocities of the electron before and after collision,

and $x=(E-\epsilon)/\epsilon=(E-h\nu)/h\nu$.

The spectral distribution of bremsstrahlung per unit volume is given by

$$F(\nu)d\nu=F_1(\epsilon)\frac{d\epsilon}{h}=\frac{1}{h}n_+d\epsilon\int_\epsilon^\infty\epsilon\Phi(E,\epsilon)\cdot\frac{1}{E}n(v)\cdot vdv \tag{2}$$

where $F(\nu)d\nu$ is the energy of bremsstrahlung per unit time per unit volume between the frequencies ν and $\nu+d\nu$, n_+ is the number of ions per unit volume, $n(v)dv$ is the number of electrons having velocities between v and $v+dv$ given for a Maxwellian distribution by

$$n(v)dv=\frac{4n_-\beta^{3/2}v^2e^{-\beta v^2}dv}{\pi^{1/2}}. \tag{3}$$

n_- is the number of electrons per unit volume,

$\beta=(m/2kT)$,

k is Boltzmann constant,

and T the temperature of the gas.

Combining eqs. (1), (2), and (3), we get

$$F(\nu)=A'\int_\epsilon^\infty f.\ln\left\{\frac{\sqrt{E}+\sqrt{E-\epsilon}}{\sqrt{\epsilon}}\right\}^2\cdot\frac{v^3}{E}e^{-\beta v^2}dv \tag{4}$$

where $A'=4A''n_+n_-\beta^{3/2}/\pi^{1/2}$.

Putting $\{(E-\epsilon)/\epsilon\}=x$ and $E=(1/2)mv^2$ in eq. (4) we get

$$F(\nu)=Abe^{-b}I(b) \tag{5}$$

where $$b = \epsilon/kT = h\nu/kT,$$

$$A = \frac{4}{m^2} A'kT = \frac{64(2\pi)^{1/2} Z^2 e^6 n_+ n_-}{3c^3 m(mkT)^{1/2} \cdot h},$$

and

$$I(b) = \int_0^\infty f \cdot \ln(\sqrt{x} + \sqrt{1+x}) \exp(-bx) dx.$$

When Born approximation is valid $f = 1$ and

$$I = \int_0^\infty \ln(\sqrt{x} + \sqrt{1+x}) \exp(-bx) dx = \frac{e^{-b/2}}{2b} K_0(b/2).$$

ABSORPTION COEFFICIENT

If $\chi(\nu)/4\pi$ is the absorption coefficient corrected for stimulated emission Kirchhoff's law gives

$$\frac{F(\nu)}{\chi(\nu)} = B(\nu) = \frac{2h\nu^3}{c^2} \{1 - \exp(-h\nu/kT)\}^{-1} \qquad \text{(Planck's function)}$$

or

$$\chi(\nu) = \frac{32(2\pi)^{1/2}}{3ch\nu^2} \cdot \frac{Z^2 e^6 n_+ n_-}{(mkT)^{3/2}} e^{-b(1-e^{-b})I(b)}. \tag{6}$$

EMISSION FROM A MASS OF IONIZED GAS

Allen and Hindmarsh (1955) have considered radiation by the surface of an ionized gas bounded by two parallel infinite planes at a distance l and have shown that

$$\Psi(\nu) = \pi B(\nu) \left[1 - \exp\left(-\frac{\chi(\nu) l}{4\pi}\right) \cdot \left(1 - \frac{\chi(\nu) l}{4\pi}\right) - \left(\frac{\chi(\nu) l}{4\pi}\right)^2 E_1\left(\frac{\chi(\nu) l}{4\pi}\right) \right] \tag{7}$$

where $\Psi(\nu)d\nu$ is the energy radiated between frequencies ν and $\nu + d\nu$ per unit area per unit time of the surface, and

$$E_1(Z) = \int_1^\infty \exp(-Zt) \frac{dt}{t}$$

is a tabulated function.

NUMERICAL RESULTS

Table I gives b, e^{-b}, $bI(b)$, and $be^{-b}I(b)$, when Born approximation is valid.

Thus we see that the spectral distribution $be^{-b}I(b)$ is much different than that obtained by Cillie (1932) (e^{-b}), on classical arguments.

Table II illustrates the variation of $I(b, T)$ with b and T, when Born approximation is not valid.

TABLE I

Variation of $I(b)$, $bI(b)$, e^{-b}, and $be^{-b}\,I(b)$ with b

b	$I(b)$	$bI(b)$	e^{-b}	$be^{-b}I(b)$
10^{-3}	3.85×10^{3}	3.85	999001×10^{-6}	3.85
10^{-2}	2.72×10^{2}	2.72	990050×10^{-6}	2.69
10^{-1}	1.64×10	1.64	904837×10^{-6}	1.48
10^{0}	7.59×10^{-1}	7.59×10^{-1}	367879×10^{-6}	2.79×10^{-1}
10^{1}	2.73×10^{-2}	2.73×10^{-1}	45×10^{-6}	12×10^{-6}
10^{2}	4.85×10^{-4}	4.85×10^{-2}	2.69×10^{-44}	13×10^{-46}

TABLE II

Variation of $I\,(b,\,T)$ with b and T

b ↓ \ T in °K →	10^{4}	10^{5}	10^{6}	10^{7}	10^{8}
10^{-3}	2.60×10^{-1}	2.06×10^{2}	1.81×10^{3}	2.37×10^{3}	1.56×10^{3}
10^{-2}	2.01×10^{-2}	1.56×10^{1}	1.35×10^{2}	1.82×10^{2}	1.32×10^{2}
10^{-1}	1.55×10^{-3}	1.15×10^{0}	9.02×10^{0}	1.00×10^{1}	5.40×10^{0}
10^{0}	2.31×10^{-4}	1.53×10^{-1}	7.54×10^{-1}	5.32×10^{-1}	2.27×10^{-1}
10^{1}	3.13×10^{-3}	5.91×10^{-2}	5.18×10^{-2}	2.17×10^{-2}	7.34×10^{-3}
10^{2}	5.56×10^{-3}	5.17×10^{-3}	2.19×10^{-3}	7.56×10^{-4}	2.46×10^{-4}

Comparison of Tables I and II shows that the spectral distribution obtained by using Born approximation is very much different than that obtained otherwise especially for higher frequencies (large values of b).

ACKNOWLEDGMENTS

The author is grateful to Dr. L. Reiffel and Dr. J. J. Brophy for kind encouragement and to Mr. B. Kallick for evaluating $I(b,\,T)$ on the electronic computer.

REFERENCES

CILLIE, G. 1932. Monthly Notices of Royal Astronomical Society, **92**, 820.
ALLEN, J. E. and HINDMARSH, W. R. 1955. Atomic Energy Research Establishment, Harwell, England, GP/R-1761.
HEITLER, W. 1944. Quantum theory of radiation (Oxford University Press, London).
SOMMERFELD, A. 1931. Ann. Physik, **11**, 257.
THOMPSON, W. B. 1957. Atomic Energy Research Establishment, Harwell, England, T/M 73.

ON THE DIFFRACTION OF ELECTROMAGNETIC PULSES BY CURVED CONDUCTING SURFACES[1]

JAMES R. WAIT AND ALYCE M. CONDA

ABSTRACT

Starting with the known steady-state solutions for diffraction by a perfectly conducting convex surface, the corresponding transient responses are derived using Fourier–Laplace inversion. Explicit results are given for an incident wave which varies with time as a step function.

INTRODUCTION

The behavior of electromagnetic fields in the presence of diffracting obstacles is usually restricted to the time-harmonic case. For example Fock (1946), in a classic paper, obtained a universal function which enables the surface current density for a time factor exp ($i\omega t$) to be calculated in the penumbral region. He thus bridged the gap between geometrical optics in the lit region and the diffraction field deep in the shadow. The corresponding treatment for a transient or pulse incident field has never been explicitly carried out as far as the authors are aware. It is the purpose of this paper to consider this problem. The method employed is quite straightforward since it is based on a Fourier–Laplace representation of the transient response. Thus the starting point is the corresponding steady-state solution. This general approach has been used recently in several related problems in electromagnetic theory (Wait 1956, 1957*a*, 1957*b*; Oberhettinger 1956; Levy and Keller 1958; Johler and Walters 1959; Weston 1959).

Four physical situations are considered in the present paper. The first two concern the currents excited on a convex metallic surface for vertical and horizontal polarization respectively. The latter two deal with the Fresnel diffraction field of a convex metallic surface in which case the source and observer are at a large distance from the crest on the convex obstacle. Again, this is carried out for both vertical and horizontal polarization.

THE EXCITED CURRENTS

For convenience, the model is chosen to be a circular cylinder of radius a, of infinite length, and of perfect conductivity. A cylindrical co-ordinate system (ρ, ϕ, z) is chosen such that the cylindrical surface is defined by $\rho = a$. A normally incident plane wave with the magnetic vector parallel to cylinder axis is represented by

$$H_z^{\text{inc}} = H_0 e^{ik\rho \cos \phi} \qquad (k = \omega/c)$$

for an implied time factor of exp($i\omega t$). The excited current density on the surface of the cylinder is numerically equal to the resultant tangential magnetic field. This is given exactly by (Wait 1959)

[1]Manuscript received August 28, 1959.
Contribution from the Central Radio Propagation Laboratory, Boulder, Colorado.

$$H_z\Big]_{\rho=a} = H_0 F(ka, \phi) \tag{1}$$

where

$$F(ka, \phi) = \frac{2}{\pi i ka} \sum_{m=0}^{\infty} \frac{\epsilon_m e^{im\pi/2} \cos n\phi}{H_m^{(2)\prime}(ka)} \tag{2}$$

where $\epsilon_0 = 1$, $\epsilon_m = 2$ $(m = 1, 2, 3, \ldots)$, and $H_m^{(2)\prime}(ka)$ is the derivative of the Hankel function of the second kind. Unfortunately this representation is poorly convergent unless ka is small. Furthermore, the analytical form is not convenient for the transient computation.

It may be shown that for large ka, $F(ka, \phi)$ may be approximated by (Wait 1959)

$$F \cong \frac{e^{-ika\theta}}{\sqrt{\pi}} \int_\Gamma \frac{\exp[-i(\omega a/2c)^{\frac{1}{3}}\theta\tau]d\tau}{w_1'(\tau)} \tag{3}$$

where Γ, the integration contour, runs from $\infty\, e^{-i2\pi/3}$ to 0, then out along the real axis to ∞. The angle θ $(= \phi - \pi/2)$ measures positive into the (geometrical) shadow and negative into the (geometrical) lit region.* The function $w_1'(\tau)$ is the derivative of the Airy integral function $w_1(\tau)$ with respect to τ.†

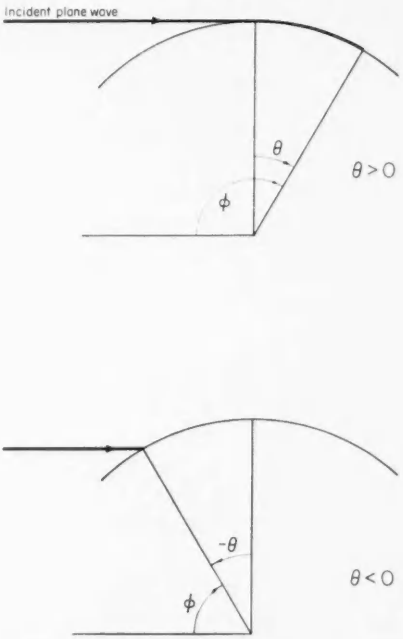

FIG. 1. Diagram indicating a plane wave incident on a cylindrical surface.

*As indicated in Fig. 1.

†This Airy integral function is related to the more conventional Hankel function of order 1/3 by

$$w_1(\tau) = e^{-i2\pi/3}(\pi/3)^{1/2}(-\tau)^{1/2}H_{1/3}^{(2)}[(2/3)(-\tau)^{3/2}].$$

Also see appendix.

The incident field is now considered to vary with time as a positive step function; for example,

$$h_z^{\text{inc}} = H_0 u\left(t - \frac{\rho}{c}\sin\theta\right) \tag{4}$$

where

$$\begin{aligned} u(x) &= 1 \qquad \text{for } x > 0 \\ &= 0 \qquad \text{for } x < 0. \end{aligned}$$

The corresponding form of the tangential magnetic field (i.e., the surface current) is given formally by the Fourier integral

$$h_z(t)\Big]_{\rho=a} = H_0 \frac{1}{2\pi}\int_{-\infty}^{\infty} \frac{F}{i\omega} e^{i\omega t}\, d\omega \tag{5}$$

where F is defined either by equation (2) or (3) and the factor $1/(i\omega)$ is the Fourier transform of the unit step function. For convenience in what follows it is desirable to use Laplace transform notation and thus

$$j^{(v)}(t) = \frac{h_z(t)]_{\rho=a}}{H_0} = \frac{1}{2\pi i}\int_{\delta-i\infty}^{\delta+i\infty} \frac{F}{s} e^{st} ds = L^{-1}\frac{F}{s} \tag{6}$$

and

$$F = s\int_0^{\infty} e^{-st} j^{(v)}(t) dt = sLj^{(v)}(t) \tag{7}$$

where formally $s = i\omega$ and L is the symbolic Laplace operator.

To facilitate the integration F is written in the following form:

$$F = e^{-ika\theta} \sum_{n=0,1,2,3,\ldots}^{\infty} \left[-i\left(\frac{\omega a}{2c}\right)^{\frac{1}{3}}\theta\right]^n I_n^{(v)} \tag{8}$$

or

$$F = e^{-ia\theta s/c} \sum_{n=0,1,2,3,\ldots}^{\infty} \left(\frac{sa}{2c}\right)^{n/3} \theta^n e^{-i2\pi n/3} I_n^{(v)} \tag{9}$$

where

$$I_n^{(v)} = \frac{1}{\sqrt{\pi}}\frac{1}{n!}\int_\Gamma \tau^n \frac{1}{w_1'(\tau)} d\tau. \tag{10}$$

By using the standard result

$$\frac{1}{s^\nu} = L\left[\frac{t^{\nu-1}}{\Gamma(\nu)} u(t)\right] \tag{11}$$

the inversion of each term leads readily to

$$j^{(v)}(t) \cong \sum_{n=0}^{\infty} \frac{I_n^{(v)} e^{-i2\pi n/3}}{\Gamma(1-n/3)} \frac{1}{T^{n/3}} \tag{12}$$

where

$$T = \frac{2c(t-a\theta/c)}{a}\,\theta^3$$

is a dimensionless time parameter. The function $j^{(v)}(t)$ is real since $I_n^{(v)}e^{-12\pi n/3}$ is real for each value of n.

Using values of $I_n^{(v)}$ listed in the Appendix, the function $j^{(v)}(t)$ was computed for various values of T. The nature of the results is shown in Fig. 2*a* for values

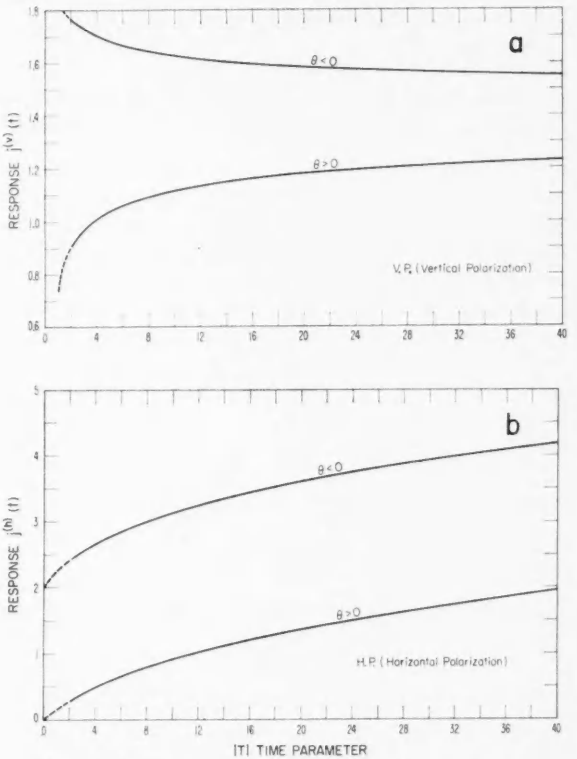

FIGS. 2*a* and 2*b*. The current density on a cylindrical surface excited by an incident plane wave whose wave front is a step function.

of T ranging from 1 to 40. For smaller values of T the convergence of the series becomes bad and considerable effort is required to obtain numerical values. For the present calculation only 10 terms in the series were retained and it is expected that this leads to a maximum error of about 1% for $T>1$. As expected, in the illuminated region (i.e., $\theta<0$) the function $j(t)$ is descending from the value 2 at very small T to the value 1.40 at very large T. In the

shadow the field increases from 0 at very small T towards the value 1.40 at very large T.

The case of horizontal polarization is now considered. The incident field has its electric vector parallel to the axis of the cylinder. Thus

$$E_z^{\text{inc}} = E_0 e^{ik\rho \cos\phi}.$$

The tangential magnetic field on the cylinder for the time-harmonic case may be expressed in the form (Wait and Conda 1959)

$$H_\phi\Big]_{\rho=a} \cong \frac{-E_0}{\eta_0} \frac{e^{-ika\theta}}{(ka/2)^{1/3}} U(X) \tag{13}$$

where

$$X = \left(\frac{\omega a}{2c}\right)^{\frac{1}{3}} \theta$$

and

$$U(X) = \frac{1}{\sqrt{\pi}} \int_\Gamma \frac{e^{-iX\tau}}{w_1(\tau)}\, d\tau. \tag{14}$$

Writing

$$U(X) = \sum_{n=0}^{\infty} (-iX)^n I_n^{(h)} \tag{15}$$

it is seen that

$$I_n^{(h)} = \frac{1}{\sqrt{\pi}} \frac{1}{n!} \int_\Gamma \tau^n \frac{1}{w_1(\tau)}\, d\tau. \tag{16}$$

For a step-function incident field

$$e_z^{\text{inc}} = E_0 u\left(t - \frac{\rho}{c} \sin\theta\right)$$

it readily follows that the transient response of the tangential magnetic field is given by

$$h_\phi(t) = \frac{E_0}{\eta_0} \theta \sum_{n=0}^{\infty} \frac{I_n^{(h)} e^{-i[(2n+1)/3]\pi}}{\Gamma[(4/3)-(n/3)]} \frac{1}{T[(n/3)-(1/3)]} \tag{17}$$

where

$$T = \frac{2c(t-a\theta/c)}{a} \theta^3.$$

For purposes of illustration a function $j^{(h)}(T)$ is introduced which is defined by

$$h_\phi(t) = \frac{E_0}{\eta_0} |\theta| j^{(h)}(t). \tag{18}$$

The quantity $j^{(h)}(t)$ is plotted in Fig. 2*b* as a function of T. As expected, in the illuminated region (i.e., $\theta<0$) the function $j^{(h)}(t)$ is approaching 2 for very small T. In the shadow region, $j^{(h)}(t)$ approaches zero for small T as it must.

In general the function $j^{(h)}(t)$ increases with T and becomes proportional to $T^{1/3}$ for large values of T.

The formulae quoted above for the functions $j^{(v)}(t)$ and $j^{(h)}(t)$ are asymptotic expansions in reciprocal powers of T. These expansions are not useful and probably not valid for $T<1$. However, from the initial value theorem in Laplace transforms it is known that the behavior of the transform for s tending to ∞ is related to the behavior of the corresponding time function as t approaches zero. Thus for small times

$$j^{(h)}(t) \cong j^{(v)}(t) \cong 2u\left(t-\frac{a\sin\theta}{c}\right) \qquad \text{for } \theta < 0 \tag{19}$$

$$\cong 0 \qquad \text{for } \theta > 0.$$

This simple formula corresponds to geometrical optics and is consistent with the trend of the curves in Figs. 2*a* and 2*b* for small values of T as described above.

FRESNEL DIFFRACTION FIELDS

Another special case of considerable practical interest is when the source and observer are both at large distances (in terms of wavelengths) from the crest of the perfectly conducting obstacle. In the vicinity of the "line-of-sight", the field may be expressed (for the time-harmonic case) as a ratio to the "free-space field" by the function (Wait and Conda 1959)

$$A \cong A_0 + A_1 e^{-t\alpha^2} \tag{20}$$

where

$$A_0 = \frac{e^{t\pi/4}}{\sqrt{\pi}} \int_\alpha^\infty e^{-tz^2} dz = \frac{1}{\sqrt{\pi}} \int_{\sqrt{t}\alpha}^\infty e^{-x^2}\, dx \tag{21}$$

$$A_1 = \frac{G(X)}{u}\,; \tag{22}$$

for vertical polarization

$$G^{(v)}(X) = \frac{e^{-t\pi/4}}{\sqrt{\pi}} \int_0^\infty e^{-tX\tau} \frac{v'(\tau)}{w_1(\tau)}\, d\tau + \frac{e^{t\pi/12}}{\sqrt{\pi}} \int_0^\infty e^{tX\tau/2 - X\tau\sqrt{3}/2} \frac{v'(\tau)}{w_2'(\tau)}\, d\tau \tag{23}$$

and for horizontal polarization

$$G^{(h)}(X) = \frac{e^{-t\pi/4}}{\sqrt{\pi}} \int_0^\infty e^{-tX\tau} \frac{v(\tau)}{w_1(\tau)}\, d\tau + \frac{e^{t\pi/12}}{\sqrt{\pi}} \int_0^\infty e^{tX\tau/2 - X\tau\sqrt{3}/2} \frac{v(\tau)}{w_2(\tau)}\, d\tau \tag{24}$$

where $v(\tau)$ and $w_2(\tau)$ are also Airy integral functions. The other symbols have their usual meaning and, for convenience, are defined below:

$$\alpha = \left[\frac{2\omega s_1 s_2}{c(s_1+s_2)}\right]^{\frac{1}{2}} \frac{\theta}{2},$$

$$X = \left(\frac{\omega a}{2c}\right)^{\frac{1}{3}} \theta,$$

$$u = \frac{\alpha}{X} = \left[\frac{2\omega s_1 s_2}{c(s_1+s_2)}\right]^{\frac{1}{2}} \frac{1}{2}\left(\frac{2c}{\omega a}\right)^{\frac{1}{3}}.$$

s_1 may be taken as the linear distance from the source to the crest and s_2 may be taken as the linear distance from the observer to the crest. θ is the angle subtended by the two plane surfaces which are tangent to the surface and contain the source and the observer respectively. a is the effective radius of curvature at the crest of the obstacle. The situation is illustrated in Fig. 3*a*.

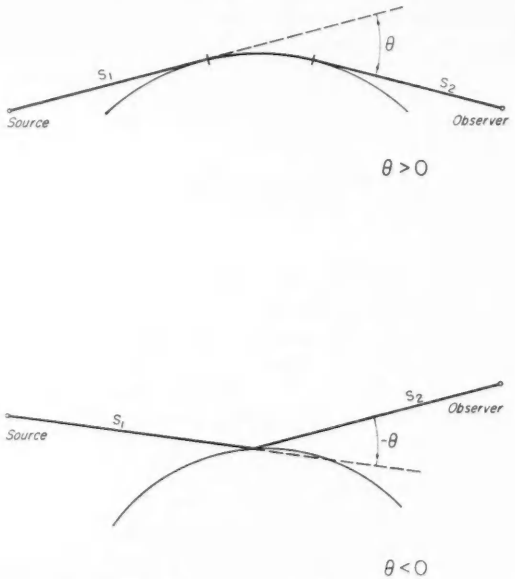

FIG. 3. The geometry for diffraction by a cylindrical crest. For $\theta>0$, the dimensions s_1 and s_2 are measured to the respective tangent points; for $\theta<0$, they are measured to the specular reflection point on the cylindrical surface.

The factor A_0 corresponds to the usual Kirchhoff diffraction whereas A_1 is a correction which depends on polarization and accounts for the finite radius of curvature of the diffracting edge. The above form for A is only valid for large obstacles (i.e., $\omega a/c \gg 1$) and small grazing angles (i.e., $|\theta| \ll 1$).

The incident field is taken to vary with time as a step function. For example, if $\psi(t)$ denotes a field component, then in the absence of the obstacle

$$\psi(t) = \psi^{\text{inc}}(t) = \frac{\text{const.}}{R} u(t-R/c) \tag{25}$$

where R is the linear distance measured between the source and the observer. Consequently, in the presence of the obstacle, the resultant field may be written

$$\psi(t) = \frac{\text{const.}}{R} [a_0(t)+a_1(t)] \tag{26}$$

where

$$a_0(t) = L^{-1}\frac{A_0}{s} \tag{27}$$

and

$$a_1(t) = L^{-1}\frac{A_1}{s}e^{-ia^2}. \tag{28}$$

Transferring to the s notation it is seen that

$$A_0 = \tfrac{1}{2}\operatorname{erf} c\,(\sqrt{bs}) \qquad \text{for } \theta > 0 \tag{29}$$

$$A_0 = 1-\tfrac{1}{2}\operatorname{erf} c\,(\sqrt{bs}) \qquad \text{for } \theta < 0, \tag{30}$$

where

$$\sqrt{b} = \left[\frac{2s_1s_2}{c(s_1+s_2)}\right]^{\frac{1}{2}}\frac{\theta}{2}.$$

Then, using the result*

$$(1/s)\operatorname{erf} c\,(\sqrt{bs}) = L\frac{2}{\pi}\arctan\left(\frac{t}{b}-1\right)^{\frac{1}{2}}u(t) \tag{31}$$

it follows that

$$a_0(t) = \frac{1}{\pi}\arctan\,(G-1)^{\frac{1}{2}}u(G-1) \qquad \text{for } \theta > 0 \tag{32a}$$

$$= u(G)-\frac{1}{\pi}\arctan\,(G-1)^{\frac{1}{2}}u(G-1) \qquad \text{for } \theta < 0 \tag{32b}$$

where

$$G = \frac{2ct}{\theta^2}\left(\frac{s_1+s_2}{s_1s_2}\right).$$

The inversion of the function A_1 is also readily carried out. First the integrals $G^{(e)}(X)$ and $G^{(h)}(X)$ are written

$$G^{(e)}(X) = \sum_{n=0}^{\infty}(-iX)^nP_n^{(e)} \tag{33}$$

and

$$G^{(h)}(X) = \sum_{n=0}^{\infty}(-iX)^nP_n^{(h)} \tag{34}$$

where

$$P_n^{(e)} = \frac{e^{-i\pi/4}}{n!\sqrt{\pi}}\int_0^{\infty}\frac{v'(\tau)}{w_1'(\tau)}\tau^n d\tau + \frac{e^{-i(2\pi n/3)}e^{i(\pi/12)}}{n!\sqrt{\pi}}\int_0^{\infty}\frac{v'(\tau)}{w_2'(\tau)}\tau^n d\tau \tag{35}$$

*This result may be obtained easily from pair 907.3 in the tables by Campbell and Foster (1949).

and

$$P_n^{(h)} = \frac{e^{-i\pi/4}}{n!\sqrt{\pi}} \int_0^\infty \frac{v(\tau)}{w_1(\tau)} \tau^n d\tau + \frac{e^{-i(2\pi n/3)} e^{i(\pi/12)}}{n!\sqrt{\pi}} \int_0^\infty \frac{v(\tau)}{w_2(\tau)} \tau^n d\tau. \tag{36}$$

Then, on transforming to s notation

$$u = \frac{s^{1/6} e^{-i\pi/12}}{2c^{1/6}} \left(\frac{2s_1 s_2}{s_1+s_2}\right)^{\frac{1}{2}} \left(\frac{2}{a}\right)^{\frac{1}{3}} \tag{37}$$

and as before

$$(-iX)^n = e^{-i(2\pi n/3)} \left(\frac{sa}{2c}\right)^{n/3} \theta^n. \tag{38}$$

Thus, on using the result

$$\frac{s^{n/3}}{s^{7/6}} = L \frac{t^{1/6-n/3}}{\Gamma[(7/6)-(n/3)]} \tag{39}$$

it immediately follows that

$$a_1(t) = L^{-1} \frac{A_1}{s} e^{-bs} \tag{40}$$

$$= -\sum_{n=0}^{\infty} \frac{e^{-i2\pi n/3} e^{(\pi/12)} P_n^{(v,h)}}{\Gamma[(7/6)-(n/3)] x^{(n+1)/3}} (G-1)^{1/6-n/3} u(G-1)$$

where

$$G = \frac{2ct}{\theta^2} \left(\frac{s_1+s_2}{s_1 s_2}\right)$$

as previously defined, and

$$x = \left(\frac{s_1 s_2}{s_1+s_2}\right) \frac{1}{a\theta}.$$

The coefficient $P_n^{(v,h)}$ is to be replaced by $P_n^{(v)}$ for vertical polarization and $P_n^{(h)}$ for horizontal polarization.

Using equations (31), (32), and (40) the resultant response $a(t)$ is plotted in Figs. 4*a* and 4*b* for lit ($\theta<0$) and shadow ($\theta>0$) regions respectively. In both figures the curve for $x = \infty$ corresponds to an infinite or very large values of s_1 and s_2. In this case the results correspond to Kirchhoff or knife-edge diffraction and the dependence on polarization disappears. It is also interesting to note that for $\theta<0$ the field at the observer has a sharp front and follows the form of the incident wave until $G = 1$ whence it decays rapidly. Physically the instant $G = 0$ corresponds to the first arrival of the direct pulse from the source whereas $G = 1$ corresponds to the first arrival of the pulse which is reflected at the crest. On the other hand, for $\theta>0$ the observer is in the geometrical shadow and there is no disturbance until $G = 1$ since the pulse must travel from the source to the observer via the crest.

The curves in Figs. 4*a* and 4*b*, for finite values of x, show strong dependence on polarization. As x decreases the field for horizontal polarization (denoted H.P.) is greatly reduced below the corresponding knife-edge value (i.e., $x = \infty$). The field for vertical polarization, on the other hand, shows a marked increase as x becomes small. This behavior is in accordance with the trends in the corresponding time-harmonic problem.

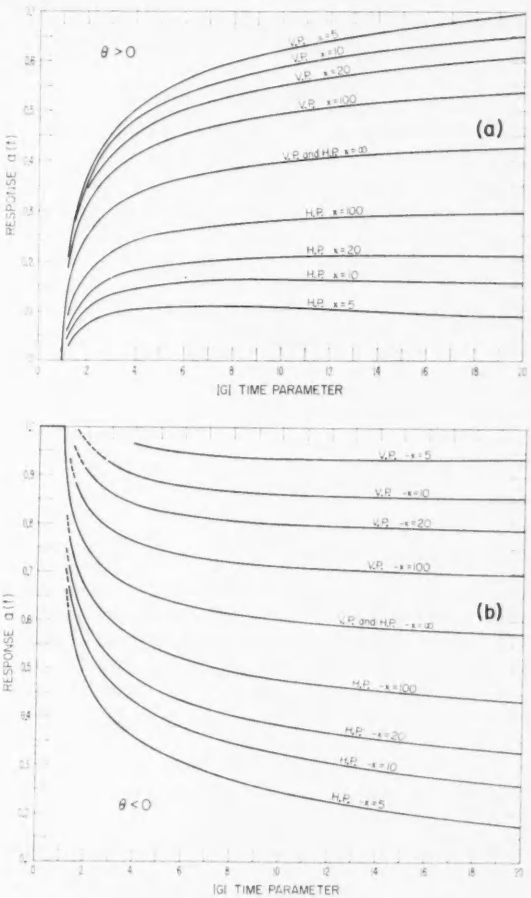

FIGS. 4*a* and 4*b*. The response $a(t)$ of the diffraction field for an incident (spherical) wave whose wave front is a step function.

CONCLUDING REMARKS

A method for obtaining the transient response of electromagnetic fields in the presence of a circular conducting cylinder has been outlined. The solution

may be used for any convex metallic surface if the local radius of curvature is large and slowly varying. Thus "a" in general is to be regarded as the principal radius of curvature.

While the results have been given explicitly for step-function excitation the response for general excitation may be obtained by superposition.

ACKNOWLEDGMENT

The research reported in this paper was supported by the U.S. Air Force Cambridge Research Center under Contract CSO and A58-40.

APPENDIX

Obtaining Numerical Values of the Coefficients $I_n^{(v)}$, $I_n^{(h)}$, $P_n^{(v)}$, and $P_n^{(h)}$

In the body of the text the following two coefficients were employed:

$$I_n^{(v)} = \frac{1}{\sqrt{\pi}}\frac{1}{n!}\int_\Gamma \tau^n \frac{1}{w_1'(\tau)}\,d\tau \tag{41}$$

$$I_n^{(h)} = \frac{1}{\sqrt{\pi}}\frac{1}{n!}\int_\Gamma \tau^n \frac{1}{w_1(\tau)}\,d\tau \tag{42}$$

where the integration contour Γ runs from $\infty \exp(-i2\pi/3)$ to the origin, then out along the real axis to ∞. The Airy integral functions are defined by

$$w_1(\tau) = \frac{1}{\sqrt{\pi}}\int_{\Gamma_1} \exp\,(x\tau - x^3/3)dx \tag{43}$$

$$w_1'(\tau) = \frac{1}{\sqrt{\pi}}\int_{\Gamma_1} x \exp\,(x\tau - x^3/3)dx \tag{44}$$

where Γ_1, the integration contour, runs from $\infty \exp(i2\pi/3)$ to the origin, then out along the real axis to ∞. The Airy integral functions $w_2(\tau)$ and $w_2'(\tau)$ have the same integral definition as $w_1(\tau)$ and $w_1'(\tau)$ but Γ_1 is replaced by Γ. The functions $v(\tau)$ and $v'(\tau)$ are thus conveniently defined by

$$v(\tau) = \frac{i}{2}\,[w_1(\tau) - w_2(\tau)] \tag{45}$$

$$v'(\tau) = \frac{i}{2}\,[w_1'(\tau) - w_2'(\tau)]. \tag{46}$$

For purposes of computation the integral formulas may be written in terms of integrals whose contours are the positive real axis. These are written:

$$I_n^{(v)} = \frac{1}{\sqrt{\pi}\,n!}\left[\int_0^\infty \frac{\tau^n d\tau}{w_1'(\tau)} + e^{-i2\pi n/3}\int_0^\infty \frac{\tau^n}{w_2'(\tau)}\,d\tau\right] \tag{47}$$

where use has been made of the identity

$$w_1'(re^{-i2\pi/3}) = e^{-i2\pi/3}\,e^{i\pi/3}\,w_2'(r) \tag{48}$$

and

$$I_n^{(h)} = \frac{1}{\sqrt{\pi}\, n!}\left[\int_0^\infty \frac{\tau^n}{w_1(\tau)}\, d\tau - e^{i\pi(2n+1)/3}\int_0^\infty \frac{\tau^n}{w_2(\tau)}\, d\tau\right] \tag{49}$$

where use has been made of the identity

$$w_1(re^{-i2\pi/3}) = e^{-i\pi/3} w_2(r). \tag{50}$$

Furthermore, since $w_2(\tau)$ is the complex conjugate of $w_1(\tau)$ if τ is real, the coefficients may be simply expressed by

$$I_n^{(v)} = M_n + e^{-i2\pi n/3}\, M_n^* \tag{51}$$

and

$$I_n^{(h)} = N_n - e^{-i\pi(2n+3)/3} N_n^* \tag{52}$$

where the asterisk denotes a complex conjugate and

$$M_n = \frac{1}{\sqrt{\pi}\, n!}\int_0^\infty \frac{\tau^n d\tau}{w_1'(\tau)} \quad \text{and} \quad N_n = \frac{1}{\sqrt{\pi}\, n!}\int_0^\infty \frac{\tau^n d\tau}{w_1(\tau)}. \tag{53}$$

Using similar reasoning, it comes about that

$$P_n^{(v)} = e^{-i\pi/4}\, V_n + e^{-i[2\pi n/3 - \pi/12]}\, V_n^* \tag{54}$$

and

$$P_n^{(h)} = e^{-i\pi/4}\, W_n + e^{-i[2\pi n/3 - \pi/12]}\, W_n^* \tag{55}$$

where

$$V_n = \frac{1}{\sqrt{\pi}\, n!}\int_0^\infty \frac{\tau^n v'(\tau) d\tau}{w_1'(\tau)} \tag{56}$$

and

$$W_n = \frac{1}{\sqrt{\pi}\, n!}\int_0^\infty \frac{\tau^n v(\tau) d\tau}{w_1(\tau)}. \tag{57}$$

The real and imaginary parts of the integrands of the integrals M_n, N_n, V_n, and W_n are now plotted on graph paper as a function of the real variable τ. Using a planimeter the area under these curves is obtained and reasonably accurate values of the integrals are thus obtained.

In Table I the values of the coefficients $I_n^{(v)}$ and $I_n^{(h)}$ are listed for n ranging from 0 to 9. They are listed in polar form because of convenience in calculating the quantities $j^{(v)}(t)$ and $j^{(h)}(t)$.

TABLE I

	$I_n^{(v)}$		$I_n^{(h)}$	
n	Ampl.	Phase	Ampl.	Phase
0	1.401	0	0.777	$+\pi/3$
1	0.746	$-\pi/3$	1.137	0
2	0.339	$+\pi/3$	0.430	$-\pi/3$
3	0.494	0	0.335	$+\pi/3$
4	0.147	$-\pi/3$	0.416	0
5	0.734(−1)	$+\pi/3$	0.121	$-\pi/3$
6	0.765(−1)	0	0.678(−1)	$+\pi/3$
7	0.228(−1)	$-\pi/3$	0.705(−1)	0
8	0.915(−2)	$+\pi/3$	0.563(−1)	$-\pi/3$
9	0.844(−2)	0	0.860(−2)	$+\pi/3$

In Table II the coefficients V_n and W_n are listed. They are given in Cartesian form.

TABLE II

	V_n		W_n	
n	Real	Imaginary	Real	Imaginary
0	$-2.27(-1)$	$8.50(-2)$	$1.74(-1)$	$5.35(-2)$
1	$-1.32(-1)$	$3.16(-2)$	$9.61(-2)$	$1.66(-2)$
2	$-6.17(-2)$	$1.01(-2)$	$4.52(-2)$	$4.75(-3)$
3	$-2.55(-2)$	$2.68(-3)$	$1.93(-2)$	$1.26(-3)$
4	$-9.66(-3)$	$6.30(-4)$	$7.77(-3)$	$3.08(-4)$
5	$-3.35(-3)$	$1.39(-4)$	$2.70(-3)$	$7.08(-5)$
6	$-1.11(-3)$	$2.88(-5)$	$9.31(-4)$	$1.53(-5)$
7	$-3.51(-4)$	$5.67(-6)$	$3.01(-4)$	$3.13(-6)$
8	$-1.08(-4)$	$1.06(-6)$	$9.42(-5)$	$6.29(-7)$
9	$-3.16(-5)$	$1.93(-7)$	$2.81(-5)$	$1.20(-7)$

After these graphical integrations were completed, a paper by Riley and Billings (1959) appeared which gave numerical values of some integrals which were closely related to ours. In fact the coefficients $I_n^{(v)}$, $I_n^{(h)}$, $P_n^{(v)}$, and $P_n^{(h)}$ may be expressed in terms of their integrals in the following way:

$$I_n^{(v)} = \frac{1}{\pi n!}\left[\int_0^\infty \frac{x^n B'}{F'^2}\,dx + i\int_0^\infty \frac{x^n A'}{F'^2}\,dx\right] \tag{58}$$

$$I_n^{(h)} = \frac{1}{\pi n!}\left[\int_0^\infty \frac{x^n B}{F^2}\,dx + i\int_0^\infty \frac{x^n A'}{F^2}\,dx\right] \tag{59}$$

$$P_n^{(v)} = \frac{1}{\sqrt{\pi} n!}\left[\int_0^\infty \frac{x^n A'B'}{F'^2}\,dx + i\int_0^\infty \frac{x^n A'^2}{F'^2}\,dx\right] \tag{60}$$

$$P_n^{(h)} = \frac{1}{\sqrt{\pi} n!}\left[\int_0^\infty \frac{x^n AB}{F^2}\,dx + i\int_0^\infty \frac{x^n A^2}{F^2}\,dx\right] \tag{61}$$

where $A = Ai(x)$, $B = Bi(x)$, $A' = dAi(x)/dx$, $B' = dBi(x)/dx$, $F^2 = A^2+B^2$, and $F'^2 = A'^2+B'^2$. $Ai(x)$ and $Bi(x)$ are the Airy functions in the usual notation. They are tabulated extensively (Miller 1946). The real infinite integrals inside the brackets of the right-hand side are tabulated by Riley and Billings for n from 0 to 20. Five significant figures are given in their tables. Spot checks indicated good agreement with their results and our more approximate coefficients.

REFERENCES

Fock, V. 1946. J. Phys. Chem. U.S.S.R. **10**, 399.

Johler, J. R. and Walters, L. C. 1959. Trans. I.R.E. AP-7, 1.

Levy, B. R. and Keller, J. B. 1958. Trans. I.R.E. AP-6, 56.

Miller, J. C. P. 1946. British Mathematical Tables (Cambridge University Press) B.

Oberhettinger, F. 1956. Z. Physik, **146**, 423.

Riley, J. A. and Billings, C. 1959. Mathematical Tables and Other Aids to Computation, **8**, 97.

Wait, J. R. 1956. Can J. Phys. **34**, 27.

——— 1957*a*. Can. J. Phys. **35**, 1146.

——— 1957*b*. Can. J. Phys. **35**, 693.

——— 1959. Electromagnetic radiation from cylindrical structures (Pergamon Press, London and New York).

Wait, J. R. and Conda, A. M. 1959. J. Research Natl. Bur. Standards, D, **63**, 181.

Weston, V. 1959. Proceedings U.R.S.I. Symposium on Electromagnetic Theory, University of Toronto. To be published.

A NEW ABSOLUTE NOISE THERMOMETER AT LOW TEMPERATURES[1]

H. J. FINK[2]

ABSTRACT

If three resistors, which are kept at different temperatures, are arranged in form of a π network and if two of the thermal noise voltages appearing across the π network are multiplied together and averaged with respect to time, then under certain conditions the correlation between those voltages can be made zero. This condition is used to calculate the temperature of one noise source provided all the resistance values and the other temperatures are known. A noise thermometer of this kind was constructed which is capable of measuring temperatures below approximately 140° K. The boiling points of liquid oxygen and liquid nitrogen were determined absolutely within 0.2%. Between 1.3° K and 4.2° K the thermometer had to be calibrated due to errors arising in the equipment and the measured temperatures were then accurate within ±1%.

I. INTRODUCTION

This paper deals with the construction of a thermometer which makes use of the thermal fluctuations of voltage across an impedance to measure absolutely temperatures below approximately 140° K. Preliminary investigations were carried out for such a device to measure accurately temperatures in the liquid helium region.

According to Nyquist's (1928) law the mean-square voltage fluctuations arising from the thermal agitation of the electrons across an impedance, Z, are given by:

$$\overline{v^2} = 4kT\mathrm{Re}[Z]\, p(f, T)\, df, \tag{1}$$

where k is Boltzmann's constant, T the absolute temperature, Re[Z] is the real part of the complex impedance, Z, $p(f, T)$ the Planck factor, and df the frequency interval in which the measurements are performed. The above formula can be derived from the equipartition law and the second law of thermodynamics and the available noise power is a universal function of the frequency and the absolute temperature (see also Van der Ziel 1954). Equation (1) has also been proved for models which describe the random motion of the electrons in a conductor (Bernamont 1937; Bakker and Heller 1939; Spenke 1939). Nyquist's theorem can also be proved for the one-dimensional form of blackbody radiation (Burgess 1941) which is received by an antenna kept in a sphere at uniform temperature. The thermodynamic method has the merit that it is independent of the mechanism causing the noise.

A number of papers have been published (Lawson and Long 1946; Brown and MacDonald 1946; Gerjuoy and Forrester 1947; Cook, Greenspan, and Wussler 1948) which suggests the possibility of using thermal fluctuations of

[1]Manuscript received July 15, 1959.
Contribution from the Department of Physics, University of British Columbia, Vancouver, British Columbia.
[2]Present address: The Clarendon Laboratory, Oxford, England.

voltage across an impedance to measure low temperatures but they do not propose any practical scheme for a thermometer of this kind and no serious attempt has been reported which indicates that such an experiment has been performed at low temperature.

In 1946 Dicke *et al.* reported a radiometer which measures thermal radiation at microwave frequencies. This method is essentially a commutation comparison technique which compares the unknown noise with that of a standard source. The radiometer has been used for observations of microwave radiation from the sun and the moon and for the measurement of atmospheric absorption at several microwave frequencies. Garrison and Lawson (1949) developed an absolute noise thermometer of the Dicke type to measure high temperatures. A chopper at the input of the amplifier is used to connect alternately the thermometer resistor and a resistor at ambient temperature (standard noise source). The principal limitation of such a switching device for comparison of noise voltages is the variation in contact potential of the chopper. Also the ultimate sensitivity of such a thermometer depends upon the noise-signal-to-amplifier-noise ratio. Aumont and Romand (1954) attempted an improvement of Garrison's and Lawson's thermometer, but the final results have not yet been reported. The National Physical Laboratory (1957) reports also an improved noise thermometer for high temperatures ($\sim$1100° C) based on the switching technique which is capable of comparing noise voltages to 0.05%. Cade (1958) uses an electronic switch instead of a chopper.

To avoid any switching device at the inputs of the amplifier and to make noise measurements virtually independent of the amplifier noise, one can arrange three resistors, which are kept at different temperatures, in form of a π network; and if now two of the thermal noise voltages appearing across the network are multiplied together and averaged with respect to time, then under certain conditions the correlation between those voltages can be made zero. From this condition one can calculate the temperature of one noise source,

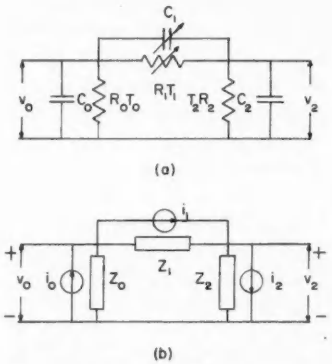

FIG. 1. (*a*) The π network as used to correlate noise between R_0 and R_2 via R_1.
(*b*) The block diagram and the equivalent noise current sources of the π network.

provided all the resistance values and other temperatures are known.[3] Consider the network of Fig. 1. By straightforward network analysis one obtains for v_0 and v_2:

$$v_0 = \frac{Z_0}{Z_T}\left[i_0(Z_1+Z_2)-i_1Z_1-i_2Z_2\right] \tag{2a}$$

$$v_2 = \frac{Z_2}{Z_T}\left[i_0Z_0+i_1Z_1-i_2(Z_1+Z_0)\right] \tag{2b}$$

where

$$Z_T = Z_0+Z_1+Z_2, \quad Z_0 = R_0/(1+j\omega C_0R_0), \text{ etc.}$$

and v_0, i_0, etc. are complex vectors. If one multiplies v_0 and v_2 and takes the time average over the product, then one forms:

$$\mathrm{Re}(\overline{v_0v_2^*}) = \mathrm{Re}\left\{\frac{Z_0Z_2^*}{|Z_T|^2}\left[\overline{|i_0|^2}Z_0^*(Z_1+Z_2)+\overline{|i_2|^2}Z_2(Z_0^*+Z_1^*)-\overline{|i_1|^2}|Z_1|^2\right]\right\}, \tag{3}$$

where

$$\overline{|i_0|^2} = 4kT_0\,df/R_0$$

(the Planck factor is assumed to be unity), similarly $\overline{|i_1|^2}$ and $\overline{|i_2|^2}$. The time average of the products $\mathrm{Re}(\overline{i_0i_1^*})$, etc. are zero because the resistors are independent noise sources. The product $\mathrm{Re}(\overline{v_0v_2^*})$ appearing in equation (3) corresponds to the direct multiplication of the physical voltages v_0 and v_2. From equation (3) one sees that if either $R_0C_0 = R_1C_1 = R_2C_2$ or $(\omega R_nC_n)^2 \ll 1$ the product $\mathrm{Re}(\overline{v_0v_2^*})$ can have a positive or a negative sign provided $T_1 > (T_0+T_2)$. For either of the above conditions the value of R_1 required to make $\mathrm{Re}(\overline{v_0v_2^*}) = 0$ can be calculated from equation (3):

$$R_1 = \frac{T_0R_2+T_2R_0}{T_1-T_0-T_2}. \tag{4}$$

In this experiment R_0 and R_2 were both kept in the helium bath so that $T_0 = T_2$. R_2 and R_0 were matched to better than 1/2%, and T_1 was in an isothermal bath at room temperature. If T_1 and the resistances are measured, T_0 can be calculated from

$$T_0 = T_1\frac{R_1}{R_0+2R_1+R_2}. \tag{5}$$

II. THE THERMOMETER AND EXPERIMENTAL PROCEDURES

The first requirement for an absolute noise thermometer of the kind described above is to find some resistors which are stable at liquid helium temperatures, whose values are preferably reproducible for several experiments, which produce no noise in addition to thermal noise, and whose resistive component

[3] This idea was proposed by Dr. J. B. Garrison to Prof. A. W. Lawson of Chicago University (verbal communication by Prof. R. E. Burgess).

is the same as the d-c. resistance (within a specified accuracy) over the frequency interval in which the measurements are performed. Many resistors have been tried at helium temperatures. The ones found most suitable are those manufactured by the Daven Co., series 850. They are hermetically sealed precision metal film type resistors composed of an alloy of pure, noble metals. They are stable over a period of at least 7 hours to better than 1 part in 10^4 and they are reproducible to that accuracy for several experiments. A 20-kΩ resistor has a resistive component of $20\text{k}\Omega \pm 1\%$ at 3 Mc/sec. The resistance values used in equation (5) should be those appropriate to the frequency range in which the noise measurements are performed. Because no sufficiently accurate audio-frequency bridge was available the metal film deposit resistors were measured at d-c. and at 3 Mc/sec. Since the 3-Mc/sec values differed from the d-c. values by less than 1%, it seems reasonable to conclude that the deviation of the resistance in the audio-frequency range from the d-c. value was less than 0.1% for the above resistors. A 20-kΩ Davohm resistor has a resistance of approximately 17.9 kΩ at liquid helium temperatures (1.3° K to 4.3° K) and the resistance value over this range varies less than 0.05%.

R_1 was a precision wire wound resistance box and C_1 a variable condenser, both kept at room temperature. C_0 and C_2 were the parasitic capacitance between the wires and the shielding, and the input to the amplifiers (including effects due to Miller capacitances), and they were equal within 3%. Unfortunately the parasitic capacity to ground was very large (~220 μμf), and about three-fifths of this was due to the shielding of C_1 and R_1 which was reflected into the input of each amplifier.

Figure 2 shows the block diagram of the thermometer. The shielding requirements of the input circuit and the preamplifiers were very stringent and great care was required to avoid ground loops and to eliminate magnetic pickup in

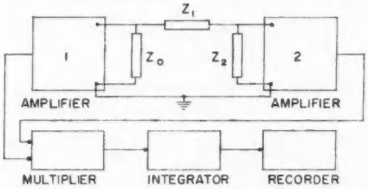

FIG. 2. The block diagram of the noise thermometer.

the π network which in effect acts like a loop. The first tube of the preamplifier was a 6922 (American equivalent to the Philips E88CC) double triode connected as a grounded-cathode-grounded-grid amplifier (cascode) followed by two RC coupled stages (7025 double triode). The cascode and the first RC coupled stage were constructed of wire wound resistors, and their filament currents were supplied by batteries. The lower and upper half power points of the amplifiers were approximately 3 and 7 kc/sec respectively. Both input voltages to the multiplier were constantly monitored by two oscilloscopes and two r.m.s. voltmeters to check the randomness of the noise spectrum and

the gain of the amplifiers. The multiplier (a commercial type manufactured by G. A. Philbrick, Inc.) is followed by an amplifier and an RC integrator of variable integration time (22.5 to 90 seconds). The output of the integrator was fed into a recorder via a cathode follower to permit better registration of the time average of the signal.

R_0 and R_2 were carefully cooled to liquid helium temperatures and then their d-c. value was measured with a Wheatstone bridge (R_1 and C_1 were disconnected). R_1 was set to approximately the value at which balance [$\mathrm{Re}(\overline{v_0 v_2^*}) = 0$] was expected and C_1 adjusted such that $R_1C_1 \simeq R_2C_2$. This was accomplished by connecting Z_1 and Z_2 in series and applying pulses across Z_1 and Z_2. C_1 was then adjusted until the shape of the pulses across the impedance Z_1+Z_2 and Z_2 were identical. This procedure adjusted the time constants τ_1 and τ_2 to approximately 10%. Similarly τ_0 and τ_1 were adjusted and the average setting of C_1 was used when R_1 was varied to achieve balance. If the change in R_1 was large τ_1 had to be rebalanced and R_1 reset. The temperature (room temperature) of R_1 was read on an ordinary mercury thermometer placed on the outside of the resistance box and the value of R_1 was read from the dial setting of the resistance box. The temperature of the helium bath was then calculated from equation (5).

The temperature of the helium bath was sometimes kept constant to better than 1 millidegree K by a temperature regulator (400 c.p.s.) similar to that of Boyle and Brown (1954). A stirrer was sometimes used to equalize the temperature, and the vapor pressure of the helium was measured on a mercury manometer with a cathetometer. A German silver tube (8-mm diameter) extending into the liquid surface was connected to the manometer. The temperature determined from equation (5) was then compared with the "1958 ^{4}He scale of temperatures" (Van Dijk and Durieux 1958; Brickwedde 1958).

III. ERRORS AND LIMITATIONS OF THE THERMOMETER

1. Errors Which Can Be Represented by Noise-Current Sources in Shunt with the π Network

These errors can be divided essentially into two groups: (*a*) errors due to the grid currents, (*b*) errors due to the finite input admittance.

(*a*) The grid current is made up of three parts; electrons arriving at the grid (I_1), electrons emitted from the grid by photoelectric emissions (I_2), and positive ions arriving at the grid (I_3). All three currents are independent of each other. The grid of the triode acts like the anode of a diode; for I_1 it acts like the anode in the exponential part of its characteristic and for I_2 and I_3 it acts like the anode of a saturated diode. Therefore the shot noise due to the grid current is:

$$\overline{i_g^2} = 2e(I_1+I_2+I_3)\,df. \tag{6}$$

The net grid current is $I_g = I_1-I_2-I_3$ and thus $i_g^2 \geqslant 2eI_g\,df$.

(*b*) The real part of the dynamic input admittance which is a function of frequency consists of three components: the ohmic loss in the input circuit, the cold loss of the first stage (leakage around the bulb of the tube, losses in

the socket, etc.), and part of the load of the first stage which is reflected into the input due to the grid-to-plate capacity. In this experiment a cascode input was used which has the advantage that the grounded grid stage reduces the capacitive feedback from output to input without introducing partition noise. However, due to the finite feedback shot noise of the grounded grid stage contributes also to this error.

The errors in (*a*) and (*b*) can be represented by noise-current sources in shunt with the π network. The noise temperature which must be ascribed to this input conductance cannot be determined by calculation because its components and their noisiness are not readily estimated. If one assumes that the real part of the input impedance to the amplifiers is R_g and its effective temperature is $T_g = \alpha T_1$, where α is a constant and T_1 room temperature, and if one also assumes that both amplifiers have the same input characteristics and that $R_g \gg R_0$ and $R_0 \simeq R_2$, then the error in the absolute temperature due to shunt current sources is:

$$\epsilon = \frac{\Delta T}{T} \simeq \frac{R_0}{2kT}\left[e(I_1+I_2+I_3)+2k\frac{\alpha T_1}{R_g}\right] = \frac{A}{T}, \tag{7}$$

where A is a constant for one particular thermometer.

2. Errors Due to Current Flow in the Resistors

Nyquist's law is based upon the assumption that the circuit is a passive network. This requires that no currents are flowing through the resistors R_0, R_1, and R_2. To minimize thermoelectric effects dissimilar materials between the amplifiers and resistors in the network were avoided and the voltage due to this effect was measured to be smaller than 3 μv at the inputs of the amplifiers when R_0 and R_2 were at helium temperatures. The grid current $I_1-(I_2+I_3)$ was approximately 2.6×10^{-9} amperes. Because thin metal layer resistors (R_0 and R_2) consist of a large number of very small conducting particles in loose contact, contact noise may be generated if a current is passed through the resistors. Christenson and Pearson (1936) did not find any contact noise in thin solid carbon filaments when large currents were passed through the specimen. Also Bittel and Scheidhauer (1956) found no noise in addition to the thermal noise when a current was passed through metallic conductors between 45 c.p.s. and 11.5 kc/s. Therefore thin solid metal layer resistors should be free of any noise in excess of thermal noise and Nyquist's law should hold accurately for the above small currents.

3. Non-linearities and Amplifier Noise

Non-linearities in the amplifiers, the multiplier, and the integrator are another source of error. Due to non-linearities the recorder deflection will be increased by an increment proportional to $(|\overline{v_0^2}|\overline{v_2^2}|)^{\frac{1}{2}}$. Because for $Z_1 = \infty$ as well as for balance (see equation 5) the correlation coefficient should be zero for no distortion of the signal, the variance should be the same for both cases. Because both amplifiers were built on different chassis and shielded from each other, the coupling capacity between the amplifiers must have been very small. The zero for balance of the recorder was then determined by grounding

the inputs to both amplifiers. Because $|\overline{v_0^2}|$ and $|\overline{v_2^2}|$ are functions of the equivalent noise resistance of the amplifiers, R_n, it is desirable to make R_n as small as possible. R_n for each amplifier was approximately 770 ohms at 300° K over a band width of 3 to 7 kc/s. This was derived by measuringthe recorder deflection (or the squared r.m.s. voltage at the inputs to the multiplier) for $|\overline{v_0^2}|$ and $|\overline{v_2^2}|$ for various input resistances to the amplifiers at room temperature. For a band width of 3 to 12 kc/s the equivalent noise resistance of the amplifiers was 650 ohms. If one assumes that the flicker noise is proportional to $1/f$, then the equivalent noise resistance of the amplifiers at high frequencies is approximately 340 ohms. Therefore, flicker noise was the main contribution to R_n between 3 and 7 kc/s.

4. Errors Due to Mismatch of the Time Constants in the π Network

Equations (4) and (5) were derived under the condition that $(\omega\tau_i)^2 \ll 1$ or that all the τ's are equal. If this does not hold, then equation (4) for $T_0 = T_2$ is modified and one gets:

$$(4a) \quad \frac{T_0(R_0+R_2)}{T_1-2T_0} = R_1 \frac{1+(\omega^2\tau_0\tau_2)/(T_1-2T_0)\ \{T_1-T_0\tau_1[(1/\tau_0)+(1/\tau_2)]\}}{1+(\omega\tau_1)^2}.$$

If

$$T_1 \gg T_0 \quad \text{and} \quad T_1 \gg T_0\tau_1\left(\frac{1}{\tau_0}+\frac{1}{\tau_2}\right),$$

one obtains:

$$(4b) \quad \frac{T_0(R_0+R_2)}{T_1-2T_0} \simeq R_1 \frac{1+(\omega\tau_1)^2(\tau_0\tau_2/\tau_1^2)}{1+(\omega\tau_1)^2} = R_1 f(\omega, \tau_i).$$

At helium temperatures it is then sufficient to make $\tau_0\tau_2 \simeq \tau_1^2$. The deviation of $f(\omega, \tau_i)$ from unity will increase with increasing frequency. If both τ_0 and τ_2 are 10% larger than τ_1, then the error at the upper half power frequency is less than 1%. The average error is smaller, because for lower frequencies the error decreases and τ_1 was always adjusted between τ_0 and τ_2. For a systematic error in adjusting τ_1 the fractional error in the noise temperature is almost a constant in the liquid helium range.

5. A-c. Resistance of Thermometer Elements

The deviation of the resistance of R_0, R_1, and R_2 in the audio-frequency range from their d-c. value was estimated to be approximately 0.1% (see above).

6. Response of the Integrator

In the case of a narrow square noise band of width B and uniform spectral intensity a RC integrator of integration time τ will measure with a relative error of a single measurement, β, (Burgess 1951):

$$(8) \quad \beta = \frac{[\overline{(A-\bar{A})^2}]^{\frac{1}{2}}}{\bar{A}} = (2B\tau)^{-\frac{1}{2}},$$

where $\bar{A}$ is the deflection of the recorder due to the d-c. component of the signal and $\overline{(A-\bar{A})^2}$ the mean-square deviation of the recorder due to the signal.

For $B = 4$ kc/sec and $\beta = 5\times10^{-3}(0.5\%)$ τ should be at least 5 seconds. Integration times from 22.5 to 90 seconds were used. The band widths of both amplifiers were approximately equal.

7. Lead Corrections

If one assumes that the temperature of the leads going to R_0 and R_2 are at room temperature (worst possible case), then the lead resistance should be less than 0.3 ohm for errors smaller than 0.5%, a requirement not difficult to satisfy.

8. Pickup

To avoid errors due to 60 c.p.s. pickup the lower half power points of the amplifiers were designed at approximately 3 kc/sec. Because no shielded room was available experiments could be performed only at night with fluorescent light, thyratron rectifiers, d-c. motors, etc. turned off. Although the amplifiers were protected against shock, audio noise was easily picked up. The voltages were constantly monitored oscillographically at the inputs of the multiplier, to check the randomness of the noise.

IV. EXPERIMENTAL RESULTS AND DISCUSSION

Table I shows the boiling points of liquid oxygen and liquid nitrogen measured with approximately 4.48 kΩ metal film deposit resistors (R_0 and R_2) at barometric pressure with an integration time of 90 seconds. They were

TABLE I

Temperatures derived from the vapor pressure, T, measured noise temperatures, T_0, and their ratios for the boiling points of oxygen and nitrogen at barometric pressure

T, °K	T_0, °K(meas.)	T_0/T
90.23	90.26±0.06	1.000±0.001
77.33	77.25±0.08	0.999±0.001

found to be within 0.2% of the temperatures determined from the vapor pressure. The results of the noise–temperature measurements at helium temperatures are shown in Fig. 3. Because, as pointed out in the introduction, the noise power of the real part of an impedance is a universal function of frequency and temperature, any systematic deviation of the noise–temperature can only be due to experimental error of the equipment. The plot in Fig. 3(*a*) can be fitted best by an equation of the form:

$$\frac{T_0}{T} = \frac{A}{T} + b, \tag{9}$$

where $A = 0.385°$ K and $b = 1$ for this thermometer. The term A/T can be explained due to errors which can be represented by noise-current sources in shunt with the π network. Equation (7) shows that this error must be proportional to $1/T$ and the constant of proportionality is $[e(I_1+I_2+I_3)+2k\alpha T_1/R_g]R_0/2k$. If errors due to R_g are neglected, then in the above experi-

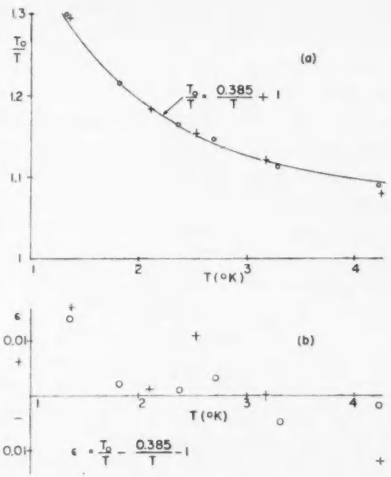

FIG. 3. (*a*) The experimental results at helium temperatures. T_0 is the noise temperature calculated from equation (5) and T the temperature determined from the 1958 helium vapor pressure scale.
(*b*) The deviation ϵ of T_0/T from the equation $A/T+1$ with $A = 0.385°$ K. ○ represents measurements with an integration time of 90 seconds and + with 67.5 seconds.

ment $I_1+I_2+I_3 = 3.7\times10^{-9}$ amperes. The measured grid current $I_1-(I_2+I_3)$ was approximately 2.6×10^{-9} amperes, which shows that shot noise due to the grid current is the main limitation of the thermometer. At 15 kc/s R_g was measured to be larger than 10^7 ohms, and because the noise temperature $T_g = \alpha T_1$ of R_g is unknown the contribution due to the second term is uncertain. If I_2 and I_3 are neglected compared with I_1 then one can conclude that $R_g/\alpha \simeq 47\times10^6$ ohms.

At helium temperatures equation (4*b*) applies, and over this temperature range a systematic error in adjusting τ_1 gives a fractional error in the noise–temperature which is essentially a constant. This means that b in the equation (9) is not unity. If $\tau_0\tau_2/\tau_1^2 = \text{constant} < 1$ for all the measured points between 1.3° K and 4.2° K, the curve in Fig. 3(*a*) will shift down.

In general it will be necessary to measure two known temperatures to calibrate a thermometer of the above kind. These measurements will determine A and b and when T_0 is measured the absolute temperature, T, can be calculated. However, if one is certain that no systematic error is made in balancing the τ's, or if $(\omega\tau_1)^2$ can be neglected with respect to unity then $b = 1$, and only one known temperature is necessary to calibrate the thermometer. Figure 3(*b*) shows the deviation ϵ of T_0/T from the equation $(A/T)+1$ with $A = 0.385°$ K plotted as a function of T. The calibrated thermometer measures temperatures accurately within $\pm1\%$ between 1.3° K and 4.2° K.

This experiment makes use of the correlation of voltages from three independent noise sources at different temperatures to determine the temperature of one (or two) noise sources. This method has the advantage that it eliminates

any switching device at the input of the amplifier. The requirements of this method are that for good absolute accuracy of the thermometer the amplifiers, the multiplier, and the integrator must be linear and that $T_1 > (T_0 + T_2)$. At present the main limitation of the absolute accuracy at low temperatures is shot noise generated at the grids of the first stages of the amplifiers. In principle, this method can also be used to measure high temperatures. R_1 could be a fixed resistor at the unknown temperature, and R_0 and R_2 could be kept at room temperature and one or preferably both of them be variable. At high temperatures errors due to shot noise can be neglected. When Z_1 is made infinite and R_0 and R_2 are replaced by two antennas which are located apart from each other, then one has in principle a radio interferometer of the kind developed by Brown and Twiss (1954).

In this experiment it was demonstrated that it is possible and feasible to measure low temperatures absolutely by making use of the thermal fluctuations of voltage across an impedance. Work will continue at this university to improve the accuracy of the noise thermometer, and to derive an absolute temperature scale in the liquid helium region.

ACKNOWLEDGMENTS

The author is most grateful to acknowledge many helpful discussions with Dr. J. B. Brown regarding the low temperature aspects of this work and with Professor R. E. Burgess regarding matters of noise. The author also wishes to thank: Dr. J. B. Garrison for his suggestion of correlating voltages from noise sources at different temperatures, Professor A. Van der Ziel for his suggestion of the tube for the first stage to Dr. J. B. Brown, Dr. J. M. Daniels for stimulating this research, Mr. H. H. M. Zerbst for the construction of the cryostat, and the National Research Council, Canada, for a studentship and the financial support of this project.

REFERENCES

AUMONT, R. and ROMAND, J. 1954. J. phys. rad. **15**, 585.
BAKKER, C. J. and HELLER, G. 1939. Physica, **6**, 262.
BERNAMONT, J. 1937. Ann. Physik, **7**, 71.
BITTEL, H. and SCHEIDHAUER, K. 1956. Z. angew. Phys. **8**, 417.
BOYLE, W. S. and BROWN, J. B. 1954. Rev. Sci. Instr. **25**, 359.
BRICKWEDDE, F. G. 1959. Kamerling Onnes Conference, Leiden, June 23–28, p. 128.
BROWN, J. B. and MACDONALD, D. K. C. 1946. Phys. Rev. **70**, 976.
BROWN, R. H. and TWISS, R. Q. 1954. Phil. Mag. **45**, 663.
BURGESS, R. 1941. Proc. Phys. Soc. (London), **53**, 293.
——— 1951. Phil. Mag. **42**, 475.
CADE, C. M. 1958. J. Roy. Aeronaut. Soc. **62**, 805.
CHRISTENSON, C. J. and PEARSON, G. L. 1936. Bell System Tech. J. **15**, 197.
COOK, R. K., GREENSPAN, M., and WUSSLER, P. G. 1948. Phys. Rev. **74**, 1714.
DICKE, R. H. 1946. Rev. Sci. Instr. **17**, 375.
DICKE, R. H. and BERINGER, R. 1946. Astrophys. J. **103**, 375.
DICKE, R. H., BERINGER, R., KYHL, R. L., and VANE, A. B. 1946. Phys. Rev. **70**, 340.
VAN DIJK, H. and DURIEUX, M. 1958. Physica, **24**, 920.
GARRISON, J. B. and LAWSON, A. W. 1949. Rev. Sci. Instr. **20**, 785.
GERJUOY, E. and FORRESTER, A. T. 1947. Phys. Rev. **71**, 375.
LAWSON, A. W. and LONG, E. A 1946. Phys. Rev. **70**, 220, 977.
NATIONAL PHYSICAL LABORATORY. 1957. Annual report (Her Majesty's Stationery Office, London), p. 84.
NYQUIST, H. 1928. Phys. Rev. **32**, 110.
SPENKE, E. 1939. Wiss. Veröffentl. Siemens-Werke, **18**, 55.
VAN DER ZIEL, A. 1954. Noise (Prentice-Hall, Inc., New York), p. 9.

CORNER-DRIVEN COUPLED SQUARE LOOP ANTENNAS[1]

SHEILA PRASAD

ABSTRACT

A theory for two identical square loop antennas driven in the zeroth-phase sequence (voltages in phase at all four corners) and the second-phase sequence (voltages in and out of phase at the corners) is formulated. Eight independent integral equations are obtained. They are solved individually by the method of iteration, and first-order formulas are obtained for the current distributions and driving point impedances. For each phase sequence, the sum of the symmetrical and antisymmetrical impedances gives the self-impedance and the difference between them gives the mutual impedance. Self and mutual impedances are also obtained for a superposition of the two phase sequences.

INTRODUCTION

The self and mutual impedances of two or more corner-driven square loops are derived when these are identical and stacked to form an array such that the centers of the loops are equally spaced along the y-axis of a rectangular co-ordinate system and the sides are parallel to the x- and z-axes. The procedure is a generalization of that used in obtaining the current for the isolated loop (King 1956).

GENERAL FORMULATION

The circuit analyzed is shown in Fig. 1. It consists of two identical square loops stacked in such a manner that the y-axis of a right-handed Cartesian co-ordinate system passes through the center of each loop, and the sides of each loop are parallel to the z- and x-axes, respectively. The two loops are designated "loop I" and "loop II" for clarity in the discussion. Their centers are separated by a distance b. The voltages V_{12}, V_{23}, V_{34}, V_{41} with appropriate superscripts are maintained across the adjacent ends of the cylindrical conductors forming loops I and II; $2h$ is the length of a side and a is the radius of each conductor. It is assumed that the inequalities $a \ll h$, $a \ll b$, $\beta_0 a = 2\pi a/\lambda \ll 1$ are satisfied. The four sides of each of the loops are numbered 1, 2, 3, 4 respectively. The required vanishing of the tangential component of the electric field on the surface of each conductor leads to four equations for each loop of which the equation for conductor 1 of loop I is typical. It is

$$-E^{\mathrm{I}}_{1z} = \frac{\partial \phi^{\mathrm{I}}_1}{\partial z} + j\omega A^{\mathrm{I}}_{1z} = \frac{\partial \phi^{\mathrm{I}}_{1z}}{\partial z} + \frac{\partial \phi^{\mathrm{I}}_{1z}}{\partial z} + j\omega A^{\mathrm{I}}_{1z} = 0 \tag{1}$$

where

$$\phi^{\mathrm{I}}_{1z} = \left[\frac{j\omega}{\beta_0^2}\frac{\partial A^{\mathrm{I}}_{1z}}{\partial x}\right]_{z=-h}; \qquad \phi^{\mathrm{I}}_{1z} = \left[\frac{j\omega}{\beta_0^2}\frac{\partial A^{\mathrm{I}}_{1z}}{\partial z}\right]_{z=-h}. \tag{2}$$

[1]Manuscript received August 17, 1959.
Contribution from the Cruft Laboratory, Harvard University, Cambridge, Massachusetts. This research was carried out under Joint Services Contract Nonr-1866(32).

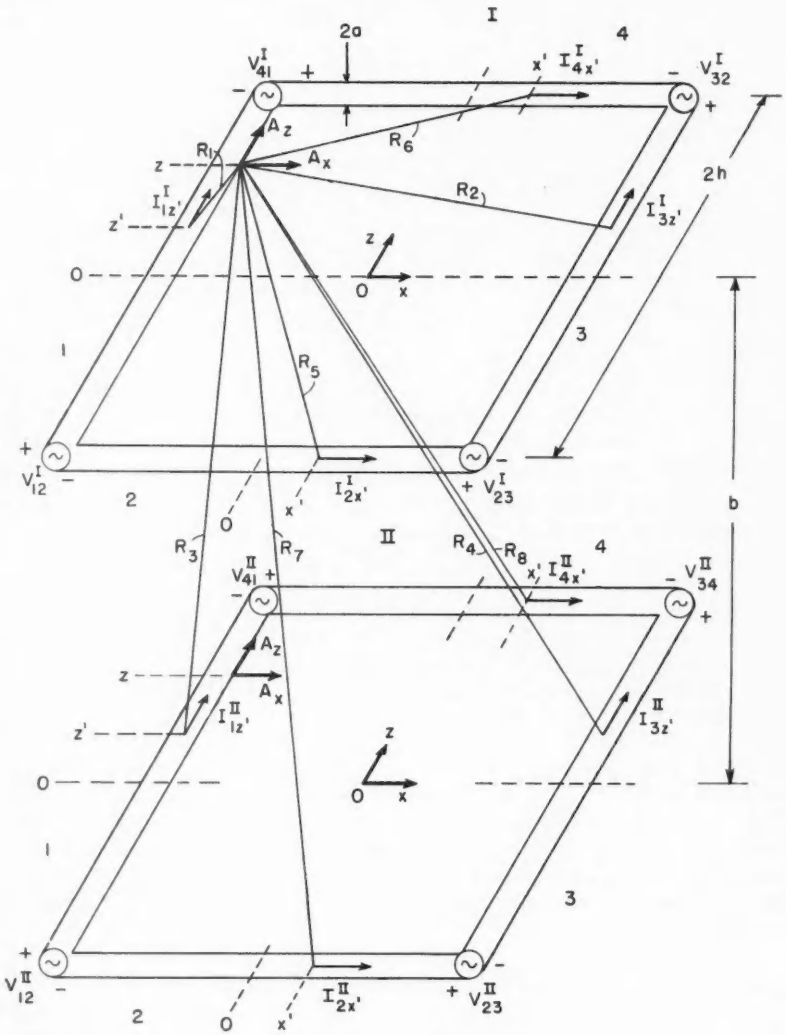

FIG. 1. Coupled loops in rectangular co-ordinate system.

The subscripts x and z denote the Cartesian components of the vector potential **A** and the parts of the scalar potential associated with these as shown in eq. (2). The components of the vector potential on the surface of side 1 of loop I are given by the following integrals:

$$(3a) \qquad A^{\mathrm{I}}_{1z}(z) = \frac{1}{4\pi\nu_0}\int_{-h}^{h} [I^{\mathrm{I}}_{1z}(z')K_1 + I^{\mathrm{I}}_{3z}(z')K_2]\,dz' + \frac{1}{4\pi\nu_0}\int_{-h}^{h} [I^{\mathrm{II}}_{1z}(z')K_3 + I^{\mathrm{II}}_{3z}(z')K_4]\,dz'$$

$$(3b) \qquad A^{\mathrm{I}}_{1x}(z) = \frac{1}{4\pi\nu_0}\int_{-h}^{h} [I^{\mathrm{I}}_{2x}(x')K_5 + I^{\mathrm{I}}_{4x}(x')K_6]\,dx' + \frac{1}{4\pi\nu_0}\int_{-h}^{h} [I^{\mathrm{II}}_{2x}(x')K_7 + I^{\mathrm{II}}_{4x}(x')K_8]\,dx'$$

where

$$(4) \qquad K_i = \frac{e^{-j\beta_0 R_i}}{R_i}; \qquad i = 1, 2, \ldots 8.$$

The vector potential on the surface of side 1 of loop II is obtained by interchanging the superscripts I and II in eq. (3). There are similar equations for each of the sides of the two loops, making up a total of 16 equations for the two identical loops. The distances R_i are shown in Fig. 1 and are given by the following equations:

$$(5) \qquad \begin{aligned} &R_1 = [(z-z')^2+a^2]^{\frac{1}{2}}; \quad R_2 = [(z-z')^2+(2h)^2]^{\frac{1}{2}}; \quad R_3 = [(z-z')^2+b^2]^{\frac{1}{2}};\\ &R_4 = [(z-z')^2+(2h)^2+b^2]^{\frac{1}{2}}; \quad R_5 = [(h+z)^2+(h+x')^2+a^2]^{\frac{1}{2}};\\ &R_6 = [(h-z)^2+(h+x')^2+a^2]^{\frac{1}{2}}; \quad R_7 = [(h+z)^2+(h+x')^2+b^2]^{\frac{1}{2}};\\ &R_8 = [(h-z)^2+(h+x')^2+b^2]^{\frac{1}{2}}. \end{aligned}$$

It should be noted here that the currents and charges per unit length on each of the two loops are I_{1z}, I_{2z}, I_{3z}, I_{4z} and $q_1(z)$, $q_2(x)$, $q_3(z)$, $q_4(x)$ with the appropriate superscripts. The equations for the scalar potential are similar to those obtained for the vector potential with ϵ_0 replacing ν_0 and charges replacing currents under the integral sign.

By substituting eq. (2) in eq. (1), the following differential equation is obtained for the z-component of the vector potential on the surface of conductor 1 of either loop:

$$(6) \qquad \frac{\partial^2 A_{1z}}{\partial z^2} + \beta_0^2 A_{1z} = \frac{j\beta_0^2}{\omega}\frac{\partial \phi_{1x}}{\partial z}.$$

The solution of this equation is the sum of a complementary function and a particular integral as given below:

$$(7) \qquad A_{1z}(z) = \frac{-j}{v_0}[C_1 \cos \beta_0 z + C_2 \sin \beta_0 z - \theta_A(z)]$$

where

$$v_0 = 1/\sqrt{(\mu_0\epsilon_0)}$$

and

$$(8) \qquad \theta_A(z) = \int_{z_0}^{z} \frac{\partial \phi_{1x}(w)}{\partial w} \sin \beta_0(z-w)\,dw.$$

The lower limit is arbitrary and may be conveniently chosen to be zero. When the expressions for vector potential obtained in eqs. (3*a*) and (7) are equated, the following integral equation is obtained:

$$(9)\qquad \int_{-h}^{h} [I^{\mathrm{I}}_{1z}(z')K_1+I^{\mathrm{I}}_{3z}(z')K_2]\,dz'+\int_{-h}^{h} [I^{\mathrm{II}}_{1z}(z')K_3+I^{\mathrm{II}}_{3z}(z')K_4]\,dz' = -j\frac{4\pi}{\zeta_0}[C^{\mathrm{I}}_1\cos\beta_0 z+C^{\mathrm{I}}_2\sin\beta_0 z-\theta^{\mathrm{I}}_A(z)].$$

A similar equation with superscripts II and I interchanged is obtained for loop II; thus two simultaneous integral equations for the currents in the two loops have been derived. It should be noted that, since $\theta_A(z)$ is a function of $I_{2z}(x')$ and $I_{4z}(x')$ for each loop, all four sides of each loop are involved in the integral equations.

The currents are to be evaluated in terms of the eight different driving voltages. The voltage at terminals 1, 2 of loop I is typical:

$$(10)\qquad V^{\mathrm{I}}_{12} = \phi^{\mathrm{I}}_1(z=-h)-\phi^{\mathrm{I}}_2(z=-h).$$

As in the case of the isolated loop, these driving voltages may be expressed in terms of sequential combinations of four phase-sequence voltages; the currents may be represented in the same manner (King 1956). Here, interest is primarily in the zeroth-phase sequence—voltages equal and in phase—and the second-phase sequence—voltages equal and alternately in and out of phase. The voltages and currents for these phase sequences are expressed below in terms of the driving voltages and currents on each side. Phase sequences are denoted by superscripts:

$$(11a)\quad V^{(0)} = \tfrac{1}{4}[V_{12}+V_{23}+V_{34}+V_{41}];\qquad V^{(2)} = \tfrac{1}{4}[V_{12}-V_{23}+V_{34}-V_{41}];$$

$$(11b)\quad I^{(0)} = \tfrac{1}{4}[I_1+I_2+I_3+I_4];\qquad I^{(2)} = \tfrac{1}{4}[I_1-I_2+I_3-I_4].$$

TWO LOOPS, EACH WITH FOUR EQUAL VOLTAGES IN PHASE: ZEROTH-PHASE SEQUENCE

The relations for either loop are:

$$V_{12} = V_{23} = V_{34} = V_{41} = V^{(0)},$$
$$I_{1z}(z) = -I_{2x}(x) = -I_{3z}(z) = I_{4z}(x) = I^{(0)},$$
$$q_1(z) = -q_2(x) = -q_3(x) = q_4(x) = q^{(0)}.$$

Because of geometrical and electrical symmetry

$$(12a)\quad I^{(0)}_{1z}(-z) = I^{(0)}_{1z}(z);\qquad A^{(0)}_{1z}(-z) = A^{(0)}_{1z}(z);\qquad A^{(0)}_{1r}(-z) = -A^{(0)}_{1r}(z)$$

$$(12b)\quad q^{(0)}_1(-z) = -q^{(0)}_1(z);\qquad \phi^{(0)}_1(-z) = -\phi^{(0)}_1(z).$$

The potentials are defined on the surface on conductor 1 of either loop. From eq. (12) it is seen that

$$(13a)\quad \phi^{(0)}_1(0) = 0,\qquad A^{(0)}_{1z}(0) = 0,\qquad A^{(0)}_{1z}(0)\quad \text{is extreme;}$$

$$(13b)\quad q^{(0)}_1(0) = 0,\qquad I^{(0)}_{1z}(0)\quad \text{is extreme.}$$

Since $A_{1z}^{(0)}(z)$ as well as $I_{1z}^{(0)}(z) = -I_{3z}^{(0)}(z)$ are even in z, it is necessary that both sides of the integral equation (9) be even in z when specialized to the zeroth-phase sequence. The integral equation becomes

$$(14) \quad \int_{-h}^{h} I_{1z}^{\mathrm{I}(0)}(z')[K_1-K_2]\,dz' + \int_{-h}^{h} I_{1z}^{\mathrm{II}(0)}(z')[K_3-K_4]\,dz' = -j\frac{4\pi}{\zeta_0}[C_1^{\mathrm{I}(0)}\cos\beta_0 z - \theta_A^{\mathrm{I}(0)}(z)].$$

An interchange of the superscripts I and II leads to a similar equation for loop II. Thus, two simultaneous integral equations are obtained which may be solved by separating the voltages into a codirectional or symmetric pair and an oppositely directed or antisymmetric pair.

Regardless of the relative magnitudes and phases of $V^{\mathrm{I}(0)}$ and $V^{\mathrm{II}(0)}$, they may be expressed as follows:

$$(15a) \qquad V^{\mathrm{I}(0)} = V^{s(0)} + V^{a(0)}; \qquad V^{\mathrm{II}(0)} = V^{s(0)} - V^{a(0)}.$$

$V^{s(0)}$ stands for the equal and codirectional parts of $V^{\mathrm{I}(0)}$ and $V^{\mathrm{II}(0)}$, and $V^{a(0)}$ and $-V^{a(0)}$ for the equal and oppositely directed parts. The currents in side 1 of each of the two loops due to the simultaneous application of the equal and codirectional voltages $V^{s(0)}$ are themselves equal and codirectional: $I_{1z}^{\mathrm{I}s(0)} = I_{1z}^{\mathrm{II}s(0)} = I_{1z}^{s(0)}$. Similarly, the currents due to the simultaneous application of the equal and opposite voltages $V^{a(0)}$ are themselves equal and opposite: $I_{1z}^{\mathrm{I}a(0)} = -I_{1z}^{\mathrm{II}a(0)} = I_{1z}^{a(0)}$. By the principle of superposition, the currents due to the combined application of the two sets of voltages in eq. (15) are

$$(15b) \qquad I_{1z}^{\mathrm{I}(0)}(z) = I_{1z}^{s(0)} + I_{1z}^{a(0)}; \qquad I_{1z}^{\mathrm{II}(0)}(z) = I_{1z}^{s(0)} - I_{1z}^{a(0)}.$$

The problem is now reduced to two independent problems:

(1) the solution of the problem of equal and codirectional voltages,

(2) the solution of the problem of equal and opposite voltages.

Symmetrically Driven Loops

If the complex amplitudes of the voltages in the two loops are both equal to $V^{s(0)}$, the currents in the two loops are also equal at the same value of z:

$$(16) \qquad I_{1z}^{\mathrm{I}s(0)} = I_{1z}^{\mathrm{II}s(0)} = I_{1z}^{s(0)}.$$

The following integral equation is obtained from eq. (14):

$$(17) \qquad \int_{-h}^{h} I_{1z}^{s(0)}(z')K_A^{s(0)}(z, z')\,dz' = -j\frac{4\pi}{\zeta_0}[C_1^{s(0)}\cos\beta_0 z - \theta_A^{s(0)}(z)],$$

where

$$K_A^{s(0)} = K_1 - K_2 + K_3 - K_4.$$

The integral equation is similar to that obtained for the isolated square loop. It may be solved by a method of iteration similar to that used for the center-driven dipole. Let

$$\psi^{s(0)}(z) = \psi^{s(0)} + \gamma^{s(0)}(z) = \int_{-h}^{h} g^{s(0)}(z, z') K_A^{s(0)}(z, z')\, dz' \tag{18}$$

where

$$g^{s(0)}(z, z') = I_{1z}^{s(0)}(z')/I_{1z}^{s(0)}(z).$$

$I_{1z}^{s(0)}(z')$ is the current at z' on side 1 of either loop, $I_{1z}^{s(0)}(z)$ is the current at z on side 1 of either loop. The function $\psi^{s(0)}(z)$ is proportional to the ratio of the vector potential A_{1z} at the point z on the surface of side 1 of the loop to the total current in that side if $g^{s(0)}(z, z')$ is exactly equal to $I_{1z}^{s(0)}(z')/I_{1z}^{s(0)}(z)$. $\psi^{s(0)}$ is the approximately constant magnitude of $\psi^{s(0)}(z)$ at an appropriate point. By the symmetry conditions stated earlier, the vector potential is a maximum at $z = 0$. So $\psi^{s(0)}$ may be defined likewise:

$$\psi^{s(0)} = |\psi^{s(0)}(z = 0)|. \tag{19}$$

$\gamma^{s(0)}(z)$ is the correction to be applied to $\psi^{s(0)}(z)$ and consequently the distribution of current along the loop.

By adding $I_{1z}^{s(0)}\psi^{s(0)}(z)$ to both sides of eq. (17) and rearranging terms:

$$I_{1z}^{s(0)} = \frac{-j4\pi}{\zeta_0 \psi^{s(0)}} [C_1^{s(0)} \cos \beta_0 z - \theta_A^{s(0)}(z)] - \frac{1}{\psi^{s(0)}} \left\{ \int_{-h}^{h} [I_{1z}^{s(0)}(z') - I_{1z}^{s(0)}(z) g^{s(0)}(z, z')] K_A^{s(0)}(z, z')\, dz' + I_{1z}^{s(0)}(z) \gamma^{s(0)}(z) \right\}. \tag{20}$$

Zeroth-order approximations of current, charge, vector, and scalar potentials are:

$$[I_{1z}^{s(0)}(z)]_0 = \frac{-j4\pi}{\zeta_0 \psi^{s(0)}} C_1^{s(0)} F_0^{s(0)}; \qquad [q_1^{s(0)}(z)]_0 = \frac{-4\pi\epsilon_0}{\psi^{s(0)}} C_1^{s(0)} G_0^{s(0)}(z) \tag{21a}$$

$$[A_{1z}^{s(0)}(z)]_0 = \frac{-j}{v_0} C_1^{s(0)} F_0^{s(0)}(z); \qquad [\phi_1^{s(0)}(z)]_0 = C_1^{s(0)} G_0^{s(0)}(z) \tag{21b}$$

where

$$F_0^{s(0)}(z) = \cos \beta_0 z; \qquad G_0^{s(0)}(z) = \sin \beta_0 z. \tag{22}$$

A first-order solution for the symmetrical currents when the two loops are driven in the zeroth-phase sequence is obtained by using the above approximations:

$$[I_{1z}^{s(0)}(z)]_1 = \frac{-j4\pi}{\zeta_0 \psi^{s(0)}} C_1^{s(0)} \left\{ F_0^{s(0)}(z) + \frac{1}{\psi^{s(0)}} [F_1^{s(0)}(z) + L_1^{s(0)}(z)] \right\} \tag{23}$$

where

$$F_1^{s(0)}(z) = -\left\{ \int_{-h}^{h} [F_0^{s(0)}(z') - F_0^{s(0)}(z) g^{s(0)}(z, z')] K_A^{s(0)}(z, z')\, dz' + F_0^{s(0)}(z) \gamma^{s(0)}(z) \right\}; \tag{24}$$

and

$$L_1^{s(0)}(z) = \int_0^z \beta_0 J_1^{s(0)}(w) \cos \beta_0(z-w)dw \tag{25}$$

where

$$J_1^{s(0)}(z) = -\int_{-h}^{h} \sin \beta_0 x' K_B^{s(0)}(z,x')\, dx'; \tag{26}$$

and

$$K_B^{s(0)}(z,x') = K_5 - K_6 + K_7 - K_8.$$

A first-order evaluation of the constant $C_1^{s(0)}$ may be made:

$$\tfrac{1}{2} V^{s(0)} = -[C_1^{s(0)}]_1 \left[\sin \beta_0(-h) + \frac{M_1^{s(0)}(-h)}{\psi^{s(0)}} \right] \tag{27}$$

where

$$M_1^{s(0)}(-h) = \int_0^{-h} \beta_0 J_1^{s(0)}(w) \sin \beta_0(-h-w)dw. \tag{28}$$

The expansion parameter may also be obtained by using the zeroth-order value of current:

$$g^{s(0)}(z,z') = \cos \beta_0 z'/\cos \beta_0 z$$

$$\begin{aligned} \psi^{s(0)}(z) &= \psi^{s(0)} + \gamma^{s(0)}(z) \\ &= \frac{1}{\cos \beta_0 z} \int_{-h}^{h} \cos \beta_0 z' K_A^{s(0)}(z,z')\, dz' \\ &= \sec \beta_0 z [C_A(h,z) - C_{2h}(h,z) + C_b(h,z) - C_n(h,z)] \end{aligned} \tag{29}$$

where

$$C_i(h,z) = \int_{-h}^{h} \cos \beta_0 z' K_i\, dz'. \tag{30}$$

K_i has been defined previously. In this case, however, $R_i = [(z-z')^2 + i^2]^{\frac{1}{2}}$ with $i = a, 2h, b, n$ where $n = \sqrt{[(2h)^2 + b^2]}$. As shown before, $\psi^{s(0)}$ is the magnitude of $\psi^{s(0)}$ at $z = 0$ so

$$\psi^{s(0)} = |C_a(h,0) - C_{2h}(h,0) + C_b(h,0) - C_n(h,0)|. \tag{31}$$

Since the same zeroth-order distribution of current is used for $g^{s(0)}(z,z')$ as for $F_0^{s(0)}(z)$, the term under the integral sign in eq. (24) vanishes and $F_1^{s(0)}(z) = -\gamma^{s(0)}(z) \cos \beta_0 z$. The first-order current is given by

$$[I_{1z}^{s(0)}(z)]_1 = \frac{j2\pi V^{s(0)}}{\zeta_0 \psi^{s(0)}} \left\{ \frac{\cos \beta_0 z + [L_1^{s(0)}(z) - \gamma^{s(0)} \cos \beta_0 z]/\psi^{s(0)}}{\sin \beta_0(-h) + M_1^{s(0)}(-h)/\psi^{s(0)}} \right\}. \tag{32}$$

The zeroth-order current is given by

$$[I_{1z}^{s(0)}]_0 = \frac{j2\pi V^{s(0)}}{\zeta_0 \psi^{s(0)}} \left\{ \frac{\cos \beta_0 z}{\sin \beta_0(-h)} \right\}. \tag{33}$$

Antisymmetrically Driven Loops

When the loops are driven antisymmetrically in the zeroth-phase sequence

$$I_{1z}^{\mathrm{I}a(0)} = -I_{1z}^{\mathrm{II}a(0)} = I_{1z}^{a(0)}. \tag{34}$$

The following integral equation is obtained for the current

$$\int_{-h}^{h} I_{1z}^{a(0)} K_A^{a(0)}(z,z')\,dz' = \frac{-j4\pi}{\zeta_0}\left[C_1^{a(0)} \cos \beta_0 z - \theta_A^{a(0)}(z)\right] \tag{35}$$

where

$$K_A^{a(0)}(z,z') = K_1 - K_2 - K_3 + K_4.$$

Assuming similar zeroth-order solutions for current, charge, and vector and scalar potentials and using the same iterative procedure as that used in the calculation of the symmetrical current, a first-order solution of the antisymmetrical zeroth-phase sequence current is obtained:

$$[I_{1z}^{a(0)}(z)]_1 = \frac{j2\pi V^{a(0)}}{\zeta_0 \psi^{a(0)}} \left\{ \frac{\cos \beta_0 z + [L_1^{a(0)}(z) - \gamma^{a(0)} \cos \beta_0 z/\psi^{a(0)}}{\sin \beta_0(-h) + M_1^{a(0)}(-h)/\psi^{a(0)}} \right\}. \tag{36}$$

TWO LOOPS, EACH WITH FOUR EQUAL VOLTAGES ALTERNATELY OUT OF PHASE: SECOND-PHASE SEQUENCE

The following relations are true for either loop:

$$V_{12} = -V_{23} = V_{34} = -V_{41} = V^{(2)},$$
$$I_{1z}(z) = -I_{2z}(x) = I_{3z}(z) = -I_{4z}(x) = I^{(2)},$$
$$q_1(z) = -q_2(x) = q_3(z) = -q_4(x) = q^{(2)}.$$

Because of geometrical and electrical symmetry,

$$I_{1z}^{(2)}(-z) = -I_{1z}^{(2)}(z); \qquad A_{1z}^{(2)}(-z) = -A_{1z}^{(2)}(z); \qquad A_{1x}^{(2)}(-z) = A_{1x}^{(2)}(z) \tag{37a}$$

$$q_1^{(2)}(-z) = q_1^{(2)}(z); \qquad \phi_1^{(2)}(-z) = \phi_1^{(2)}(z) \tag{37b}$$

where the potentials are defined on the surface of side 1. From the above relations it follows that

$$A_{1z}^{(2)}(0) = 0, \quad \phi_1^{(2)}(0) \quad \text{is extreme;} \tag{38a}$$

$$I_{1z}^{(2)}(0) = 0, \quad q_1^{(2)}(0) \quad \text{is extreme.} \tag{38b}$$

Since current and vector potential are odd functions of z, both sides of the integral equation (9) must necessarily be even in z when specialized to the second-phase sequence. The integral equation becomes

$$\int_{-h}^{h} I_{1z}^{\mathrm{I}(2)}(z')[K_1+K_2]\,dz' + \int_{-h}^{h} I_{1z}^{\mathrm{II}(2)}(z')[K_3+K_4]\,dz' = \frac{-j4\pi}{\zeta_0}\left[C_2^{\mathrm{I}(2)} \sin \beta_0 z - \theta_A^{\mathrm{I}(2)}(z)\right]. \tag{39}$$

An interchange of the superscripts I and II leads to a similar equation for loop II. In this manner two simultaneous integral equations for the currents

are obtained. They may again be solved by separating the voltages into a codirectional or symmetric pair and an oppositely directed pair.

Symmetrically Driven Loops

Using a procedure similar to that used in the zeroth-phase sequence

$$\int_{-h}^{h} I_{1z}^{s(2)}(z')K_A^{s(2)}(z,z')\,dz' = \frac{-j4\pi}{\zeta_0}\left[C_2^{s(2)}\sin\beta_0 z - \theta_A^{s(2)}(z)\right] \tag{40}$$

where

$$K_A^{s(2)}(z,z') = K_1+K_2+K_3+K_4.$$

The function

$$\begin{aligned}\psi^{s(2)}(z) &= \psi^{s(2)}+\gamma^{s(2)}\\ &= \frac{1}{\sin\beta_0 z}\int_{-h}^{h}\sin\beta_0 z' K_A^{s(2)}(z,z')\,dz' \qquad (41)\\ &= \csc\beta_0 z[S_a(h,z)+S_{2h}(h,z)+S_b(h,z)+S_n(h,z)]\end{aligned}$$

where

$$S_t(h,z) = \int_{-h}^{h}\sin\beta_0 z'\,K_t\,dz'. \tag{42}$$

K_t has been defined for the zeroth-phase sequence. As stated before, $\psi^{s(2)}$ is the magnitude of $\psi^{s(2)}(z)$ at $z = 0$. Since the expression for $\psi^{s(2)}(z)$ becomes indeterminate at $z = 0$, the limiting value is taken and the following expression is obtained:

$$\psi^{s(2)} = \left| C_a(h,0)+C_{2h}(h,0)+C_b(h,0)+C_n(h,0)-\frac{2\sin\beta_0 h}{\beta_0}K_A^{s(2)}(0,h)\right|. \tag{43}$$

The first-order current becomes

$$[I_{1z}^{s(2)}(z)]_1 = \frac{-j2\pi V^{s(2)}}{\zeta_0\psi^{s(2)}}\left[\frac{\sin\beta_0 z+\{L_1^{s(2)}(z)-\gamma^{s(2)}(z)\sin\beta_0 z\}/\psi^{s(2)}}{\cos\beta_0(-h)+M_1^{s(2)}(-h)/\psi^{s(2)}}\right]. \tag{44}$$

The zeroth-order current is given by

$$[I_{1z}^{s(2)}(z)]_0 = \frac{-j2\pi V^{s(2)}}{\zeta_0\psi^{s(2)}}\frac{\sin\beta_0 z}{\cos\beta_0(-h)}. \tag{45}$$

Antisymmetrically Driven Loops

Assuming the zeroth-order solutions for current, charge, and associated potentials similar to the symmetrical case and using the same iterative procedure, a first-order solution of the antisymmetrical current in the second-phase sequence is obtained:

$$[I_{1z}^{a(2)}(z)]_1 = \frac{-j2\pi V^{a(2)}}{\zeta_0\psi^{a(2)}}\left[\frac{\sin\beta_0 z+\{L_1^{a(2)}(z)-\gamma^{a(2)}(z)\sin\beta_0 z\}/\psi^{a(2)}}{\cos\beta_0(-h)+M_1^{a(2)}(-h)/\psi^{a(2)}}\right]. \tag{46}$$

The zeroth-order value of the antisymmetric current in the second-phase sequence is given by

$$[I_{1z}^{a(2)}(z)]_0 = \frac{-j2\pi V^{a(2)}}{\zeta_0\psi^{a(2)}}\frac{\sin\beta_0 z}{\cos\beta_0(-h)}. \tag{47}$$

SELF AND MUTUAL IMPEDANCES

From the expressions for symmetrical and antisymmetrical currents in terms of the general currents in the loops, the following equations are obtained:

$$V^{\mathrm{I}} = I^{\mathrm{I}}\cdot\tfrac{1}{2}[Z^s+Z^a]+I^{\mathrm{II}}\cdot\tfrac{1}{2}[Z^s-Z^a], \tag{48a}$$

$$V^{\mathrm{II}} = I^{\mathrm{I}}\cdot\tfrac{1}{2}[Z^s-Z^a]+I^{\mathrm{II}}\cdot\tfrac{1}{2}[Z^s+Z^a]. \tag{48b}$$

The above equations are in the general form of circuit equations in which $\frac{1}{2}[Z^s+Z^a]$ is the self-impedance and $\frac{1}{2}[Z^s-Z^a]$ the mutual impedance for loops driven in both the zeroth- and second-order sequences.

SUPERPOSITION OF ZEROTH- AND SECOND-PHASE SEQUENCES

When there is a simple superposition of the zeroth- and second-phase sequences, the following relations hold true for either loop:

$$V_{12} = V_{34} = V^{(0)}+V^{(2)}; \qquad V_{23} = V_{41} = V^{(0)}-V^{(2)} \tag{49}$$

$$I_1 = I_3 = I^{(0)}+I^{(2)}; \qquad I_2 = I_4 = I^{(0)}-I^{(2)}. \tag{50}$$

From the relations between the symmetrical and antisymmetrical voltages and the voltages of the zeroth- and second-phase sequences, the following results are obtained:

$$V^{\mathrm{I}}_{12} = V^{s(0)}+V^{s(2)}+V^{a(0)}+V^{a(2)}, \tag{51a}$$

$$V^{\mathrm{I}}_{23} = V^{s(0)}-V^{s(2)}+V^{a(0)}-V^{a(2)}, \tag{51b}$$

$$V^{\mathrm{II}}_{12} = V^{s(0)}+V^{s(2)}-V^{a(0)}-V^{a(2)}, \tag{51c}$$

$$V^{\mathrm{II}}_{23} = V^{s(0)}-V^{s(2)}-V^{a(0)}+V^{a(2)}. \tag{51d}$$

The relations between the phase-sequence currents and the symmetrical and antisymmetrical components lead to:

$$V^{\mathrm{I}}_{12} = I^{\mathrm{I}}_1Z_{\mathrm{ss}}+I^{\mathrm{I}}_2Z_{\mathrm{st}}+I^{\mathrm{II}}_1Z_{\mathrm{ms}}+I^{\mathrm{II}}_2Z_{\mathrm{mt}}, \tag{52a}$$

$$V^{\mathrm{I}}_{23} = I^{\mathrm{I}}_1Z_{\mathrm{st}}+I^{\mathrm{I}}_2Z_{\mathrm{ss}}+I^{\mathrm{II}}_1Z_{\mathrm{mt}}+I^{\mathrm{II}}_2Z_{\mathrm{ms}}, \tag{52b}$$

$$V^{\mathrm{II}}_{12} = I^{\mathrm{I}}_1Z_{\mathrm{ms}}+I^{\mathrm{I}}_2Z_{\mathrm{mt}}+I^{\mathrm{II}}_1Z_{\mathrm{ss}}+I^{\mathrm{II}}_2Z_{\mathrm{st}}, \tag{52c}$$

$$V^{\mathrm{II}}_{23} = I^{\mathrm{I}}_1Z_{\mathrm{mt}}+I^{\mathrm{I}}_2Z_{\mathrm{ms}}+I^{\mathrm{II}}_1Z_{\mathrm{st}}+I^{\mathrm{II}}_2Z_{\mathrm{ss}}, \tag{52d}$$

where

$$\begin{aligned} Z_{\mathrm{ss}} &= \tfrac{1}{2}[Z^{(0)}_{\mathrm{s}}+Z^{(2)}_{\mathrm{s}}]; \qquad Z_{\mathrm{st}} = \tfrac{1}{2}[Z^{(0)}_{\mathrm{s}}-Z^{(2)}_{\mathrm{s}}], \\ Z_{\mathrm{ms}} &= \tfrac{1}{2}[Z^{(0)}_{\mathrm{m}}+Z^{(2)}_{\mathrm{m}}]; \qquad Z_{\mathrm{mt}} = \tfrac{1}{2}[Z^{(0)}_{\mathrm{m}}-Z^{(2)}_{\mathrm{m}}]. \end{aligned} \tag{53}$$

If a load or tuning impedance Z_{L} is connected in place of the driving voltages V_{23} and V_{41} for either loop, $V_{23} = -I_2Z_{\mathrm{L}} = V_{41}$.

Equations (52) may be reduced to two simultaneous equations in the two variable currents I^{I}_1 and I^{II}_1, the other two currents I^{I}_2 and I^{II}_2 also being expressed in terms of these currents. The equations reduce to the following simultaneous equations for coupled circuits:

$$V_{12}^{\mathrm{I}} = I_1^{\mathrm{I}} Z_{\mathrm{self}}^{\mathrm{I}} + I_1^{\mathrm{II}} Z_{\mathrm{mut}} \tag{54a}$$

$$V_{12}^{\mathrm{II}} = I_1^{\mathrm{I}} Z_{\mathrm{mut}} + I_1^{\mathrm{II}} Z_{\mathrm{self}} \tag{54b}$$

where

$$Z_{\mathrm{self}}^{\mathrm{I}} = Z_{\mathrm{ss}} + \frac{2Z_{\mathrm{st}}Z_{\mathrm{ms}}Z_{\mathrm{mt}} - Z_{\mathrm{st}}^2(Z_{\mathrm{ss}} + Z_{\mathrm{L}}^{\mathrm{II}}) - Z_{\mathrm{mt}}^2(Z_{\mathrm{ss}} + Z_{\mathrm{L}}^{\mathrm{I}})}{(Z_{\mathrm{ss}} + Z_{\mathrm{L}}^{\mathrm{I}})(Z_{\mathrm{ss}} + Z_{\mathrm{L}}^{\mathrm{II}}) - Z_{\mathrm{ms}}^2}. \tag{55}$$

$Z_{\mathrm{self}}^{\mathrm{II}}$ is obtained by interchanging $Z_{\mathrm{L}}^{\mathrm{I}}$ and $Z_{\mathrm{L}}^{\mathrm{II}}$:

$$Z_{\mathrm{mut}} = Z_{\mathrm{ms}} + \frac{Z_{\mathrm{ms}}(Z_{\mathrm{st}}^2 + Z_{\mathrm{mt}}^2) - Z_{\mathrm{mt}}Z_{\mathrm{st}}[2Z_{\mathrm{ss}} + Z_{\mathrm{L}}^{\mathrm{I}} + Z_{\mathrm{L}}^{\mathrm{II}}]}{(Z_{\mathrm{ss}} + Z_{\mathrm{L}}^{\mathrm{I}})(Z_{\mathrm{ss}} + Z_{\mathrm{L}}^{\mathrm{II}}) - Z_{\mathrm{ms}}^2}. \tag{56}$$

All results are worked out in detail in (Prasad 1959).

ACKNOWLEDGMENT

The author is deeply grateful to Professor Ronold W. P. King for his guidance and encouragement during this research.

REFERENCES

KING, R. W. P. 1956. Trans. IRE, **AP-4** (3), 393.
PRASAD, S. 1959. Theory of Corner-Driven Coupled Square Loop Antennas, Cruft Laboratory, Harvard University, Cambridge, Massachusetts, Technical Report No. 277.

THE ANGULAR DISTRIBUTION OF PHOTOFISSION FRAGMENTS[1]

A. P. BAERG,[2] R. M. BARTHOLOMEW,[2] F. BROWN,[2] L. KATZ,[3] AND S. B. KOWALSKI[3]

ABSTRACT

Angular distributions of photofission fragments relative to the photon beam have been measured as a function of maximum bremsstrahlung energy in the range 6–20 Mev. The nuclides U-233, U-235, Np-237, Pu-239, and Am-241 give an isotropic distribution at all energies studied. The nuclides Th-232, U-234, U-236, U-238, and Pu-240 give anisotropic distributions which can be described by an equation of the form $W(\theta) = 1+\alpha \sin^2 \theta$ where θ is the angle between fragment and beam. The degree of anisotropy is large at low energy and falls rapidly as the energy is increased. At a given energy Th-232 has the greatest degree of anisotropy and Pu-240 the least.

INTRODUCTION

Measurements of the angular distributions of photofission fragments relative to the photon beam have been summarized by Winhold and Halpern (1956). The experiments consisted of catching fragments at various angles and measuring their radioactivity either with or without prior chemical separation of the fission product species. The conclusions were as follows. Photofission of U-235 is isotropic at all maximum bremsstrahlung energies, E_0, from 6.5 to 10.5 Mev. Photofission of Th-232 and U-238 is anisotropic and the form of the angular distribution for Th-232 at $E_0 = 16$ Mev, which was measured only approximately, is of the type $W(\theta) = 1+\alpha \sin^2 \theta$ where $W(\theta)$ is the distribution function and θ is the angle between the direction of fragment emission and the photon beam. This is the form expected for dipole absorption of photons. The values of α for both nuclides fall with increasing bremsstrahlung energy, being in the order of 1.0 at $E_0 = 8$ Mev and 0.2 at $E_0 = 14$ Mev. There appears to be a correlation between the degree of anisotropy and the mass ratio of the fragments; at $E_0 = 16$ Mev α was greater for asymmetric fission than for symmetric.

Lazareva *et al.* (1957) and Baz *et al.* (1958) have obtained angular distributions by photographic plate techniques and interpret these results to show that the form of the angular distribution for U-238 at $E_0 = 9.4$ Mev contains terms of $\sin^4 \theta$ (or $\sin^2 \theta$), implying some quadrupole absorption.

The present work was undertaken in the hope of obtaining more accurate distributions, of measuring the distribution forms at a variety of energies, and of extending the range of nuclides studied. Results for Th-232, U-233,

[1]Manuscript received August 11, 1959.
Contribution from Research Chemistry Branch, Atomic Energy of Canada Limited, Chalk River, Ontario and from Department of Physics, University of Saskatchewan, Saskatoon, Saskatchewan.
Issued as A.E.C.L. No. 896.
[2]Atomic Energy of Canada Limited, Chalk River, Ontario.
[3]University of Saskatchewan, Saskatoon, Saskatchewan.

U-235, U-238, Np-237, Pu-239, and Am-241 have been presented in a previous publication (Katz 1958). The present paper gives some new data for these nuclides and also results for U-234, U-236, and Pu-240.

EXPERIMENTAL TECHNIQUES

The fission fragments were detected in an ionization chamber. The fission chamber and associated electronic apparatus have been described by Katz (1958). The collimating system is shown diagrammatically in Fig. 1. It consisted of two aluminum plates 0.318 cm thick, one on each side of the source disk and each drilled with sufficient holes 0.159 cm in diameter to give 50% optical transmission. The holes were at 45° to the surface of the plates and all parallel. The two plates were aligned so that the two sets of holes were also parallel. The complete assembly, plates and source which could not move relative to one another, could be rotated in the plane of the source by means of an indexed system of gears without opening the fission chamber. The X-ray beam was directed at 45° to the plane of the source such that in one position the collimator holes were parallel to the beam (Fig. 1) and hence when the

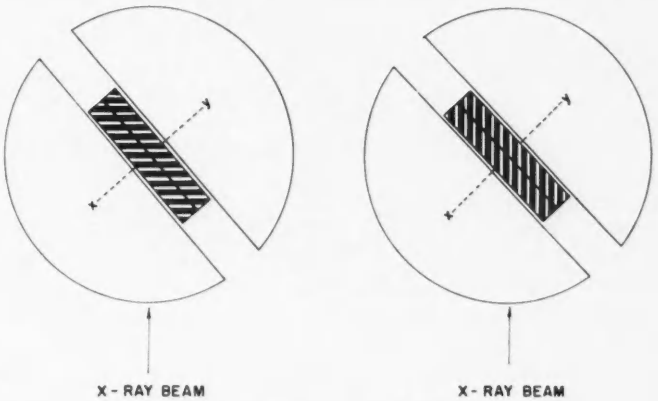

FIG. 1. Collimating system.

collimator assembly had been rotated through 180° about the x–y axis the holes were perpendicular to the beam. Thus any angle θ between beam and collimator holes in the range $\theta = 0°$ to $\theta = 90°$ could be selected by rotating the assembly through the angle ψ where $\cos\theta = (1+\cos\psi)/2$. Because each fission gives two fragments travelling in opposite directions and because no attempt was made to distinguish the light and heavy fragments it was not necessary to distinguish between the forward and backward directions; both directions parallel to the beam are referred to as 0°.

The sources in the cases of Th-232, U-235, and U-238 consisted of disks of metal about 0.005 cm thick (~75 mg/cm²). They were thus infinitely thick compared with the fission fragment ranges. For the remaining nuclides the

sources were aluminum disks, 0.08 cm thick, coated on both sides with oxide layers of thickness about 1.0 mg/cm². They were thus relatively thin to fission fragments coming out from the oxide layer but infinitely thick to fragments going inwards through the aluminum backing.

The source of photons was the University of Saskatchewan betatron. The method of operation was to set the desired betatron energy and to measure the number of fissions per arbitrary X-ray dose unit at various chosen settings of the angle θ. Changes of setting were made frequently to eliminate the effect of possible 'drifts'. The collimator holes accepted fragments travelling within a finite angle and thus, in calculating the forms and parameters of the angular distribution functions it was necessary to introduce resolution corrections. The method of applying the corrections was kindly determined by Drs. E. Vogt and J. M. Kennedy of the Theoretical Physics Branch, A.E.C.L., and their results are given in the Appendix to this paper. The correction factor applying to the anisotropy coefficient α varied from unity at small anisotropy to approximately two at the largest anisotropy observed.

RESULTS AND DISCUSSION

Odd A Nuclei

The ideas put forward by Bohr (1956), based on the collective model of the nucleus, suggest that these nuclides should show an isotropic or near isotropic distribution of fission fragments. Measurements were made on U-233, U-235, Np-237, Pu-239, and Am-241 at $\theta = 0$ and $\theta = 90$. Most attention was paid to the lower energies where any anisotropy might be expected to be greatest. Special attention was given to Pu-239 because, having the smallest possible non-zero spin, i.e. 1/2, it has some chance of showing an anisotropic distribution. Thus for this nuclide the measurements were extended to lower energies than for the others and a measurement at $\theta = 45°$ was included at one energy. The results are shown in Table I, where the errors in the ratios are standard deviations based only on the counting statistics. There is no evidence for anisotropy.

TABLE I

Angular distributions
Ratio, counts at 90°/counts at 0°*

Nuclide	E_0† = 6.0	E_0 = 6.5	E_0 = 8.0	E_0 = 10.0	E_0 = 20.0
U-233			1.048±0.07	1.032±0.04	0.994±0.03
U-235			1.024±0.05		
Np-237			1.024±0.10		
Pu-239‡	1.034±0.26	0.927±0.12	1.002±0.06	1.013±0.05	0.952±0.03
Am-241			0.958±0.07		

*The ratio is the number of counts observed at 90° per unit X-ray dose divided by the number observed at 0° for the same dose.
†E_0 is the maximum energy in million electron volts of the bremsstrahlung spectrum.
‡The 45°/0° ratio at E_0 = 6.5 Mev was 1.09±0.23.

Even–Even Nuclei

Photofission of Th-232 and U-238 is known to be anisotropic from the work of Winhold and Halpern (1956). The Bohr model attributes the anisotropy,

peaked at 90°, to nuclei which pass the saddle point of fission in the lowest available state which for dipole photon absorption in an even–even nucleus is a rotational excitation having total angular momentum $I = 1$, negative parity, and projection of angular momentum on the nuclear symmetry axis $K = 0$. Fission through such a state will give an angular distribution of the form $W(\theta) = \sin^2\theta$, i.e. peaked at 90°.

The saddle point state with $I = 1$, negative parity, and $K = 1$ is expected to lie higher by about 1 Mev because in order to produce the $K = 1$ state it is necessary to bring about an intrinsic excitation, i.e. to excite one or more nucleons to higher levels which in turn requires breaking a nucleon–nucleon pair and hence the pairing energy, about 1 Mev, must be supplied. Fission through this $K = 1$ state will have an angular distribution of the form $W(\theta) = 2-\sin^2\theta$, i.e. peaked at 0°.

Thus the barrier for fission through the $(1-)K = 0$ saddle point state is lower than that for the $K = 1$ state and at excitation energies close to threshold, where barrier penetration is the important consideration, fission through the $K = 0$ state will be preferred and will display the corresponding anisotropy peaked at 90°. At higher energies, where barrier penetration is not so important, fission will take place through both $K = 0$ and $K = 1$ states and the superposition of the two opposed distributions will result in one which is near isotropic. In general, therefore, the distribution expected is $W(\theta) = 1 + \alpha \sin^2\theta$ with α decreasing with increasing photon energy.

In the case that quadrupole absorption occurred, leading to a $(2+)$ state, the angular distributions expected are as follows: for $K = 0$, $W(\theta) = \sin^2(2\theta)$; for $K = 1$, $W(\theta) = 2-\sin^2\theta-\sin^2(2\theta)$; and for $K = 2$, $W(\theta) = \sin^2\theta + 1/4\sin^2(2\theta)$. Assuming that the $(2+)K = 0$ saddle point state is the lowest, then at low energies quadrupole absorption would introduce a $\sin^2(2\theta)$ term, or its equivalent $4(\sin^2\theta-\sin^4\theta)$, i.e. peaking at 45°. However, the $K = 1$ state leads to a negative $\sin^2(2\theta)$ term, or positive $\sin^4\theta$, whilst the $K = 2$ state gives a considerable $\sin^2\theta$ term and it is clear that if there is any appreciable mixing of fissions through the $K = 0$, 1, and 2 states the resulting distribution, of the form $W(\theta) = 1+\alpha\sin^2\theta+\beta\sin^4\theta$, might be difficult to distinguish experimentally from the simple form $W(\theta) = 1+\alpha\sin^2\theta$ corresponding to dipole absorption.

The experimental results for Th-232, U-234, U-236, U-238, and Pu-240 are shown in Table II. The numbers given are the ratio of the counts observed at angle θ per unit X-ray dose to the number observed at 0° for the same dose. The maximum bremsstrahlung energy, E_0, is indicated. The errors quoted are standard deviations based on the counting statistics. The figures quoted in Table II are the actual experimental observations not corrected for isotopic composition or resolution.

Some of the targets were not isotopically pure; the compositions are given in Table III. In order to correct for isotopic composition we need to know the relative fissionabilities of the isotopes at the energies used. These were obtained in the following manner, which is similar to the experiments described by Katz (1958) except that the present results are not sufficiently detailed to give accurate yield or cross-section curves. The fission chamber was operated

TABLE II

Angular distributions

Relative fission fragment yields as a function of peak bremsstrahlung energy E_0 and angle θ to X-ray beam

	E_0, Mev	Angle θ 0	25	45	60	90
Th-232	6.5	1.00±0.3				20±5
	7.0	1.00±0.04		4.1±0.2	6.7±0.3	8.4±0.3
	7.5	1.00±0.1		5.1±0.4	6.0±0.4	7.9±0.5
	8.0	1.00±0.09		2.4±0.2	3.6±0.3	5.1±0.3
	9.0	1.00±0.1				3.4±0.3
	10.0	1.00±0.04	1.16±0.05	1.67±0.08	1.97±0.08	2.4±0.1
	14.0	1.00±0.05				1.43±0.08
	20.0	1.00±0.05				1.13±0.06
U-238	6.0	1.00±0.3				6.0±1.4
	6.3	1.00±0.1		3.6±0.4		5.9±0.6
	6.5	1.00±0.2				4.5±0.7
	7.0	1.00±0.08	1.5±0.1	2.0±0.2	2.4±0.2	2.9±0.2
	8.0	1.00±0.06				2.1±0.1
	9.4	1.00±0.023	1.094±0.029	1.224±0.029	1.274±0.034*	1.452±0.033
	10.0	1.00±0.04				1.38±0.04
	14.0	1.00±0.04				1.08±0.04
	20.0	1.00±0.03				1.05±0.03
		*θ = 65° in this case				
U-236	6.0	1.00±0.25				4.6±0.8
	6.5	1.00±0.1		2.06±0.2		2.55±0.25
	7.0	1.00±0.06		1.65±0.10		2.11±0.12
	8.0	1.00±0.04		1.39±0.06		1.66±0.07
	9.0	1.00±0.04	1.10±0.07	1.15±0.04	1.31±0.08*	1.46±0.05
	10.0	1.00±0.03		1.07±0.03		1.28±0.04
	14.0	1.00±0.02				1.03±0.02
		*θ = 65° in this case				
U-234	6.5	1.00±0.1		1.41±0.14		1.98±0.20
	7.0	1.00±0.05		1.19±0.06		1.53±0.08
	8.0	1.00±0.03		1.11±0.03		1.30±0.04
	10.0	1.00±0.03				1.12±0.03
	15.0	1.00±0.03				1.01±0.03
Pu-240	6.5	1.00±0.10		1.49±0.15		1.55±0.16
	7.0	1.00±0.06		1.03±0.06		1.35±0.08
	8.0	1.00±0.03		1.01±0.03		1.21±0.04
	15.0	1.00±0.02				1.01±0.02

The values quoted are counts observed for unit X-ray dose normalized to unit yield at θ = 0°. No corrections have been applied.

without collimators so that the observed counting rates were, to a good approximation, a measure of the total number of fissions occurring, independent of angular distribution. Measurements were made relative to U-238 for the U-234 mixture, the U-236 mixture, and the Pu-240 mixture and for pure U-235 and Pu-239 (which together with U-238 were the only significant contaminants) and knowing the isotopic compositions and weights of all the

TABLE III

Isotopic composition of targets

	Atom percentage			
Target	U-234	U-235	U-236	U-238
U-234	53.15	34.51		12.34
U-235	0.90	93.17	0.46	5.47
U-236	0.07	4.62	94.77	0.54
	Pu-239	Pu-240	Pu-241	Pu-242
Pu-239	98.70	1.25	0.05	
Pu-240	12.20	87.17	0.58	0.04

NOTE: The remaining targets were isotopically pure.

sources the number of fissions per nucleus was calculated for each isotope relative to the number per U-238 nucleus for the same X-ray dose and energy. The fissions per roentgen-nucleus for U-238 were known at all energies relative to 20 Mev. Thus we have obtained the relative fissionabilities, i.e. the fissions per roentgen-nucleus for each isotope at each energy normalized arbitrarily to U-238 equals 100 at 20 Mev. The results are given in Table IV. With these

TABLE IV

Relative fissionabilities, U-238 = 100 at 20 Mev

E_0	U-234	U-235	U-236	U-238	Pu-239	Pu-240
6.0		0.45±0.05	0.303±0.013	0.387±0.040		
6.5	1.165±0.033	1.134±0.025	1.159±0.026	1.08±0.07	0.239±0.024	1.145±0.051
7.0	2.515±0.053	2.282±0.038	2.358±0.037	2.14±0.14	4.50±0.22	2.528±0.075
8.0	6.285±0.085	5.519±0.067	5.285±0.056	4.87±0.24	11.35±0.34	6.09±0.12
9.0		11.00±0.33	8.94±0.13	8.65±0.26		
10.0	17.36±0.53	18.75±0.30	14.29±0.20	14.41±0.28	45.1±2.2	
14.0		88.0±4.5	43.11±0.53	57.7±1.4		
15.0	84.3±1.9	119.0±0.9	73.58±0.78	70.5±1.8	255.0±7.6	82.3±1.8
20.0	127.5±2.5	180.8±2.2	109.4±1.0	100±2.5	352±10	120.8±2.3

data, Tables II, III, and IV, we seek to establish the form of the angular distributions and the value of the parameter α (and β if present) for each nuclide and its dependence upon E_0.

Distribution Forms

The first step was to fit the data by the method of least squares to the equation $W(\theta) = a+bh_2$ where a and b are parameters to be found and h_2 is a modified $\sin^2\theta$ function which takes account of the resolution of the collimators. This function is described in the Appendix; it is such that if the true distribution is $W(\theta) = a+b\sin^2\theta$ the observed distribution will be $W(\theta) = a+bh_2$ with the same values of a and b. The ratio b/a so obtained is the anisotropy coefficient $\bar{\alpha}$ in the equation $W(\theta) = 1+\bar{\alpha}\sin^2\theta$ where the symbol $\bar{\alpha}$ refers to the average observed for the mixture of isotopes in the target, i.e. not corrected for isotopic composition. The results of the fitting are given in Table V and in Figs. 2–19; the errors are based on the standard deviations of counting data.

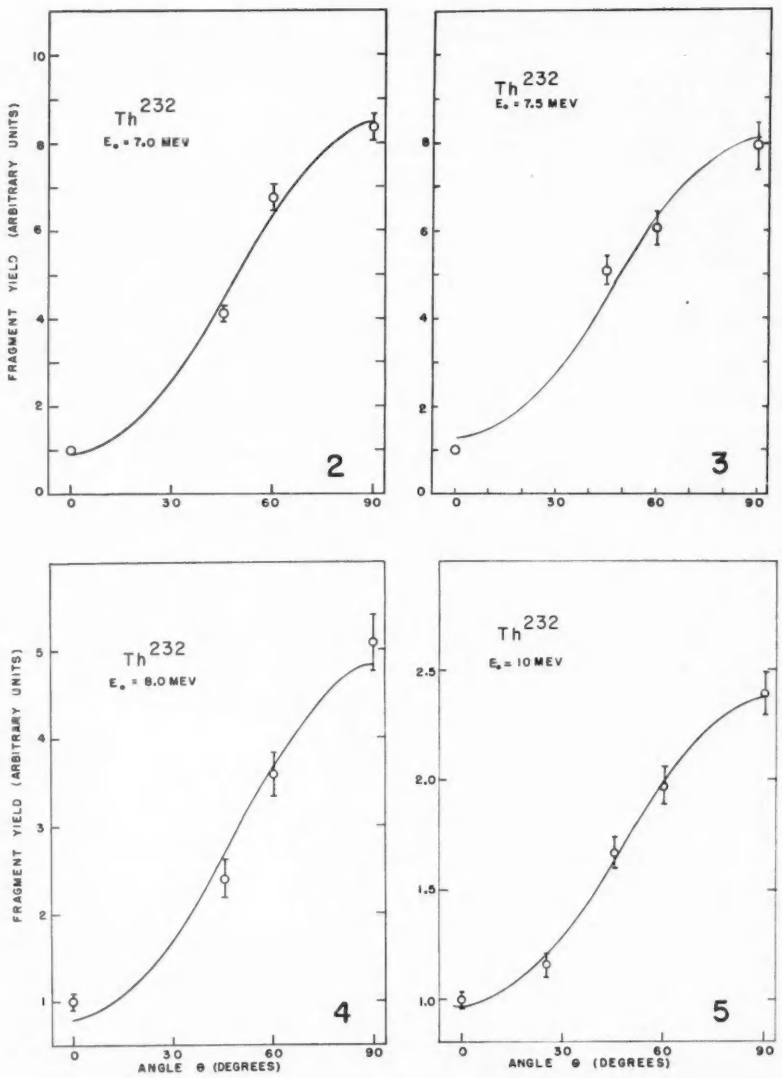

FIGS. 2–19. Angular distribution: relative fragment yields as a function of the angle θ. The curve is calculated from the equation $W(\theta) = a + bh_2$ and a and b determined by least-square fitting. This curve therefore shows what should have been observed experimentally if the true distribution is of the form $W(\theta) = 1 + \bar{\alpha} \sin^2 \theta$. The points are the experimental data normalized to unity at $\theta = 0$. The errors shown are standard deviations.

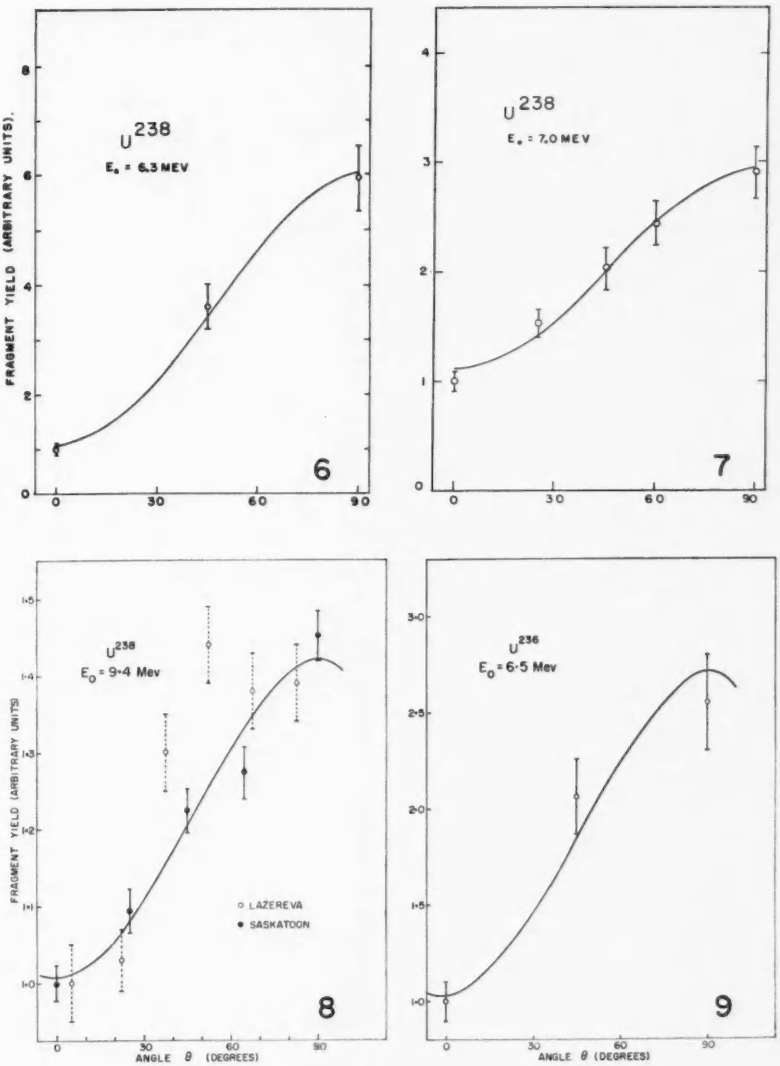
FRAGMENT YIELD (ARBITRARY UNITS).
U238
E0 = 6.3 MEV
6
U238
E0 = 7.0 MEV
7
FRAGMENT YIELD (ARBITRARY UNITS)
U238
E0 = 9·4 Mev
○ LAZEREVA
● SASKATOON
8
ANGLE θ (DEGREES)
U236
E0 = 6·5 Mev
9
ANGLE θ (DEGREES)

FIGS. 6–9.

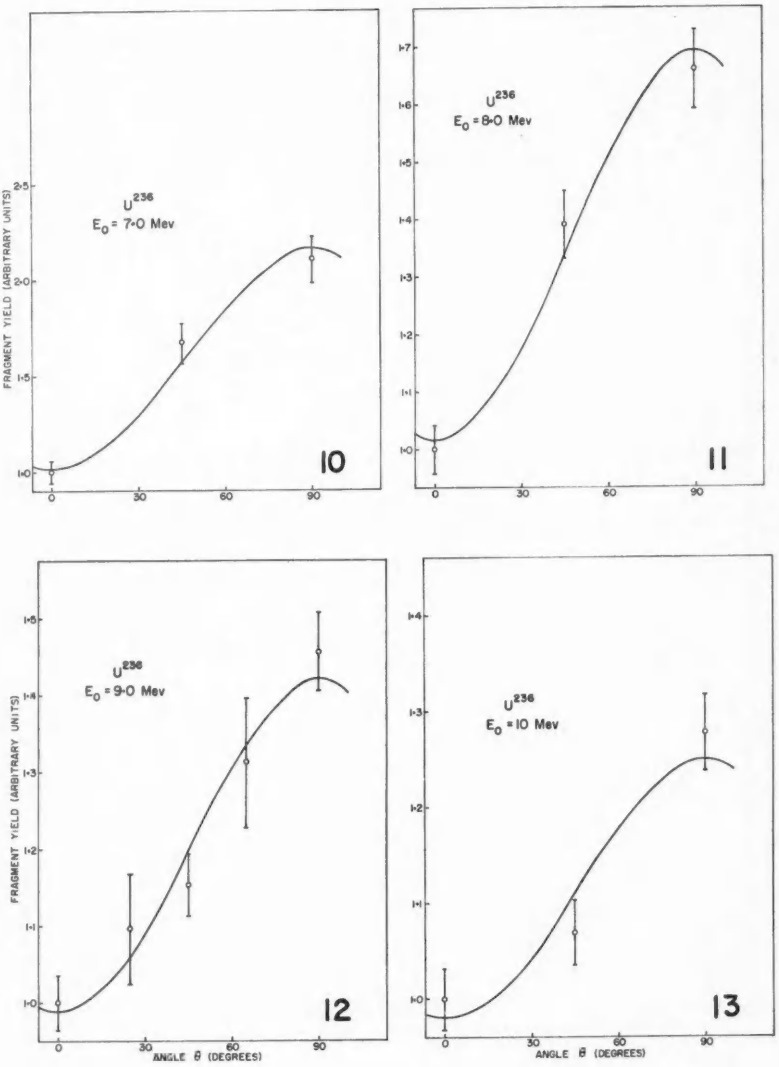
FRAGMENT YIELD (ARBITRARY UNITS)
U236
E0 = 7·0 Mev
10
U236
E0 = 8·0 Mev
11
U236
E0 = 9·0 Mev
12
U236
E0 = 10 Mev
13
ANGLE θ (DEGREES)
ANGLE θ (DEGREES)

FIGS. 10–13.

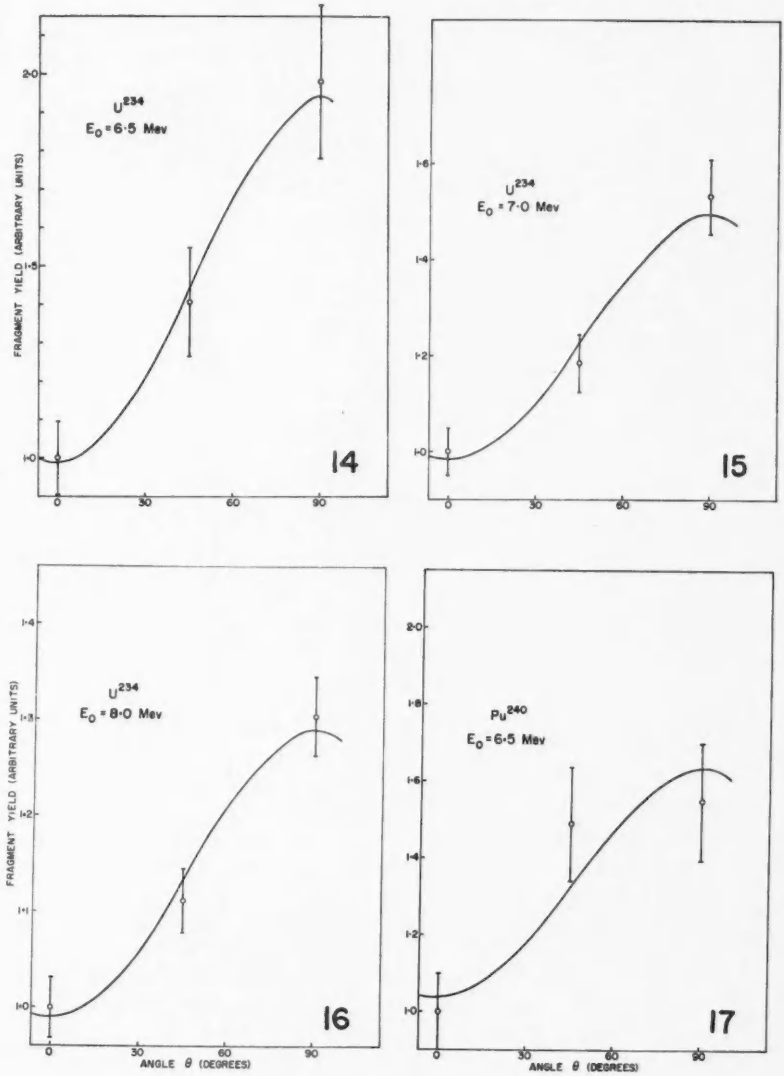
FRAGMENT YIELD (ARBITRARY UNITS)
U^{234}
$E_0 = 6.5$ Mev
14
U^{234}
$E_0 = 7.0$ Mev
15
U^{234}
$E_0 = 8.0$ Mev
16
Pu^{240}
$E_0 = 6.5$ Mev
17
ANGLE θ (DEGREES)
ANGLE θ (DEGREES)

FIGS. 14–17.

Most of the Th-232 and U-238 data have been presented previously in the paper by Katz (1958). The present figures differ slightly in detail from the earlier ones due in part to accumulation of additional data and partly to an improved fitting procedure. The earlier fittings were made by giving each point an equal weight whereas the present fits were made using the Chalk River Datatron with each point weighted according to its error. In some cases only the ratio of counts at 90° to counts at 0° was available. No fitting was then possible and the $\bar{a}$ values were obtained directly from the 90°/0° ratios, using resolution corrections. These $\bar{a}$ values are listed in Table V but there are no corresponding figures.

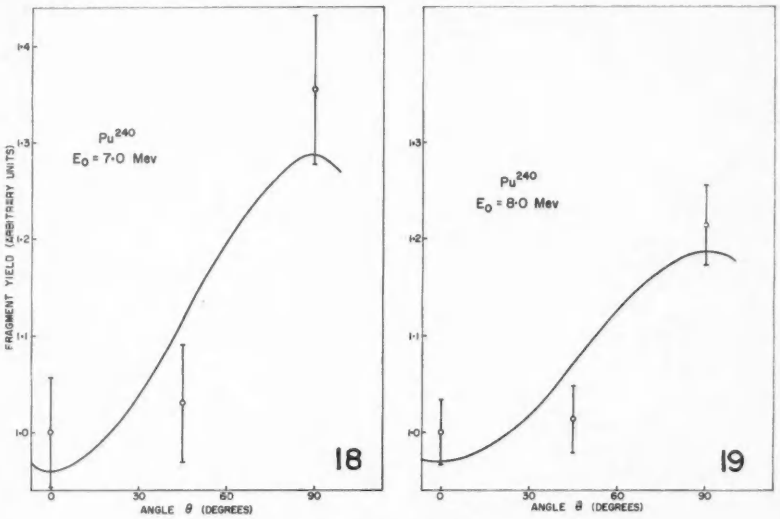

FIGS. 18 and 19.

It is clear from the figures that the assumed form of the distribution is consistent with the data in most cases. There are, however, a few cases in which the fit appears to be unsatisfactory. In order to confirm this intuitive conclusion the χ^2 test was applied to each case separately using the methods and tables given by Fisher (1944). As expected most cases were found to be entirely consistent with the assumed distribution; three cases were suspect (Th-232 at 7.0 Mev, Th-232 at 8.0 Mev, and Pu-240 at 7.0 Mev); one case was not acceptable (Pu-240 at 8.0 Mev). Two further tests were made by (*a*) comparing the sum of all the χ^2 values with the expected sum and (*b*) comparing the distribution of χ^2 values found with the distribution expected. These procedures test the hypothesis that the data for all 18 cases taken collectively are consistent with the assumed distribution. This hypothesis was found to be suspect (as one might expect in view of the above conclusion for Pu-240 at 8.0 Mev) but not unacceptable.

TABLE V

Values of $\bar{\alpha}$ in $W(\theta) = 1+\bar{\alpha}\sin^2\theta$ and of $\bar{\alpha}$ and $\bar{\beta}$ in $W(\theta) = 1+\bar{\alpha}\sin^2\theta+\bar{\beta}\sin^4\theta$

		$W(\theta) = 1+\bar{\alpha}\sin^2\theta$	$W(\theta) = 1+\bar{\alpha}\sin^2\theta+\bar{\beta}\sin^4\theta$	
Target	E_0	$\bar{\alpha}$	$\bar{\alpha}$	$\bar{\beta}$
Th-232	6.5	>25		
	7.0	11.0±0.8	8.5±1.5	2.1±1.6
	7.5	10.3±1.6	16±4	−4.7±3.5
	8.0	4.9±0.6	1.8±1.1	2.8±1.3
	9.0	2.8±0.4		
	10.0	1.61±0.12	1.32±0.38	0.28±0.40
	14.0	0.46±0.09		
	20.0	0.14±0.06		
U-238	6.0	7±2		
	6.3	6.7±1.1	8.5±3.2	−1.6±3.1
	6.5	4.4±1.0		
	7.0	2.05±0.24	3.07±0.89	−0.96±0.88
	8.0	1.3±0.1		
	9.4	0.44±0.04	0.43±0.16	0.01±0.16
	10.0	0.41±0.05		
	14.0	0.09±0.04		
	20.0	0.05±0.03		
U-236	6.0	4.4±1.7		
	6.5	1.86±0.34	3.6±1.3	−1.7±1.3
	7.0	1.23±0.15	1.87±0.60	−0.61±0.61
	8.0	0.73±0.09	1.12±0.36	−0.38±0.36
	9.0	0.47±0.07	0.18±0.24	0.28±0.24
	10.0	0.29±0.06	−0.02±0.2	0.31±0.21
	14.0	0.04±0.04		
U-234	6.5	1.06±0.25	0.76±0.85	0.31±0.88
	7.0	0.57±0.10	0.23±0.36	0.34±0.37
	8.0	0.33±0.06	0.16±0.21	0.16±0.21
	10.0	0.12±0.05		
	15.0	0.02±0.04		
Pu-240	6.5	0.62±0.20	1.8±0.9	−1.2±0.9
	7.0	0.37±0.11	−0.30±0.37	0.66±0.37
	8.0	0.22±0.06	−0.27±0.21	0.48±0.21
	15.0	0.01±0.03		

NOTE: The results given in this table have not been corrected for the isotopic compositions of the target, but do include the corrections for resolution.

The second step was to fit the data to the equation $W(\theta) = a+bh_2+ch_4$ where a, b, and c are to be found and h_4 is a modified $\sin^4\theta$ function. The ratios b/a and c/a then give $\bar{\alpha}$ and $\bar{\beta}$, respectively, in the distribution $W(\theta) = 1+\bar{\alpha}\sin^2\theta+\bar{\beta}\sin^4\theta$. The results are given in Table V. As expected most of the β values appear to be meaningless in view of the errors attached but a few might be significant. The four cases which were suspected of not fitting the simple $\sin^2\theta$ distribution (see above) gave $\bar{\beta}$ values with errors which although still large were nevertheless smaller than most. It should be noted that in these cases the $\bar{\beta}$ values were positive, corresponding to negative $\sin^2(2\theta)$ terms. It was not possible to apply the χ^2 test to all the individual cases because the test requires that there be more data points than adjustable para-

meters. Of the four cases of particular interest two contained data at more than three angles so that the test could be used; for Th-232 at 7.0 Mev the fit to the three-parameter equation was no better than to the two-parameter equation; for Th-232 at 8.0 Mev it was better. The hypothesis was then made that in all 18 cases the true value of $\bar{\beta}$ is zero and a χ^2 test applied. This hypothesis was found to be suspect but would have been acceptable if, for example, the case of Pu-240 at 8.0 Mev had been removed.

The coefficients α and β are not independently variable if a fit to the data is to be retained. The data are consistent in each case with a range of values for α and β provided they are properly related. Thus if β is allowed to be any value in the quoted range the error on α becomes large as is evident from Table V. In view of this and the tests described above we have chosen to work with the simplest distribution $W(\theta) = 1+\alpha \sin^2\theta$. In so doing we imply that it is consistent with most of the data but we do not imply that terms of $\sin^4\theta$ are necessarily absent. One individual case should be mentioned: U-238 at 9.4 Mev. We have included in Fig. 8 the results of Baz *et al.* (1958). Although the two sets of data are not strictly comparable because of small differences in angular resolution, it seems clear that a disagreement exists. The reason for this disagreement is not known. The results for Th-232 and U-238 agree qualitatively with those of Winhold and Halpern (1956) but the present experiment gives greater anisotropies throughout.

Corrections for Isotopic Compositions

Using a $1+\alpha \sin^2\theta$ distribution the observed α values were corrected for the isotopic compositions of the targets. With this distribution form the number of fissions, Y^θ, in a solid angle Ω at an angle θ to the photon beam is related to the total number of fissions at all angles, Y, as follows:

$$Y^\theta = Y\frac{\Omega}{4\pi}\frac{1+\alpha h_2}{1+2/3\,\alpha},$$

where h_2 is the modified $\sin^2\theta$ function.

For a target containing a mixture of i species the yield, Y^θ_{mix}, at angle θ is the sum of the yields Y^θ_i of the individual species at the same angle. Thus:

$$Y^\theta_{\text{mix}} = \sum_i Y^\theta_i = \frac{\Omega}{4\pi}\sum_i Y_i\frac{(1+\alpha_i h_2)}{1+2/3\,\alpha_i}.$$

If $\bar{\alpha}$ is the anisotropy coefficient observed for the mixture then:

$$Y^\theta_{\text{mix}} = \frac{\Omega}{4\pi}\,Y_{\text{mix}}\frac{(1+\bar{\alpha}h_2)}{1+2/3\,\bar{\alpha}}.$$

The total number of fissions at all angles from the mixture Y_{mix} is just the sum of the individual totals, i.e. $Y_{\text{mix}} = \sum_i Y_i$. Thus:

$$\frac{\sum_i Y_i\,(1+\bar{\alpha}h_2)}{1+2/3\,\bar{\alpha}} = \sum_i Y_i\frac{(1+\alpha_i h_2)}{1+2/3\,\alpha_i}.$$

From this the anisotropy coefficient α_x of any species x is related to $\bar{\alpha}$ and the remaining anisotropy coefficients $i \neq \alpha_x$ as follows:

$$\alpha_x = \frac{\bar{\alpha}+k}{1-2/3k} \qquad \text{where} \qquad k = \sum_{i \neq x} \frac{Y_i}{Y_x} \frac{(\bar{\alpha}-\alpha_i)}{(1+2/3\,\alpha_i)}.$$

Since the total numbers of fissions in all angles Y_i occur only in the form of ratios Y_i/Y_x we can replace them by quantities $N_i f_i$ where N_i is the atom per cent of species i in the mixture and f_i the relative fissionability of the species i at the appropriate energy. Thus we can obtain the value of α_x from the data in Tables III, IV, and V. The anisotropy coefficients thus corrected for isotopic composition are given in Table VI. Graphs of the coefficient α versus maximum bremsstrahlung energy E_0 are shown in Figs. 20–24.

TABLE VI

Corrected values of α in $W(\theta) = 1+\alpha \sin^2\theta$

E_0	Th-232	U-238	U-236	U-234	Pu-240
6.0		6.6±2	6.0±2.3		
6.3		6.7±1.1			
6.5	>25	4.4±1.0	2.1±0.4	2.3±0.6	0.65±0.20
7.0	11.0±0.8	2.05±0.24	1.33±0.17	0.90±0.16	0.49±0.12
7.5	10.3±1.6				
8.0	4.9±0.6	1.3±0.1	0.79±0.09	0.44±0.08	0.29±0.07
9.0	2.8±0.4		0.51±0.07		
9.4		0.44±0.04			
10.0	1.61±0.12	0.41±0.05	0.32±0.06	0.17±0.07	
14.0	0.46±0.09	0.09±0.04	0.04±0.03		
15.0				0.02±0.04*	0.01±0.03*
20.0	0.14±0.06	0.05±0.03			

*These values, which do not differ from zero, have not been corrected for isotopic composition.

The coefficients show the expected decrease with increasing energy. The observed energy dependence is not the true one since we are dealing with a bremsstrahlung spectrum; if monoenergetic photons were used the decrease of α with increasing energy would be more rapid. At any given energy there is a considerable variation of α values between the different nuclides. In terms of the Bohr theory the simplest explanation for this last observation is that the thresholds are different for different nuclides. Thus the same applied excitation energy gives different excitations above threshold. If one adjusts the energy scales by the differences in thresholds to obtain a measure of α values at the same energy above threshold one finds that there is still a considerable difference in α values for different nuclides. One concludes, therefore, that the difference in barrier height for $K = 0$ and $K = 1$ saddle point states is not constant from nuclide to nuclide. This idea was in fact suggested by Bohr (1956) to account for the difference between Th-232 and U-238 observed by Winhold and Halpern (1956).

If y is the proportion of fissions proceeding through the $K = 1$ saddle point state and $(1-y)$ the proportion through the $K = 0$ state then by comparison with the distribution form $W(\theta) = 1+\alpha \sin^2\theta$ it is found that $y = 1/(2\alpha+2)$.

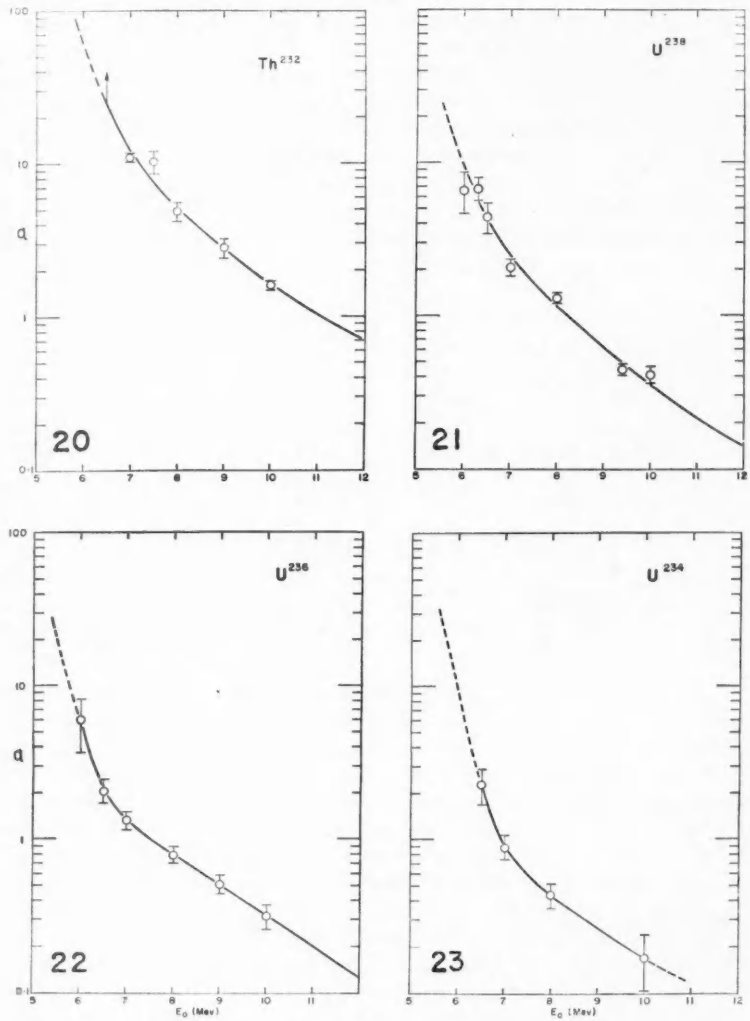

FIGS. 20–24. Anisotropy coefficients α as a function of maximum bremsstrahlung energy E_0.

For fission proceeding by barrier penetration we have the penetration probability P given by Hill and Wheeler (1953):

$$P = \frac{1}{1+e^{-B(E-E_t)}}$$

where E is the excitation energy, E_t the threshold (defined as the energy at which $P = 0.5$), and B is a constant which is a measure of the curvature of the

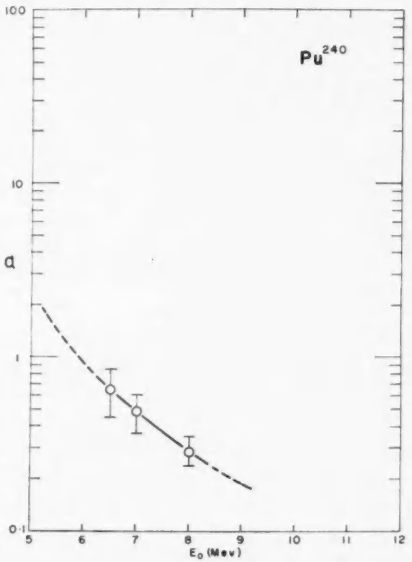

FIG. 24.

barrier. For fissions proceeding through two alternative states $K = 0$ and $K = 1$ whose thresholds differ by Δ we have:

$$\frac{P_{k=1}}{P_{k=0}} = \frac{1+e^{-B(E-E_t)}}{1+e^{-B(E-E_t-\Delta)}} = \frac{y}{1-y}.$$

We have assumed that B is the same for both saddle point states. If we consider now an excitation E which is just equal to the threshold E_t for the $K = 0$ state and substitute $y = 1/(2\alpha+2)$ we find:

$$4\alpha+1 = e^{B\Delta}.$$

The advantage of considering the situation at threshold is that with a bremsstrahlung spectrum of maximum energy E_0 close to threshold the effective width of the spectrum is small because the photofission cross section falls rapidly with decreasing energy below threshold. In order to obtain the values of α at the thresholds we have extrapolated the experimental data

(Figs. 20–24) and read off the values of α at $E_0 = E_t + 0.2$ Mev. Estimates made for nuclides for which the energy dependence of cross section is known indicate that by choosing E_0 to be 0.2 Mev above E_t most fissions will be induced by photons of energy close to E_t. The quantity B can be estimated from the energy dependence of fission cross sections, from neutron fission to capture ratios, and from the systematics of spontaneous fission half lives: B is about 8 Mev^{-1}. Thus we have obtained estimates for Δ, the difference in barrier heights for the $K = 0$ and $K = 1$ saddle point states. The results are given in Table VII.

TABLE VII

Estimated values of Δ

	E_t, Mev	α_t	Δ, kev
Th-232	6.0	40	640
U-234	5.7	12	490
U-236	5.8	6	400
U-238	5.8	10	460
Pu-240	5.4	1.3	230

NOTE: α_t is the value of α from Figs. 20–24 read off at $E_t + 0.2$ Mev.

The extrapolation of α values and the experimental errors (Figs. 20–24) make the value of α at threshold decidedly uncertain, perhaps by a factor of two in some cases. The threshold values used are to some extent a matter of choice; to be rigorous we would need the thresholds applying specifically to fission through $1(-)K = 0$ states. We have used values suggested by Cameron (1959) and assumed that these apply. Thus the values of Δ are no more than estimates. However, any reasonable choice of thresholds and any reasonable extrapolation of α values lead to a range of values having the same general properties:* Δ is in the order of several hundred kiloelectron volts, is largest for Th-232, and is smallest for Pu-240. The differences shown in Table VII between the uranium isotopes are probably not significant.

In the Bohr theory the quantity Δ is expected to be approximately equal to the pairing energy ($\sim$ 1 Mev) minus the energy of the first $(1-)$ state (a few hundred kiloelectron volts (Stephens *et al.* 1955)). Thus Δ should itself be in the order of a few hundred kiloelectron volts and this appears to be the case. The higher the $(1-)$ state the less will Δ be. It may be significant that the energies of the low-lying $(1-)$ excitation of the ground state of heavy elements increase as one goes to heavier elements, thus Δ should decrease, which also appears to be the case (of Bohr 1956).

If we accept the pairing energy as being constant at about 1 Mev for all the nuclide studies we see that $(1-\Delta)$ Mev is a measure of the difference between the $1(-)K = 0$ saddle point state and the lowest possible saddle point state which is $0(+)K = 0$ (and is not reached by dipole photon absorption from a $0(+)$ ground state). Since Δ appears to be considerably less than

*For example, in the case of U-238 a choice of $E_t = 5.5$ Mev gives $\Delta = 530$ kev and $E_t = 6.2$ Mev gives $\Delta = 380$ kev, whilst a change in α by a factor 2 makes about 100-kev change in Δ.

1 Mev, especially for Pu-240, we can conclude tentatively that the 1(−) saddle point state lies considerably higher than the 0(+) state.

The experimental points of Figs. 20 and 21 do not all lie closely on the smooth curves which have been drawn through them. In neutron-induced fission the corresponding curves of anisotropy versus neutron energy show pronounced maxima and minima (Brolley 1955; Henkel 1956; Blumberg 1959). It is possible that such structure exists for photofission but the use of a bremsstrahlung spectrum would make its observation and interpretation very difficult.

ACKNOWLEDGMENTS

The authors wish to thank G. C. Hanna of Atomic Energy of Canada Limited for many helpful suggestions and J. M. Kennedy of Atomic Energy of Canada Limited for carrying out the least-squares fittings and χ^2 tests on the Chalk River Datatron computer. They also wish to thank W. R. Falk of the University of Saskatchewan for assistance with the measurements and D. A. S. Walker of Atomic Energy of Canada Limited for assistance with electronic circuits and measurements. Finally, thanks are due to the United States Atomic Energy Commission for loan of U-234, U-235, and U-236.

REFERENCES

Baz, A. I., Kulikova, N. M., Lazareva, L. E., Nikitina, N. V., and Semanov, V. A. 1958. Second United Nations International Conference on the Peaceful Uses of Atomic Energy, paper 2037.
Blumberg, L. and Leachman, R. B. 1959. Phys. Rev. (to be published).
Bohr, A. 1955. Proceedings of the International Conference on the Peaceful Uses of Atomic Energy, Geneva, 1955, Vol. 2, p. 151.
Brolley, J. E., Dickinson, W. C., and Henkel, R. L. 1955. Phys. Rev. **99**, 159.
Cameron, A. G. W. 1959. Private communication to the authors.
Fisher, R. A. 1944. Statistical methods for research workers, 9th ed. (Oliver and Boyd Ltd.).
Henkel, R. L. and Brolley, J. E. 1956. Phys. Rev. **103**, 1292.
Hill, D. L. and Wheeler, J. A. 1953. Phys. Rev. **89**, 1140.
Katz, L., Baerg, A. P., and Brown, F. 1958. Second United Nations International Conference on the Peaceful Uses of Atomic Energy, paper 200.
Lazareva, L. E. and Nikitina, N. V. 1957. Soviet Journal of Atomic Energy Suppl. No. 1 (English Translation of Consultants Bureau, New York), p. 125.
Stephens, F. S., Asaro, F., and Perlman, I. 1955. Phys. Rev. **100**, 1543.
Winhold, E. J. and Halpern, I. 1956. Phys. Rev. **103**, 990.

APPENDIX:

CALCULATION OF ANGULAR RESOLUTION CORRECTIONS

P. M. Dyson, J. M. Kennedy, and E. Vogt

The collimating system to which these calculations apply has been described in the text of this paper. The definitions used in the calculations are illustrated in the diagram (Fig. 25) and are as follows:

t = thickness of plate,
r = radius of collimating holes,
θ = angle between photon beam and axis of holes,

ψ = angle of rotation of plate about an axis perpendicular to the plate and defined such that $\psi = 0$ corresponds to $\theta = 0$,

$\Delta = t/r$.

The experiments described in the foregoing text were made with $\Delta = 4$, but calculations have been made for $\Delta = 2$, 4, and 8. The photon beam and the axis of the holes are both inclined at 45° to the plate, hence:

$$\cos\theta = 1/2(1+\cos\psi),$$

and Fig. 25 illustrates the case when $\psi = 180°$ and $\theta = 90°$.

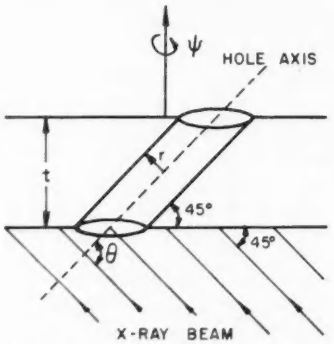

FIG. 25. Illustration of the definitions used in the text of the Appendix.

It is assumed that the differential cross section is $\sigma(\theta)d\Omega$ with $\sigma(\theta)$ proportional to:

$$1+\alpha\sin^2\theta+\beta\sin^4\theta.$$

It can then be shown that the counting rate as a function of Δ and ψ is proportional to $c(\Delta, \psi)$ defined by:

$$c(\Delta, \psi) = I(\Delta)[1+\alpha h_2(\Delta, \psi)+\beta h_4(\Delta, \psi)]$$

where $I(\Delta)$ is a normalizing factor, independent of ψ (and equal to the average solid angle subtended by the exit of the holes at the entrance to the holes), and h_2 and h_4 are the contributions due to the $\sin^2\theta$ and $\sin^4\theta$ components of the cross section.

The quantities h_2 and h_4 can be expanded in powers of $\cos\psi$ as follows:

$$h_2 = a_2+b_2\cos\psi+c_2\cos^2\psi$$

$$h_4 = a_4+b_4\cos\psi+c_4\cos^2\psi+d_4\cos^3\psi+e_4\cos^4\psi.$$

No higher powers of $\cos\psi$ can occur. The coefficients a, b, c, etc. depend upon Δ and can be obtained from the following table in which the values of I are also given.

Table of coefficients

Δ	I	a_2	b_2	c_2	a_4	b_4	c_4	d_4	e_4
2	.4232	.6556	−.3571	−.1263	.4774	−.4523	−.0629	.0765	.0177
4	.1019	.7173	−.4707	−.2095	.5271	−.6637	−.0890	.1860	.0423
8	.0248	.7414	−.4937	−.2394	.5525	−.7285	−.1132	.2329	.0564
∞		.7500	−.5000	−.2500	.5625	−.7500	−.1250	.2500	.0625

NOTE: The values for $\Delta = \infty$ are simply the coefficients of the powers of $\cos\psi$ in the expansion of $\sin^2\theta$ and of $\sin^4\theta$.

It will be seen that the resolution corrections involve, basically, replacing $\sin^2\theta$ and $\sin^4\theta$ by the functions $h_2(\Delta, \psi)$ and $h_4(\Delta, \psi)$, the values of which can be obtained using the equations and table given.

SOME PHYSICAL PROPERTIES OF SEA ICE. II[1]

M. P. LANGLEBEN

ABSTRACT

Some properties of annual sea ice at mid-temperate latitudes are investigated. It is found that the salinity is comparable to, and the density much lower than, annual arctic sea ice. Permeability to air flow compares favorably to calculations based on the model of sea ice of Anderson and Weeks (1958). Small sample ring tests of ultimate tensile strength yield values ranging from 9.5 to 24.8 kg cm^{-2} at test temperatures of $-3.6°$ C to $-17.2°$ C. Tensile strength appears to depend on crystal size rather than on brine content.

1. INTRODUCTION

The physical properties of sea ice are dependent not only on the immediate conditions during testing but also on its past history. Environmental conditions can be dealt with fairly readily in the arctic and subarctic, where the winters are remarkably stable. In the north, the diurnal variation in temperature is small and temperatures are consistently well below the freezing point of sea ice during the winter months. Also, precipitation generally decreases as one proceeds northward. The insulating effect of a thin snow cover is slight and the ice sheet is therefore exposed to the extreme environmental temperatures. It appears that, under these conditions, the ice sheet freezes to the extent that there is little subsequent migration of brine until the approach of spring. Experience gained this past winter bears out these statements. Several members of the McGill Ice Research Project were associated with studies of sea ice at Fort Churchill and Resolute Bay. It was found that any 2 months between January and April were very similar as regards temperature. As a consequence of this, observations at Fort Churchill indicate that there is little, if any, change in the physical properties of the ice, such as its density and salinity, during the winter. At Resolute Bay, the total snowfall for the winter 1958–59, accumulated gradually, was only approximately 10 inches and the average snow cover on the ice only amounted to 5 or 6 inches.

In contrast, environmental conditions at Shippegan, N.B., are markedly different. Changes take place rapidly and the variations are large, as is typical of mid-temperate latitudes. In spite of the inherent difficulties of dealing with such varying conditions, the lack of knowledge of the properties of sea ice at mid-temperate latitudes and the awakening interest in winter navigation through the Saint Lawrence estuary provided sufficient motive for this study to be attempted. The work reported here, principally for the winter 1958–59, is a follow-up to an initial study by Pounder and Little (1959) in the winter 1956–57. Since the oceanography at the site of operations and the process of sea ice formation are adequately described in their paper, they need not be

[1]Manuscript received July 9, 1959.
Contribution from the Ice Research Project, Department of Physics, McGill University, Montreal, Que.

discussed here. Field tests were also attempted in the intervening winter, 1957–58, but the winter was abnormally mild and the ice sheet formed was of poor quality and of insufficient thickness to warrant thorough investigation. It was thought worth while, however, to interject some climatological data pertaining to this winter for purposes of illustrating the annual variations that are possible. The observations during 1958–59 were made during field trips of approximately 5 days' duration, spaced at intervals roughly 1 month apart.

2. ENVIRONMENTAL CONDITIONS

(*a*) *Ambient Temperature*

The average daily temperatures at Shippegan for the winters 1957–58 and 1958–59 are shown in Fig. 1. The rapid and large variations in temperature

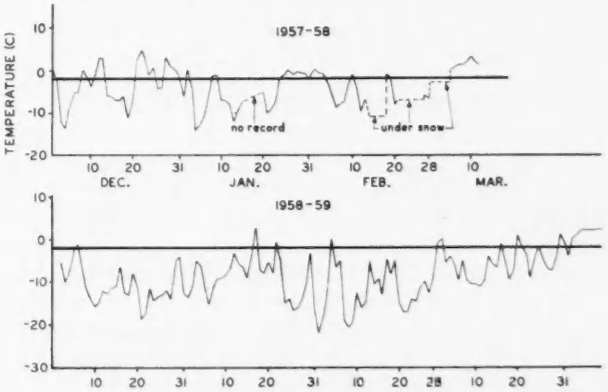

FIG. 1. Average daily temperatures at Shippegan, N.B., for the winter seasons 1957–58 and 1958–59. The freezing point of sea water of normal salinity is shown as a heavy horizontal line.

are at once apparent. Taking the freezing point of sea water of normal salinity (about 35 ‰ by weight) as −1.9° C, it is seen that the exposure to freezing temperatures during the winter 1958–59 was very much greater than in the previous winter. For the months of December and January, the period during which most of the growth of the ice sheet occurs, it can be calculated that the exposure was equivalent to an average of 7.9 centigrade degrees of relative frost, i.e. below −1.9° C. In the corresponding period of the previous winter, the exposure was, on the average, 2.0 centigrade degrees of frost. Now the thickness of ice formed is roughly proportional to the square root of the exposure (see, for example, Pounder and Little 1959). If differences in snow cover are neglected, it is seen that the winter 1958–59 was twice as favorable for ice formation as the winter before.

(*b*) *Precipitation*

The total daily precipitation for the Shippegan area has been plotted in Fig. 2. Snowfalls have been converted to their melted equivalent using the

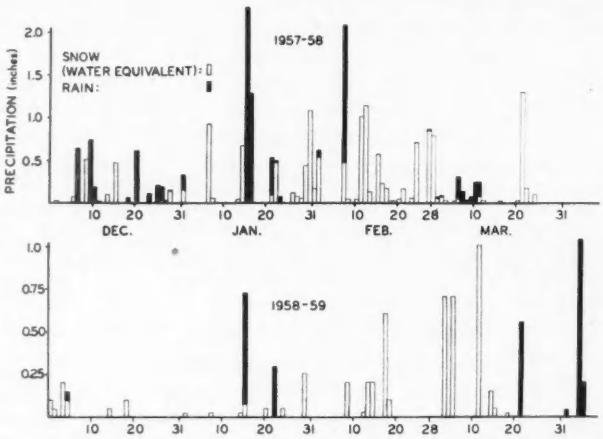

FIG. 2. Daily precipitation in the vicinity of Shippegan for the winter seasons 1957–58 and 1958–59.

standard density ratio of 10:1. It is seen that the rainfall of the winter 1957–58 far exceeds that of the winter following. With the associated mild temperatures, this would lead to erosion of the ice sheet which was, in fact, observed. The earlier winter also had heavier snowfalls, particularly during the growth stage of the ice sheet. A summary of the total monthly snowfall and of the snow remaining on the ground at the end of each month is given in Table I for the two winters. This information was obtained from the Bathurst Power and Paper Company, which maintains a weather observatory on their premises at Bathurst, N.B., about 42 miles west of Shippegan.

TABLE I

	Monthly snowfall, inches		Snow on ground, inches	
	1957–58	1958–59	1957–58	1958–59
31 Dec.	13.4	6.0	TR	7
31 Jan.	41.3	5.0	14	5
28 Feb.	53.0	13.2	32	9
31 Mar.	26.0	26.2	3	6

(c) Ice Thickness

The winter 1957–58 was an exceptionally mild one. In addition, the large amounts of precipitation, both as rain and snow, were detrimental to the growth of the ice sheet. The ice was therefore of poor quality and attained a maximum thickness of only 10 inches. It is not thought worth while reporting any other findings of that year. Henceforth, unless specifically stated otherwise, all data, graphs, etc. refer to the winter 1958–59.

Now an ice sheet, under ideal conditions, thickens because of growth from its bottom surface. At mid-temperate latitudes, considerable thickening may

also occur at the top surface. The snow cover, during periods of thaw or after a rainfall, undergoes change and forms, what is called, snow ice. This is a granular form of ice as opposed to the normal crystalline structure. Flooding of the ice sheet after heavy snowfalls, by sea water flowing up through tidal cracks, may also lead to snow ice formation. The observed salinities of snow ice are not very different from those of the ice below. Further, a metamorphosis gradually takes place in the snow ice and the granular structure may change to relatively small crystals. The problem of distinguishing normal growth, i.e. from the bottom, is of importance if one desires to compare observations of physical properties for an entire winter season.

A square grid of accumulation stakes, consisting of nine meter sticks spaced at 50-ft intervals and frozen into the ice at the beginning of the season, was installed for this purpose. These stakes have been used with considerable success to determine ablation and accumulation of glaciers. As it turned out, they were not suitable in this area of heavy snowfalls which drifted under strong northwest winds. It was found that the snow surface was undulated so that readings on adjacent meter sticks frequently differed by more than 30 centimeters. Similar undulations of the top surface of the snow ice were observed when the surface snow was removed. Fortunately, another means of identifying position (vertically) in the ice sheet with the passage of time presented itself. Air bubbles are sometimes trapped in horizontal layers during periods of rapid freezing. Several of these layers (Fig. 3) were observed in the January ice. These were easily identified in later months, thus serving as reference levels that persisted through the season.

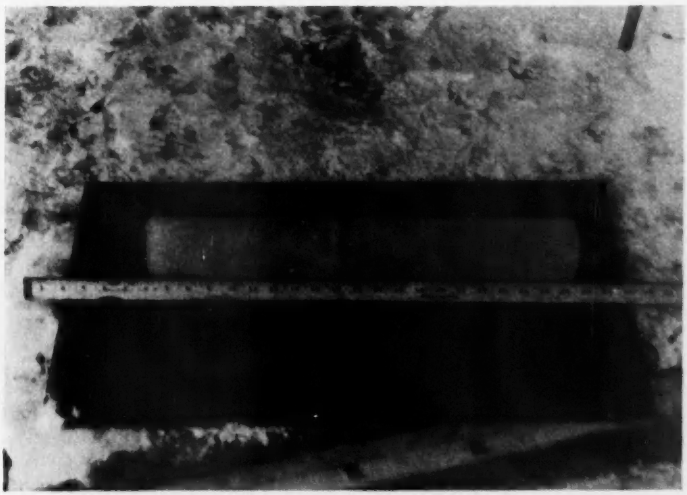

FIG. 3. A typical vertical ice core extracted from the ice sheet in January. Pronounced horizontal layers are visible opposite the 15-in. mark and the 24½-in. mark of the scale shown. Several other layers could be seen under more suitable lighting.

Vertical cylinders of 3-in. diameter were extracted from the ice sheet by means of a special coring auger. Measurements of ice thickness were always made with reference to the layered pattern of air bubbles first observed in January when the tests were initiated. The adjusted thicknesses are listed in Table II. Thus, the figure quoted for January represents the total thickness of

TABLE II

	Sea ice thickness (inches) at Shippegan	
	1956–57	1958–59
23 Dec.	10	15.4*
8 Jan.	15	20.7
21 Feb.	30	28.5
13 Mar.	30	28.7
7 Apr.	27	28.0

*Observation by H. J. Robichaud prior to commencement of tests.

ice, snow ice included. The thickness in February, however, was actually several inches greater than the 28.5 inches listed; but, relative to January and making use of the identifying layers, a growth of only 7.8 inches was observed at the base of the ice sheet. The total thickness of snow ice and ice is not listed because of the large variations in snow ice thickness mentioned above. Table II also includes thicknesses for the same location in the winter 1956–57, taken from Fig. 2 of Pounder and Little (1959). The growth was initially more rapid in 1958–59. Although the exposures during December and January were almost identical in both winters, there was more snow in 1956–57 and this would tend to retard the rate of growth. The maximum thickness is roughly the same in both cases. However, in 1956–57, the thickness referred to is the total of snow ice plus sea ice so that the observations are not strictly comparable.

(d) Ice Temperature

The temperature profile through the ice sheet was measured with thermistors imbedded at the surface of a long 2 in. × 4 in. piece of lumber. The string of thermistors ran from 50 cm above the ice surface, referred to January, to 150 cm below that surface. An accuracy of 0.1 centigrade degree was achieved. Typical temperature profiles, one for each trip made, are shown in Fig. 4. The water temperature (dashed part of curves) was about −1.8° C with the exception that it increased, i.e. became warmer, in April. The temperature gradients in the ice are not large because of relatively mild environmental temperatures. It is seen that, in each case, the temperature varies almost linearly with depth, from which it appears that the thermal conductivity may be fairly uniform throughout the ice sheet. Departures from linearity are probably reflections of changing air temperatures which gradually penetrate to greater depths into the ice but with decreasing amplitude. The curve for April is indicative of ice in a decaying state. The high temperatures measured in the upper part of the ice sheet are probably caused by surface melt water which has worked its way down around the thermistor pole.

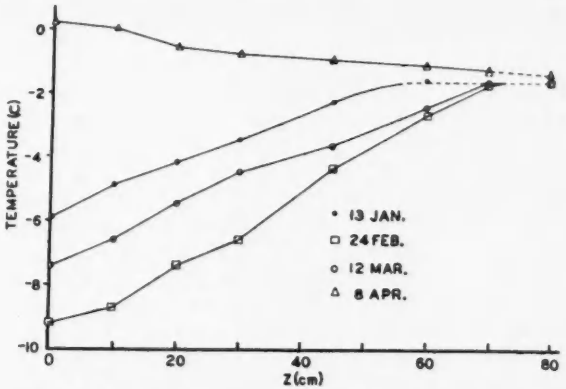

FIG. 4. Typical temperature profiles through the ice sheet. The dashed portions of the curves represent water temperatures.

As was shown in Fig. 1, the average daily ambient temperature was subject to variations. This resulted in changes of the temperature profile. In fact, profiles over a range comparable to those shown in Fig. 4, the April curve excepted, have been observed within 1 week. The thermal history of any sample in the ice is therefore seen to be quite complex. Moreover, since the temperatures of the ice are never more than a few degrees below its freezing point, the medium is far from being solid and conditions are favorable for migration of the brine cells trapped in the ice. It is even possible that the brine passages in the lower part of the ice sheet are in hydraulic connection with the sea.

3. METHODS AND RESULTS

(*a*) *Crystal Structure*

The top surface of an ice sheet is predominantly composed of horizontal platelets with the *C*-axis pointing vertically (Perey and Pounder 1958). When the ice sheet forms from an impure melt (e.g. sea water) under natural one-dimensional cooling, the orientation of the *C*-axis changes rapidly with depth and a marked transition occurs. The crystals below this transition layer are long and candle-like with their *C*-axes horizontal. Their secondary axes are still randomly oriented. A typical photograph of a vertical section including the transition layer is shown in Fig. 5*a*. The abrupt change in crystal structure is quite apparent. Horizontal sections (Figs. 5*b* and 5*c*) at distances of 1 inch above and below the transition layer further illustrate the difference in crystal structure. The structure is most commonly granular in the snow ice above the transition layer. In horizontal section, the crystals just below the transition layer, showing in varying shades of gray in Fig. 5*c*, are rather small in extent, most of them being less than ¼ inch across. They increase in horizontal area with increasing depth as can be seen from Fig. 5*d*, a vertical section at depth 24 to 28 inches, and Fig. 5*e*, a horizontal section at depth 25 inches, where many of the crystals have horizontal dimensions greater than ½ inch. Their extent

in the vertical may be many inches, some crystals being pinched off in the growth process after 3 or 4 inches but most apparently extending the full thickness of the ice sheet. Figure 5*f* is a horizontal section taken about 7 inches above the transition layer. It shows that recrystallization of the snow ice can occur. These photographs are obtained by cutting thin samples, reducing their thickness by melting to the order of 2 mm, and then photographing them between crossed polaroids.

In the absence of snow ice, the transition layer has been found to occur within 1 inch or 2 of the surface (see, for example, Weeks 1958). Pounder and Little (1959), on the other hand, reported the transition layer as being many inches below the surface. They further found large erratic changes in its position as the season progressed and were at a loss to explain this. Observations in the winter 1958–59, making use of identifying layers of air bubbles in the ice sheet, indicate that the transition layer is not mobile. Its depth in January was 9 inches below the top surface of the ice sheet, the upper part being composed of snow ice. Further observations during the 3 succeeding months showed that the transition layer maintained the same position throughout the life of the annual ice. The anomaly observed by Pounder and Little (1959) may be explained in terms of snow ice which can accumulate rapidly in this region of heavy snowfalls. During periods of thaw or rain, the snow ice may also be eroded. Since the upper surface of the ice sheet is not persistent, it is clear that measurements with respect to that surface would lead to erratic results.

(*b*) *Density and Salinity Profiles*

As an approach to *in situ* conditions, the ice cores were prepared for testing as soon as possible after extraction from the ice sheet. The cores were sectioned into samples which were measured accurately, weighed, and then stored away in airtight polythene containers. This procedure took less than ½ hour and brine drainage was probably negligible. The salinity, expressed in grams of solute per kilogram of solution and therefore as ‰ by weight, was measured with a hydrometer after the samples had melted and had warmed up to room temperature. The hydrometer readings were reduced to the standard temperature of 15° C. The volume of solution required to float the hydrometer was such that the ice cores, of 3-in. diameter, had to be cut in lengths of about $2\frac{3}{4}$ inches. The density and salinity measurements are therefore not point values but rather averages, each for depths of about 3 inches.

The observed density of the ice is plotted against depth in Fig. 6. The variation in density from month to month is probably due to migration of brine under changing temperature conditions. The snow ice, at depths less than about 20 cm, shows the widest variation. With the exception of the April data, values are almost all below 0.917 g cm^{-3}, the density of fresh water ice, indicating the high air content of the ice. In April, the temperature of the ice sheet (Fig. 4) was at or close to its melting point. It is likely that surface melt water, of which there was about 5 inches, penetrated the ice sheet and so increased the measured density. In the other cases, the density increases

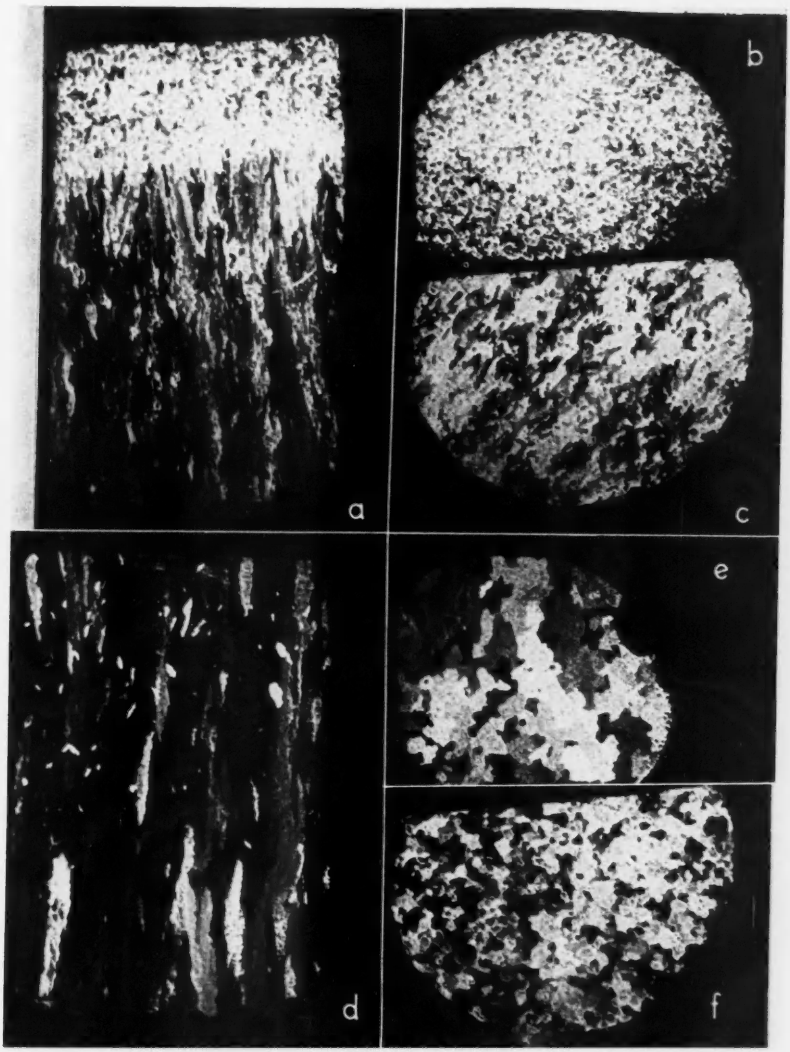

FIG. 5. Photographs of thin sections of February sea ice between crossed polaroids. (*a*) Vertical section about 4 inches long showing transition layer near top. (*b*) Horizontal section, radius of curvature about 1.5 inches, at 1 inch above transition layer. Structure is granular in the snow ice. (*c*) Horizontal section at 1 inch below the transition layer. The crystals are small. (*d*) Vertical section at the base of the ice sheet showing long crystals. (*e*) Horizontal section near bottom. Crystals much larger than in (*c*). (*f*) Horizontal section some 7 inches above transition layer showing recrystallization of snow ice.

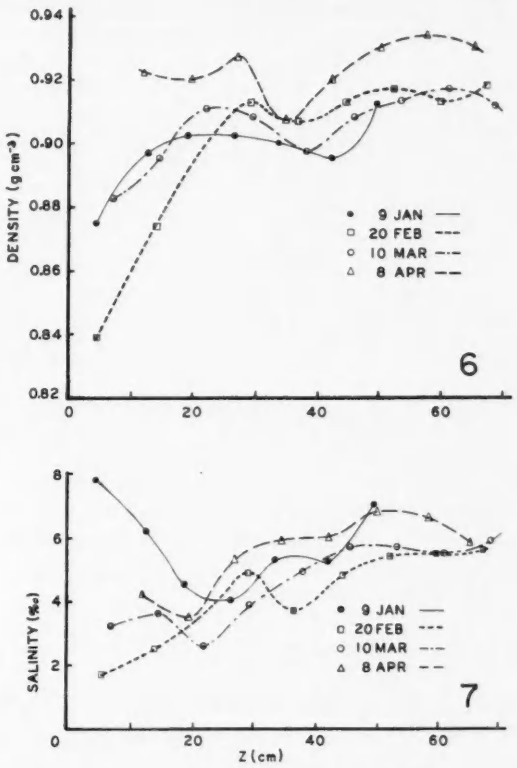

FIG. 6. Density profiles through the ice sheet observed during monthly visits to Shippegan in 1959.
FIG. 7. Salinity profiles of sea ice at Shippegan in 1959.

rapidly with depth until the transition layer, at about 23 cm, is reached after which the trend is for a very gradual increase with depth. The average increase with depth below the transition layer is about 2.06×10^{-4} g cm^{-3}/cm.

Corresponding salinity profiles are shown in Fig. 7. The salinity in the snow ice sometimes increases with depth and, at other times, decreases. Below the transition layer, on the other hand, a general trend towards increasing salinity with depth is observed, on the average about 0.0578‰/cm. Since the rate of freezing decreases as the ice sheet thickens, one might expect an opposite trend, i.e. higher salinities towards the top of the ice sheet, which has been observed in arctic regions. The discrepancy may be accounted for in terms of differences in climatic conditions. At mid-temperate latitudes, the temperature at all points in the ice sheet, particularly when there is some snow cover, is but a few degrees below the freezing point. Migration of brine in the direction of warmer temperatures, i.e. towards the bottom, could lead to the indicated

trend. The range of salinities below the transition layer, as seen in Fig. 7, lies between about 3‰ and 6‰. A wider range of salinities is found further north (Weeks and Anderson 1958; Assur 1958).

(*c*) *Permeability*

Ice crystals growing from sea water consist initially of alternating layers of pure ice and of brine, the layers being vertical. With further freezing, the brine layers become thinner; bridges form between adjoining layers of ice; and the brine becomes confined to long vertical cylinders of elliptical cross section. On slight reduction of temperature, the cylinders are usually reduced to circular cross section. The length and diameter of these circular cylinders depend on both the current temperature and the past thermal history of the ice. These notions have arisen through the work of many people. Recent experimental evidence has been presented by Perey and Pounder (1958) and Anderson and Weeks (1958).

The presence of these circular cylinders leads to a reduction in the strength properties of the ice, irrespective of whether they are filled with brine or whether the brine has drained out and they are air-filled. The permeability of ice to fluid flow should then be related to its strength, i.e. the lower the permeability the greater must be its strength if other factors are kept constant. The permeability C has been defined as the rate of mass transport dM/dt of some fluid per unit area divided by the pressure gradient dp/dz, the area A being normal to the pressure gradient. That is

$$\frac{dM}{dt} = C A \frac{dp}{dz}. \tag{1}$$

The permeability to air, C_A, was measured using the apparatus shown schematically in Fig. 8. The samples of ice tested were disks of about 1.5-cm

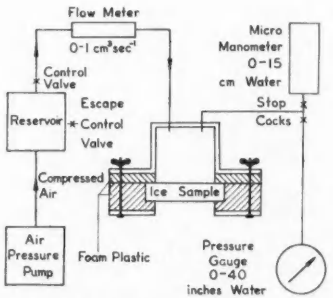

FIG. 8. Schematic diagram of permeability meter.

thickness cut from a vertical ice core at intervals of 2 inches in depth. These were clamped between soft foam plastic gaskets exposing only the central area of diameter 5 cm to the air flow. The pressure differential across the ice sample was measured with an ordinary pressure gauge when the pressures

required were high, and with a micromanometer of range 0.001 cm to 15 cm of water at low pressures. The rate of flow of air through the sample was read on a flowmeter of the floating ball, tapered tube type.

Air permeabilities are plotted against depth on a semilog scale in Figs. 9 and 10, the thickness of the samples used being about 1.5 cm. The data for the lower curves were obtained from samples stored at the indicated temperatures for about 24 hours. The results for the upper curves pertain to the same samples after they had been exposed to the indicated ambient temperature for about 2 hours. The actual ice temperature, in the latter cases, is unknown, hence the question marks. There were, however, no signs of surface melting on the samples.

Some similarities exist between the two sets of curves. In each case, the shape of the bottom curve is fairly well preserved with a displacement towards higher permeabilities with increasing temperature. The permeability increases by a factor of 10 roughly for an increase in temperature of about 4 to 7 centigrade degrees. The differences in the two figures are caused by changes in the condition of the ice sheet in the interim between January and April. The permeability in January, Fig. 9, is highest in the snow ice as one might expect.

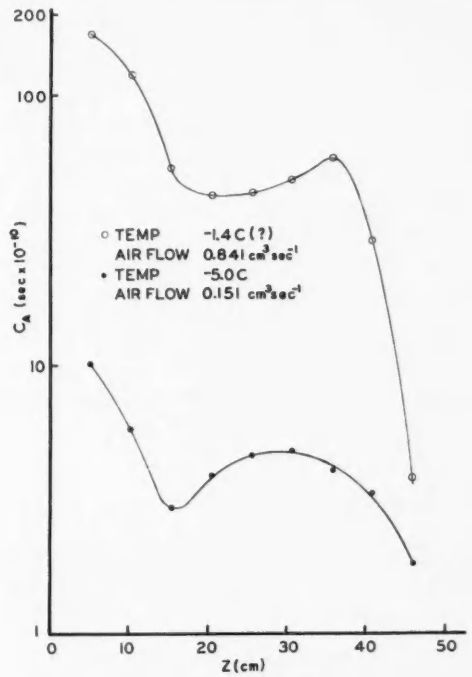

FIG. 9. Permeability to air flow C_A as function of depth z for January ice. Thickness of samples approximately 1.5 cm.

It decreases with depth as the porosity decreases (or the density increases, see Fig. 6) to the vicinity of the transition layer. Just below the transition layer, in the zone of rapid freezing, the permeability increases. It falls off again at greater depths where the ice has been formed more slowly. In April, on the other hand, erosion had taken place at the surface and was working its way through the ice sheet. The data, neglecting one point in each set of values which lies far off the straight lines drawn in Fig. 10, indicate that the permeability decreases logarithmically with depth, by a factor of 10 for every 75 cm.*

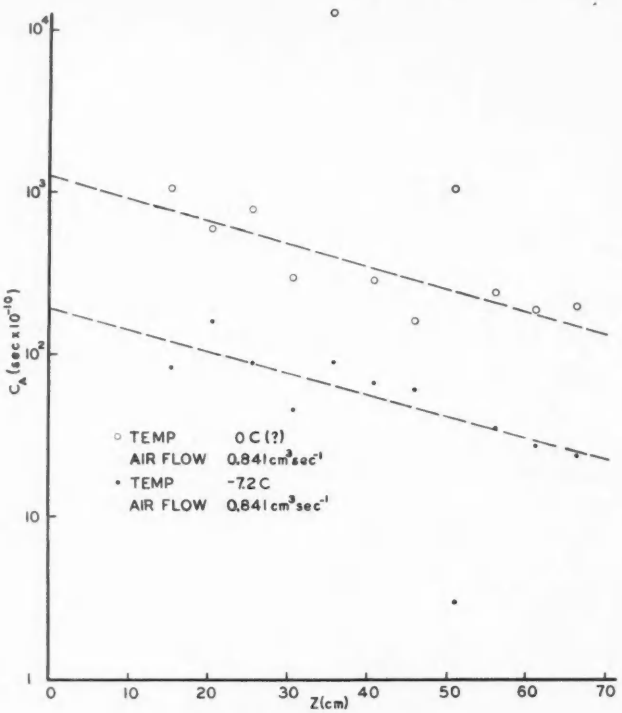

FIG. 10. Permeability for April ice.

Assuming that the air flow is streamline through the cylinders mentioned at the beginning of this section, the permeability can be calculated by combining Poiseuille's equation and equation (1), providing the dimensions, spacing, etc. of the cylinders are known. Let n be the number of cylinders of radius r per unit area, and η be the viscosity and ρ the density of the air. Then the rate of volume transport

*One would expect that the *in situ* thermal gradient would tend to oppose the effects observed at constant temperature.

$$\frac{dV}{dt} = \frac{1}{\rho}\frac{dM}{dt} = \frac{\pi n r^4 A}{8\eta}\frac{dp}{dz}. \tag{2}$$

From equations (1) and (2),

$$C_A = \frac{\pi n r^4 \rho}{8\eta}. \tag{3}$$

As a first approximation, the distribution and dimensions of the cylinders may be obtained from the simplified model of sea ice (Anderson and Weeks 1958), based on microphotographs of thin sections of sea ice. They find that the cylinders lie along parallel lines 0.46 mm apart, that they are spaced at intervals of 0.23 mm, and that their diameter is 0.07 mm. These are average values. No mention is made of the ice temperature nor is the length of the cylinders stipulated. One vertical section, about 3 mm long, is shown and the cylinders run the full length of the microphotograph.

From Anderson and Weeks' data then,

$$n = \frac{10^2}{0.46 \times 0.23}\ \text{cm}^{-2} = 945\ \text{cm}^{-2}$$

and

$$r = 0.035\ \text{mm}$$

so that

$$C_A = 4.1 \times 10^{-7}\ \text{sec}.$$

Now the measured permeabilities range from about 2×10^{-10} sec to 10^{-6} sec. The calculated permeability is therefore greater by factors roughly of 2×10^3 to 0.4 times, with the greatest difference for the January ice at the colder test temperature. According to equation (3) the permeability is proportional to the fourth power of the radius of the cylinders, assumed equal here; also to the number of cylinders per unit area. Implicit, in the last statement, is the assumption that each of the cylinders is continuous throughout the thickness of the sample under test, in our case about 1.5 cm. It is quite likely that many of the cylinders are pinched off and do not attain such a length, except at exceedingly warm ice temperatures. It is also apparent that a small decrease in radius, since the fourth power is involved, will greatly decrease the permeability. More microscopic information on sea ice, particularly on the temperature dependency of the dimensions of the cylinders, is required before a fair comparison can be made.

(d) Ultimate Tensile Strength

Small sample tests of ring tensile strength, as recommended and currently performed by investigators from the Snow, Ice, and Permafrost Research Establishment (Butkovich 1958), were used exclusively. The samples were about 2¼-in. long sections of the ice cylinders extracted with the 3-in. diameter coring auger. A hole of ½-in. diameter was drilled along the axis of each sample. It was then placed with its axis horizontal in a hydraulic press, so that the

direction of load application was normal to its axis, i.e. was along a diameter. The sample was then loaded to fracture, keeping the loading rate in excess of 1 kg cm^{-2} sec^{-1} to reduce effects of plasticity of the ice.

It may be shown that, under these conditions, failure in the sample occurs because of tensile stresses. The hollow cylinders split in half, the rupture plane including the diameter of the cylinder which is in the direction of load application. The tensile strength, σ, is according to Ripperger and Davids (1947)

$$\sigma = K \frac{P}{\pi r_0 l} \tag{4}$$

where r_0 is the outer radius and l the length of the sample,

P is the load at failure,

and $K = f(r_i/r_0)$ is the concentration factor, a complicated function of the ratio of inner (r_i) to outer radius of the sample. In our case, $K = -7.09$.

On extraction from the ice sheet, the cores were stored in an upright position inside a deep-freeze unit for periods of about 15 to 48 hours at some selected temperature. This was so that any series of tests could be performed at constant temperature, thereby leaving only salinity and density as variables. Since the sectioning of the cores into small samples and the subsequent breaking of the samples only took a few minutes, it is safe to assume that the test temperature corresponds to the temperature of storage.

The results are shown in Fig. 11. Each curve represents data obtained at roughly monthly intervals for sea ice stored at the temperatures noted. Because

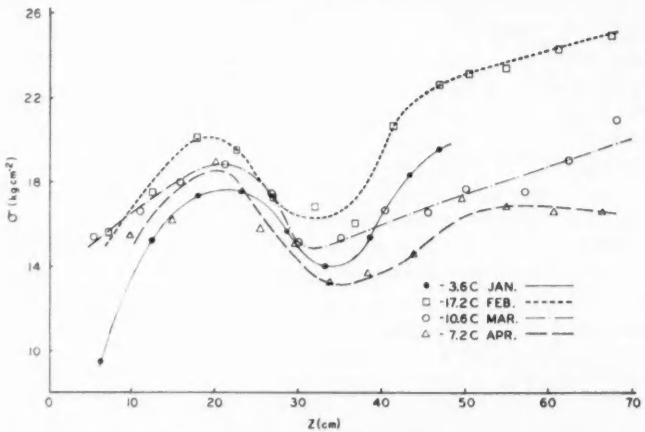

FIG. 11. Profiles of ultimate ring tensile strength. Each point is average of about 20 tests.

of the inhomogeneous nature of sea ice, individual values of tensile strength are subject to large scatter. Many samples were therefore broken and the results averaged. The number of tests n and the average deviation Δ_{av} from the mean value of the tensile strength are given in Table III for the January to March

TABLE III

Z	n	σ	Δ_{av}	$\sigma(10)$	D	S	ν
			1. January at −3.6° C				
6.3	28	9.5	1.9	9.9	0.878	7.5	103
12.5	22	15.2	3.0	15.8	0.897	6.2	85.0
17.8	23	17.3	2.8	18.0	0.902	4.6	63.0
23.1	24	17.5	2.8	18.2	0.902	4.0	54.8
28.7	25	15.6	3.0	16.3	0.902	4.1	56.2
33.3	21	14.0	1.9	14.6	0.900	5.2	71.3
38.6	26	15.3	2.6	16.0	0.897	5.4	74.0
43.2	19	18.3	2.4	19.1	0.896	5.4	74.0
46.7	20	19.5	3.1	20.3	0.901	6.2	85.0
			2. February at −17.2° C				
7.1	20	15.6	3.8	14.8	0.851	1.8	6.86
12.5	22	17.5	3.3	16.7	0.869	2.3	8.77
17.7	17	20.1	4.6	19.2	0.886	2.9	11.0
22.6	16	19.5	5.5	18.6	0.901	3.7	14.1
26.9	18	17.2	3.3	16.4	0.912	4.7	17.9
32.0	20	16.8	2.5	16.0	0.909	4.4	16.7
36.8	16	16.0	3.3	15.2	0.907	3.7	14.1
41.3	18	20.6	6.1	19.6	0.909	4.4	16.7
47.0	15	22.5	6.4	21.4	0.915	5.2	19.8
50.5	15	23.0	5.0	21.9	0.917	5.4	20.6
54.8	20	23.3	5.8	22.2	0.916	5.5	20.9
61.4	23	24.2	6.4	23.0	0.913	5.5	20.9
67.5	26	24.8	5.9	23.6	0.918	5.6	21.3
			3. March at −10.6° C				
5.3	23	15.4	2.7	15.3	0.881	3.1	16.7
10.9	24	16.6	2.9	16.5	0.888	3.5	18.9
15.7	18	18.0	4.6	17.9	0.900	3.5	18.9
21.1	21	18.8	4.8	18.7	0.910	2.7	14.6
25.4	22	17.4	4.0	17.3	0.911	3.2	17.3
29.9	21	15.1	2.5	15.0	0.906	4.0	21.6
35.0	22	15.3	3.3	15.2	0.900	4.6	24.9
40.3	22	16.6	3.3	16.5	0.898	5.2	28.1
45.4	23	16.5	2.8	16.4	0.907	5.7	30.8
50.0	25	17.6	3.2	17.5	0.911	5.7	30.8
56.7	26	17.5	3.3	17.4	0.915	5.6	30.3
62.3	25	19.0	3.8	18.9	0.917	5.5	29.7
68.1	27	20.9	4.7	20.8	0.912	5.8	31.3

NOTE: n, number of tests of tensile strength averaged; Z, average position or depth in ice sheet in centimeters; σ, average tensile strength in kilograms per square centimeter; Δ_{av}, average of the absolute values of deviation in tensile strength in kilograms per square centimeter; $\sigma(10)$, tensile strength in kilograms per square centimeter adjusted to temperature −10° C; D, density of ice in grams per cubic centimeter; S, salinity of ice in ‰ by weight; ν, brine content of ice in ‰ by volume.

data. It is seen that the average deviations are usually within 20% of the average tensile strengths. The scatter in tensile strength determinations is illustrated in Fig. 12 using the April data. Here the frequency of occurrence of a given deviation is plotted against the percentage deviation, each histogram being related to a point on the April curve of Fig. 11. The ratio of the average deviation to the average tensile strength, and the average tensile strength, are both noted in Fig. 12. These distributions are typical of all the results and, as can be seen, are for the most part normal error distributions. In 9 of the 12 histograms shown, the probability that a single determination of tensile strength falls within 15% of the mean value is greater than 50%. For deviations within 30%, the probability increases to more than 85% in 10 of the 12 cases.

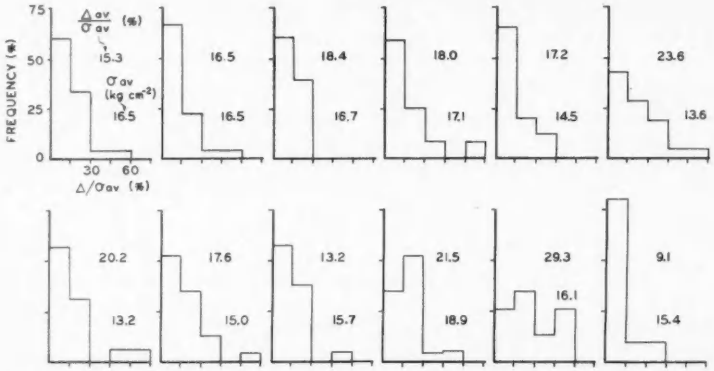

FIG. 12. Probability or frequency of occurrence of a given deviation Δ from average tensile strength for each point on the April curve of Fig. 11. Ratios of average deviation to average tensile strength are beside each histogram as are also average tensile strengths.

Comparing the curve for January (Fig. 11) with the corresponding density and salinity curves (Figs. 6 and 7) it appears that high strength is associated with high density and low salinity, and low strength with low density and high salinity. This reasonable association is not readily apparent when comparing the remaining curves with their density and salinity profiles. The tensile strength curves of January and February are similar in shape with a displacement towards higher strengths in February when the test temperature was colder. The shape and location of the curves for March and April, which represent temperatures intermediate to the former two, are reasonable in the upper half of the ice sheet but deviate below that. The values of tensile strength are in good agreement with those presented by Pounder and Little (1959) but are higher than those reported by Butkovich (1956). This may be a reflection of real differences in the type of sea ice formed under widely differing conditions at temperate latitudes and in the arctic.

4. DISCUSSION

A recent theory of the strength properties of sea ice by Assur (1958) contends that, at constant temperature, the tensile strength depends solely on the brine content by volume of the ice. His relationship is of the form

$$\sigma = A_0 (1 - B_0 \sqrt{\nu}) \tag{5}$$

where A_0 is a constant representing the basic strength in the absence of brine,

B_0 is a constant determined by the distribution of brine in the intracrystalline structure of the ice,

ν is the relative volume of brine, i.e. volume of brine per unit volume of sea ice,

and σ is the tensile strength at some constant temperature.

The brine content by volume of sea ice is a complex function of its salinity and temperature. Its evaluation is complicated by the fact that the various salts normally present in sea water begin to precipitate at different tempera-

tures. An analysis of the phase relationships, based on information on the relative abundance of ions in solution, allowed Assur to compute a detailed table of brine content in terms of salinity and temperature. He then proceeded to adjust some tensile strength values to a common temperature of $-10°$ C by means of an empirical formula derived from Butkovich's (1956) results. Plotting adjusted tensile strength, σ (10), against the square root of the brine content, he established limited verification of his theory with data on arctic ice but had to offer other explanations for the behavior of antarctic ice.

A similar attempt was made here. The brine contents listed in Table III were evaluated from the salinity and temperature of the samples, using Assur's table of values. Tensile strengths were also reduced to a temperature of $-10°$ C and are shown in Table III. On plotting the data, no apparent correlation could be found between strength and the square root of brine content. Since the density of the ice at Shippegan (Table III) is low compared with that of arctic ice, quoted as normally 0.926 g cm^{-3}, it is reasonable to expect strength to depend not only on the brine content but also on the air content. The latter, to a close approximation, is the difference between the standard specific gravity of sea ice (0.926) and the observed specific gravity. The sum of the brine and air content by volume might be termed the effective void content v_t, i.e. the fraction of an ice sample devoid of ice. Adjusted tensile strength has been plotted as a function of the square root of the void content in Fig. 13. Because of the very low density and the inhomogeneity of snow ice, only data from below the transition layer is shown. The numbers beside the points indicate relative position or depth from which the samples originated, number 1 referring to samples immediately below the transition layer. It is evident that there is no correlation between strength and void content and that the theory presented cannot explain the Shippegan observations.

Looking further at Fig. 13, now at individual sets of data (i.e. dots, circles, or squares), the strength almost invariably increases with increasing depth

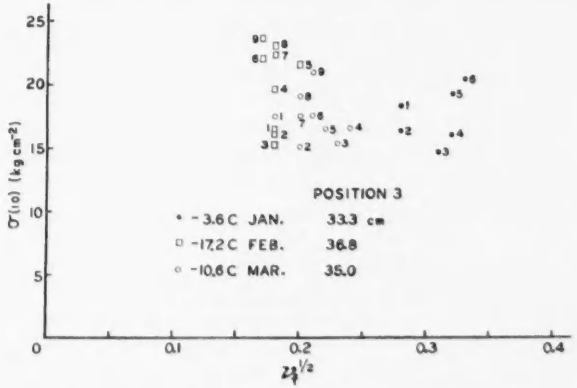

FIG. 13. Tensile strength, adjusted to $-10°$ C, is plotted against square root of void content. Numbers adjacent to points become larger as depth from which samples originated increases.

providing one starts at depth number 3. The positions noted for the number 3 samples are roughly alike, being about 10 to 13 cm below the transition layer. It appears that the strength of a sample of ice is somehow related to the position it occupied in the ice sheet and it is interesting to speculate on why this should be so.

The variation of salinity and so of brine content with depth (Fig. 7) definitely does not offer an explanation. If anything, the increase of salinity with depth below the transition layer would be expected to result in decreasing strength with increasing depth which is contrary to the data of Fig. 13. Density, Fig. 6, is to all intents and purposes uniform below the transition layer and so cannot contribute to the desired effect. Significant increases with depth are observed in the horizontal dimensions of the crystals (Fig. 5). The reduction in number of crystals with depth may have a bearing on the problem.

It was stated earlier that brine is trapped between layers in the intracrystalline structure during freezing. It is, however, also trapped at the intercrystalline surfaces. For the ring tensile tests, the force is applied in a direction which tends to shred the crystals apart. The smaller the crystals, the more likely is it that a point of stress concentration will happen to fall on an intercrystalline boundary. With increasing crystal size, and a consequently lower probability of a point of stress concentration coinciding with an intercrystalline boundary, the tensile strength would be expected to increase. It seems that, for Shippegan at least, crystal size predominantly determines strength for small sample tests. It appears that brine between crystal boundaries is rather more efficient at reducing strength than brine trapped within the crystals. The points 1, 2, and 3 of Fig. 13 show strength decreasing with depth for about 10 cm below the transition layer. They are in the zone where some crystals with *C*-axes not horizontal are still present. The number of these randomly oriented crystals which would tend to strengthen the ice decreases with depth and is apparently reduced to zero some 10 cm below the transition layer.

ACKNOWLEDGMENTS

The author is indebted to Prof. E. R. Pounder, Director of the Ice Research Project, for a critical review of this manuscript. Special thanks are due to Mr. H. J. Robichaud of the Canadian Department of Fisheries for his willing assistance with the preparation of the many ice samples used in the tests.

This work was supported by the Defence Research Board under D.D.P. Contracts C-69-700102 and GC-69-800103.

REFERENCES

ANDERSON, D. L. and WEEKS, W. F. 1958. Trans. Am. Geophys. Union, **39**, 632.
ASSUR, A. 1958. Arctic sea ice. Washington, NAS–NRC Publication No. 598, 106.
BUTKOVICH, T. R. 1956. Snow, Ice, and Permafrost Research Establishment, SIPRE Research Report 20 (U.S. Army Corps of Engineers, Wilmette, Ill.).
BUTKOVICH, T. R. 1958. Trans. Can. Inst. Engrs. **2**, 112.
PEREY, F. G. J. and POUNDER, E. R. 1958. Can. J. Phys. **36**, 494.
POUNDER, E. R. and LITTLE, E. M. 1959. Can. J. Phys. **37**, 443.
RIPPERGER, E. A. and DAVIDS, N. 1947. Proc. Am. Soc. Civil Engrs. **12**, 619.
WEEKS, W. F. 1958. Arctic sea ice. Washington, NAS–NRC Publication No. 598, 96.
WEEKS, W. F. and ANDERSON, D. L. 1958. Trans. Am. Geophys. Union, **39**, 641.

BETATRON ENERGY CALIBRATION[1]

L. KATZ

ABSTRACT

A new betatron energy controlling circuit is described which has many advantages over those previously used. It is shown that there is a linear relationship between the helipot control on this circuit and the momentum of the electrons in the betatron just prior to striking the X-ray producing target. It is also shown that photoneutron thresholds can be used to calibrate the betatron energy scale with good internal consistency.

INTRODUCTION

In calibrating betatron energy scales use is made of certain photonuclear reactions whose threshold energies are well known from mass data. Photoneutron reactions are used since the emitted neutrons have no coulomb barrier to surmount, and if there is no large centrifugal barrier, the neutron yield curve starts from threshold with a finite slope making it easy to detect.

The experimental accuracy with which these threshold positions can be established on the energy scale has not always been satisfactory for the precision desired. This has been due to the inadequacies in the betatron photon flux relative to the sensitivity of the reaction-detecting system. The net result has been a poor signal-to-noise ratio in the threshold region. This is especially troublesome when studying the thresholds of light (up to $A \approx 40$) elements, as the photoneutron activation curves of these elements exhibit fine structure or breaks (Katz *et al.* 1954; Penfold and Spicer 1955) and one may mistake a break above the threshold (Bendel *et al.* 1958; Geller and Muirhead 1958; Spicer and Penfold 1955) in combination with a high background for the true threshold.

In particular, Spicer and Penfold (1955) using the University of Illinois betatron and a Geiger counter detection system found the $C^{12}(\gamma,n)C^{11}$ threshold much more accurately than it had been previously. They found a previously undetected weak break 300 kev above threshold and suggested that this break combined with the high background activity could have been previously mistaken for the true threshold.

Bendel *et al.* (1958) using an energy scale, based on the (γ,n) thresholds of F^{19}, N^{14}, and C^{12}, observe the neutron yield from $O^{16}(\gamma,n)O^{15}$ to start at 15.74+0.05 Mev. This is about 0.1 Mev above the expected value. Similar results have been obtained by Geller and Muirhead (1958), only they find this apparent threshold 0.15 Mev above the true threshold.

In view of these surprising results we felt it desirable to report the betatron energy calibration techniques used in our laboratory for the past few years as well as the electronic circuits used for this purpose. We find that our energy

[1]Manuscript received June 22, 1959.
Contribution from the Department of Physics, University of Saskatchewan, Saskatoon, Saskatchewan.

scale can be expressed by a linear relation between the electron momentum giving rise to the bremsstrahlung and a helipot dial setting on the energy-controlling circuit. The observed thresholds for the (γ,n) reactions in Be^9, D^2, Pb^{207}, Be^{209}, Cu^{63}, K^{39}, O^{16}, and C^{12} define this line accurately with internal consistency. We interpret this to indicate that we observe the true thresholds in all cases. Our energy scale so established was used to measure the (γ,n) thresholds in a number of elements (Chidley, Katz, and Kowalski 1958). Good agreement was found in all cases where accurate mass data was available.

ENERGY-CONTROLLING CIRCUIT

This circuit can be most conveniently analyzed in two parts: first, the part which gives a signal whose amplitude is at each instant proportional to the instantaneous electron energy, and secondly, the circuit which translates this signal into an expander pulse, causing the electrons to strike a target, at some predetermined energy, and giving rise to the bremsstrahlung beam whose peak energy is equal to the electron kinetic energy.

(*a*) The first part of the circuit is shown in Fig. 1. If ϕ is the instantaneous flux linking the electron orbit, then to a good approximation*

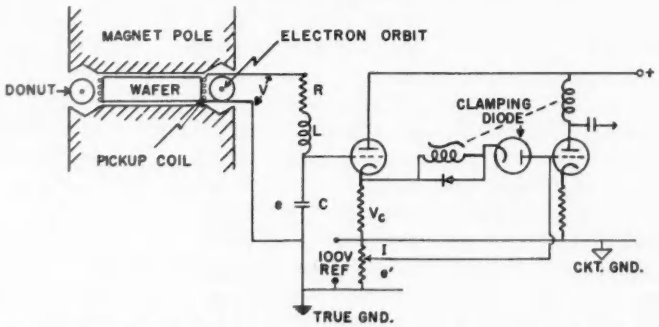

FIG. 1. Schematic diagram of the betatron energy controlling circuit. Voltage V, across the pickup coil in the magnetic field, is at each instant proportional to the time rate of change of magnetic flux; e across c is the time integral of V and is thus proportional at each instant to the magnetic field intensity at the electron orbit or the electron momentum. When e reaches some predetermined value e', itself determined by the helipot setting I, the multiar circuit fires resulting in an expander pulse which causes the betatron electrons to strike a target.

$$\phi = \phi_0 \sin \omega t. \tag{1}$$

The electrons in the orbit then have an instantaneous momentum

$$p = reB = k_1 r \phi_0 \sin \omega t \tag{2}$$

where B is the magnetic field strength at the orbit, r is the instantaneous radius of curvature, and k_1 is a constant. We assume here that there is no magnetic saturation in the iron so B is directly proportional to ϕ.

*The betatron is energized by resonating its windings against a large condenser bank so the flux is almost pure sin ωt. Any distortion due to saturation effects in the magnetic circuit can give rise only to odd harmonics. Analysis shows that these will not affect our conclusions significantly.

The relation between $p(t)$ and $\phi(t)$ can be established on more general grounds. Penfold (1959) has recently shown that the momentum of an electron in an axially symmetric field depends only on the flux enclosed by the orbit. If the center of symmetry of the field remains fixed he finds

$$p(t) = \frac{e}{2\pi cr(t)} \cdot \{\phi(0) - \phi(t)\},$$

where ϕ (0) is the orbit flux at zero magnetic field, e.g. biased machine.

Again, in the absence of magnetic saturation† the voltage induced in the pickup coil is proportional to the time rate of change of ϕ, so

$$v = -k_2 \omega \phi_0 \cos \omega t \tag{3}$$

where k_2 is a constant.

Impressing this voltage across the series LRC circuit of Fig. 1, we find the voltage across the condenser to be

$$e = \frac{k_2 \phi_0}{RC(1+\theta^2)^{\frac{1}{2}}} \sin(\omega t + \theta) \tag{4}$$

where

$$\tan \theta = \frac{1-\omega^2 LC}{\omega RC} \approx \theta. \tag{5}$$

When this voltage rises negatively to a predetermined value, e' in the circuit of Fig. 1, it gives rise to a current pulse in the electron orbit expander causing the electrons to strike the target. If τ is the delay time in this part of the circuit, then the momentum of the electron on striking the target is

$$p = rk_1 \phi_0 \sin \omega(t + \tau); \tag{6}$$

combining this with equation (4) we find

$$e' = \frac{k_3}{rRC(1+\theta^2)^{\frac{1}{2}}} p \frac{\sin(\omega t + \theta)}{\sin(\omega t + \omega\tau)}. \tag{7}$$

If the circuit parameters can be adjusted so that $\theta = \omega\tau$, then p is directly proportional to e'. Note that ω does not appear explicitly in this equation whereas it does when an ordinary RC integrating network is used.

Usually τ is very small, say 3 μsecond, and for our betatron the operating frequency is 180 c.p.s.; then $\omega\tau = 3.4 \times 10^{-3}$. Thus in making $\theta = \omega\tau$ we find from equation (5) $LC \approx 1/\omega^2$. Our circuit was designed for e' to have a maximum value of 100 volts, $V_0 = 1400$ volts, and choosing $C = 0.5$ μf, we calculate $R = 3.1 \times 10^4$ ohms and $L = 1.56$ h. To make $\theta = 3.4 \times 10^{-3}$ we find from equation (5) that $\omega^2 LC = 0.94$, a resonance condition not difficult to achieve to the given accuracy experimentally. If we made an error in θ by a factor of 2, the energy scale would deviate from linearity at low energy, being in error by about 70 kev at 2 Mev.

†If the pickup coil were of small area, centered on the electron target (X-ray radiator), then these assumptions of no magnetic saturation would not have to be made. However, linearity of our calibration curve shows them to be satisfied.

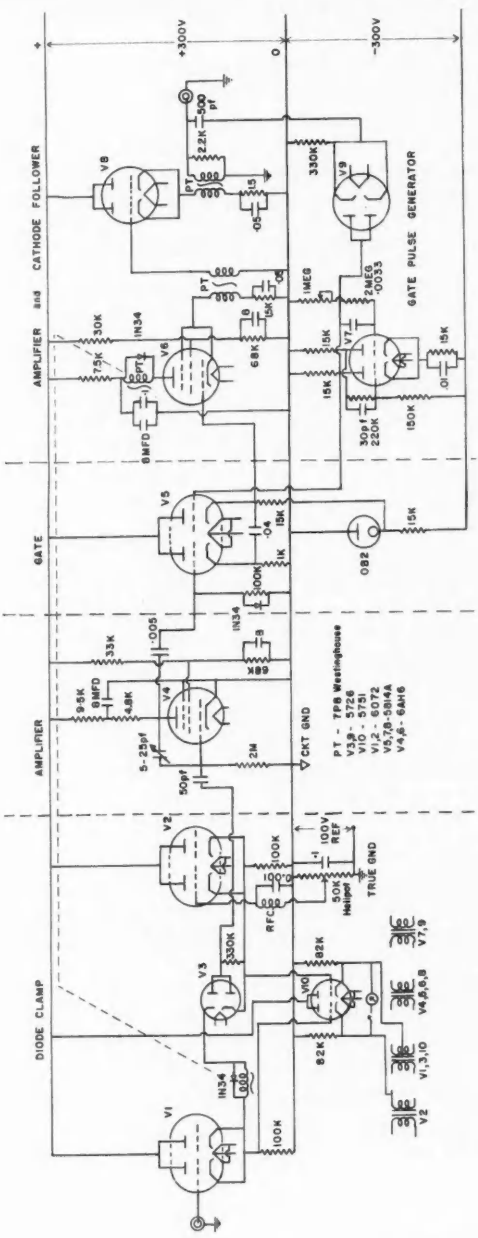

FIG. 2. Voltage comparator and associated circuits.

(*b*) The basic voltage comparison circuit is also shown in Fig. 1 and is a modification of the "multiar" (Waveforms 1949). Conduction starts in the clamping diode when $e+100$ $(=V_c)$ is less than $100-e'$ or when $e \leqslant -e'$, that is, when the negative going part of the *ac* on the condenser exceeds negatively the voltage e'. This voltage is determined by the helipot setting I. Once conduction starts, positive feedback through the pulse transformer accelerates the process. Rise times of 100 volts per μsecond can be obtained in this way. The pulse so obtained is amplified and used to trigger a hydrogen thyratron which delivers a current pulse through the electron orbit expander. The 100-volt reference voltage is a highly stabilized d-c. supply. The actual circuit used is shown in greater detail in Fig. 2.

Since the voltage e' is determined by the helipot setting I and is directly proportional to it then for $\theta = \omega\tau$, equation (7) can be written

$$I = ap+b = a\sqrt{E(E+2m_0c^2)}+b \tag{8}$$

where a and b are constants and E is the electron kinetic energy on striking the target, that is, the peak energy of the bremsstrahlung spectrum.

When τ is not cancelled out, keeping I fixed, E is found to depend on the betatron operating energy. This effect was first discussed by Seren *et al.* (1953). To check whether we have effectively made $\theta = \omega\tau$, the $Be^9(\gamma,n)Be^8$ threshold was measured as the betatron magnet excitation was changed from 7 Mev to 23 Mev. The threshold was found to shift by -10 kev. Similarly, a break in the $O^{16}(\gamma,n)O^{15}$ yield curve near threshold shifted by $+4$ kev when the betatron magnet excitation was changed from 18 Mev to 24 Mev.

Our energy scale is also independent of the betatron frequency. Thus in changing the operating frequency from 179.4 c.p.s. to 180.6 c.p.s. the energy scale at 17 Mev changed by less than 2 kev.

Combining equations (2) and (8) gives

$$I = a'B+b \tag{9}$$

where a' and b are constants.

This equation was subjected to direct experimental verification by placing two pickup coils symmetrically with respect to the stable electron orbit: one of slightly smaller radius than the orbit and the other slightly larger. The value of B averaged over the area enclosed by the two coils was measured and found to be linearly dependent on I as shown in Fig. 3.

Though the accuracy of our measurements was not very high (±90 kev) the linearity of this graph is well established within these limits. Geller and Muirhead (1958) found their energy scale highly non-linear above 20 Mev and apparently blowing up at about 22.5 Mev. Penfold (1955) also concluded that the University of Illinois betatron energy scale was non-linear. He found the calibration curve crossed a straight line three times with major deviations of 0.2 Mev in one direction at 15 Mev and 0.4 Mev in the opposite direction at 22 Mev.

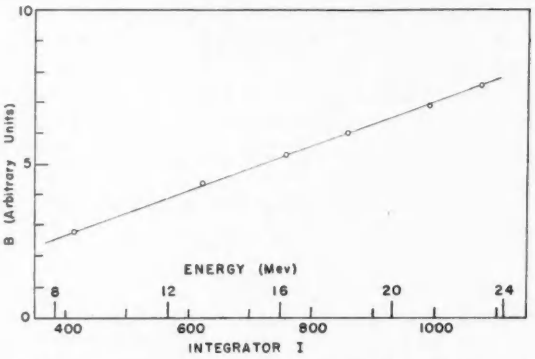

FIG. 3. Experimental results illustrating the linear relation between the magnetic flux density averaged over the electron orbit at the instant the electrons strike the target and the helipot setting I.

CALIBRATION OF THE ENERGY SCALE

The energy scale was calibrated by establishing the photoneutron thresholds for a number of reactions, whose reaction energies are known, relative to the integrator setting I. The data is summarized in Table I.

TABLE I

Calibration of the betatron energy scale

Reaction	Threshold energy, Mev (C.M.)	Measured I	I_{calc} from eq. 10	$I_{meas} - I_{calc}$
$Be^9(\gamma,n)Be^8$	1.666 ± 0.001[a]	99.2 ± 0.3	98.9 ± 0.1	$+0.3\pm0.3$
$D^2(\gamma,n)H^1$	2.226 ± 0.001[a]	124.7 ± 0.3	125.0 ± 0.1	-0.3 ± 0.3
$Pb^{207}(\gamma,n)Pb^{206}$	6.734 ± 0.008[b]	333.6 ± 1.0	331.0 ± 0.4	$+2.6\pm1.0$
$Bi^{209}(\gamma,n)Bi^{208}$	7.43 ± 0.05[c]	361.1 ± 1.0	362.7 ± 2.2	-1.6 ± 2.4
$Cu^{63}(\gamma,n)Cu^{62}$	10.826 ± 0.018[d]	517.6 ± 1.0	517.0 ± 0.8	$+0.6\pm1.0$
$K^{39}(\gamma,n)K^{38}$	13.09 ± 0.03[e]	620.9 ± 1.5	619.8 ± 1.4	$+1.1\pm2.0$
$O^{16}(\gamma,n)O^{15}$ break	~17.15[f]	805.6 ± 0.5		
$C^{12}(\gamma,n)C^{11}$	18.721 ± 0.006[a]	875.8 ± 0.7	876.3 ± 0.3	-0.5 ± 0.8

[a] Mattauch, Waldman, Bieri, and Everling (1956).
[b] Kinsey, Bartholomew, and Walker (1951); also Benson, Damerow, and Ries (1959).
[c] Huizenga, J. R. (1955).
[d] Quisenberry, Scolman, and Nier (1956).
[e] Endt, Bueckner, Braams, Paris, and Sperduto (1957).
[f] Characteristic break in the $O^{16}(\gamma,n)O^{15}$ yield curve. Actually two breaks $\sim$17.12 and $\sim$17.18 Mev are seen as one break unless great care is taken to resolve them. See King and Katz, following paper.

To monitor the drift of the energy scale and to correlate it from threshold measurement to threshold measurement, a point on the $O^{16}(\gamma,n)O^{15}$ activation curve near 17.3 Mev was checked frequently. At this energy, the yield per unit dose changes by 10% per integrator division ($\approx$ 22 kev) and $\sim10^4$ counts can readily be accumulated, so that drifts of $\sim$3 kev in the energy scale can be readily detected. The monitor points at 17.3 Mev were related to the position of a break in the yield curve and the day-to-day drift of this break was used to correct the measured thresholds to a consistent energy scale. The drift from

the average calibration during these measurements was less than one integrator division (22 kev).

Since the residual nuclei resulting from (γ,n) reactions in D^2, Be^9, Pb^{207}, and Bi^{209} yield no detectable activity, the positions of the thresholds for these reactions on the I scale were determined by detecting the emitted neutrons. The apparatus previously described (Montalbetti, Katz, and Goldenberg 1953) was used for this purpose. These thresholds are shown in Figs. 4–7, and the pertinent data is summarized in Table I. Errors in the measured values of I are estimated from the precision with which the thresholds could be localized on the graphs. The graphs show the measured points uncorrected for the day-to-day drift of the energy scale.

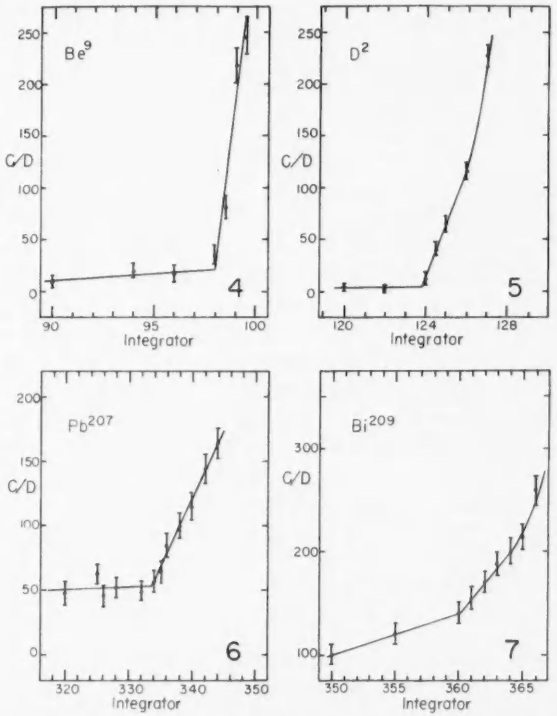

FIG. 4. Threshold for the $Be^9(\gamma,n)Be^8$ reaction. The threshold energy for this reaction is 1.666 ± 0.001 Mev and the corresponding helipot setting is $I = 99.2\pm0.3$ units (after corrections for the day-to-day drift of this scale).

FIG. 5. Threshold for the $D^2(\gamma,n)H$ reaction. The threshold energy for this reaction is 2.226 ± 0.001 Mev and the corresponding helipot setting is 124.7 ± 0.3 units (after correction for the day-to-day drift of this scale).

FIG. 6. Threshold for the $Pb^{207}(\gamma,n)Pb^{206}$ reaction. The threshold energy for this reaction is 6.734 ± 0.008 Mev and the corresponding helipot setting is 333.6 ± 1.0 units (after correction for the day-to-day drift of this scale).

FIG. 7. Threshold for the $Bi^{209}(\gamma,n)Bi^{208}$ reaction. The threshold energy for this reaction is 7.43 ± 0.05 Mev and the corresponding helipot setting is 361.1 ± 1.0 units (after correction for the day-to-day drift of this scale).

The copper and potassium thresholds and oxygen break were found by detecting the residual β^+ activity with Geiger counters. The two thresholds are shown in Figs. 8 and 9. In the heavier elements the threshold positions were determined as outlined by Chidley *et al.* (1958).

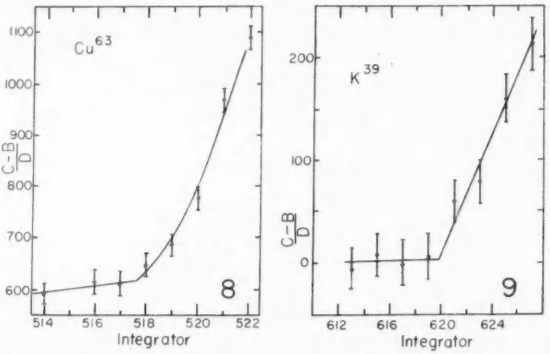

FIG. 8. Threshold for the $Cu^{63}(\gamma,n)Cu^{62}$ reaction. The threshold energy for this reaction is 10.826 ± 0.018 Mev and the corresponding helipot setting is 517.6 ± 1.0 units (after correction for the day-to-day drift of this scale).

FIG. 9. Threshold for the $K^{39}(\gamma,n)K^{38}$ reaction. The threshold energy for this reaction is 13.09 ± 0.03 Mev and the corresponding helipot setting is 620.9 ± 0.8 units (after correction for the day-to-day drift of this scale).

To detect the $C^{12}(\gamma,n)C^{11}$ threshold, we used a sensitive scintillation technique (also used about the same time by Cohen and McElhinney 1956). Our method was to irradiate carbon-rich plastic scintillators in the betatron X-ray beam and to detect the resulting β's from C^{11} by their scintillations. The sensitivity of ordinary Geiger counters for detecting this activity is limited by self-absorption in the sample, while in the scintillation technique this limitation does not exist. This method of studying the $C^{12}(\gamma,n)C^{11}$ reaction resulted in an improvement of signal-to-noise by a factor of 40. The C^{12} threshold so detected is shown in Fig. 10 and the first few breaks above threshold are shown in Fig. 11. The improved statistics in this work allows us to detect two extra breaks between threshold and the first break found by Penfold and Spicer (1955) at $19.10+0.05$ Mev.

The four most carefully above-measured thresholds, beryllium, deuterium, copper, and carbon, were used to establish an energy scale for the betatron by solving for the constants a and b of equation (8) by the method of least squares with both variables subject to error (Scarborough 1958). The equation so found was

$$I = 45.39\sqrt{E(E+1.022)}+2.9 \tag{10}$$

with E measured in million electron volts in the laboratory system.

Values of I calculated from this equation for the threshold energies listed in

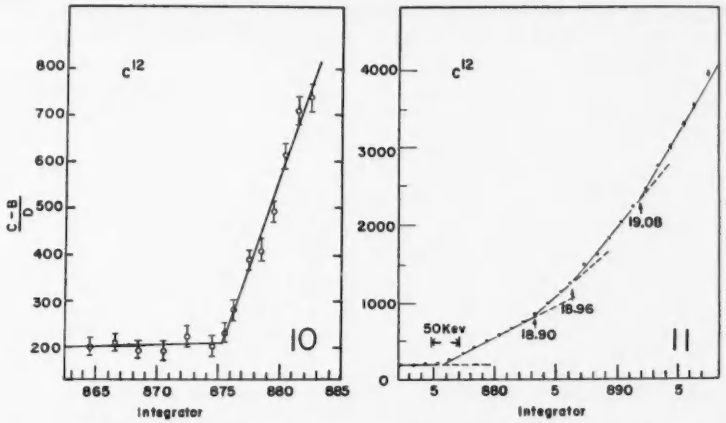

FIG. 10. Threshold for the $C^{12}(\gamma,n)C^{11}$ reaction. The threshold energy for this reaction is 18.721 ± 0.006 Mev. The corresponding helipot setting $I = 875.8 \pm 0.7$ units (after correction for the day-to-day drift of this scale).

FIG. 11. The first few breaks above threshold in the $C^{12}(\gamma,n)C^{11}$ neutron yield curve.

the table are tabulated in column 4. The differences $(I_{\text{meas}} - I_{\text{calc}})$ are shown in the last column and are plotted as a function of energy in Fig. 12. The energy on this scale corresponding to the oxygen break is $17.18 + 0.04$ Mev (Lab).

DISCUSSION

The magnetic measurements shown in Fig. 3 and threshold measurements in Fig. 12 are seen to be consistent with a linear relationship between I and p for our betatron. Furthermore, at no time have we found an inconsistency between

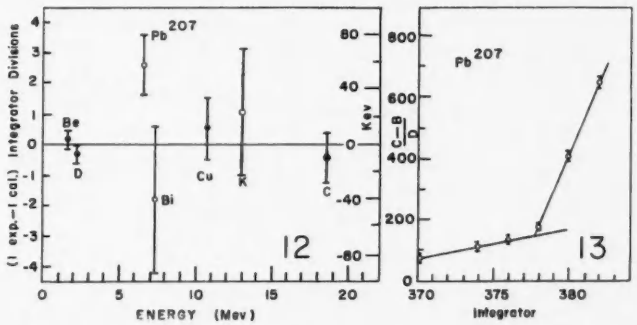

FIG. 12. The Be^9, D^2, Cu^{63}, and C^{12} thresholds were used to establish a relation by least squares between I and the maximum bremsstrahlung energy E. In this graph are plotted the differences between the measured values of I, I_{meas}, and the corresponding values calculated from the equation from the known threshold energies.

FIG. 13. A recent measurement of the $Pb^{207}(\gamma,n)Pb^{206}$ threshold. Using this measured value of I and the calibration equation established by other thresholds we find the threshold energy 70 kev (3.5 integration units) above the accepted value of 6.734 Mev.

the energy scale so established and the measured thresholds for photoneutron reactions, where the reaction energy is also known from independent data (Chidley *et al.* 1958).

In all measurements carried out over the past 2 years we have found the Pb^{207} threshold to be above the calibration curve by 50 to 70 kev. A recent example of one such measurement is shown in Fig. 13 (using a new pickup coil and reference voltage supply). The position of this threshold on our energy scale is readily established and the use of a new reference voltage supply moved it to a new position on our helipot, thus avoiding the possibility of any local non-linearity of our energy scale. Again it fell about 70 kev above the accepted value of 6.73 ± 0.008 Mev. If there were a level at about this energy in Pb^{207} above the ground state, then one could reason that the neutron capture γ-rays observed by Kinsey *et al.* (1951) were not ground state transitions, but no such level has been observed to date.

ACKNOWLEDGMENTS

The work reported in this paper is the result of many years of experience in our laboratory and many people have been associated with it. E. C. Pederson and G. B. Chidley contributed considerably to circuit design and construction. Some of the early monitoring techniques owe much to Dr. R. N. H. Haslam and his group, particularly L. B. Robinson. D. McPherson also assisted in this work. Calibration measurements reported in this paper were made by Dr. K. H. Lindenberger, I. M. Thorson, and H. King. Thanks are also due to Dr. N. Sklov and W. Zwirner for programing the least-square fit with error in both variables for our computer. The recent measurement of the Pb^{207} threshold was made by Dr. R. Parsons.

REFERENCES

Bendel, L. B., McElhinney, J., and Tobin, R. A. 1958. Phys. Rev. **111**, 1297.
Benson, J. L., Damerow, R. A., and Ries, R. R. 1959. Phys. Rev. **113**, 1105.
Chidley, B. G., Katz, L., and Kowalski, S. 1958. Can. J. Phys. **36**, 407
Cohen, L. and McElhinney, J. 1956. Rev. Sci. Instr. **27**, 7731.
Endt, P. M., Bueckner, W. W., Braams, C. M., Paris, C. H., and Sperduto, A. 1957. Phys. Rev. **105**, 1005.
Geller, K. N. and Muirhead, E. G. 1958. Precision energy measurements with a 25 Mev betatron. University of Pennsylvania Report.
——— 1959. Bull. Am. Phys. Soc. **4** (II), 32.
Huizenga, J. R. 1955. Physica, **21**, 410.
Katz, L., Haslam, R. N. H., Hosley, R. J., Cameron, A. G. W., and Montalbetti, R. 1954. Phys. Rev. **95**, 464.
Kinsey, B. B., Bartholomew, G. A., and Walker, W. H. 1951. Phys. Rev. **82**, 380.
King, H., and Katz, L. 1958. Photonuclear conference, Washington, D.C.
Mattauch, J., Waldman, L., Bieri, R., and Everling, F. 1956. Ann. Rev. Nuclear Sci. **6**, 179.
Montalbetti, R., Katz, L., and Goldenberg, J. 1953. Phys. Rev. **91**, 659.
Penfold, A. S. 1955. Photonuclear cross section of oxygen. Ph.D. Thesis, University of Illinois, Chicago, Illinois.
——— 1959. Private communication.
Penfold, A. S. and Spicer, B. M. 1955. Phys. Rev. **100**, 1377.
Quisenberry, K. S., Scolman, T. T., and Nier, A. O. 1956. Phys. Rev. **104**, 461.
Scarborough, J. B. 1958. Numerical mathematical analysis. 4th ed. (Johns Hopkins Press, Baltimore, Md.), p. 484.
Seren, L., Brinbaum, M., Harth, E., and Tobin, R. 1953. Phys. Rev. **91**, 474A.
Spicer, B. M. and Penfold, A. S. 1955. Phys. Rev. **100**, 1375.
Waveforms. 1949. M.I.T. Radiation Laboratory Series (McGraw-Hill Book Co., Inc., New York).

NOUVELLES ÉMULSIONS IONOGRAPHIQUES À L'ALCOOL POLYVINYLIQUE[1]

ETSUO FUJII,[2] HIDEKO FUJII,[3] JOSEPH DEMERS ET PIERRE DEMERS

RÉSUMÉ

Nous décrivons la préparation et quelques propriétés de deux émulsions ionographiques à base d'alcool polyvinylique, qui montrent dans leur épaisseur les trajectoires des rayons α et des protons (et même des électrons lents) contenant environ 84% de bromure d'argent. Ces émulsions ne contiennent ni azote ni gélatine. On peut espérer, de l'emploi de l'alcool polyvinylique comme support, des propriétés mécaniques intéressantes. On décrit un procédé de détection fortement directionnel basé sur l'emploi des émulsions ionographiques.

INTRODUCTION

Parmi les procédés disponibles jusqu'ici en physique nucléaire pour manifester les trajectoires des particules chargées, deux utilisent des fluides comme milieu sensible: la chambre à condensation (gaz et vapeur) et la chambre à bulles (liquide). La chambre à cristal luminescent photographié avec déclenchement, et l'émulsion ionographique à base de gélatine, utilisent un milieu solide. L'émulsion ionographique qui présente sur les systèmes précédents l'intérêt de fonctionner continûment et d'accumuler les impressions, sans surveillance, possède cependant quelques défauts qui peuvent gêner et limiter les expériences et les mesures possibles. Sa composition est essentiellement fixe (HCNOAgBrI...) et ses propriétés mécaniques laissent parfois à désirer: écaillement, distension, distorsion.

Les essais plus ou moins fructueux de production d'émulsions photographiques et rayons X, où la gélatine a pu être remplacée par l'alcool polyvinylique (APV), suggèrent la même possibilité pour les émulsions ionographiques. Les premières expériences de Schwerin et Demers (1954) ont permis effectivement d'enregistrer les trajectoires des rayons α, mais seulement à la surface des couches sensibles. Les expériences actuelles ont confirmé les résultats précédents et ont permis d'étendre la sensibilité plus profondément dans l'épaisseur des couches, et de l'accroître au point de manifester les trajectoires des protons. La sensibilité strictement superficielle qu'on obtient parfois nous a suggéré un procédé particulier pour l'analyse angulaire des faisceaux de particules chargées.

Deux formules sont décrites, une formule neutre et une formule à l'ammoniaque, au bromure pur dans les deux cas. Avec la formule à l'ammoniaque, on a obtenu les trajectoires des protons de 6 à 7 Mev.

PRÉPARATION

Alcool polyvinylique

Les expériences de Schwerin et Demers (1957, 1958) portaient sur un mélange APV, types Elvanol de Dupont 72-60 et 52-22, dans le rapport 2 à

[1]Manuscrit reçu le 13 juillet 1959.
Contribution du Département de Physique de la Faculté des Sciences, Université de Montréal, Montréal, Qué.
[2]Adresse actuelle: Laboratoire de chimie industrielle du Gouvernement, Tokyo, Japon.
[3]Adresse actuelle: Université du Sacré-Coeur, Tokyo, Japon.

1. Les expériences actuelles se sont poursuivies avec le type 72-60 seul, qui est hydrolysé. Voici l'analyse que nous avons faite de l'échantillon employé (lot UB.6.0.52 du 6 décembre 1956) (pour la méthode employée, voir Fujii 1952):

Degré moyen de polymérisation 2720,
Eau retenue 3.84%,
Hydrolyse 99.89%,
Cendre calculée comme Na_2CO_3 1.1%,
pH de la solution aqueuse à 5% 6.8.

Ces résultats s'accordent sensiblement avec ceux du fabricant pour ce type d'Elvanol.

La dissolution s'opère en gonflant la poudre dans l'eau froide avec agitation pendant quelques heures, puis en élevant la température lentement au bain-marie jusqu'à 75–80° C avec agitation pendant une demi-heure environ.

Formule neutre

Sauf l'absence du type 52-22, la formule employée est celle décrite déjà sous le No 20 (Demers et Schwerin 1957, 1958; voir Ionographie, p. 137). On s'est servi de la machine à deux pompes avec deux réservoirs à huile intermédiaire (voir Ionographie, fig. 46, p. 133). Avec les quantités employées, voici la formule.

Solution A	Solution B	Solution C
115 cm³, 197 tours	116.8 cm³, 200 tours	APV72-60, 15.19 g
Solution $AgNO_3$ 600 g/l.	Solution KBr 420 g/l.	Eau distillée 202 cm³

Dans la solution C agitée régulièrement et gardée à 70° C dans un bécher de 600 cm³, on verse un excès initial de 3 tours B (1.75 cm³), puis ensemble des volumes égaux et équivalents de A et de B. Les becs sont immergés pendant toute la précipitation. L'émulsion liquide contient alors 3.57% APV. Elle est placée immédiatement au congélateur, où elle reste à −10° C environ, pendant 24 heures. On la laisse dégeler pendant quelques heures à +5° C dans la glacière. À ce moment l'émulsion forme un gel, qu'on met en nouilles de 3 mm de côté et qu'on lave à l'eau froide à 5–10° C pendant 7 heures. Le lavage a besoin d'être plus prolongé qu'avec l'émulsion correspondante à la gélatine.

On recueille, on égoutte, on garde à la glacière; on refond sans difficulté à 70° C en 5 minutes avec agitation. On pose environ 1.2 cm³ par lame 2.5×7.5 cm. Le séchage à 23° C et 58% d'humidité relative a pris 18 heures; la couche obtenue était lisse et mesurait 50 μ d'épaisseur. L'émulsion sèche contient 83.4% AgBr (calculé). Au besoin les lames sont ensuite trempées dans des bains divers et séchées à nouveau avant l'irradiation.

Formule à l'ammoniaque

Cette émulsion a été faite aussi par la méthode du double jet, mais avec des burettes; les solutions A et B ne sont pas équivalentes. Sa solution A est préparée à partir de 58 cm³ $AgNO_3$ 600 g/l., additionnés d'ammoniaque jusqu'à dissolution du précipité initialement formé.

Solution A	Solution B	Solution C
$AgNO_3$ 34.8 g	NH_4Br 20.43 g	APV 10 g
NH_4OH q.s.	Total 59 cm³	Eau distillée 100 cm³
Total 95 cm³		

Dans la solution C agitée et gardée à 70° C dans un bécher de 400 cm³, on verse d'abord 1 cm³ B, puis ensemble et en quantités équivalentes autant que possible, A et B. L'émulsion liquide renferme alors 3.94% APV. La suite des opérations est comme pour l'émulsion neutre, sauf les points suivants. La congélation doit être plus longue pour assurer la formation d'un gel. Le lavage a duré 6 heures. La refonte a lieu à 55° C en 5 minutes. L'émulsion sèche renferme 79.4% AgBr.

On a aussi essayé de précipiter avec une machine à deux pompes. Pour cela le volume de la solution B a été porté à 95 cm³ afin d'assurer l'équivalence des solutions, versées en volumes égaux. L'essai en question n'a pas été poursuivi au delà du stade de la précipitation. En effet la liqueur obtenue après quelques minutes de repos montrait des signes évidents de sédimentation. Une ligne de démarcation apparaissait à peu près à mi-hauteur, et le bas paraissait à simple inspection, plein d'une suspension de grosses particules. Cela suggère que la protection colloïdale de la solution APV, suffisante dans le cas précédent (3.94%), est insuffisante dans le cas actuel (3.45%). On pourrait d'ailleurs opérer avec des pompes avec les volumes précédents si on changeait les engrenages de la machine, ou encore, ou pourrait réaliser une solution argentique A plus concentrée, totalisant 59 cm³ seulement.

IRRADIATION

L'irradiation forte aux rayons α s'est faite à l'aide d'un bouton de 0.8 cm de diamètre, chargé du dépôt actif de 3 mc de radiothorium (Ionographie, fig. 99, p. 201). Ce bouton a été posé sur la couche sensible pendant une durée atteignant 5 minutes. De la sorte une émulsion peu sensible montre au moins un noircissement collectif visible, et si elle peut manifester les trajectoires individuelles, en surface ou en profondeur, celles-ci apparaîtront à l'exploration sous le microscope, en s'éloignant de la tache noircie de quelques centimètres. La gamme d'irradiation obtenue va d'environ 10^9 à environ 10^5 α/cm^2.

L'irradiation aux protons s'est faite en approchant le paquet de plaques de la cible de l'accélérateur Cockcroft–Walton du Département de Physique, de façon que les neutrons *dt* qu'il fournit soient incidents selon l'axe des plaques (deutérons de 600 kev, neutrons de 15 Mev vers l'avant). On obtient une bonne irradiation en 5 minutes à 5 cm. On observe les protons de recul, dont l'énergie atteint 15 Mev.

DÉVELOPPEMENT

On a utilisé notamment le révélateur à la chlorohydroquinone déjà décrit (Ionographie, p. 165):

Eau 600 cm³	KOH 32.5 g
Na_2SO_3 30 g	KBr 8 g
Chlorohydroquinone 45 g	Eau q.s. 1 litre

On emploie dilué 1:4; le pH est alors 11.9. On fabrique, garde et emploie sous azote; développement 10 minutes à 20° C.

On a essayé aussi d'autres révélateurs qui sont tous moins bons, à des degrés divers, que le précédent. Dans l'ordre de qualité décroissante, se place d'abord le glycin qui est assez satisfaisant, l'amidol, la formule D19 (métol-hydroquinone) et la phénidone qui donne de mauvais résultats. La durée optimum du développement est environ moitié ou deux tiers de celle qui s'applique à l'émulsion correspondante à base de gélatine.

RÉSULTATS

Les premiers essais, sur l'émulsion neutre, ont montré le noircissement. Ce noircissement est formé de gros amas, atteignant 10 μ de côté. Plus loin de la source la couche était peu voilée. Un examen attentif a montré les traces incidentes sous incidence rasante (figure 1), qui paraissent formées exclusivement

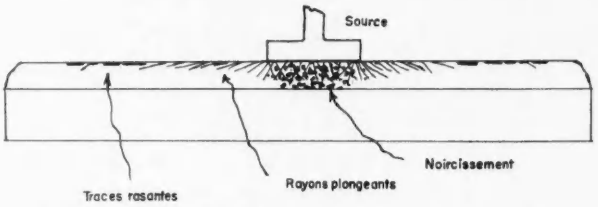

FIG. 1. Irradiation par le dépôt actif ThB + C + C′ + C″.

par les grains superficiels. Les traces ne peuvent à peu près jamais s'inscrire dans toute leur longueur, puisqu'elles subissent souvent des déviations vers le bas ou vers le haut qui les font sortir de la couche très mince où existe la sensibilité (un cristal, épaisseur 0.1 μ). On a observé des rayons atteignant 33 μ et comptant 38 grains avec parfois des déviations dans le plan horizontal. Les longueurs observées sont inférieures au parcours résiduel des particules α (jusqu'à 48 μ).

Apparemment les rayons α pénètrent en profondeur (impressionnant un grain par 5 à 50 μ) assez pour causer un effet collectif, et trop peu pour laisser une trace individuelle. Mais la sensibilité des grains superficiels est plus grande. Le diamètre des grains développés est environ 0.1 à 0.2 μ.

Les régions de visibilité optimum de ces traces rasantes peuvent se trouver, plus ou moins près de la source, selon la géométrie exacte et selon l'intensité. Les bosses et les creux de l'émulsion sont ainsi marqués, à la façon des plages éclairées sur un terrain au soleil couchant. La surface des émulsions précédentes (Demers et Schwerin 1956) était grenue, ce qui explique les observations sur les plages de visibilité.

On a ensuite cherché à sensibiliser par trempé dans la triéthanolamine (TEA) 6%. On a obtenu alors des trajectoires α visibles dans toute l'épaisseur par un traitement de 2 minutes, et la densité des traces superficielles a paru augmenté. Les traces avaient, par exemple, 20 μ et comptaient 15 grains. Le

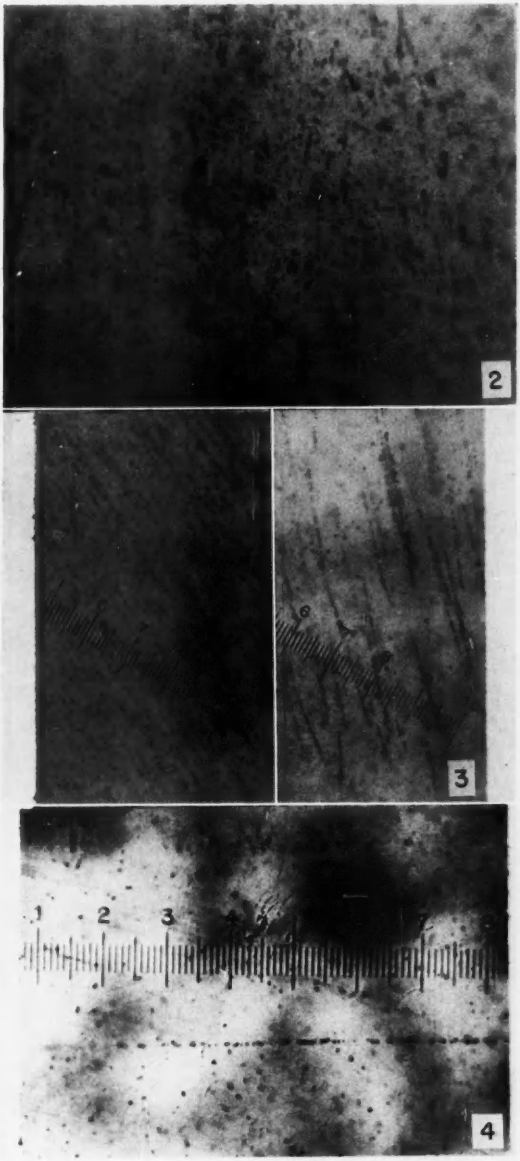

FIG. 2. Traces de rayons α à la surface d'une émulsion APV neutre.
FIG. 3. Traces de rayons α dans l'épaisseur d'une émulsion APV neutre (à gauche), et convertie (à droite); 1 div. = 1.11 μ.
FIG. 4. Trace de proton dans l'épaisseur d'une émulsion APV convertie, à un parcours résiduel d'environ 300 μ; 1 div. = 1.11 μ.

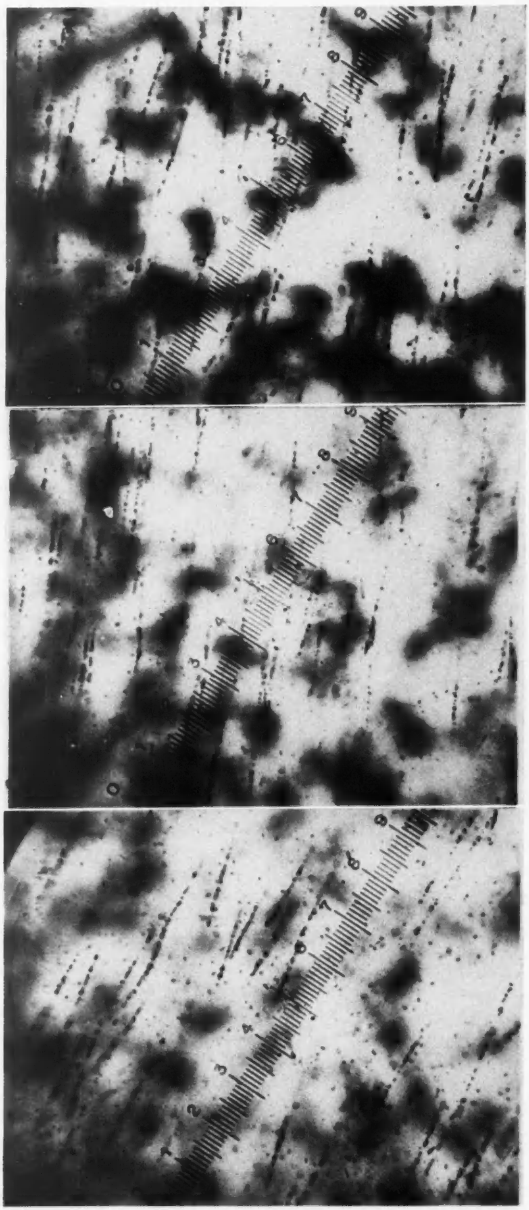

FIG. 5. Régression dans l'émulsion convertie: de haut en bas, 11 heures, 8 jours, 30 jours. Noter l'image floue des paquets du voile; 1 div. = 1.11 μ.

traitement de 10 minutes a réduit le voile et n'a pas fait apparaître les traces dans l'épaisseur de l'émulsion.

La figure 3 montre des rayons α inscrits dans l'épaisseur d'une couche d'émulsion APV neutre. Cependant cette photo a été obtenue sans traitement à la TEA. En effet d'autres lots de fabrication de la même émulsion ont montré, sans traitement spécial, les rayons α dans leur épaisseur. La TEA a une action variable: parfois favorable parfois nuisible, et de toute façon elle n'est pas indispensable.

Ces émulsions présentent un voile plus ou moins fort qui consiste en grains isolés et en paquets plus ou moins gros pouvant atteindre 10 à 30 μ de côté, et disposés le plus souvent à la surface verre. Il apparaît au cours de la précipitation, en quantité variable, des gros grains qui précipitent et sédimentent, si on laisse reposer. Cependant une décantation de 10 minutes après laquelle on rejeta le tiers inférieur du bécher ne suffit pas à supprimer le voile dans un cas où on l'a essayé. Sauf dans cet essai les émulsions liquides n'ont pas été décantées de façon systématique. La qualité de l'émulsion (sensibilité et voile) semble dépendre beaucoup du mode exact de mélange et d'agitation au cours de la précipitation, et ensuite du degré de refonte avant la coulée. La refonte doit être faite avec agitation énergique et prolongée afin de briser tous les grumeaux et de fluidifier parfaitement le gel. On peut croire qu'on libère ainsi des tensions capables de créer du voile et qu'on favorise du même coup une maturation sensibilisante.

Les couches d'émulsion converties ont les mêmes propriétés générales que les précédentes. Le grain développé mesure de 0.3 à 0.4 μ. Les rayons α s'y inscrivent en profondeur, et les protons aussi (figures 3 et 4). On a vu jusqu'ici des traces de protons de 400 μ. Les derniers 100 μ d'un proton contiennent environ 100 grains et les rayons α sont légèrement plus denses. On a aussi observé dans cette émulsion des étoiles de désintégration radioactive du thorium. L'action de la TEA 6%, traitement de 5 minutes, a un effet variable.

TRAITEMENTS DIVERS

La TEA a parfois un effet heureux (émulsions neutres surtout); d'autres fois son effet est nuisible ou inutile. Avec un traitement par la chaleur ou par le chlorure d'or, on a obtenu un accroissement du voile de l'émulsion neutre. Dans une expérience, on a ajouté 0.5 cm³ d'une solution de 6-nitrobenzimidazole à 0.001% à 150 cm³ d'émulsion refondue (émulsion neutre ou convertie); le voile s'en est trouvé réduit. Une solution alcoolique d'alpha-naphtol ajoutée, pour faciliter la prise, n'exerce pas d'effet favorable sur la sensibilité ni sur le voile.

RÉGRESSION

Des couches d'émulsion convertie ont été irradiées avec les rayons α, conservées à 39% d'humidité relative, 22° C, et développées après 30 minutes, 12 heures, 24 heures, 36 heures, 2 jours, 3 jours, 8 jours et 30 jours. Jusqu'à 8 jours on observe aucun signe de régression. Même après 30 jours les rayons α sont encore nombreux et clairement visibles (figure 5).

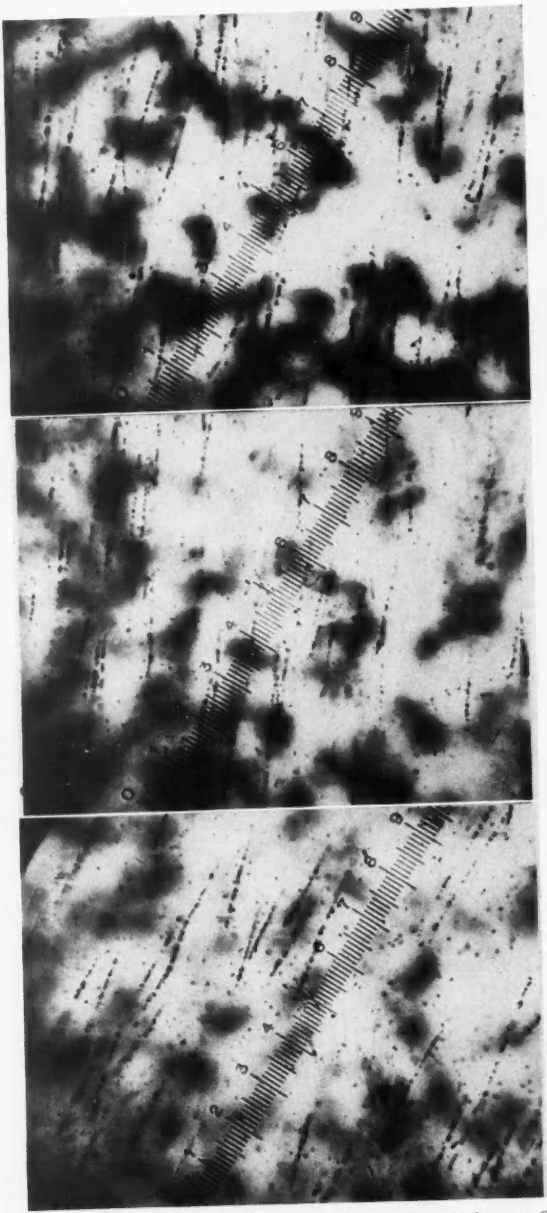

FIG. 5. Régression dans l'émulsion convertie: de haut en bas, 11 heures, 8 jours, 30 jours. Noter l'image floue des paquets du voile; 1 div. = 1.11 μ.

traitement de 10 minutes a réduit le voile et n'a pas fait apparaître les traces dans l'épaisseur de l'émulsion.

La figure 3 montre des rayons α inscrits dans l'épaisseur d'une couche d'émulsion APV neutre. Cependant cette photo a été obtenue sans traitement à la TEA. En effet d'autres lots de fabrication de la même émulsion ont montré, sans traitement spécial, les rayons α dans leur épaisseur. La TEA a une action variable: parfois favorable parfois nuisible, et de toute façon elle n'est pas indispensable.

Ces émulsions présentent un voile plus ou moins fort qui consiste en grains isolés et en paquets plus ou moins gros pouvant atteindre 10 à 30 μ de côté, et disposés le plus souvent à la surface verre. Il apparaît au cours de la précipitation, en quantité variable, des gros grains qui précipitent et sédimentent, si on laisse reposer. Cependant une décantation de 10 minutes après laquelle on rejeta le tiers inférieur du bécher ne suffit pas à supprimer le voile dans un cas où on l'a essayé. Sauf dans cet essai les émulsions liquides n'ont pas été décantées de façon systématique. La qualité de l'émulsion (sensibilité et voile) semble dépendre beaucoup du mode exact de mélange et d'agitation au cours de la précipitation, et ensuite du degré de refonte avant la coulée. La refonte doit être faite avec agitation énergique et prolongée afin de briser tous les grumeaux et de fluidifier parfaitement le gel. On peut croire qu'on libère ainsi des tensions capables de créer du voile et qu'on favorise du même coup une maturation sensibilisante.

Les couches d'émulsion converties ont les mêmes propriétés générales que les précédentes. Le grain développé mesure de 0.3 à 0.4 μ. Les rayons α s'y inscrivent en profondeur, et les protons aussi (figures 3 et 4). On a vu jusqu'ici des traces de protons de 400 μ. Les derniers 100 μ d'un proton contiennent environ 100 grains et les rayons α sont légèrement plus denses. On a aussi observé dans cette émulsion des étoiles de désintégration radioactive du thorium. L'action de la TEA 6%, traitement de 5 minutes, a un effet variable.

TRAITEMENTS DIVERS

La TEA a parfois un effet heureux (émulsions neutres surtout); d'autres fois son effet est nuisible ou inutile. Avec un traitement par la chaleur ou par le chlorure d'or, on a obtenu un accroissement du voile de l'émulsion neutre. Dans une expérience, on a ajouté 0.5 cm³ d'une solution de 6-nitrobenzimidazole à 0.001% à 150 cm³ d'émulsion refondue (émulsion neutre ou convertie); le voile s'en est trouvé réduit. Une solution alcoolique d'alpha-naphtol ajoutée, pour faciliter la prise, n'exerce pas d'effet favorable sur la sensibilité ni sur le voile.

RÉGRESSION

Des couches d'émulsion convertie ont été irradiées avec les rayons α, conservées à 39% d'humidité relative, 22° C, et développées après 30 minutes, 12 heures, 24 heures, 36 heures, 2 jours, 3 jours, 8 jours et 30 jours. Jusqu'à 8 jours on observe aucun signe de régression. Même après 30 jours les rayons α sont encore nombreux et clairement visibles (figure 5).

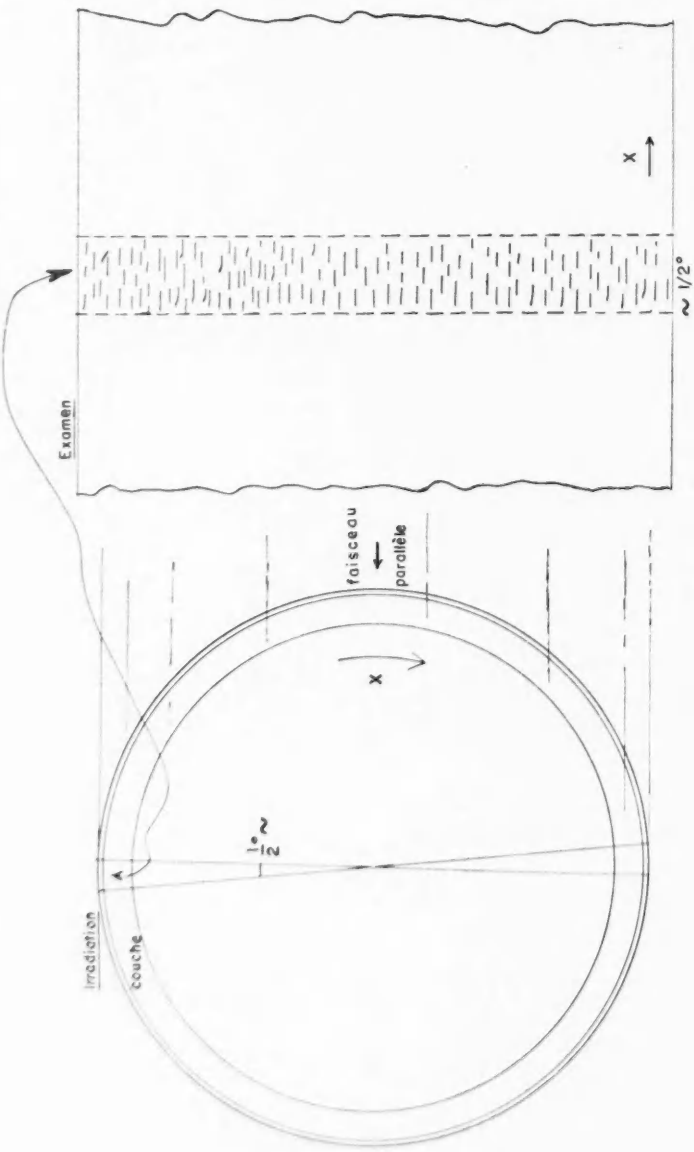

FIG. 6. Détecteur directionnel, schéma.

La stabilité très satisfaisante de l'image latente est attribuée aux caractères de l'APV. Les films d'APV sont notoirement imperméables aux gaz et on sait que l'oxygène cause la régression (protection des films RX contre la régression). D'autre part les molécules d'APV autour des cristaux de bromure d'argent leur sont liées par de fortes valences hydrogène, susceptibles de protéger les images latentes contre l'oxydation.

ÉMULSIONS CYLINDRIQUES, DÉTECTEUR DIRECTIONNEL

Lorsque les couches d'émulsion ionographique à base APV sont sensibles en surface seulement, elles constituent des détecteurs de haute sélection angulaire, puisqu'ils ne détectent que les trajectoires incidentes sous un angle très faible, compris probablement entre 0° et $\frac{1}{2}$° environ ou peut-être seulement $\frac{1}{4}$°. Ils pourraient rendre des services dans les applications où l'on aurait besoin d'isoler des pinceaux ou des nappes de petite ouverture angulaire (figure 6).

Supposons une telle couche enroulée sur un cylindre et placée dans un faisceau de rayons exactement parallèles. Elle portera des trajectoires exclusivement au voisinage de deux génératrices diamétralement opposées. La largeur angulaire de la région impressionnée serait de $\frac{1}{2}$ à $\frac{1}{4}$°. S'il y a deux faisceaux parallèles ils laisseront des traces selon deux paires de génératrices. On voit immédiatement les possibilités du système dans les études de diffusion angulaire, toujours difficiles aux angles faibles, inférieurs à 5° par exemple. En réalité, la largeur angulaire de la région impressionnée est sans doute accrue par la diffusion angulaire à l'intérieur de la couche détectrice.

Les couches sensibles seraient naturellement déroulées et collées à plat pour l'observation.

Les trajectoires ainsi inscrites se prêtent idéalement au dénombrement par photométrie puisqu'elles sont toutes exactement horizontales.

L'expérience a été tentée (figure 7) avec une source étroite de rayons α et une couche d'émulsion non convertie décollée de son support. Contrairement

FIG. 7. Détecteur directionnel, montage.

à ce qu'on espérait (figure 8*a*), la sensibilité n'était pas exclusivement superficielle, et on a vu des rayons α plongeant dans l'émulsion sous des angles variables (figure 8*b*), rares sous incidence faible, nombreuses sous incidence très plongeante vu les angles solides d'irradiation. La densité Σ des trajectoires entrant par unité de surface varie avec x selon une loi sinusoïdale (pour un faisceau parallèle):

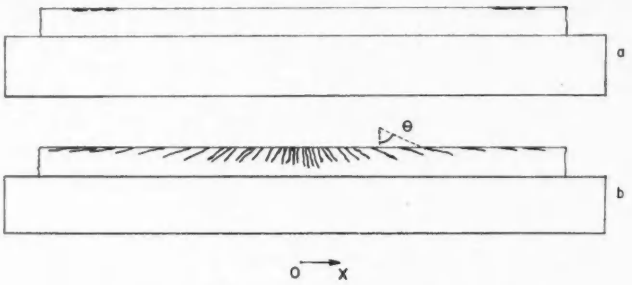

FIG. 8. Détecteur directionnel, distribution des trajectoires.

$$\Sigma = \Sigma_0 \cos 2\pi x/X,$$

$$\theta' = 2\pi x/X, \qquad \text{ctg } \theta' = (\text{ctg } \theta)/f.$$

Σ_0 est la densité pour l'incidence normale qui définit l'origine des coordonnées x, X est la circonférence; θ' et θ sont les angles avant et après l'irradiation, f le coefficient d'affaissement.

Dans cette expérience, nous avons remarqué la grande densité centrale des traces verticales ou très penchées. Cela nous a suggéré la possibilité de mesures angulaires sur les faisceaux de rayons α ou autres, utilisant les procédés photométriques appliqués à ces traces. Ces mesures pourraient se faire avec des émulsions ionographiques ordinaires à la gélatine, puisqu'elles n'exigent pas une sensibilité exclusivement superficielle. Ces possibilités sont actuellement à l'étude dans le laboratoire, avec l'aide de Ph. Colle et du photomètre rapide qu'il a réalisé.

Un autre moyen d'obtenir un détecteur sensible en surface seulement, serait de réaliser une couche très mince d'émulsion normale, épaisse de 0.5 μ, par exemple, sur un substrat suffisamment épais de gélatine.

CONCLUSION

Les résultats sur plusieurs points sont préliminaires et requièrent plus amples mesures et expériences. Ils se basent sur un petit nombre de lots de précipitation (une quinzaine). Il reste beaucoup à faire avant d'avoir déterminé les conditions optimum de sensibilité et le minimum de voile. Il faudra aussi accroître l'épaisseur des couches, qui n'ont jusqu'ici pas dépassé 50 μ d'épaisseur.

Cependant quelques résultats sont clairement acquis. On a pu réaliser un détecteur manifestant les trajectoires des rayons α et des protons dans un milieu solide nouveau, contenant les éléments HCOAgBr, dont les propriétés mécaniques, adhérence au verre, distorsion, solidité, résistance à l'humidité, sont très satisfaisantes.

BIBLIOGRAPHIE

DEMERS, P. 1958. Ionographie (Les Presses Universitaires de Montréal, Montréal, Qué).
DEMERS, P. et SCHWERIN, A. 1957*a*. Ann. Acfas, **23**.
——— 1957*b*. Sci. Ind. Phot. **28**, 151.
——— 1958*a*. Sci. Ind. Phot. **29**, 209.
——— 1958*b*. Phot. Corp. I, 145.
FUJII, E. 1952. Rapp. Inst. Rech. Chimie Ind. Gouv. Japon, **47**, 1.

THE EFFECT OF DEFORMATION ON THE INTERNAL FRICTION OF IRON MEASURED AT THE CARBON PEAK POSITION[1]

F. W. C. BOSWELL[2]

ABSTRACT

Experiments have been carried out to investigate the influence of deformation on the internal friction of iron measured at the carbon peak. As a result of deformation the internal friction increased and then decreased with time. These changes, corrected for a background change associated with the deformation, were shown to follow a time law predicted for carbon segregation to dislocations. It is concluded that the amount of carbon in random solid solution is increased by the deformation. By analyzing the rate of decrease of internal friction following deformation in terms of strain-aging theory the final dislocation densities were determined. The results also indicate that in some cases the carbon put into solution by the deformation was initially present in the form of iron carbide particles.

INTRODUCTION

Alpha iron will dissolve up to 0.02 wt.% carbon at the maximum solid solubility temperature of 726° C. This carbon can be retained in metastable solid solution by rapid cooling to room temperature. On aging at room temperature or slightly elevated temperatures some carbon will segregate along dislocation lines and the remainder will precipitate in the form of iron carbide particles. The presence of carbon in iron has a marked influence on the mechanical properties. In particular it can cause the yield point effect (Cottrell 1953) which has been extensively investigated (Hundy 1956) since it is of both theoretical and practical concern. By far the most successful theory to account for this yielding behavior of iron-containing carbon is that developed by Cottrell and Bilby (1949). This theory is based on the hypothesis that carbon atoms will segregate along dislocation lines due to the elastic strain interactions. Under stress, some of the dislocations may be torn free of their atmospheres leaving the carbon atoms in solution. When the stress is removed the carbon atoms will segregate to the glide dislocations. The rate at which this segregation occurs has been derived by Cottrell and Bilby (1949) and is given by the expression

$$N_t = 3\left(\frac{\pi}{2}\right)^{1/3} N_0 L \left(\frac{ADt}{kT}\right)^{2/3} \tag{1}$$

where N_t is the number of solute atoms per unit volume that have migrated to dislocations after time t, N_0 is the solute concentration at zero time, D is the diffusion coefficient of carbon at the absolute temperature T, A is a parameter depending on elastic constants, and L is the total length of edge

[1]Manuscript received July 15, 1959.
Contribution from the Physical Metallurgy Division, Department of Mines and Technical Surveys, Ottawa, Canada. This work (Internal Report PMM-59-5) was published by permission of the Director, Mines Branch, Department of Mines and Technical Surveys, Ottawa, Canada.
[2]Metal Physics Section, Physical Metallurgy Division, Mines Branch, Department of Mines and Technical Surveys, Ottawa, Canada.

dislocation per unit volume. Using an internal friction technique, Harper (1951) verified this expression for the early stages of carbon precipitation in deformed iron. He modified the expression to take into account the mutual interference of the developing atmospheres as the precipitation process progressed, and obtained

$$\ln(1-q) = -3\left(\frac{\pi}{2}\right)^{1/3} L\left(\frac{ADt}{kT}\right)^{2/3} \tag{2}$$

where q is the fraction of the original amount of solute that has precipitated after time t. This latter expression was shown to hold up to at least 90% of the total precipitation. Further experimental evidence in favor of the theory was put forward by Cottrell and Churchman (1949), who measured the change in electrical resistivity following the deformation of aged iron wires. From these experiments they were able to estimate the amount of interstitial solute segregating at the dislocations and in addition they showed that the activation energy of the process causing the resistivity changes was equal to that for interstitial diffusion.

Cottrell and Bilby (1949) estimated that it would require two carbon atoms per atom plane along the dislocation lines to relieve the elastic stresses. However, from the work of Harper (1951) and subsequent work by Dahl and Lucke (1954) and Thomas and Leak (1955) it appears that the $t^{2/3}$-aging law derived by Cottrell and Bilby (1949) is valid long after the dislocations should be saturated. It was suggested in the latter two papers and also by Bilby (1956) that nucleation and growth of a carbide phase may occur which would drain the dislocations of carbon atoms. Doremus (1958) has measured carbon precipitation rates at 120° C in deformed iron and concluded that the results may best be explained on the basis of diffusion-controlled growth of asymmetric particles with segregation by the Cottrell–Bilby mechanism possibly playing a minor role in the very early stages of the process.

The theory of Cottrell and Bilby (1949) has recently been extended by Ham (1959), who took into account diffusion currents due to concentration gradients in addition to the stress-induced drift considered by the earlier workers. He calculated the shape of the precipitation curve for carbon in alpha iron and his results show a significant disagreement with Harper's formula (2). However, Ham noted that Harper's formula is in better agreement with the experimentally determined precipitation curves and suggested that the actual precipitation process may be more complicated than is assumed in the model used. Thus the details of the precipitation process for carbon in iron are not yet clear and it would be desirable to have further experimental evidence relating to the amount of carbon segregated at dislocations after aging and the extent to which carbon is put into solution by deformation of aged specimens.

The height of the internal friction peak due to carbon in iron is a measure of the amount of carbon in random solid solution. It should therefore be possible to use this method to obtain a direct measure of any changes in the amount of carbon in solution following deformation of an aged iron specimen. Such experiments have been carried out by Kunz (1955) using single-crystal

iron wires and strains in the range 0–7%. He reported large increases in the damping after deformation, which he attributed to carbon atmospheres being put into random solution when the dislocations were torn free. If the dislocation density of the quenched and aged wires is taken to be 10^8 lines cm^{-2} or less, then the results of Kunz (1955) imply an extremely large number of carbon atoms segregated per atom plane along the dislocations. In his paper no analysis was made of the rate of carbon segregation subsequent to deformation. Attempts by Doremus (1958) to repeat these results were not successful and he noted only slight increases in internal friction after deforming aged specimens. The present paper describes similar experiments on polycrystalline iron in which the internal friction at the carbon peak position was measured as a function of time following deformation. The rate of decrease of the internal friction was analyzed in terms of the strain-aging theory of Cottrell and Bilby (1949), and the effect of dislocation density prior to aging was investigated.

EXPERIMENTAL DETAILS

The iron used in this investigation was Ferrovac-E* containing about 1.0×10^{-2} wt.% carbon and less than 1.0×10^{-3} wt.% nitrogen. This concentration of nitrogen was considered to have a negligible effect on the internal friction results and all measurements concerned the behavior of carbon. The wire was drawn to 0.030-in. diameter, cut to 12-in. lengths, and vacuum annealed. The average grain diameter was about 0.004 in. The internal friction, Q^{-1}, of the iron wires was measured using a conventional torsion pendulum of the type described by Kê (1948). Measurements were carried out at 40° C at a frequency of 1 c.p.s. in which case Q^{-1} (corrected for background damping) is linearly proportional to the weight per cent carbon in solution. We have taken the factor of proportionality to be 1.0 as reported by Dijkstra (1949), although more recent work by Lindstrand (1955) and Lagerberg and Wolff (1958) has indicated that the factor may be somewhat greater than 1.0 and is affected by grain size.

The wires were deformed by being drawn at a slow, steady rate through lubricated dies.

For some experiments carried out to examine changes in background damping due to deformation, it was necessary to have specimens free from carbon. These were produced by annealing Ferrovac-E iron in wet hydrogen at 720° C. This treatment reduced the carbon level to less than 3×10^{-4} wt.% as determined by internal friction.

EXPERIMENTAL RESULTS

Three aged wire specimens with different dislocation densities were prepared as follows: specimen I was quenched from 720° C and aged at 100° C without any deformation; specimens II and III were quenched, immediately deformed different amounts by drawing, and then aged at 100° C. The deformation introduced immediately after quenching will be referred to as the "initial

*Ferrovac-E is a vacuum melted electrolytic iron obtained from the Vacuum Metals Corporation Division of the Crucible Steel Company of America.

deformation". Aging times at 100° C were such that no further changes were occurring in the internal friction. The history of these specimens is summarized in Table I. It should be noted that the values of the internal friction after aging include the background damping, which is about 6×10^{-4}. Thus the carbon remaining in random solution after aging was less than 3×10^{-4} wt. % in each case.

TABLE I

Specimen histories

Specimen No.	Initial deformation, % reduction in area	Aging time at 100° C, hours	Final Q^{-1} (including background)
I	0	425	8.7×10^{-4}
II	6	445	8.2×10^{-4}
III	28	593	8.7×10^{-4}

Each of the specimens was next deformed a further 10% reduction in area (referred to as the "final deformation") and the internal friction was measured at 40° C as a function of time. The first measurements were made about 10 minutes after drawing was completed, this being the time required to insert the wire in the internal friction apparatus and make necessary adjustments. For each specimen it was found that Q^{-1} had increased after the final deformation and subsequently decreased with time. Figure 1 shows these results with Q^{-1} plotted versus time. No background correction has been applied to the

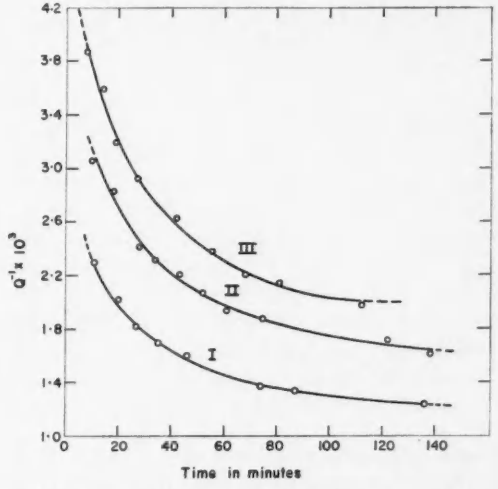

FIG. 1. Internal friction at 40° C plotted against time measured after a final deformation of 10% reduction in area. Previous histories: I quenched and aged; II quenched, 6% R.A., aged; III quenched, 28% R.A., aged.

values of Q^{-1} plotted in this graph. The observed increase in damping could arise from the following two sources:

(*a*) A general increase in damping level associated with imperfections introduced into the lattice by the deformation.

(*b*) Any carbon put into random solid solution by the deformation will give rise to an internal friction peak at the frequency and temperature at which the measurements were made.

It is probable that the observed damping is made up of contributions arising from both (*a*) and (*b*).

It has been reported by Kê (1948) and Kōster, Bangert, and Hahn (1954) that plastic deformation changes the background damping of iron in the frequency range around 1 c.p.s. To determine the magnitude of the background changes, three specimens of decarburized iron were used. These were treated in the same manner as the specimens listed in Table I. After aging to equilibrium at 100° C these wires were deformed by a 10% reduction in area and the internal friction measured at 40° C. In each case Q^{-1} increased after deformation and decreased at a very slow rate of aging at 40° C (about 4% decrease in 10 hours). Thus the background introduced by deformation may be considered constant over a period of 2 hours. The results of this experiment are given in Table II.

TABLE II

Internal friction of decarburized specimens after deformation

Specimen No.	Deformation treatment, % reduction in area	Q^{-1} after deformation
I(*a*)	0+10	1.25×10^{-3}
II(*a*)	7+10	1.50×10^{-3}
III(*a*)	29+10	2.10×10^{-3}

In the case of these decarburized wires the increase in internal friction due to deformation is much greater than could be caused by carbon re-solution and is almost entirely due to a general background increase associated with the lattice damage. The appropriate values of the background damping from Table II were subtracted from the Q^{-1} values of Fig. 1 to give Q_t, the internal friction due to carbon in solution at time t after deformation. These values are numerically equal to C_t, the wt.% of carbon in solution. If C_0 represents the amount of carbon in solution immediately after deformation, then the fraction of the carbon atoms remaining in solution at time t is C_t/C_0 and we may write equation (2) in the form

$$\ln C_t = \ln C_0 - 3\left(\frac{\pi}{2}\right)^{1/3} L\left(\frac{ADt}{kT}\right)^{2/3}. \tag{3}$$

For each of specimens I, II, and III a plot of $\log_{10} C_t$ versus $t^{2/3}$ has been made and a reasonable straight line obtained in each case. The data for specimen I are plotted in Fig. 2 as a typical example. From these plots values of C_0 have been determined by extrapolation and the dislocation densities, L, calculated.

Once C_0 has been found, q, the fraction of C_0 precipitated after time t, may be calculated and the variation of q is shown on the right-hand scale of Fig. 2. In the calculations of L the value taken for the constant A was that used by Thomas and Leak (1955), viz., $A = 1.4\times10^{-20}$ dyne cm^2. The value D was

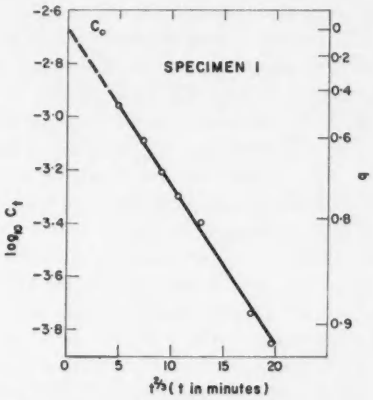

FIG. 2. Variation of carbon in solution following deformation, C_t (log scale), versus $t^{2/3}$. Measurements made at 40° C. The fraction of C_0 precipitated, q, after various times is shown on the right-hand scale.

taken from the equation given by Thomas and Leak (1955). The uncertainty in the constants of equation (3) is such that the resultant values of L are only considered good to an order of magnitude. The results of these calculations for the three specimens are listed in Table III.

TABLE III

Carbon in solution and dislocation densities after deformation

Specimen No.	Deformation treatment, % reduction in area	C_0, wt.%	Dislocation density, L, lines cm^{-2}
I	0+10	2.1×10^{-3}	1.4×10^{12}
II	6+10	2.8×10^{-3}	1.2×10^{12}
III	28+10	3.3×10^{-3}	1.6×10^{12}

DISCUSSION

In this work it was not possible to obtain internal friction versus temperature curves for the aged and deformed specimens on account of the very rapid decay in the damping at 40° C. Thus there is no direct justification for the procedure used above for the determination of the amount of carbon in random solution after deformation. The background changes observed in carbon-free iron (Table II), which were used to correct the measurements on carbon-containing specimens, are in reasonable agreement with background changes reported by Kōster, Bangert, and Hahn (1954) for iron deformed immediately after quenching. However, the effect of the presence of carbide particles is not known.

An alternative possible interpretation of the results would be that the entire change in the internal friction after deformation of aged specimens was a result of some mechanism associated with lattice damage and that subsequent migration of carbon atoms caused a decrease in the damping with time. The interpretation of the internal friction changes in terms of carbon in solution appears more plausible in view of the fact that these changes give a good fit to a time law of equation (2) and it has been established by Harper (1951) that this equation is closely followed for precipitation of carbon in quenched and deformed iron at temperatures around 40° C. Further, when the results are treated on this basis the values obtained for C_0, the amount of carbon put into random solution by the deformation, and the dislocation density are of reasonable magnitudes. The dislocation densities listed in Table III may be compared with a value of 2.5×10^{11} lines per cm^2 reported by Harper (1951) for an iron wire deformed 10% in tension. It may also be noted that Cottrell and Churchman (1949) measured resistivity changes in aged iron following deformation and they showed that the magnitude of the observed changes was compatible with carbon (and nitrogen) being put into solution by the deformation and subsequently migrating to the dislocations.

A striking feature of the results is that 2.1×10^{-3} wt.% carbon was put into solution during deformation of specimen I which had been simply quenched and aged. The dislocation density after aging would not have been more than 10^8 lines per cm^2 and it would require only 2×10^{-6} wt.% carbon to provide two carbon atoms per atom plane along these dislocations. Thus the deformation caused precipitate particles to dissolve. A possible explanation of this behavior is that subcritical precipitate particles are formed along the dislocation lines and that these particles redissolve when the dislocations are removed by straining. This type of behavior was suggested by Bilby (1956). An alternative possibility is that the passage of glide dislocations past the precipitate particles caused partial solution to occur. In specimens II and III there was an increase with initial deformation in the amount of carbon put into solution by the final deformation. This increase is probably associated with a progressively greater degree of dispersion of carbide particles in these specimens.

CONCLUSIONS

1. An increase in the internal friction measured at the carbon peak temperature is observed immediately following deformation of aged iron specimens containing carbon.

2. The increase due to carbon in solution decays with time according to the strain-aging theory of Cottrell and Bilby (1949) as modified by Harper (1951).

3. In the case of an aged iron specimen with relatively low dislocation density it is clear that the carbon put into solution by the deformation must have been present as carbide particles.

4. The dislocation density in an iron wire reduced 10% in area by drawing through a die is 1.4 times that reported by Harper (1951) for a wire extended 10% in tension.

REFERENCES

BILBY, B. A. 1956. J. Iron Steel Inst. (London), **184**, 65.
COTTRELL, A. H. 1953. Dislocations and plastic flow in crystals (Oxford University Press, London).
COTTRELL, A. H. and BILBY, B. A. 1949. Proc. Phys. Soc. (London), A, **62**, 49.
COTTRELL, A. H. and CHURCHMAN, A. T. 1949. J. Iron Steel Inst. (London), **162**, 271.
DAHL, VON W. and LUCKE, K. 1954. Arch. Eisenhüttenw. **25**, 241.
DIJKSTRA, L. J. 1949. Trans. Am. Inst. Mining Met. Engrs. **185**, 252.
DOREMUS, R. H. 1958. Acta Met. **6**, 674.
HAM, F. S. 1959. J. Appl. Phys. **30** (6), 915.
HARPER, S. 1951. Phys. Rev. **83**, 709.
HUNDY, B. B. 1956. Metallurgia, **3**, 202.
KÊ, T. S. 1948. Trans. Am. Inst. Mining Met. Engrs. **176**, 448.
KÖSTER, VON W., BANGERT, L., and HAHN, R. 1954. Arch. Eisenhüttenw. **25**, 569.
KUNZ, F. W. 1955. Acta Met. **3**, 126.
LAGERBERG, G. and WOLFF, E. G. 1958. Acta Met. **6**, 136.
LINDSTRAND, E. 1955. Acta Met. **3**, 431.
THOMAS, W. R. and LEAK, G. M. 1954. Phil. Mag. **45**, 986.
——— 1955. J. Iron Steel Inst. (London), **180**, 155.

MULTILAYER PROBLEMS IN THE MULTIGROUP SPHERICAL HARMONICS METHOD[1]

B. DAVISON

ABSTRACT

In applying the spherical harmonics method to multilayer neutron transport problems it is necessary to invert certain matrices. It is already known that in the case of one-group theory for the problems with plane, spherical, or cylindrical symmetry, these inverse matrices can easily be written down explicitly, so that there is no need for numerical matrix inversion. In the present paper this result is extended to the case of multigroup theory.

1. INTRODUCTION

In the present paper we are concerned with neutron transport problems in multigroup theory for multilayer systems with plane, spherical, or cylindrical symmetry, and, in particular, with the application of the spherical harmonics method to such systems. By multigroup theory we mean the treatment in which the entire range of neutron energies is subdivided into a finite number of intervals, called energy groups. We assume that within each energy group the cross sections for each medium are constant, and we ascribe definite probabilities for the transfer of a neutron, on collision, from one group to another.

In applying the spherical harmonics method to multilayer problems an important part of the calculations, which, unless properly handled can be most time-consuming, is the determination of the constants of integration for one layer in terms of those for the preceding layer. What is involved is expressing the constants of integrations in terms of the spherical harmonics moments, that is the inversion of the matrix which gives the spherical harmonics moments in terms of the constants of integration. In principle this inversion of the matrix can always be done numerically. The matrix in question is, however, of order $(N+1)S$ in the cases of plane and of spherical symmetry, and of order $\frac{1}{4}(N+1)(N+3)S$ in the case of cylindrical symmetry, where N is the order of approximation and S is the number of energy groups, so that with increasing order of approximation and/or of the number of groups, the numerical inversion of this matrix soon becomes prohibitively laborious. However, it is now known (Davison 1957*a* and *b*) that in the case of one-group theory ($S = 1$) the numerical inversion of the matrix in question is not necessary since, owing to some orthogonality properties of the functions involved, the inverse matrix can easily be written down in a closed form. The purpose of the present paper is to establish the corresponding result for the case of multigroup theory. In what follows we shall refer to the formula giving the

[1]Manuscript received August 28, 1959.
Contribution from the Computation Centre, Department of Physics, University of Toronto, Toronto, Ontario, and Atomic Energy of Canada Limited, Chalk River, Ontario.
Issued as A.E.C.L. No. 915.

elements of the inverse matrix, i.e. giving the constants of integration in terms of the spherical harmonics moments, simply as the "inversion formula".

In Section 2 we deal with the plane case; we review first the basic formulae of the spherical harmonics method in the multigroup theory for this case, then introduce certain auxiliary quantities, and produce the required inversion formula. The cases of spherical and of cylindrical symmetry are similarly dealt with in Sections 3 and 4 respectively.

It will be assumed throughout the analysis given below, that the scattering is isotropic in the laboratory system of co-ordinates.

The order of approximation, N, will be assumed as usual, to be odd.

2. PLANE CASE

2.1 General Outline of the Multigroup Spherical Harmonics Method

The general transport (Boltzmann) equation in the multigroup theory for scattering isotropic in the laboratory system is (see, for example, Davison 1957*c*)

$$(2.1)\qquad \boldsymbol{\Omega}\cdot\operatorname{grad}\psi^{(j)}(\mathbf{r},\boldsymbol{\Omega})+\frac{1}{l_j}\psi^{(j)}(\mathbf{r},\boldsymbol{\Omega})=\frac{1}{4\pi}\sum_i\frac{c_{i\to j}}{l_i}\int\int\psi^{(i)}(\mathbf{r},\boldsymbol{\Omega}')d\Omega'.$$

Here $\mathbf{r}$ is the position vector, $\boldsymbol{\Omega}$ is the unit vector in the direction of neutron travel, $\psi^{(j)}(\mathbf{r},\boldsymbol{\Omega})$ is the distribution in position and direction of the flux of neutrons of the jth group (i.e. of the jth energy interval), l_j is the total mean free path for the neutrons of that group, and $c_{i\to j}$ is the probable number of neutrons of jth group emerging from a collision of a neutron of ith group.

In the case of plane symmetry $\psi^{(j)}(\mathbf{r},\boldsymbol{\Omega})$ will depend only upon one Cartesian position co-ordinate, x, say, and the corresponding component of the direction vector $\Omega_x=\mu$, say, i.e. $\psi^{(j)}(\mathbf{r},\boldsymbol{\Omega})=\psi^{(j)}(x,\mu)$ and the first term in (2.1) reduces to $\mu\,\partial\psi^{(j)}(x,\mu)/\partial x$. In the P_N approximation, one expands $\psi^{(j)}(\mathbf{r},\boldsymbol{\Omega})$ in terms of the spherical harmonics in $\boldsymbol{\Omega}$, terminating the expansion after order N. Thus in the plane case one puts

$$(2.2)\qquad \psi^{(j)}(x,\mu)\cong\frac{1}{4\pi}\sum_{n=0}^{N}(2n+1)P_n(\mu)\psi_n{}^{(j)}(x),$$

where $P_n(\mu)$ are the Legendre polynomials, and substitutes this into equation (2.1). This gives the following system of equations for the spherical harmonics moments $\psi_n{}^{(j)}(x)$

$$(2.3)\qquad (n+1)\frac{d\psi_{n+1}^{(j)}(x)}{dx}+n\frac{d\psi_{n-1}^{(j)}(x)}{dr}+\frac{2n+1}{l_j}\psi_n^{(j)}(x)=\delta_{0n}\sum_i\frac{c_{i\to j}}{l_i}\psi_0^{(i)}(x)$$

where δ_{0n} is the Kronecker symbol: $\delta_{ij}=1$ if $i=j$, and is zero if otherwise.

The fact that the series (2.2) has been terminated after $n=N$ implies that (2.3) should be satisfied for $n\leqslant N$ only, but at the same time, supplemented by the conditions:

$$(2.4)\qquad \psi_{N+1}^{(j)}(x)=0 \qquad (\text{all } j).$$

To get a particular solution of (2.3) put

$$(2.5)\qquad \psi_n^{(j)}(x)=g_n^{(j)}e^{\kappa x}$$

where κ and the $g_n^{(j)}$ are some constants. Equations (2.3) and (2.4) then give

$$(n+1)g_{n+1}^{(j)}+ng_{n-1}^{(j)}+\frac{2n+1}{\kappa l_j}g_n^{(j)} = \delta_{0n}\sum_i \frac{c_{i\to j}}{\kappa l_i}g_0^{(i)} \tag{2.6}$$

and

$$g_{N+1}^{(j)} = 0 \qquad \text{(all } j\text{)}. \tag{2.7}$$

Now the recurrence formulae for the Legendre polynomials and for the Legendre functions Q_n of the second kind (Whittaker and Watson 1950) show that (2.6) will be satisfied if we take

$$g_n^{(j)} = \beta^{(j)}P_n\left(\frac{-1}{\kappa l_j}\right)+\left[Q_0\left(\frac{-1}{\kappa l_j}\right)P_n\left(\frac{-1}{\kappa l_j}\right)-Q_n\left(\frac{-1}{\kappa l_j}\right)\right]\cdot\sum_i \frac{\beta^{(i)}c_{i\to j}}{\kappa l_i} \tag{2.8}$$

where the $\beta^{(j)}$ are some further constants. By substituting (2.8) into (2.7) one obtains the system of linear homogeneous equations for determining these latter constants. In order that this system should have a solution, its determinant must vanish, i.e.

$$\text{Det.}\left[\left\{\left[Q_0\left(\frac{-1}{\kappa l_j}\right)P_{N+1}\left(\frac{-1}{\kappa l_j}\right)-Q_{N+1}\left(\frac{-1}{\kappa l_j}\right)\right]\frac{c_{i\to j}}{\kappa l_i}+\delta_{ij}P_{N+1}\left(\frac{-1}{\kappa l_i}\right)\right\}\right] = 0, \tag{2.9}$$

which gives us the equation for determining the permissible values of κ in (2.5). Notice that while $Q_n(z)$ is not a polynomial, $[Q_0(z)P_n(z)-Q_n(z)]$ is a polynomial in z of order $(n-1)$. So that (2.9) is a polynomial equation of the order $(N+1)S$, where S is the number of groups. Consequently there are $(N+1)S$ permissible values of κ. It can be also shown that if N is odd (as we have assumed it to be) and unless various $c_{i\to j}$ and l_i/l_j satisfy a certain equation (which in general they will not) all the roots of (2.9) will be distinct. Accordingly, and for the sake of simplicity, we shall assume henceforth that these roots are all different.

Notice next that for odd N each element in the determinant (2.9) is an even function of κ, and consequently the roots of (2.9) will come in pairs: if $\kappa = \kappa_s$ is a root, so is $\kappa = -\kappa_s$. We shall label these roots in accordance with the convention

$$\kappa_{-s} = -\kappa_s \tag{2.10}$$

and shall denote by $\beta_s^{(j)}$ and $g_n^{(j;s)}$ the values of $\beta^{(j)}$ and $g_n^{(j)}$ corresponding to a particular root $\kappa = \kappa_s$ of (2.9). In this notation the general solution of the system of equations (2.3) and (2.4) is then given by

$$\psi_n^{(j)}(x) = \sum_{s=\pm 1}^{\pm\frac{1}{2}(N+1)S} A_s g_n^{(j;s)}\, e^{\kappa_s x} \tag{2.11}$$

where the A_s are the constants of integration, referred to in the introduction and determined by the boundary conditions

$$\psi_n^{(j)}(x) \quad \text{continuous} \tag{2.12}$$

at an interface between any two adjacent layers.

It may be noted also that in view of the symmetry properties of $P_n(z)$ and of $[Q_0(z)P_n(z)-Q_n(z)]$, and with our labelling convention (2.10) we shall have

$$\beta_{-s}^{(j)} = \beta_s^{(j)}; \qquad g_n^{(j;-s)} = (-1)^n g_n^{(j;s)}. \tag{2.13}$$

2.2 The Adjoint Quantities and a Biorthogonality Condition. The Inversion Formula

Our purpose now is to supplement the formula (2.11) by the inverse one, giving the A_s in terms of the $\psi_n^{(j)}(x)$. In the case of the one-group theory (Davison 1957*a*) this was achieved by establishing a certain orthogonality relationship between the $g_n|_{\kappa=\kappa_s}(G_n(\nu_j)$ in the notations of that reference). In our present case of multigroup theory, instead of an orthogonality relationship, we shall need a biorthogonality relationship between the $g_n^{(j;s)}$ and certain adjoint quantities. To introduce these latter we consider now, simultaneously with the $g_n^{(j;s)}$, the set of constants $\hat{g}_n^{(j)}$, say, defined by the equations

$$(n+1)\hat{g}_{n+1}^{(j)}+n\hat{g}_{n-1}^{(j)}+\frac{2n+1}{\kappa l_j}\hat{g}_n^{(j)} = \delta_{0n}\sum_i \frac{c_{j\to i}l_i}{\kappa l_j^2}\hat{g}_0^{(i)} \tag{2.14}$$

and

$$\hat{g}_{N+1}^{(j)} = 0. \tag{2.15}$$

(Notice that if equations (2.6) and (2.14) are multiplied through by κl_j and rewritten in matrix notation, the resulting form of (2.14) differs from that of (2.6) only by the fact that the matrix appearing on the right-hand side is transposed. In this sense the $\hat{g}_n^{(j)}$ can be considered as adjoint to the $g_n^{(j)}$.)

Now similarly to (2.8), one can readily verify that (2.14) will be satisfied if we put

$$\hat{g}_n^{(j)} = \hat{\beta}^{(j)}P_n\left(\frac{-1}{\kappa l_j}\right)+\left[Q_0\left(\frac{-1}{\kappa l_j}\right)P_n\left(\frac{-1}{\kappa l_j}\right)\right]-\left[Q_n\left(\frac{-1}{\kappa l_j}\right)\right]\sum_i \frac{\hat{\beta}^{(i)}c_{j\to i}l_i}{\kappa l_j^2}. \tag{2.16}$$

By substituting (2.16) into (2.15) we obtain a system of equations for the determination of the constants $\hat{\beta}^{(j)}$; and the condition for solvability of these latter equations is

$$\text{Det.}\left(\left\{\left[Q_0\left(\frac{-1}{\kappa l_j}\right)P_{N+1}\left(\frac{-1}{\kappa l_j}\right)-Q_{N+1}\left(\frac{-1}{\kappa l_j}\right)\right]\frac{c_{j\to i}l_i}{\kappa l_j^2}+\delta_{ij}P_{N+1}\left(\frac{-1}{\kappa l_j}\right)\right\}\right)=0. \tag{2.17}$$

After some slight manipulation, and bearing in mind that transposing a matrix does not affect the value of its determinant, one can readily show that the left-hand side of (2.17) is identical with that of (2.9). Consequently the κ values, for which (2.14) and (2.15) have a solution, are identical with those for which (2.6) and (2.7) have a solution, i.e. with our κ_s ($s = \pm 1, \ldots \pm\frac{1}{2}(N+1)S$). We shall denote by $\hat{g}_n^{(j;s)}$ and $\hat{\beta}_s^{(j)}$ the values of $\hat{g}_n^{(j)}$ and $\hat{\beta}^{(j)}$ corresponding to $\kappa = \kappa_s$, and note that similarly to (2.13)

$$\hat{\beta}_{-s}^{(j)} = \hat{\beta}_s^{(j)}; \qquad \hat{g}_n^{(j;-s)} = (-1)^n\hat{g}_n^{(j;s)}. \tag{2.18}$$

We now proceed to show that the quantities $g_n^{(j;s)}$ and $\hat{g}_n^{(j;s)}$ are connected by a set of biorthogonality relationships. Consider for this purpose the quantity

$$R_{n+1} = (n+1) \sum_j l_j [\hat{g}_{n+1}^{(j;t)} g_n^{(j;s)} - g_{n+1}^{(j;s)} \hat{g}_n^{(j;t)}]. \tag{2.19}$$

Substituting here for $\hat{g}_{n+1}^{(j;t)}$ and $g_{n+1}^{(j;s)}$ from (2.14) and (2.6), respectively, we get

$$R_{n+1} = R_n + \left(\frac{1}{\kappa_s} - \frac{1}{\kappa_t}\right)\left\{(2n+1) \sum_j g_n^{(j;s)} \hat{g}_n^{(j;t)} - \delta_{0n} \sum_j \sum_i c_{i \leftrightarrow j} \frac{l_j}{l_i} g_0^{(i;s)} \hat{g}_0^{(j;t)}\right\}. \tag{2.20}$$

Now the definition (2.19) implies $R_0 = 0$, while (2.7) and (2.15) show that $R_{N+1} = 0$, so that by repeated application of (2.20) we obtain

$$\left(\frac{1}{\kappa_s} - \frac{1}{\kappa_t}\right)\left\{\sum_{n=0}^{N} \sum_j (2n+1) g_n^{(j;s)} \hat{g}_n^{(j;t)} - \sum_j \sum_i c_{i \leftrightarrow j} \frac{l_j}{l_i} g_0^{(i;s)} \hat{g}_0^{(j;t)}\right\} = 0. \tag{2.21}$$

Thus unless $\kappa_s = \kappa_t$, i.e. unless $s = t$, since the roots of (2.9) have been assumed to be distinct, the quantity in braces in (2.21) should vanish. In other words

$$\sum_{n=0}^{N} \sum_j (2n+1) g_n^{(j;s)} \hat{g}_n^{(j;t)} - \sum_j \sum_i c_{i \leftrightarrow j} \frac{l_j}{l_i} g_0^{(i;s)} \hat{g}_0^{(j;t)} = \delta_{s,t} X_s \tag{2.22}$$

where X_s is a certain constant. It is shown in the appendix that (at least in the case when $c_{i \leftrightarrow j}$ and l_i/l_j are such that (2.9) has no multiple roots) this constant does not vanish, so that we may divide (2.22) through by X_s. By comparing the resulting identity with (2.11) one can readily see that

$$A_s = \frac{1}{X_s} e^{-\kappa_s z} \sum_{n=0}^{N} \sum_j \psi_n^{(j)}(x) \left[(2n+1) \hat{g}_n^{(j;s)} - \delta_{0n} \sum_i c_{j \leftrightarrow i} \frac{l_i}{l_j} \hat{g}_0^{(i;s)}\right], \tag{2.23}$$

which is the required "inversion formula". Alternatively, using (2.14), it may be rewritten as

$$A_s = -\frac{\kappa_s}{X_s} e^{-\kappa_s z} \sum_{n=0}^{N} \sum_j \psi_n^{(j)}(x) l_j [(n+1) \hat{g}_{n+1}^{(j;s)} + n \hat{g}_{n-1}^{(j;s)}]. \tag{2.24}$$

2.3 The Normalization Constant

It remains to evaluate the constant X_s, whose inverse, $(1/X_s)$, may be referred to, in view of (2.23), as the normalization constant. In principle it could be calculated directly from (2.22). There is, however, an alternative and more convenient expression. To derive this latter, consider two adjacent media, taking their interface for the $x = 0$ plane, denoting by $c_{i \leftrightarrow j}'$, κ_s', A_s', etc. the values of $c_{i \leftrightarrow j}$, κ_s, A_s etc. for the first medium, and by $c_{i \leftrightarrow j}''$, κ_s'', A_s'', etc. their values for the second medium, and suppose the two media differ only in the values of the $c_{i \leftrightarrow j}$ while the total mean free path for each energy group is the same for both media ($l_j'' = l_j' = l_j$). Let the roots of the determinantal equation (2.9) be labelled for both media in accordance with the

same convention (so that, if $c_{i\to j}''$ should tend to $c_{i\to j}'$ for all i and j, κ_s'' will tend to κ_s', rather than to some κ_t' with $t \neq s$), and consider the quantity

$$(2.25) \qquad (n+1)\sum_j l_j[\hat{g}_{n+1}''^{(j;i)} g_n'^{(j;s)} - g_{n+1}'^{(j;s)} \hat{g}_n''^{(j;i)}].$$

This is closely analogous to the quantity (2.19). By evaluating (2.25) much in the same way as we previously evaluated (2.19) we get, as a generalization of (2.21), the relationship

$$(2.26) \qquad \left(\frac{1}{\kappa_s'} - \frac{1}{\kappa_t''}\right) \sum_{n=0}^{N} \sum_j (2n+1)\hat{g}_n''^{(j;i)} g_n'^{(j;s)} - \sum_i \sum_j \frac{l_j}{l_i} \hat{g}_0''^{(j;i)} g_0'^{(i;s)} \left(\frac{c'_{i\to j}}{\kappa_s'} - \frac{c''_{i\to j}}{\kappa_t''}\right) = 0.$$

On the other hand, if we express the values of $\psi_n^{(j)}(x)$ at the interface ($x = 0$), by means of (2.11), in terms of the constants of integration for the first medium, A_s', if we recall the boundary conditions (2.12), and if we substitute the resulting values of $\psi_n^j(0)$ into (2.23) to determine the constants of integration for the second medium, A_s'', then, on using (2.26) to simplify the results, we obtain

$$(2.27) \qquad X_s'' A_s'' = -\kappa_s'' \sum_i A_i' \sum_j \frac{l_j}{l_i} \hat{\beta}_s''^{(j)} \beta_i'^{(i)} \frac{c''_{i\to j} - c'_{i\to j}}{\kappa_s'' - \kappa_i'}$$

(notice that $g_0'^{(i;i)} = \beta_i'^{(i)}$, etc.).

Now, if we pass to the limit with $c_{i\to j}''$ tending to $c_{i\to j}'$ for all i and j, then in this limit the properties of medium II become identical with those of medium I, $x = 0$ is no longer an interface, and A_s'' should therefore be equal to A_s'. The formula (2.27) then gives

$$(2.28) \qquad X_s' = -\kappa_s' \lim_{\substack{c_{i\to j}'' \to c_{i\to j}' \\ \text{(all } i \text{ and } j\text{)}}} \sum_i \sum_j \frac{l_j}{l_i} \hat{\beta}_s''^{(j)} \hat{\beta}_s'^{(i)} \frac{c''_{i\to j} - c'_{i\to j}}{\kappa_s'' - \kappa_s'}.$$

The double summation under the sign of limit can be eliminated if we make use of the equations defining $\beta_s'^{(j)}$ and $\hat{\beta}_s''^{(j)}$ (i.e. the equations resulting from substituting (2.8) into (2.7) and (2.16) into (2.15); after this the passage to the limit becomes straightforward, and suppressing the dashes we finally have

$$(2.29) \qquad X_s = \sum_j \beta_s^{(j)} \hat{\beta}_s^{(j)} \left\{ \mu \frac{d}{d\mu} \left[\frac{(1/\mu)P_{N+1}(\mu)}{Q_0(\mu)P_{N+1}(\mu) - Q_{N+1}(\mu)} \right] \right\} \Bigg|_{\mu = -(1/\kappa_s l_j)}.$$

3. THE CASE OF SPHERICAL SYMMETRY

3.1 The Expressions for the Spherical Harmonics Moments

We turn now to the case of spherically symmetrical systems. In this case $\psi^{(j)}(\mathbf{r},\boldsymbol{\Omega})$ will depend on the radial spherical co-ordinate, $r = |\mathbf{r}|$, and the cosine, μ, of the angle between the direction of the neutron travel and the direction in which r is measured, i.e.

$$\mu = \boldsymbol{\Omega} \cdot \mathbf{r}/r$$

and $\psi^{(j)}(\mathbf{r},\boldsymbol{\Omega}) = \psi^{(j)}(r,\mu)$. It is known (Davison 1957*c*) that in this presentation we have

$$\boldsymbol{\Omega}\cdot\text{grad}\,\psi^{(j)}(\mathbf{r},\boldsymbol{\Omega}) = \mu\frac{\partial\psi^{(j)}(r,\mu)}{\partial r}+\frac{(1-\mu^2)}{r}\frac{\partial\psi^{(j)}(r,\mu)}{\partial\mu}.$$

Substituting this into (2.1) and using again the expression (2.2) we get now, instead of (2.3), the equations

$$(3.1)\quad (n+1)\left[\frac{d}{dr}+\frac{(n+2)}{r}\right]\psi_{n+1}^{(j)}(r)+n\left[\frac{d}{dr}-\frac{(n-1)}{r}\right]\psi_{n-1}{}^{(j)}(r) +\frac{2n+1}{l_j}\psi_n^{(j)}(r) = \delta_{0n}\sum_i\frac{c_{i\to j}}{l_i}\psi_0^{(i)}(r).$$

These, of course, should again be supplemented by (2.4). One can readily verify, using the known recurrence relations for the Bessel functions, that a particular solution of (3.1) is given by

$$\psi_n^{(j)}(r) = g_n^{(j)}\sqrt{\frac{-2\kappa}{\pi r}}K_{n+\frac{1}{2}}(-\kappa r)$$

where $K_m(z)$ is the modified Bessel function of the second kind, of which we use the Macdonald definition

$$(3.2)\qquad K_m(z) = \tfrac{1}{2}\pi\{I_{-m}(z)-I_m(z)\}\text{cosec}\,m\pi,$$

while the $g_n{}^{(j)}$ must satisfy the same equation (2.6) as in the plane case. The last stipulation, and the fact that we use the same supplementary equation (2.4) as in the plane case, imply that the permissible values of κ, and the corresponding values of $g_n{}^{(j)}$, should in themselves be the same as in the plane case. Thus the general solution of the system of equations (3.1) and (2.4) is given by

$$(3.3)\qquad \psi_n^{(j)}(r) = \sum_{s=\pm 1}^{\pm\frac{1}{2}(N+1)S} A_s g_n^{(j;s)}\sqrt{\frac{-2\kappa_s}{\pi r}}K_{n+\frac{1}{2}}(-\kappa_s r)$$

where the A_s are again the constants of integration.

3.2 The Inversion Formula

Our purpose now is to supplement the formula (3.3) by the inverse one, giving the A_s in terms of the $\psi_n{}^{(j)}(r)$. The analogy with the formula (2.24) above, and with the available results for the case of one-group theory (Davison 1957*a*) suggests that we consider for this purpose the quantity

$$(3.4)\quad \sqrt{\frac{2\kappa_s}{\pi r}}\sum_{n=0}^{N}\sum_j l_j\psi_n^{(j)}(r)[(n+1)\hat{g}_{n+1}^{(j;s)}K_{n+3/2}(\kappa_s r)+n\hat{g}_{n-1}^{(j;s)}K_{n-\frac{1}{2}}(\kappa_s r)]$$

or, on substituting for $\psi_n{}^{(j)}(r)$ from (3.3), singling out the coefficient accompanying A_t, say, and omitting the common factor, the quantity

$$(3.5)\quad \sum_{n=0}^{N}\sum_j l_j g_n^{(j;t)}K_{n+\frac{1}{2}}(-\kappa_t r)[(n+1)\hat{g}_{n+1}^{(j;s)}K_{n+3/2}(\kappa_s r)+n\hat{g}_{n-1}^{(j;s)}K_{n-\frac{1}{2}}(\kappa_s r)]$$

where the $\hat{g}_n{}^{(j;s)}$ have the same meaning as in Section 2.

On the other hand, using (2.6), (2.14) and the known recurrence formulae for the Bessel functions one can easily verify the identity:

$$\sum_j l_j \Big\{ g_n^{(j;t)} K_{m-1}(\kappa_s r)[(n+1)\hat{g}_{n+1}^{(j;s)} + n\hat{g}_{n-1}^{(j;s)}][K_m(-\kappa_t r) - K_{m-2}(-\kappa_t r)] + \hat{g}_n^{(j;s)} K_{m-1}(-\kappa_t r)[(n+1)g_{n+1}^{(j;t)} + n g_{n-1}^{(j;t)}][K_m(\kappa_s r) - K_{m-2}(\kappa_s r)] \Big\} = 0. \tag{3.6}$$

Consider now the evaluation of the quantity (3.5) in detail, bearing in mind (2.7) and (2.15). The highest-order Bessel functions appearing in (3.5) are $K_{N+\frac{1}{2}}(\kappa_s r)$ and $K_{N+\frac{1}{2}}(-\kappa_t r)$. The terms containing these may be rewritten as

$$K_{N+\frac{1}{2}}(-\kappa_t r) K_{N-\frac{1}{2}}(\kappa_s r) \sum_j l_j g_N^{(j;t)}[(N+1)\hat{g}_{N+1}^{(j;s)} + N\hat{g}_{N-1}^{(j;s)}] + K_{N+\frac{1}{2}}(\kappa_s r) K_{N-\frac{1}{2}}(-\kappa_t r) \sum_j l_j \hat{g}_N^{(j;s)}[(N+1)g_{N+1}^{(j;t)} + N g_{N-1}^{(j;t)}]$$

and the identity (3.6) shows that the value of this expression will remain unaltered if we replace $K_{N+\frac{1}{2}}(-\kappa_t r)$ and $K_{N+\frac{1}{2}}(\kappa_s r)$ by $K_{N-3/2}(-\kappa_t r)$ and $K_{N-3/2}(\kappa_s r)$ respectively. After this replacement the highest-order Bessel functions appearing in our expression are $K_{N-\frac{1}{2}}(-\kappa_t r)$ and $K_{N-\frac{1}{2}}(\kappa_s r)$, and the terms involving these are

$$K_{N-\frac{1}{2}}(-\kappa_t r) K_{N-3/2}(\kappa_s r) \sum_j l_j g_{N-1}^{(j;t)}[N\hat{g}_N^{(j;s)} + (N-1)\hat{g}_{N-2}^{(j;s)}] + K_{N-\frac{1}{2}}(\kappa_s r) K_{N-3/2}(-\kappa_t r) \sum_j l_j \hat{g}_{N-1}^{(j;s)}[N g_N^{(j;t)} + (N-1) g_{N-2}^{(j;t)}].$$

But the identity (3.6) shows this latter expression will remain unaltered if we replace $K_{N-\frac{1}{2}}(-\kappa_t r)$ and $K_{N-\frac{1}{2}}(\kappa_s r)$ by $K_{N-5/2}(-\kappa_t r)$ and $K_{N-5/2}(\kappa_s r)$, respectively and so on. In this manner we can replace in (3.5) any of the $K_{2p\pm\frac{1}{2}}(-\kappa_t r)$, where p is any integer, by $K_{\pm\frac{1}{2}}(-\kappa_t r)$; and similarly for the $K_{2p\pm\frac{1}{2}}(\kappa_s r)$. But

$$K_{-\frac{1}{2}}(z) = K_{\frac{1}{2}}(z) = \sqrt{\pi/2z}\exp(-z).$$

Thus the quantity (3.5) is equal to

$$\frac{\pi}{2r\sqrt{-\kappa_t\kappa_s}} \exp[(\kappa_t - \kappa_s)r] \sum_{n=0}^{N} \sum_j l_j g_n^{(j;t)}[(n+1)\hat{g}_{n+1}^{(j;s)} + n\hat{g}_{n-1}^{(j;s)}]$$

or else, in view of (2.14) and (2.22), to

$$-\frac{\pi\delta_{s,t}X_s}{2r\kappa_s\sqrt{-\kappa_s\kappa_t}}. \tag{3.7}$$

The quantity (3.4) is then equal to $-(A_s X_s/\kappa_s r^2)$ and hence the final inversion formula is

$$A_s = -\frac{\kappa_s r^2}{X_s}\sqrt{\frac{2\kappa_s}{\pi r}} \sum_{n=0}^{N} \sum_j l_j \psi_n^{(j)}(r) \times[(n+1)\hat{g}_{n+1}^{(j;s)} K_{n+3/2}(\kappa_s r) + n\hat{g}_{n-1}^{(j;s)} K_{n-\frac{1}{2}}(\kappa_s r)]. \tag{3.8}$$

4. THE CASE OF CYLINDRICAL SYMMETRY

4.1 Introductory Remarks

We turn now to the systems with cylindrical symmetry. By this we mean that the neutron distribution is assumed to be invariant under both rotations around and translations parallel to the axis of symmetry, as well as under the appropriate reflections.

In the case of cylindrical systems the analysis is more involved than it was in the plane and in the spherical case. However, the additional features are entirely due to the geometry, and consequently are much the same whether one works in the one-group or in the multigroup theory. So, to avoid the repetition of the lengthy arguments, already given for cylindrical systems in the one-group theory (Davison, 1957*b*) we refer extensively below to that earlier paper. Namely, at all those stages where the analysis is identical whether one deals with one-group or with the multigroup theory, we give here only the main landmarks of the argument, and give the detailed analysis only where it is different from that in the one-group theory. In order to facilitate the references to that earlier paper we follow the notations and the normalizations adopted there, as closely as possible.

4.2 Multigroup Spherical Harmonics Method for General Geometrical Arrangements

While in the cases of plane and of spherical symmetry the expansion in spherical harmonics amounts to the expansion in Legendre polynomials of the cosine of one angular co-ordinate, in the more general case this is not so. Then a convenient way of applying the spherical harmonics method is as follows.

Let $\mathbf{U}$ be a vector of an arbitrary magnitude U and direction $\boldsymbol{\Omega}$,

$$\mathbf{U} = U\boldsymbol{\Omega}, \tag{4.1}$$

and let $\Psi_n^{(j)}(\mathbf{r},\mathbf{U})$ be $4\pi U^n/(2n+1)$ times the contribution of all spherical harmonics of order n to $\psi^{(j)}(\mathbf{r},\boldsymbol{\Omega})$, so that the spherical harmonics expansion of $\psi^{(j)}(\mathbf{r},\boldsymbol{\Omega})$ can be expressed as

$$\psi^{(j)}(\mathbf{r},\boldsymbol{\Omega}) = (1/4\pi) \sum_n (2n+1)\Psi_n^{(j)}(\mathbf{r},\mathbf{U})|_{U=1}. \tag{4.2}$$

The quantities $\Psi_n^{(j)}$ are functions of two vector variables $\mathbf{r}$ and $\mathbf{U}$. In dealing with such functions we shall distinguish the operators grad, div, and ∇^2 by corresponding subscripts. Then, much as in the case of one-group theory, the definition of $\Psi_n^{(j)}(\mathbf{r},\mathbf{U})$ implies that it is a polynomial in U_x, U_y, and U_z, satisfying the equation

$$\nabla_U^2\Psi_n^{(j)} = 0; \qquad \mathbf{U}\cdot\mathrm{grad}_U\Psi_n^{(j)} = n\Psi_n^{(j)}. \tag{4.3}$$

By substituting (4.2) into (2.1) and collecting separately the spherical harmonics of order n we obtain

$$\mathrm{div}_U \,\mathrm{grad}_r\, \Psi_{n+1}^{(j)} + \{(2n-1)\,\mathbf{U}\cdot - U^2\mathrm{div}_U\}\,\mathrm{grad}_r\,\Psi_{n-1}^{(j)} + \frac{(2n+1)}{l_j}\Psi_n^{(j)} = \delta_{0n}\sum_i \frac{c_{i\to j}}{l}\Psi_0^{(i)}. \tag{4.4}$$

In the P_N approximation the equations (4.4) are satisfied only for $n \leqslant N$, and supplemented by the conditions

$$\Psi_{N+1}^{(j)} = 0 \qquad \text{(all } j\text{)}. \tag{4.5}$$

4.3 Spherical Harmonics Moments for the Case of Cylindrical Symmetry

We now specialize the treatment to the cylindrical systems. Let z be measured along the symmetry axis, r perpendicular to it, and θ be the azimuthal angle. Let $\mathbf{U} = U\boldsymbol{\Omega}$ be specified by its components U_z and U_r and the azimuthal angle θ'. Then, exactly as in the one-group case, it can be shown that the most general expression for $\Psi_n^{(j)}$, polynomial in U_x, U_y, and U_z, compatible with the conditions of the complete cylindrical symmetry and satisfying the equations (4.3), may be written down as

$$\Psi_n^{(j)} = U^n \sum_{\substack{m=0 \\ n-m \text{ even}}}^{n} \cos m(\theta'-\theta)\psi_{n,m}^{(j)}(r)P_n^m(\Omega_z)/P_n^m(0), \tag{4.6}$$

so that, from (4.2),

$$\psi^{(j)}(\mathbf{r},\boldsymbol{\Omega}) = \frac{1}{4\pi}\sum_n (2n+1) \sum_{\substack{m=0 \\ n-m \text{ even}}}^{n} \cos m(\theta'-\theta)\psi_{n,m}^{(j)}(r)P_n^m(\Omega_z)/P_n^m(0). \tag{4.7}$$

Here $P_n^m(\mu)$ are the associated Legendre functions, where Ferrer's definition

$$P_n^m(\mu) = (1-\mu^2)^{m/2}\, d^m P_n(\mu)/d\mu^m$$

is used (Whittaker and Watson 1950).

Substituting (4.6) into (4.4) and (4.5) one obtains the differential equations for the $\psi_{n,m}^{(j)}(r)$, and again the particular solution of these equations is given by

$$\psi_{n,m}^{(j)}(r) = b_{n,m}^{(j)} K_m(-\kappa r) \tag{4.8}$$

provided that the constants $b_{n,m}{}^{(j)}$ satisfy the equations

$$\begin{aligned}(1+\delta_{0,m-1})(n-m+2)b_{n+1,m-1}^{(j)} + (n+m+2)b_{n+1,m+1}^{(j)} \\ + (1+\delta_{0,m-1})(n+m-1)b_{n-1,m-1}^{(j)} + (n-m-1)b_{n-1,m+1}^{(j)} \\ + 2(2n+1)b_{n,m}^{(j)}/(\kappa l_j) = \delta_{0m}\sum_i c_{i\to j} b_{0,0}^{(i)}/(\kappa l_i)\end{aligned} \tag{4.9}$$

and

$$b_{N+1,m}^{(j)} = 0 \qquad \text{(all } m \text{ and all } j\text{)}. \tag{4.10}$$

To facilitate the solution of the equations (4.9) and (4.10) introduce the auxiliary quantities $W_n{}^{(j)}$ defined by

$$W_n^{(j)} = U^n \sum_{\substack{m=0 \\ n-m \text{ even}}}^{n} \tilde{b}_{n,m}^{(j)} \cos m\theta' P_n^m(\Omega_z)/P_n^m(0) \tag{4.11}$$

where $\tilde{b}_{n,m}{}^{(j)}$ are some constants, and try to determine these so that the $W_n{}^{(j)}$ satisfy the conditions

$$(4.12)\quad \partial W_{n+1}^{(j)}/\partial U_x+[(2n-1)U_x-U^2\partial/\partial U_x]W_{n-1}^{(j)}+\frac{2n+1}{\kappa l_j}W_n^{(j)} = \delta_{0n}\sum_i \frac{c_{i\to j}}{\kappa l_i}W_0^{(i)}$$

(where $U_x = U_r\cos\theta'$) together with

$$(4.13)\quad W_{N+1}^{(j)} = 0 \qquad \text{(all } j\text{)}.$$

Substituting (4.12) and (4.13) into (4.11) one arrives at a set of equations between the $\tilde{b}_{n,m}^{(j)}$; and these are found to be identical with the equations (4.9) and (4.10) for the $b_{n,m}^{(j)}$, so that a particular solution of the latter system of equations is

$$(4.14)\quad \tilde{b}_{n,m}^{(j)} = b_{n,m}^{(j)}.$$

Thus the solution of the system of equations (4.9) and (4.10) is reduced to the solution of the equations (4.12) and (4.13).

On the other hand, much as in the one-group theory, a particular solution of the latter system is given by

$$(4.15)\quad W_n^{(j)} = g_{n,k}^{(j)}U^n\cos[k\tan^{-1}(\Omega_y/\Omega_z)]P_n^k(\Omega_z)/[d^kP_n(\mu)/d\mu^k]|_{\mu=1}$$

provided the constants $g_{n,k}^{(j)}$ satisfy the equations

$$(4.16)\quad (n-k+1)g_{n+1,k}^{(j)}+(n+k)g_{n-1,k}^{(j)}+\frac{2n+1}{\kappa l_j}g_{n,k}^{(j)} = \delta_{0n}\sum_i \frac{c_{i\to j}}{\kappa l_i}g_{0,k}^{(i)},$$

$$(4.17)\quad g_{N+1,k}^{(j)} = 0,$$

$$(4.18)\quad g_{n,k}^{(j)} = 0 \qquad \text{for } 0 \leqslant n \leqslant k-1,$$

and provided k is even (this last stipulation arises on account of the symmetry conditions we have imposed).

If we introduce now the constants $I_{n,m}^{(k)}$ defined by

$$(4.19)\quad \cos[k\tan^{-1}(\Omega_y/\Omega_z)]P_n^k(\Omega_z)/[d^kP_n(\mu)/d\mu^k]|_{\mu=1} = \sum_{\substack{m=0\\ n-m \text{ even}}}^{n} I_{n,m}^{(k)}\cos[m\tan^{-1}(\Omega_y/\Omega_z)]P_n^m(\Omega_z)/P_n^m(0)$$

(these were tabulated in the earlier paper (Davison 1957*b*)) and compare (4.15) with (4.11) and (4.14), we can readily see that if $\{g_{n,k}^{(j)}\}_0$ is a particular solution of (4.16) to (4.18), the corresponding particular solution of (4.9) and (4.10), $\{b_{n,m}^{(j)}\}_0$ is given by

$$(4.20)\quad \{b_{n,m}^{(j)}\}_0 = I_{n,m}^{(k)}\{g_{n,k}^{(j)}\}_0.$$

It remains to examine the equations (4.16) to (4.18). Here we should consider the case of $k = 0$, and the case of $k \neq 0$ (i.e., in fact, of $k \geqslant 2$, since k is a non-negative even integer) separately.

If $k = 0$ the equations (4.18) disappear, while the equations (4.16) and

(4.17) become identical with (2.6) and (2.7) respectively, so that in this case the permissible values of κ and the corresponding values of $g_{n,0}^{(j)}$ are given by

$$\kappa = \kappa_s, \qquad g_{n,0}^{(j)} = g_n^{(j;s)} \tag{4.21}$$

determined by (2.9) and (2.8) respectively.

On the other hand, if $k \geqslant 2$ then in virtue of (4.18) the terms involving the $c_{i\to j}$ vanish, so that the $g_{n,k}^{(j)}$ for different j are no longer coupled. In other words each energy group can be considered on its own, and we can directly apply the already available results derived for the one-group theory. Namely if, as in the earlier paper (Davison 1957*b*) we define the functions $G_{n,k}(\nu)$ for $k \geqslant 1$ by the recurrence relationship

$$\left\{\begin{array}{l}(n-k+1)G_{n+1,k}(\nu)+(2n+1)G_{n,k}(\nu)/\nu+(n+k)G_{n-1,k} = 0 \\ \text{together with} \\ \qquad G_{k,k}(\nu) = 1, \qquad G_{k-1,k} = 0\end{array}\right. \tag{4.22}$$

and denote by $\nu_{p,k}$ the roots of the equation

$$G_{N+1,k}(\nu_{p,k}) = 1 \tag{4.23}$$

then each root of (4.23) and each i $(i = 1, 2, \ldots S)$ will give rise to a particular solution of (4.16) to (4.18) of the form

$$\begin{aligned}\kappa &= \nu_{p,k}/l_i, \\ g_{n,k}^{(j)} &= \delta_{ij}G_{n,k}(\nu_{p,k}).\end{aligned} \tag{4.24}$$

Combining the above results, and bearing in mind that the number of roots of (4.23) is $(N+1-k)$, and these roots, like those of (2.9) come in pairs (Davison 1957*b*) we see that the general solution of the equations for $\psi_{n,m}^{(j)}(r)$ is given by

$$\begin{aligned}\psi_{n,m}^{(j)}(r) = I_{n,m}^{(0)} \sum_{s=\pm 1}^{\pm\frac{1}{2}(N+1)S} A_s g_n^{(j;s)} K_m(-\kappa_s r) \\ + \sum_{\substack{k=2 \\ k \text{ even}}}^{n} I_{n,m}^{(k)} \sum_{p=\pm 1}^{\pm\frac{1}{2}(N+1-k)} B_{p,k}^{(j)} G_{n,k}(\nu_{p,k}) K_m(-\nu_{p,k} r/l_j)\end{aligned} \tag{4.25}$$

where the A_s and the $B_{p,k}^{(j)}$ are the constants of integration.

4.4 The Inversion Formula

Our purpose now is to supplement the formula (4.25) by the inverse formulae giving the A_s and the $B_{p,k}^{(j)}$ in terms of the $\psi_{n,m}^{(j)}(r)$. The analogy with the corresponding result in the one-group theory, on one hand, and with (2.24) and (3.8) on the other, suggests that we consider for this purpose the quantities

$$\begin{aligned}T_s(\psi) = \sum_j l_j \sum_{n=0}^{N} \sum_{\substack{m=0 \\ n-m \text{ even}}}^{n} \psi_{n,m}^{(j)}(r) \{(1-\delta_{0,m})(n+m)K_{m-1}(\kappa_s r)\hat{g}_{n-1}^{(j;s)} \\ + (1+\delta_{0,m})(n-m)K_{m+1}(\kappa_s r)\hat{g}_{n-1}^{(j;s)} + (1-\delta_{0,m})(n-m+1)K_{m-1}(\kappa_s r)\hat{g}_{n+1}^{(j;s)} \\ + (1+\delta_{0,m})(n+m+1)K_{m+1}(\kappa_s r)\hat{g}_{n+1}^{(j;s)}\}\end{aligned} \tag{4.26}$$

and

$$(4.27)\quad Y^{(j)}_{p;k}(\psi) = \sum_{n=k-1}^{N} \sum_{\substack{m=0 \\ n-m \text{ even}}}^{n} \psi^{(j)}_{n,m}(r)$$
$$\Big\{(1-\delta_{0,m})(n+m)S^{(k)}_{n-1,m-1}K_{m-1}(\nu_{p,k}r/l_j)G_{n-1,k}(\nu_{p,k})$$
$$+(1+\delta_{0,m})(n-m)S^{(k)}_{n-1,m+1}K_{m+1}(\nu_{p,k}r/l_j)G_{n-1,k}(\nu_{p,k})$$
$$+(1-\delta_{0,m})(n-m+1)S^{(k)}_{n+1,m-1}K_{m-1}(\nu_{p,k}r/l_j)G_{n+1,k}(\nu_{p,k})$$
$$+(1+\delta_{0,m})(n+m+1)S^{(k)}_{n+1,m+1}K_{m+1}(\nu_{p,k}r/l_j)G_{n+1,k}(\nu_{p,k})\Big\}$$
$$(k \geqslant 2)$$

where the constants $S_{n,m}{}^{(k)}$ are defined by

$$(4.28)\quad \cos[m\tan^{-1}(\Omega_y/\Omega_x)]P^m_n(\Omega_z/)P^m_n(0)$$
$$= \sum_{\substack{k=0 \\ k \text{ even}}}^{n} \frac{(n+k)!}{(n-k)!(2k)!} S^{(k)}_{n,m} \cos[k\tan^{-1}(\Omega_y/\Omega_z)]P^k_n(\Omega_z)/[d^kP_n(\mu)/d\mu^k]|_{\mu=1}$$

and have been tabulated in the earlier paper (Davison 1957*b*) while $\nu_{p,k}$ and $G_{n,k}(\nu)$ are defined by (4.23) and (4.22) above, and have also been tabulated in that earlier paper.

The expression in the braces in (4.27) is identical with the corresponding quantity in the inversion formula for the one-group theory, given there, except that the one and only total mean free path entering that theory is now replaced by the total mean free path for the jth energy group, l_j. The expression in the braces in (4.26) arises from that in (4.27) by replacing $\nu_{p,k}/l_j$ and $G_{n\pm1,k}(\nu_{p,k})$ by κ_s and $\hat{g}_{n\pm1}{}^{(j;s)}$ respectively. The factors $S_{n\pm1;m\pm1}{}^{(k)}$ do not enter into (4.26) since, as it had been shown in the earlier paper, for $k = 0$ these factors are all equal to unity.

We proceed now to evaluate the quantities (4.26) and (4.27). Substituting for $\psi_{n,m}{}^{(j)}(r)$ from (4.25) we can rewrite these as

$$(4.29)\quad T_s(\psi) = \sum_{t=\pm1}^{\pm\frac{1}{2}(N+1)S} A_t \Lambda_{t\to s} + \sum_j \sum_{\substack{k'=2 \\ k' \text{ even}}}^{N-1} \sum_{p'=\pm1}^{\pm\frac{1}{2}(N+1-k')} l_j B^{(j)}_{p',k'} \hat{\Xi}^{(j)}_{p',k'\to s}$$

and

$$(4.30)\quad Y^{(j)}_{p;k}(\psi) = \sum_{t=\pm1}^{\pm\frac{1}{2}(N+1)S} A_t \Xi^{(j)}_{t\to p,k} + \sum_{\substack{k'=2 \\ k' \text{ even}}}^{N-1} \sum_{p'=\pm1}^{\pm\frac{1}{2}(N+1-k')} B^{(j)}_{p',k'} Z^{(j)}_{p',k'\to p,k}$$

with the self-evident definition of $\Lambda_{t\to s}$, $\Xi^{(j)}_{t\to p,k}$, etc.

Now, except for the fact that l is replaced by l_j, the expression $Z_{p',k'\to p,k}{}^{(j)}$ is identical with the corresponding expression in the case of one-group theory (one can readily see that it is bound to be so, since none of the quantities entering into the expression for $Z_{p',k'\to p,k}{}^{(j)}$ depend upon the $c_{t\to j}$, through which various energy groups are mutually coupled). Thus we can apply directly the result derived in the earlier paper, which is

$$Z_{p',k'\to p,k}^{(j)} = \delta_{k,k'}\delta_{p,p'}\frac{l_j}{r}\frac{\pi h_k(\nu_{p,k})}{i\nu_{p,k}^2} \tag{4.31}$$

where $h_k(\nu)$ is defined by

$$h_k(\nu) = \frac{(N-k+1)!(2k)!}{(N+k)!}\nu^2 G_{N,k}(\nu)\frac{dG_{N+1,k}(\nu)}{d\nu} \tag{4.32}$$

and was also tabulated in the earlier paper. The factor $i = \sqrt{-1}$ appearing in (4.31) arises because for negative z, the $K_m(z)$ are complex. Once they are expressed in terms of $K_m(-z)$ and $I_m(z)$, i will cancel out.

Consider now the other type of terms appearing in (4.30), namely the quantities $\Xi_{t\to p,k}^{(j)}$. These differ from what $Z_{p',k'\to p,k}^{(j)}$ would have been for $k' = 0$, only by the fact that $\nu_{p',0}/l_j$ and $G_{n,0}(\nu_{p',0})$ are replaced by κ_t and $g_n^{(j;t)}$ respectively. However, since $k \geqslant 2$, the $g_n^{(j;t)}$ enter into $\Xi_{t\to p,k}^{(j)}$ only for $n \geqslant k-1 \geqslant 1$ while for $n \geqslant 1$ the equation (2.6) governing the $g_n^{(j;t)}$ are identical with what (4.22) would have become for $k = 0$ and $\nu = \kappa_t l_j$. On the other hand, the derivation of (4.31) given in the earlier paper depended, for $k \neq k'$, only upon the properties of the constants $I_{n,m}^{(k)}$ and $S_{n,m}^{(k)}$, and upon the correlation between the arguments under the signs of Bessel functions and of the functions $G_{n,k}(...)$, rather than upon the actual values of those arguments. Hence we can still apply the old result to conclude

$$\Xi_{t\to p,k}^{(j)} = 0 \tag{4.33}$$

and, by a similar argument,

$$\hat{\Xi}_{p',k'\to s}^{(j)} = 0. \tag{4.34}$$

It remains to consider the quantities $\Lambda_{t\to s}$. It will be more convenient to evaluate these latter quantities *ab initio*, noting, however, the following properties of the coefficients $I_{n,m}^{(0)}$, proved in the earlier paper:

$$\begin{cases}(1+\delta_{0,m-1})(n+m-1)I_{n-1,m-1}^{(0)}+(n-m-1)I_{n-1,m+1}^{(0)} = 2nI_{n,m}^{(0)}\\ (1+\delta_{0,m-1})(n-m+2)I_{n+1,m-1}^{(0)}+(n+m+2)I_{n+1,m+1}^{(0)} = 2(n+1)I_{n,m}^{(0)}\end{cases} \tag{4.35}$$

(where $I_{n\pm1,-1}^{(0)}$ is taken to be zero) and

$$\sum_{\substack{0\leqslant m\leqslant n\\ n-m \text{ even}}} I_{n,m}^{(0)} = 1. \tag{4.36}$$

To save writing we shall use the following abbreviations:

$$\begin{cases} K_m(\kappa_s r) = K_m \qquad K_m(-\kappa_t r) = K_m'\\ \sum_j l_j\hat{g}_n^{(j;s)}g_{n-1}^{(j;t)} = \gamma_n^- = \gamma_{n-1}'^+\\ \sum_j l_j\hat{g}_n^{(j;s)}g_{n+1}^{(j;t)} = \gamma_n^+ = \gamma_{n+1}'^- \end{cases} \tag{4.37}$$

and shall introduce the auxiliary quantities $t_{n,m}^-$, $t_{n,m}^+$, $t_{n,m}'^-$, and $t_{n,m}'^+$ defined as follows: $t_{n,m}^-$ is the sum of coefficients accompanying $\gamma_n^- K_m K_{m-1}'$, $\gamma_n^- K_m K_{m+1}'$, $\gamma_n^- K_{m+2} K_{m+1}'$, $\gamma_n^- K_{m+2} K_{m+3}'$, etc., and similarly for $t_{n,m}^+$, etc. If

the expression for $\Lambda_{t\to s}$ is written down, it becomes obvious by inspection that

$$(4.38)\qquad \begin{cases} t'^{-}_{n,m} = 2n \sum\limits_{\substack{m'=m \\ m'-m \text{ even}}}^{n} I^{(0)}_{n,m'}, \\ t'^{+}_{n,m} = 2(n+1) \sum\limits_{\substack{m'=m \\ m'-m \text{ even}}}^{n} I^{(0)}_{n,m'}, \\ t^{-}_{n,m} = t'^{+}_{n-1,m+1} + (1+\delta_{0,m-1})(n+m-1) I^{(0)}_{n-1,m-1}, \\ t^{+}_{n,m} = t'^{-}_{n+1,m+1} + (1+\delta_{0,m-1})(n+m-2) I^{(0)}_{n+1,m-1}. \end{cases}$$

Combining (4.35) with (4.38) one can easily verify that $t_{n,m}{}^{-} = t_{n,m}{}'^{-}$ and $t_{n,m}{}^{+} = t_{n,m}{}'^{+}$, and hence also

$$\frac{t^{-}_{n,m}}{n} = \frac{t'^{-}_{n,m}}{n} = \frac{t^{+}_{n,m}}{n+1} = \frac{t'^{+}_{n,m}}{n+1}.$$

Then the identity (3.6) shows that the quantity

$$(4.39)\qquad \sum_{\substack{n=m \\ n-m \text{ even}}}^{N} \left\{ [t^{-}_{n,m}\gamma_n{}^{-} + t^{+}_{n,m}\gamma_n{}^{+}] K_m K'_{m-1} + [t'^{-}_{n,m}\gamma_n{}'^{-} + t'^{+}_{n,m}\gamma_n{}'^{+}] K'_m K_{m-1} \right\}$$

will remain unaltered if we replace there K_m and K_m' by K_{m-2} and K_{m-2}' respectively. Using this result one can readily eliminate from $\Lambda_{t\to s}$ all the higher-order Bessel functions. The highest-order Bessel functions initially present in $\Lambda_{t\to s}$ are those of order N: K_N and K_N'. The assembly of terms containing these is given by (4.39) with $m = N$. (Notice that in view of (4.37), (2.7), and (2.15) $\gamma_N{}^{+} = \gamma_N{}'^{+} = 0$.) Then by the property of (4.39) proved above we can replace in the expression for $\Lambda_{t\to s}$ K_N and K_N' by K_{N-2} and K_{N-2}' respectively. The highest-order Bessel functions present are now K_{N-1} and K_{N-1}'. Recalling that $\gamma_n{}^{-} = \gamma_{n-1}{}'^{+}$, $\gamma_n{}'^{-} = \gamma_{n-1}{}^{+}$ and the definition of $t_{n,m}{}^{-}$, etc. one readily sees that the assembly of terms involving these is given by (4.39) with $m = N-1$. Thus by the properties of (4.39) we can now replace K_{N-1} and K_{N-1}' by K_{N-3} and K_{N-3}', respectively, and so on. Proceeding in this manner we can eliminate all the Bessel functions of order $\geqslant 2$, and the entire expression for $\Lambda_{t\to s}$ reduces to (4.39) with $m = 1$. On the other hand, comparing (4.36) with (4.38) and $t_{n,m}{}^{-} = t_{n,m}{}'^{-}$, $t_{n,m}{}^{+} = t_{n,m}{}'^{+}$ we see that for odd n

$$t^{-}_{n,1} = t'^{-}_{n,1} = 2n; \qquad t^{+}_{n,1} = t'^{+}_{n,1} = 2(n+1).$$

Thus

$$\Lambda_{t\to s} = 2 \sum_{\substack{n=1 \\ n \text{ odd}}}^{N} \{ [(n+1)\gamma_n{}^{+} + n\gamma_n{}^{-}] K_0 K'_1 + [(n+1)\gamma_n{}'^{+} + n\gamma_n{}'^{-}] K'_0 K_1 \};$$

or, recalling the abbreviations (4.37) and using equations (2.6) and (2.14)

$$\Lambda_{t\to s} = \left\{K_0(\kappa_s r)\frac{K_1(-\kappa_t r)}{\kappa_t} + K_0(-\kappa_t r)\frac{K_1(\kappa_s r)}{\kappa_s}\right\} 2\sum_j \sum_{\substack{n=1\\ n \text{ odd}}}^{N} (2n+1) g_n^{(j;t)} \hat{g}_n^{(j;s)}. \tag{4.40}$$

On the other hand, replacing in (2.22) t by $-t$, using (2.13), and subtracting the result from the original form of (2.22) we get

$$2\sum_j \sum_{\substack{n=1\\ n \text{ odd}}}^{N} (2n+1) g_n^{(j;t)} \hat{g}_n^{(j;s)} = X_s[\delta_{s,t} + \delta_{s,-t}] \tag{4.41}$$

which shows that the quantity (4.40) vanishes unless $\kappa_t = \pm\kappa_s$. Next, for $\kappa_t = -\kappa_s$ the first factor (i.e. the quantity in braces) in (4.40) vanishes. While for $\kappa_t = \kappa_s$, bearing in mind that

$$K_m(-z) = \exp(-\pi i m) K_m(z) - \pi i I_m(z)$$

(Whittaker and Watson 1950), this first factor is easily found to be $(-\pi i/r\kappa_s^2)$. Thus finally

$$\Lambda_{s\to s} = -\pi i X_s \delta_{s,t}/r\kappa_s^2; \tag{4.42}$$

while combining this with formulae (4.29) to (4.34) we get

$$\begin{cases} A_s = \dfrac{ir\kappa_s^2}{\pi X_s} T_s(\psi) \\ B_{p,k}^{(j)} = \dfrac{ir\nu_{p,k}^2}{\pi l_j h_k(\nu_{p,k})} Y_{p,k}^{(j)}(\psi) \end{cases} \tag{4.43}$$

where $T_s(\psi)$ and $Y_{p,k}^{(j)}(\psi)$ are defined by (4.27) and (4.28) while $h_n(\nu_{p,k})$ and X_s are defined by (4.32) and (2.29) respectively.

APPENDIX

The purpose of this appendix is to show that the X_s, defined by (2.29), do not vanish, except perhaps for such sets of values of l_j and $c_{t\to j}$ $(i, j = 1, 2, \ldots S)$ for which the equation (2.9) has multiple roots.

We shall regard the set of l_j values as fixed throughout the discussion and refer to each set of $c_{t\to j}$ values as a "point in $c_{t\to j}$ space", denoting by $X_s(c_{t\to j})$ the value of X_s for this particular set of $c_{t\to j}$ values.

The result we wish to prove is already known for the one-group theory,*

*In the one-group theory the formula (2.28) above reduces to $X_s = -\nu_s/(d\nu_s/dc)$, or, which is the same,

$$X_s = \frac{-2\nu_s^2}{d(\nu_s^2)/dc} \tag{*}$$

where $\nu_s = l\kappa_s$. Now in the odd-order approximations ν_s^2 for each s varies monotonically with c and has no singularities as long as c is real and positive (Davison 1957c). Thus the denominator in (*) cannot become infinite for any permissible c values. Thus (*) can vanish only if $\nu_s = 0$. On the other hand it is known that if $\nu = 0$ is a root, it is necessarily a double root of the equation defining ν_s and corresponding to our present equation (2.9).

and consequently it is also correct in the multigroup theory if the energy groups are not coupled ($c_{i\to j} = c^{(j)}\delta_{ij}$, say) or if their coupling is weak. Thus, there exist points in the $c_{i\to j}$ space for which $X_s(c_{i\to j}) \neq 0$. On the other hand, the formula (2.29) shows that $X_s(c_{i\to j})$ is an analytical (in fact an algebraic) function of the $c_{i\to j}$ $(i, j = 1, \ldots S)$. Thus if X_s can vanish at all, it can do so only if the $c_{i\to j}$ are connected by some algebraic relationships. In other words $X_s(c_{i\to j})$ can vanish, at the most, only upon some surfaces or hypersurfaces in the $c_{i\to j}$ space. Our purpose, then, is to show that if such hypersurfaces in the $c_{i\to j}$ exist, they will coincide with those for which the equation (2.9) has multiple roots.

Suppose now that there exists a point $c_{i\to j}^*$ in the $c_{i\to j}$ space, such that $X_s(c_{i\to j}^*) = 0$. Now since X_s can vanish, at the most, only on some superface or hypersurface in the $c_{i\to j}$ space, there will exist a sequence of point $c_{i\to j}^{(p)}$ converging to $c_{i\to j}^*$, and yet such that $X_s(c_{i\to j}^{(p)}) \neq 0$ for any finite p. Consequently, for any prescribed set of values of $\psi_n^{(j)}(x)$ and $c_{i\to j} = c_{i\to j}^{(p)}$ $(i, j = 1, \ldots S)$ we can use the formula (2.24) to determine the value of A_s. Call it $A_s(\psi; c_{i\to j}^{(p)})$. On the other hand, since $X_s(c_{i\to j})$ is an algebraic function of the $c_{i\to j}$, $X_s(c_{i\to j}^*) = 0$ and $\lim_{p\to\infty} c_{i\to j}^{(p)} = c_{i\to j}^*$ imply

$$\lim_{p\to\infty} X_s(c_{i\to j}^{(p)}) = 0$$

and hence, for any prescribed values of $\psi_n^{(j)}(x)$, $A_s(\psi; c_{i\to j}^{(p)})$ will tend to infinity as $c_{i\to j}^{(p)}$ tend to $c_{i\to j}^*$. But this would mean that for a fixed non-zero value of A_s, $\psi_n^{(j)}(x)$ should tend to zero as the $c_{i\to j}$ tend to $c_{i\to j}^*$. But this latter situation is possible only if with $c_{i\to j}$ tending to $c_{i\to j}^*$ some other term in (2.11) increasingly compensates the contribution of A_s, i.e. only if for $c_{i\to j}$ tending to $c_{i\to j}^*$ some other root of (2.9) tends to coincide with κ_s. So that for $c_{i\to j} = c_{i\to j}^*$ the equation (2.9) is then bound to have multiple roots.

Thus, provided that (2.9) has no multiple roots for the particular set of the $c_{i\to j}$ values the quantity X_s will not vanish.

REFERENCES

DAVISON, B. 1957*a*. Can. J. Phys. **35**, 55.
——— 1957*b*. Can. J. Phys. **35**, 576.
——— 1957*c*. Neutron transport theory (Oxford University Press, London).
WHITTAKER, E. T. and WATSON, G. N. 1950. A course of modern analysis (Cambridge University Press, London).

ON THE THEORY OF THE SPECTROPHONE[1]

R. KAISER

ABSTRACT

The spectrophone consists essentially of a constant gas volume that is exposed to intensity-modulated infrared radiation of a spectral range corresponding to one of the vibration–rotation bands of the gas.

After a brief review of the history of the instrument a theoretical analysis of the processes in the spectrophone cell is presented on the basis of a two-state gas model. Expressions are derived for the time dependence of the upper-state population, of the gas pressure, and of the infrared absorption, emphasizing the effects due to a finite rate of exchange between vibrational and translational energy of the gas molecules. Numerical values are calculated for the 15-μ CO_2 band and it is suggested that information on the mechanism of vibrational relaxation in polyatomic gases and gas mixtures can be obtained from experimental studies of the gas pressure in the spectrophone cell.

INTRODUCTION

Alexander Graham Bell (1880) observed that audible sound can be produced by exposing a gas in a transparent, constant-volume container to intensity-modulated infrared radiation. He explained that a part of the radiation is absorbed by the gas, and the temperature and pressure in the constant-volume enclosure increase. A periodic modulation of the incident intensity thus produces an alternating pressure component, and this becomes audible for proper choice of the experimental parameters. Bell realized the possibility of using the effect for an investigation of the spectral absorption of gases and vapors. He proposed the name "spectrophone" for the instrument constructed for this purpose. A number of studies with the spectrophone were made soon afterward (Bell, Mercadier, Preece, Roentgen, Tyndall 1881), but the effect then was forgotten until Veingerov (1938, 1945, 1946, 1947) renewed interest in it with an extensive series of experiments on qualitative and quantitative analysis of gas mixtures. Since then there has been much interest in this method of gas analysis (Luft 1943; Luchin 1945; Fastie and Pfund 1947) and it is now widely used in industry.*

The use of the spectrophone effect for the measurement of vibrational relaxation times was first suggested by Gorelik (1946). Following this suggestion Slobodskaya (1948) adapted Veingerov's spectrophone for the measurement of the lifetimes of the excited vibrational states in the 2.7-μ, 4.3-μ, 14.8-μ CO_2 bands, and a theoretical analysis of this experiment was later given by Stepanov and Girrin (1950). Independently, Cottrell (1950) suggested using the d-c. pressure rise (rather than the a-c. pressure amplitude or phase) in the spectrophone cell for the determination of vibrational relaxation times, but experiments on this basis have not yet met with success (Kaiser 1955).

[1]Manuscript received May 26, 1959.

Contribution from the Department of Physics, University of New Brunswick, Fredericton, New Brunswick.

*Gas analyzers based on the spectrophone are manufactured by, for example, Infrared Development Corp., Welwyn Garden City, Hertfordshire, England; Godart Mijnhardt NV, Utrecht, Holland, Keulsekade 9.

Slobodskaya's method has been refined in more recent experiments (Turrell 1954; Jacox and Bauer 1957; Jones 1958; Delany 1959) and the results are in general agreement with standard ultrasonic measurements of relaxation times, so that a theoretical analysis of the spectrophone processes appears to be of interest.

THEORETICAL ANALYSIS

1. Equation of Balance

We consider a gas that is enclosed in a transparent container of constant volume, and that is heated by intensity-modulated infrared irradiation. We assume the spectral range of the radiation to be limited to one of the vibration–rotation absorption bands of the gas, so that transitions are optically induced only between a "lower" (index 0) and an "upper" (index 1) vibrational state of the gas molecules. While the spectrophone processes can thus be made optically specific for a certain vibrational transition, it must be kept in mind that either vibrational state can in intermolecular collisions interact with any other state. Consideration of these interactions would exceed the scope of this investigation, and we shall therefore base the analysis on a two-state gas model. (Ultrasonic relaxation effects for a three-state model have been discussed by Beyer (1957).)

Let N be the number of molecules per unit volume, of which n_0 molecules are in the lower vibrational state (summed over all rotational levels of this state) and $n_1 = N - n_0$ molecules are in the upper vibrational state (summed over all rotational levels of the upper state). The number of transitions $0 \rightarrow 1$ per second and unit volume is

$$
(1)\quad \left\{ \begin{array}{l} \rho \cdot B \cdot n_0 \text{ induced by radiation with density } \rho, \\ f_{01} \cdot n_0 \text{ due to inelastic collisions.} \\ \text{The number of transitions } 1 \rightarrow 0 \text{ per second and unit volume is} \\ \rho \cdot B \cdot n_1 \text{ induced by radiation with density } \rho, \\ f_{10} \cdot n_1 \text{ due to inelastic collisions,} \\ A \cdot n_1 \text{ due to spontaneous emission of the vibration–rotation energy quantum } E. \end{array} \right.
$$

The symbols in (1) are explained as follows:

$$
\rho = \text{photon density} = \frac{\text{no. of photons in appropriate wave number interval}}{\text{unit volume}},
$$

$$
B = \text{Einstein transition coefficient} = \frac{\text{no. of induced transitions}}{\text{second} \cdot \text{molecule} \cdot \text{unit photon density}},
$$

$$
\left.\begin{matrix} f_{10} \\ f_{01} \end{matrix}\right\} = \text{collisional transfer rates} = \frac{\text{no. of collisions}}{\text{second} \cdot \text{molecule}} \cdot \text{transfer probability},
$$

$$
A = \text{Einstein transition coefficient} = \frac{\text{no. of spontaneous transitions}}{\text{second} \cdot \text{molecule}}.
$$

The collisional transfer rates are related by the Boltzmann factor

(1a) $$f_{01} = f_{10} \cdot e^{-(E/k\theta)}, \qquad \theta = \text{translational temperature},$$

and the Einstein coefficients are functions of the wave number σ related by (Herzberg 1955)

(1b) $$A(\sigma) = 8\pi\sigma^2 B(\sigma) \cdot \Delta\sigma.$$

From (1) one obtains the equation of balance

(2) $$\frac{dn_1}{dt} = -n_1(2\rho B + A + f_{10} + f_{01}) + N(\rho B + f_{01})$$

$$= -n_1 \cdot C + N \cdot D \qquad \text{with } N = n_0 + n_1 \text{ and } t = \text{time}.$$

Let the total photon density ρ be given by

(3) $$\rho = \rho^0 + \rho''(1 + \sin \omega t) = \rho' + \rho'' \sin \omega t$$

where ρ^0 is the photon density in a cavity at room temperature, and $2\rho''$ is the maximum additional photon density produced by irradiation of the gas from an external source. ω is the angular frequency with which the external radiation is sinusoidally modulated, and $\rho' = \rho^0 + \rho''$ is the resulting time average of the total photon density. One obtains then

(4) $$C = C'(1 + \alpha \cdot \sin \omega t) \qquad D = D'(1 + \beta \cdot \sin \omega t)$$

with

(4a) $$C' = 2\rho' B + A + f_{10} + f_{01} \qquad D' = \rho' B + f_{01}$$

and

(4b) $$\alpha = \frac{2\rho'' B}{C'} \qquad \beta = \frac{\rho'' B}{D'}.$$

The equation of balance can now be written in the form

(5) $$\frac{dn_1}{dt} = -C'(1 + \alpha \cdot \sin \omega t)\left(n_1 - N\frac{D'}{C'}\right) + ND'(\beta - \alpha) \cdot \sin \omega t.$$

2. Low-Frequency Solution

When the external radiation is unmodulated, i.e. $\alpha = \beta = 0$, one obtains immediately the solution

(6) $$n_1 - N\frac{D'}{C'} = \text{const.} \cdot e^{-C't},$$

i.e. after a sudden disturbance of the equilibrium (e.g. by suddenly changing ρ' to a new value), n_1 approaches the new equilibrium value $N(D'/C')$ with a time constant $\tau = 1/C'$. τ is the relaxation time for the transition $0 \rightleftharpoons 1$ that has been selected by the proper spectral limitation of the incident radiation.

The behavior of the gas for modulation frequencies $\omega \ll C'$ is easily found by studying the dependence of the equilibrium value $N(D'/C')$ on ρ, because the gas will at all times be in equilibrium if only small changes in ρ occur during times long compared with τ. A sketch of the function

$$N\frac{D'}{C'}(\rho) = N\frac{\rho B+f_{01}}{2\rho B+A+f_{10}+f_{01}} \tag{7}$$

is presented in Fig. 1.

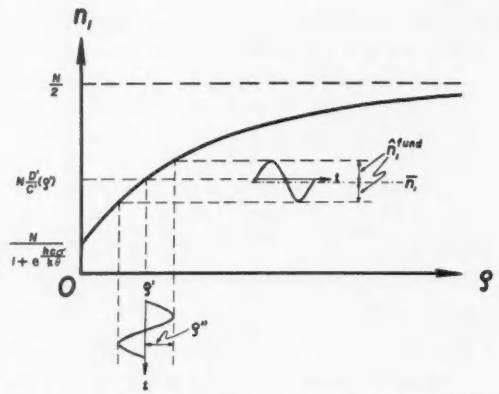

FIG. 1. Upper state equilibrium population n_1 as a function of radiation density ρ (schematic).

The Taylor expansion in the vicinity of the point $\{\rho', N(D'/C')(\rho')\}$ reads

$$N\frac{D'}{C'}(\rho) = N\frac{D'}{C'}(\rho')+N(\rho-\rho')\left[\frac{d}{d\rho}\left\{\frac{D'}{C'}\right\}\right]_{\rho=\rho'} + \frac{N}{2}(\rho-\rho')^2\left[\frac{d^2}{d\rho^2}\left\{\frac{D'}{C'}\right\}\right]_{\rho=\rho'}+\ldots. \tag{8}$$

Introduction of eq. (3) shows that in first approximation the population of the upper state, n_1, varies with the same frequency and in phase with the modulation of the photon density:

$$n_1^{\text{fund}} = N\left[\frac{d}{d\rho}\left\{\frac{D'}{C'}\right\}\right]_{\rho=\rho'}\cdot\rho''\sin\omega t = N\frac{D'}{C'}\left(\frac{\beta}{\alpha}-1\right)\cdot\alpha\cdot\sin\omega t \qquad \text{for } \omega\ll C'. \tag{9}$$

However, because of the non-linearity of eq. (7), the time average $\bar{n}_1$ differs from the equilibrium value $N(D'/C')(\rho')$, and in the approximation written in eq. (8) one obtains

$$\bar{n}_1 - N\frac{D'}{C'} = \frac{N}{4}\left[\frac{d^2}{d\rho^2}\left\{\frac{D'}{C'}\right\}\right]_{\rho=\rho'}\cdot\rho''^2 = -N\frac{D'}{C'}\left(\frac{\beta}{\alpha}-1\right)\cdot\frac{\alpha^2}{2} \qquad \text{for } \omega\ll C'. \tag{10}$$

3. General Solution

To obtain the frequency dependence of n_1^{fund} and $\tilde{n}_1$ one has to solve the complete differential equation (5). The result is obtained in the form

$$(11)\quad n_1(t)-N\frac{D'}{C'}=N\frac{D'}{C'}\left(\frac{\beta}{\alpha}-1\right)\left[1-C'e^{-C'\{t-(\alpha/\omega)\cos\omega t\}}\int e^{+C'\{t-(\alpha/\omega)\cos\omega t\}}dt\right].$$

The integral can be solved using the expansion (Sommerfeld 1948)

$$(12)\qquad e^{-(C'\alpha/\omega)\cos\omega t}=\sum_{k=-\infty}^{+\infty} i^k J_k\left(i\frac{C'\alpha}{\omega}\right)\cdot e^{ik\omega t}$$

where J_k is the Bessel function of the first kind of order k. The result is

$$(13)\qquad \int e^{C'\{t-(\alpha/\omega)\cos\omega t\}}dt=e^{C't}\sum_{k=-\infty}^{+\infty}\frac{i^k J_k\{i(C'\alpha/\omega)\}}{C'+ik\omega}e^{ik\omega t}+\text{const.}$$

Applying the expansion (12) also to the exponential in front of the integral, eq. (11) becomes

$$(14)\quad n_1(t)-N\frac{D'}{C'}=N\frac{D'}{C'}\left(\frac{\beta}{\alpha}-1\right)\left(1-C'\left[\sum_{l=-\infty}^{+\infty} i^l J_l\{-i(C'\alpha/\omega)\}e^{il\omega t}\right]\right.$$
$$\left.\times\left[\sum_{k=-\infty}^{+\infty}\frac{i^k J_k\{i(C'\alpha/\omega)\}}{C'+ik\omega}e^{ik\omega t}\right]\right)+\text{const.}\cdot e^{-C'\{t-(\alpha/\omega)\cos\omega t\}}.$$

The last term represents the transient and can be neglected for $t\gg\tau$. Multiplication of the two sums gives the Fourier expansion of $n_1(t)$:

$$(14a)\quad n_1(t)-N\frac{D'}{C'}=N\frac{D'}{C'}\left(\frac{\beta}{\alpha}-1\right)$$
$$\times\left[1-C'\sum_{k,\,l=-\infty}^{+\infty} i^{k+l}\frac{J_k\{i(C'\alpha/\omega)\}\cdot J_l\{-i(C'\alpha/\omega)\}}{C'+ik\omega}e^{i((k+l)\omega t}\right]+\text{transient.}$$

Before proceeding it is best to note some of the properties of the Bessel functions of imaginary argument and integral order k:

$$(15)\quad J_k(2iy)=(iy)^k\left\{\frac{1}{k!}+\frac{y^2}{1!(k+1)!}+\frac{y^4}{2!(k+2)!}+\frac{y^6}{3!(k+3)!}+\cdots\right\}\quad\begin{matrix}y\text{ real}\\ 0\leqslant k<\infty.\end{matrix}$$

It follows that

$$(15a)\qquad J_k(-iy)=(-1)^k J_k(iy).$$

The Bessel functions of negative order are defined by

$$(15b)\qquad J_{-k}(iy)=(-1)^k J_k(iy).$$

4. First-Order Effects

We now proceed to obtain the fundamental frequency component n_1^{fund} from eq. (14*a*) by dropping the time-independent terms and putting $k+l=\pm1$:

$$(16)\quad n_1^{\text{fund}} = -N\frac{D'}{C'}\left(\frac{\beta}{\alpha}-1\right)C'\sum_{k=-\infty}^{+\infty}\left[i\frac{J_k\{i(C'\alpha/\omega)\}\cdot J_{1-k}\{-i(C'\alpha/\omega)\}}{C'+ik\omega}\,e^{i\omega t}\right.$$

$$\left.+i^{-1}\frac{J_k\{i(C'\alpha/\omega)\}\cdot J_{-1-k}\{-i(C'\alpha/\omega)\}}{C'+ik\omega}\,e^{-i\omega t}\right].$$

Changing k to $-k$ in the second term of the sum and applying eqs. (15*a*) and (15*b*), one recognizes this term to be the complex conjugate of the first term. The latter can be rewritten

$$\sum_{k=-\infty}^{+\infty} i\frac{J_k\{i(C'\alpha/\omega)\}\cdot J_{1-k}\{-i(C'\alpha/\omega)\}}{C'+ik\omega} = \sum_{k=0}^{+\infty} i\frac{J_k\{i(C'\alpha/\omega)\}\cdot J_{1-k}\{-i(C'\alpha/\omega)\}}{C'+ik\omega}$$

$$+\sum_{k=1}^{+\infty} i\frac{J_{-k}\{i(C'\alpha/\omega)\}\cdot J_{1+k}\{-i(C'\alpha/\omega)\}}{C'-ik\omega}$$

$$=\sum_{k=0}^{+\infty} i\frac{J_k\{i(C'\alpha/\omega)\}\cdot J_{1-k}\{-i(C'\alpha/\omega)\}}{C'+ik\omega}$$

$$+\sum_{k=2}^{+\infty} i\frac{J_{1-k}\{i(C'\alpha/\omega)\}\cdot J_k\{-i(C'\alpha/\omega)\}}{C'-i(k-1)\omega}$$

and one obtains finally with the use of eqs. (15*a*) and (15*b*)

$$(16a)\quad n_1^{\text{fund}} = -N\frac{D'}{C'}\left(\frac{\beta}{\alpha}-1\right)C'\sum_{k=1}^{+\infty} iJ_k\{i(C'\alpha/\omega)\}\cdot J_{k-1}\{i(C'\alpha/\omega)\}$$

$$\left\{\frac{1}{C'+ik\omega}-\frac{1}{C'-i(k-1)\omega}\right\}e^{i\omega t}+\text{conj. compl.}$$

Application of the expansion given in eq. (15) shows that the sum in eq. (16*a*) contains only odd powers of $(C'\alpha/\omega)$. Relaxation effects will become important when the modulation frequency is of the order of the inverse relaxation time $1/\tau = C'$, so that $C'/\omega \simeq 1$. Except for gases with extremely long relaxation times the photon density attainable in the infrared region will induce much fewer transitions than occur in collisions, hence $\alpha \ll 1$ (see numerical values below). In most cases it will therefore be permissible to neglect the third and higher powers of $C'\alpha/\omega$ with respect to the first. If this is done, eq. (16*a*) simplifies to

$$(16b)\qquad n_1^{\text{fund}} = N\frac{D'}{C'}\left(\frac{\beta}{\alpha}-1\right)\frac{\alpha}{\sqrt{1+(\omega/C')^2}}\cdot\sin(\omega t-\phi),$$

$$\text{with}\quad \tan\phi = \frac{\omega}{C'};\qquad \text{for}\ \frac{C'\alpha}{\omega}\ll 1.$$

This agrees with eq. (9) for $\omega \ll C'$. As the frequency ω is increased, the amplitude of the fundamental frequency component of the modulation of the upper-state population decreases to zero and a phase shift up to 90° occurs. Amplitude and phase are plotted vs. frequency in Figs. 2 and 4 respectively (see discussion in connection with eq. (19)).

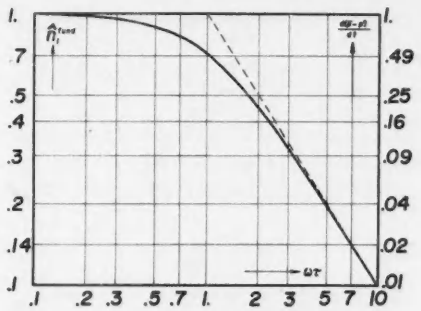

FIG. 2. Relative amplitude of n_1^{fund} and $\{d(\bar{p}-p')\}/dt$ as functions of the relative modulation frequency $\omega\tau$.

It follows from the kinetic theory of an ideal gas that the gas pressure p is related to the average molecular translational energy ϵ per unit volume, viz.

$$p = \frac{2}{3}\epsilon. \tag{17}$$

It is evident from eq. (2) that

$$\frac{d\epsilon}{dt} = E\{(f_{10}+f_{01})\cdot n_1 - f_{01}\cdot N\} \qquad \text{for } t \ll T \tag{17a}$$

(see definition of T following eq. (21)) so that one obtains for the fundamental frequency component of the alternating pressure

$$\frac{dp^{\text{fund}}}{dt} = \frac{2}{3}E(f_{10}+f_{01})\cdot n_1^{\text{fund}}$$

and, substituting eq. (16b) for n_1^{fund}

$$p^{\text{fund}} = -\frac{2}{3}NE\frac{D'}{C'}\left(\frac{\beta}{\alpha}-1\right)\frac{f_{10}+f_{01}}{C'}\frac{\alpha}{(\omega/C')\sqrt{1+(\omega/C')^2}}\cdot\cos(\omega t-\phi), \tag{18}$$

$$\text{with} \quad \tan\phi = \frac{\omega}{C'}; \qquad \text{for} \begin{cases} C'\alpha/\omega \ll 1 \\ \omega T \gg 1. \end{cases}$$

The frequency dependence of amplitude and phase of p^{fund} is shown in Figs. 3 and 4 respectively. At the relaxation frequency $\omega_{\text{rel}} = C'$ the amplitude changes from the low-frequency ω^{-1} dependence to the high-frequency ω^{-2} dependence. The phase of p^{fund} as referred to the phase of the intensity modulation changes continuously from a 90° lag at low frequencies through a 135° lag at the relaxation frequency to a 180° lag at high frequencies.

As the collisional transfer rates f_{10} and f_{01} are proportional to pressure it follows from eq. (4a) that $C' = 1/\tau$ and D' are proportional to pressure, if

$$\rho' B + A \ll f_{01}. \tag{19}$$

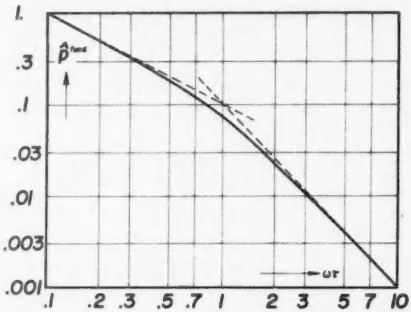

FIG. 3. Relative amplitude of the fundamental frequency pressure component p^{fund} as a function of the relative modulation frequency $\omega\tau$.

This condition is satisfied for most gases under normal experimental conditions, so that, since N is also proportional to pressure, the amplitude and phase of p^{fund} and n_1^{fund} in eqs. (16*b*) and (18) normally depend on pressure p only in the ratio ω/p, i.e. a reduction of p by a certain factor is equivalent to an increase of ω by the same factor.

5. Second-Order Effects

To obtain the frequency dependence of $\bar{n}_1$ (eq. (10)) one has to evaluate the time average of eq. (14*a*) over one period of the modulation of the incident radiation. With

$$\frac{\omega}{2\pi}\int_0^{2\pi/\omega} e^{i(k+l)\omega t}dt = \begin{cases} 0 & \text{for } k+l \neq 0 \\ 1 & \text{for } k+l = 0 \end{cases}$$

one obtains

$$(20)\quad \bar{n}_1 - N\frac{D'}{C'} = N\frac{D'}{C'}\left(\frac{\beta}{\alpha}-1\right)\left[1-C'\sum_{k=-\infty}^{+\infty}\frac{J_k\{i(C'\alpha/\omega)\}\cdot J_{-k}\{-i(C'\alpha/\omega)\}}{C'+ik\omega}\right].$$

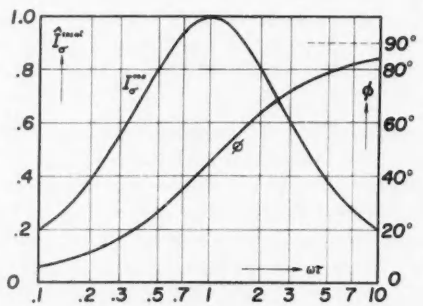

FIG. 4. Relative amplitude of the transmitted quadrature component of radiation, and phase angle ϕ as functions of the relative modulation frequency $\omega\tau$.

Using eqs. (15*a*) and (15*b*) this can be written in the form

$$(20a)\quad \bar{n}_1 - N\frac{D'}{C'} = N\frac{D'}{C'}\left(\frac{\beta}{\alpha}-1\right)\left[1 - J_0^2\{i(C'\alpha/\omega)\} - \sum_{k=1}^{+\infty}\frac{2J_k^2\{i(C'\alpha/\omega)\}}{1+(k\omega/C')^2}\right].$$

Application of the expansion given in eq. (15) shows that eq. (20*a*)) contains only even powers of $C'\alpha/\omega$. Neglecting the fourth and higher powers with respect to the second (see discussion following eq. (16*a*)) simplifies eq. (20*a*) to

$$(20b)\qquad \bar{n}_1 - N\frac{D'}{C'} = -N\frac{D'}{C'}\left(\frac{\beta}{\alpha}-1\right)\cdot\frac{\alpha^2}{2}\cdot\frac{1}{1+(\omega/C')^2}, \qquad \text{for } \frac{C'\alpha}{\omega} \ll 1.$$

This agrees with eq. (10) for $\omega \ll C'$. With increasing frequency the difference $\bar{n}_1 - N(D'/C')$ decreases continuously to zero; at the relaxation frequency it has fallen to half its low-frequency value.

From eqs. (17) and (17*a*) one obtains for the initial rate of increase of the d-c. pressure difference between a cell exposed to the modulated irradiation and one exposed to the constant average photon density ρ',

$$(21)\quad \frac{d(\bar{p}-p')}{dt} = -\frac{2}{3}NE\frac{D'}{C'}\left(\frac{\beta}{\alpha}-1\right)(f_{10}+f_{01})\cdot\frac{\alpha^2}{2}\cdot\frac{1}{1+(\omega/C')^2}, \quad \text{for} \begin{cases} C'\alpha/\omega \ll 1 \\ t \ll T. \end{cases}$$

The frequency (or pressure) dependence of this expression is shown in Fig. 2 (right-hand scale). It is seen that, immediately after the radiation has been turned on, the pressure in a cell exposed to intensity-modulated irradiation increases more slowly than that in a cell exposed to the average irradiation, and that the rate difference decreases with increasing modulation frequency. At the relaxation frequency the pressure difference develops half as fast as at low frequencies. It is this development of a pressure difference between the two cells that Cottrell (1950) suggested to utilize for a measurement of vibrational relaxation times.

As the illumination continues the pressure in either cell will rise to an asymptotic limit at which the power absorbed by the gas equals the power lost to the surroundings because of the increased temperature of the gas. This power loss has been neglected in eq. (17*a*), and consequently eqs. (17*a*) and (21) hold only for times short compared to the time constant T for establishment of the power equilibrium, and the condition $\omega T \gg 1$ has to be imposed on eq. (18). T will depend on cell size, geometry, heat conduction, and convection, and Jones (1958) shows that $\omega T \gg 1$ is easily satisfied except possibly for gases with extremely long relaxation times.

Comparing eqs. (18) and (21) with respect to the magnitude of the pressure that has to be measured experimentally it appears that Slobodskaya's a-c. method is to be preferred in cases where $\rho''BT < 1$, while Cottrell's d-c. method might be advantageous when $\rho''BT > 1$.

6. Infrared Absorption

Equations (16) and (20) suggest that the power absorbed by the gas from the incident radiation will depend on the modulation frequency. To investigate this effect, we note that the radiation intensity I_σ (number of photons per unit wave number interval flowing per second through unit cross section) is related to the σ-photon density ρ_σ (number of photons per unit volume and unit wave number interval) by

$$I_\sigma = c \cdot \rho_\sigma \tag{22}$$

where c = speed of light. It follows from (1) that the number of σ-photons absorbed per second and unit volume is $\rho_\sigma \cdot B(\sigma) \cdot n_0$, so that the decrease of σ-photon flux density I_σ in a layer of thickness dx is

$$-dI_\sigma = \rho_\sigma \cdot B(\sigma) \cdot n_0 \cdot dx = I_\sigma \cdot \frac{B(\sigma)}{c} \cdot n_0 \cdot dx. \tag{23}$$

This differential equation for I_σ is readily solved, giving

$$I_\sigma = I_{0_\sigma} \cdot e^{-[B(\sigma)/c] n_0 x} \tag{23a}$$

with I_{0_σ} = intensity incident at $x = 0$. Equation (23*a*) shows how the Einstein coefficient $B(\sigma)$ is related to the infrared absorption coefficient $k(\sigma)$. The latter is normally referred to unit pressure and measured without consideration of modulation effects so that $n_0 = N - \bar{n}_1$, and

$$k(\sigma) = \frac{B(\sigma)}{c} \cdot \frac{N - \bar{n}_1}{p}. \tag{24}$$

To find the effect of the modulation, we set for the incident intensity in accordance with eq. (3)

$$I_{0_\sigma} = I''_{0_\sigma}(1 + \sin \omega t) \tag{25}$$

and for n_0

$$n_0 = N - \bar{n}_1 - n_1^{\text{fund}}. \tag{26}$$

Equation (23*a*) then yields for the transmitted intensity

$$I_\sigma = I''_{0_\sigma}(1 + \sin \omega t) e^{-k(\sigma) p x} \cdot e^{+[B(\sigma)/c] n_1^{\text{fund}} x}. \tag{27}$$

The second exponent is smaller than the first by a factor $\alpha \ll 1$, so that throughout the usable range of x a first-order approximation of the second exponential will be sufficient. Using eq. (16*b*) one obtains thus for the fundamental frequency component of the transmitted σ-intensity

$$I_\sigma^{\text{fund}} = I''_{0_\sigma} e^{-k(\sigma) p x} \sin \omega t + I''_{0_\sigma} \frac{B(\sigma)}{c} N \frac{D'}{C'} \left(\frac{\beta}{\alpha} - 1 \right) \frac{\alpha x}{\sqrt{1 + (\omega / C')^2}} e^{-k(\sigma) p x} \sin (\omega t - \phi). \tag{28}$$

The second term can be split into a $\sin \omega t$ component, which will be small compared to the first term and therefore difficult to detect, and a $\cos \omega t$

component which can be separated from the relatively large total sin ωt component using phase-sensitive detection techniques. The quadrature component is

$$(29) \qquad I_\sigma^{(\cos)} = -I_{0\sigma}'' \alpha \frac{B(\sigma)}{c} N \frac{D'}{C'} \left(\frac{\beta}{\alpha} - 1\right) \cdot x \cdot e^{-k(\sigma)px} \frac{\omega/C'}{1+(\omega/C')^2} \cos \omega t.$$

The frequency dependence of the amplitude of the quadrature component is shown in Fig. 4. This graph does not give the pressure dependence. It is seen that the amplitude reaches a maximum at the relaxation frequency. For $D'/C' \ll 1$ eq. (24) can be used to write eq. (29) in the form

$$(29a) \qquad I_\sigma^{(\cos)} = -\tfrac{1}{2} I_{0\sigma}'' \alpha \, k(\sigma) px e^{-k(\sigma)px} \frac{\omega/C'}{1+(\omega/C')^2} \cos \omega t \qquad \text{for } \frac{D'}{C'} \ll 1$$

and this expression is maximized with respect to x for $k(\sigma)px = 1$. When x has been so optimized, the maximum quadrature amplitude at the relaxation frequency equals $\alpha/4$ times the amplitude of the sin ωt component in eq. (28).

7. Numerical Values for the 15-μ CO_2 Band

Combination of (1) and eq. (24) shows the number of transitions per second and molecule induced by radiation in the wave number interval σ to $\sigma + d\sigma$ to be given by

$$(30) \qquad \rho_\sigma B(\sigma) d\sigma = \rho_\sigma c k(\sigma) \frac{p}{N - \tilde{n}_1} d\sigma.$$

The density of σ-photons, ρ_σ, is related to the energy density $\mathbf{e}_\sigma$ by

$$(31) \qquad \rho_\sigma d\sigma = \frac{1}{hc\sigma} \mathbf{e}_\sigma d\sigma \qquad \text{with } h = \text{Planck's const.}$$

At the focus of a mirror which is illuminated by a source of strength S_σ (power radiated per unit wave number interval and unit area into unit solid angle) $\mathbf{e}_\sigma$ is given by

$$(32) \qquad \mathbf{e}_\sigma \, d\sigma = \frac{\Omega}{c} S_\sigma d\sigma$$

where Ω is the solid angle subtended by the mirror at the focus. Assuming the source to be a black body at temperature θ, S_σ (unpolarized) is given by Planck's law

$$(33) \qquad S_\sigma d\sigma = \frac{2hc^2\sigma^3}{e^{(hc\sigma/k\theta)} - 1} d\sigma.$$

Substituting eqs. (33), (32), and (31) into (30) the number of transitions per second and molecule induced by σ-radiation becomes

$$(34) \qquad \rho_\sigma B(\sigma) d\sigma = \Omega \frac{2c\sigma^2}{e^{(hc\sigma/k\theta)} - 1} k(\sigma) \frac{p}{N - \tilde{n}_1} d\sigma.$$

According to what has been said in Section 1, eq. (34) must be integrated

over the vibration–rotation band of width $\Delta\sigma$. While the Planck function is slowly varying with σ, $k(\sigma)$ is not, and one obtains

$$\rho B = \int_{\Delta\sigma} \rho_\sigma B(\sigma) d\sigma = \Omega \frac{p}{N-\tilde{n}_1} \frac{2c\sigma^2}{e^{(hc\sigma/k\theta)}-1} \int_{\Delta\sigma} k(\sigma) d\sigma. \tag{34a}$$

The integrated absorption coefficient for the 15-μ CO_2 band centered at $\sigma = 667\ \text{cm}^{-1}$ has been measured by Thorndyke (1947) with the result

$$\int_{\Delta\sigma} k(\sigma) d\sigma = \frac{1}{c} \cdot 560 \cdot 10^{10} \frac{\text{sec}^{-1}}{\text{cm} \cdot \text{atm}}. \tag{35}$$

Putting $(N-\tilde{n}_1)/p \simeq$ Avogadro's number, one obtains

$$\rho B = \frac{0.18}{\text{sterad}} \cdot \frac{\Omega}{e^{(960^\circ\text{K}/\theta)}-1} \frac{\text{radiation-induced transitions}}{\text{second} \cdot \text{molecule}}.$$

The cavity radiation of the gas container ($\Omega = 4\pi$ sterad) at room temperature $\theta = 295^\circ$ K thus produces a molecular transition frequency

$$\rho^0 B = 9.3 \cdot 10^{-2} \frac{\text{radiation-induced transitions}}{\text{second} \cdot \text{molecule}}$$

and the additional transition frequency due to a 1500° K black-body source focussed by an f:3 mirror ($\Omega = 8.5 \cdot 10^{-2}$ sterad) amounts to

$$2\rho'' B = 1.8 \cdot 10^{-2} \frac{\text{radiation-induced transitions}}{\text{second} \cdot \text{molecule}}.$$

One obtains thus

$$\rho' B = \rho^0 B + \rho'' B = 0.10 \frac{\text{radiation-induced transitions}}{\text{second} \cdot \text{molecule}}$$

and

$$\rho'' B = 0.88 \cdot 10^{-2} \frac{\text{radiation-induced transitions}}{\text{second} \cdot \text{molecule}}.$$

The total number of spontaneous vibrational transitions per second and molecule is found to be

$$A \simeq 8\pi\sigma^2 \int_{\Delta\sigma} B(\sigma) d\sigma = 2.3 \frac{\text{spontaneous transitions}}{\text{second} \cdot \text{molecule}}$$

where use has been made of eqs. (1*b*), (24), and (35). Ultrasonic measurements yield for the relaxation time τ in CO_2 at room temperature and atmospheric pressure a value $\tau = 5\ \mu$sec (Henderson and Klose 1959) so that, assuming this to be the relaxation time for the bending mode fundamental, one obtains

$$C' = \frac{1}{\tau} = 2 \cdot 10^5 \frac{\text{transitions}}{\text{second} \cdot \text{molecule}}.$$

This is seen to be very much greater than $2\rho' B + A$ so that eq. (4*a*) yields within the accuracy of the measurement of τ

$$f_{10} = 2\cdot 10^5 \ \frac{\text{collision-induced transitions}}{\text{second}\cdot\text{molecule}},$$

and eq. (1*a*) gives

$$f_{01} = 8\cdot 10^3 \ \frac{\text{collision-induced transitions}}{\text{second}\cdot\text{molecule}}.$$

Equations (4*a*) and (4*b*) can now be used to find

$$D' = 8\cdot 10^3 \ \frac{\text{vibrational transitions}}{\text{second}\cdot\text{molecule}},$$

$$\alpha = 8.8\cdot 10^{-8}, \qquad \beta = 1.1\cdot 10^{-6},$$

and the relative amplitude of the modulation of the upper-state population can be evaluated from eq. (16*b*) with the result

$$\frac{n_1^{\text{fund}}}{N(D'/C')} = \frac{1.0\cdot 10^{-6}}{\sqrt{1+(\omega\tau)^2}} \sin(\omega t-\phi) \qquad \text{for } \omega \gg 0.02 \text{ sec}^{-1}.$$

It is seen that the condition $(C'\alpha/\omega) \ll 1$ is easily satisfied. The relative change of the average upper state population is found from eq. (20*b*) to be

$$\frac{\bar{n}_1 - N(D'/C')}{N(D'/C')} = -\frac{4.6\cdot 10^{-14}}{1+(\omega\tau)^2}.$$

From equation (18) one obtains for the fundamental frequency component of the alternating pressure

$$p^{\text{fund}} = -\frac{9.5\cdot 10^{-2}}{\omega\tau\sqrt{1+(\omega\tau)^2}} \cos(\omega t-\phi) \ \frac{\text{dynes}}{\text{cm}^2} \qquad \text{for } \begin{cases} \omega \gg 0.02 \text{ sec}^{-1}, \\ \omega T \gg 1. \end{cases}$$

At the relaxation frequency $\omega_{\text{rel}} = 1/\tau$, the pressure amplitude equals $6.75\cdot 10^{-2}$ dynes/cm^2, which is 50 db above the acoustical reference $2\cdot 10^{-4}$ dynes/cm^2 and should be measurable without difficulty by standard electroacoustic techniques. Equation (21) gives for the initial rate of increase of the d-c. pressure difference

$$\frac{d(\bar{p}-p')}{dt} = -\frac{8.4\cdot 10^{-4}}{1+(\omega\tau)^2} \ \frac{\text{dynes}}{\text{cm}^2\cdot\text{sec}} \qquad \text{for } \begin{cases} \omega \gg 0.02 \text{ sec}^{-1}, \\ t \ll T. \end{cases}$$

Turning to a discussion of the effect on the infrared absorption of the gas, we obtain from eq. (35) for the average absorption coefficient of the band with width $\Delta\sigma = 90 \text{ cm}^{-1}$ (Thorndyke 1947)

$$\bar{k} = \frac{1}{\Delta\sigma}\int_{\Delta\sigma} k(\sigma)d\sigma = 2.1 \quad (\text{cm}\cdot\text{atm})^{-1}.$$

However, due to the rotational structure of the band, $k(\sigma)$ depends strongly on σ (and also on the gas pressure) and the above average should only be taken as an order of magnitude guidance for the design of an absorption cell. Infrared spectrophotometers can not yet be constructed to measure the trans-

mission in a wavelength interval that is small compared to the rotational line width, so that eq. (29*a*) will have to be integrated over the effective spectral slit width of the instrument before it can be compared with experimental measurements.

Yet the feasibility of such measurements can be judged easily, on the basis of the result derived in Section 6, that the maximum amplitude of the quadrature component at the relaxation frequency equals $\alpha/4$ times the amplitude of the $\sin \omega t$ component in eq. (28). In the case that has been evaluated above, $\alpha/4$ equals $2.2 \cdot 10^{-8}$, so that the use of the quadrature component for relaxation time measurements does not appear to be possible in this case.

CONCLUSION

The theory presented in the foregoing sections shows how it is possible to deduce vibrational relaxation times of gases from measurements on the spectrophone processes. The advantage of the spectrophone method over other methods used hitherto for this purpose (excess sound attenuation, sound velocity dispersion, structure of shock waves, impact tube; see references given by Jacox and Bauer (1957)) is that it permits measurement of the relaxation time of a specified vibrational transition that can be selected by the proper limitation of the spectral band width of the incident radiation. This should permit studies of details of the relaxation mechanism in polyatomic molecules. Measurements with conventional methods have shown (McCoubrey and McGrath 1957) that in almost all gases and vapors investigated so far, the total vibrational contribution to the specific heat appears to be "decoupled" in a single relaxation process. Investigations on how this is to be explained can be carried out with conventional methods only by extending the measurements over a large temperature range, and it is here as well as in studies of gas mixtures that the spectrophone method promises new insights with less experimental difficulty.

The limitations of the spectrophone method rest in the fact that it is difficult to obtain high energy densities of infrared radiation in a limited spectral range. The only experiment known to the author where the signal amplitude was sufficient to allow the use of a monochromator in the optical path is that of Slobodskaya (1948). Also the study of vibrational transitions with short relaxation times is likely to be difficult, firstly because the factor α, and with it the magnitude of the spectrophone effects, becomes too small, and secondly because the modulation frequency must be of the order of magnitude of $1/\tau$ for the measurements to yield relaxation effects. The latter condition is not easily satisfied because it is difficult to construct infrared intensity modulators that operate at high frequencies. Reduction of the gas pressure in order to increase τ can ease the difficulty but to a limited extent.

It should be pointed out finally that the spectrophone method cannot be used for infrared inactive vibrational transitions (because $B = 0$), but it is felt that this limitation should not be too serious for the investigation of the relaxation mechanism in polyatomic gases and gas mixtures.

ACKNOWLEDGMENT

The author gratefully acknowledges a grant given by the National Research Council of Canada in aid of this research.

REFERENCES

BELL, A. G. 1880. Proc. Am. Assoc. Advance. Sci. **29**, 115.
——— 1881. Phil. Mag. **11** (5), 510.
BEYER, R. T. 1957. J. Acoust. Soc. Am. **29**, 243.
COTTRELL, T. L. 1950. Trans. Faraday Soc. **46**, 1025.
DELANY, M. 1959. To be published.
FASTIE, W. G. and PFUND, A. H. 1947. J. Opt. Soc. Am. **37**, 762.
GORELIK, G. 1946. Compt. rend. acad. sci. U.R.S.S. **54**, 779.
HENDERSON, M. C. and KLOSE, J. Z. 1959. J. Acoust. Soc. Am. **31**, 29.
HERZBERG, G. 1955. Molecular spectra and molecular structure, Vol. I, 2nd ed. (D. Van Nostrand Company, Princeton, N.J.), pp. 20–21.
JACOX, M. E. and BAUER, S. H. 1957. J. Phys. Chem. **61**, 833.
JONES, W. D. June 1958. Vibrational relaxation time studies of CO by the infrared spectrophone method. Ph.D. Thesis, Oregon State College, Corvallis, Oregon.
KAISER, R. 1955. Report to the German Research Council (unpublished).
LUCHIN, S. M. 1945. Doklady Acad. Nauk U.S.S.R. **49**, 418.
LUFT, K. F. 1943. Z. tech. Physik, **24**, 97.
MCCOUBREY, J. C. and MCGRATH, W. D. 1957. Quart. Rev. Chem. Soc. (London), **11**, 87.
MERCADIER, M. E. 1881. Phil. Mag. **11** (5), 78.
PREECE, W. H. 1881. Proc. Roy. Soc. (London), **31**, 506.
ROENTGEN, W. C. 1881. Ann. Physik u. Chemie, **12**, 155.
——— Phil. Mag. **11** (5), 308.
SLOBODSKAYA, P. V. 1948. Izvest. Acad. Nauk U.S.S.R. (Physics), **12**, 656.
SOMMERFELD, A. 1948. Vorlesungen über theoretische Physik, Vol. VI, 2nd ed. (Akademische Verlagsgesellschaft M.B.H., Leipzig), p. 109.
STEPANOV, B. I. and GIRRIN, O. P. 1950. J. Exptl. Theoret. Phys. U.S.S.R., **20**, 947.
THORNDYKE, A. M. 1947. J. Chem. Phys. **15**, 868.
TURRELL, G. C. 1954. Determination of the vibrational lifetime of CO by the spectrophone method. Ph.D. Thesis, Oregon State College, Corvallis, Oregon.
TYNDALL, J. 1881. Proc. Roy. Soc. (London), **31**, 307.
VEINGEROV, M. L. 1938. Doklady Akad. Nauk U.S.S.R. **19**, 687.
——— 1945. Doklady Akad. Nauk U.S.S.R. **46**, 182, 200.
——— 1946. Doklady Akad. Nauk U.S.S.R. **51**, 195.
——— 1947. Zavodskaya Laboratoriya, **13**, 426. (*Abstracted in* Chem. Abstr. 1948. **42**, 1467.)

STUDIES OF (p,n) REACTIONS IN THE PROTON ENERGY RANGE FROM 2 TO 10 MEV[1]

D. A. Bromley, A. J. Ferguson, H. E. Gove, J. A. Kuehner, A. E. Litherland, E. Almqvist, and R. Batchelor[2]

ABSTRACT

Reaction thresholds have been studied for (p,n) reactions on B^{11}, F^{19}, Al^{27}, Si^{30}, P^{31}, K^{39}, Ni^{58}, and Ni^{60}. Using the $C^{13}(p,n)N^{13}$ and $Cu^{65}(p,n)Zn^{65}$ thresholds, which have previously been measured with precision, to calibrate the magnetic beam analyzer of the tandem accelerator, and the $H^2(O^{16},n)F^{17}$ threshold to establish the linearity of this calibration to an equivalent proton energy of 14.57 Mev, threshold energies of 3.019 ± 0.004, 4.229 ± 0.006, 5.800 ± 0.008, 5.174 ± 0.030, 6.456 ± 0.020, 7.227 ± 0.070, 9.480 ± 0.025, and 7.016 ± 0.015 Mev, respectively, have been established. These data are in reasonable agreement with the available positron decay data except in the case of Ca^{39} where an unexplained discrepancy exists. Resonances of total width less than 20 kev have been observed in the neutron-excitation curves of the $Al^{27}(p,n)Si^{27}$ and $Si^{30}(p,n)P^{30}$ reactions corresponding to excitations of approximately 17 Mev and 13 Mev in the compound systems Si^{28} and P^{31}, respectively. In the latter case isolated resonances are found without overlapping broad resonances. The reaction threshold falls between resonances and is not directly observable; the counter-ratio technique was calibrated for use in such situations. Neutron yield measurements have been made on thick targets of C, Al, $Ni^{60}O$, $Ni^{58}O$, Ni^{58}, W, Pb, Au, Th, and U as functions of the incident proton energy in the energy range from 4 to 10 Mev.

1. INTRODUCTION

Endothermic (p,n) reactions are particularly suited to the precise determination of nuclear mass differences. In general the slow neutrons associated with ground state thresholds are easy to detect and in many cases the precision with which the threshold energy may be measured is limited by the energy resolution and stability of the proton beam itself and by the precision with which the absolute energy calibration can be established. Conversely, once determined with precision, these (p,n) thresholds constitute excellent calibration points with which to establish the energy calibration of an accelerator beam-analyzing system and to check its stability of operation.

Extensive reports of the results and techniques of threshold measurements using proton energies up to 6 Mev are available in the literature (Marion and Bonner 1959). Above this energy the most precise measurements are those carried out during the tests and preliminary calibration (Gove *et al.* 1958) of the Chalk River tandem accelerator* at the High Voltage Engineering Corporation laboratories prior to its installation at Chalk River. In these measurements calibrations at beam analyzer magnet fields equivalent to proton energies of 9.33 ± 0.015 and 14.47 ± 0.024 were obtained by observation

[1]Manuscript received August 31, 1959.
Contribution from the Physics Division, Atomic Energy of Canada Limited, Chalk River, Ontario.
Issued as A.E.C.L. No. 933.
[2]Seconded from the Atomic Research Establishment, Aldermaston, England.
*Designed and built for Atomic Energy of Canada Limited by High Voltage Engineering Corporation, Burlington, Massachusetts.

of the $H^2(O^{16},n)F^{17}$ threshold using O^{16} ions accelerated in the 5^+ and 4^+ charge states respectively. These tests together with others showed no departure from a linear relationship between proton momentum and analyzer magnet field over the proton energy range from 3 to 14 Mev.

Following installation of the tandem accelerator at Chalk River the analyzing system has been recalibrated using (p,n) thresholds below 6 Mev and a number of (p,n) thresholds in the energy range from 5 to 10 Mev have been determined. In relating the threshold energies to the reaction Q values an approximate relativistic relation given by Langsdorf *et al.* (1954)

$$E_{\text{th}}(0°) = |Q| \left\{1+\frac{m_1}{m_2}+\frac{|Q|}{2m_2c^2}\right\} \tag{1}$$

has been used; m_1 and m_2 are the atomic masses of the incident particle and target, respectively, which were taken from the table of atomic mass data given by Kravtsov (1958). The measurements reported here are of interest in that the isobars involved were previously inaccessible to precision nuclear reaction measurement. The mass differences obtained are compared with those deduced from earlier measurements of the end points of the positron decay of the product nuclei.

In addition the energy resolution inherent in the tandem accelerator design permitted the observation of detailed resonance structure in the neutron yield curves at incident proton energies higher than had previously been used in (p,n) reaction studies. Similar resonance structure has been studied in (α,n) reactions for incident alpha-particle energies in the region of 5 Mev (Gibbon and Macklin 1959, to be published; Litherland and Gove 1959, to be published). A brief study was also made of the neutron yields as a function of energy for a number of elements and compounds throughout the periodic table to test their suitability for beam stopping and collimation.

2. EXPERIMENTAL EQUIPMENT

(*A*) *General*

Figure 1 is a plan view of the Chalk River accelerator building. The gap shown in the 3-foot ilmenite concrete-shield wall between the target and machine rooms has been closed following completion of the installation.

The 90°, 34-in. radius, beam-analyzing magnet uses a uniform field and is designed for second-order, single focussing (i.e. in the median plane only). Such a design has conjugate focal points, one radius of curvature (34 inches) removed from the field boundaries along the beam axis, and entrance and exit beam-defining slits have been provided at these points. The output beam from the accelerator is focussed by a strongly astigmatic magnetic quadrupole pair (Bromley and Bruner 1954) such that a beam crossover point in the horizontal plane is produced at the magnet entry slits while the vertical crossover occurs at the exit slits to coincide with the image of the horizontal crossover point produced by the analyzing magnet itself. In the measurement to be reported herein the entrance and exit slits were fixed at 0.150 and 0.050 inch respectively. Following the exit slit is a uniform field deflecting magnet which is

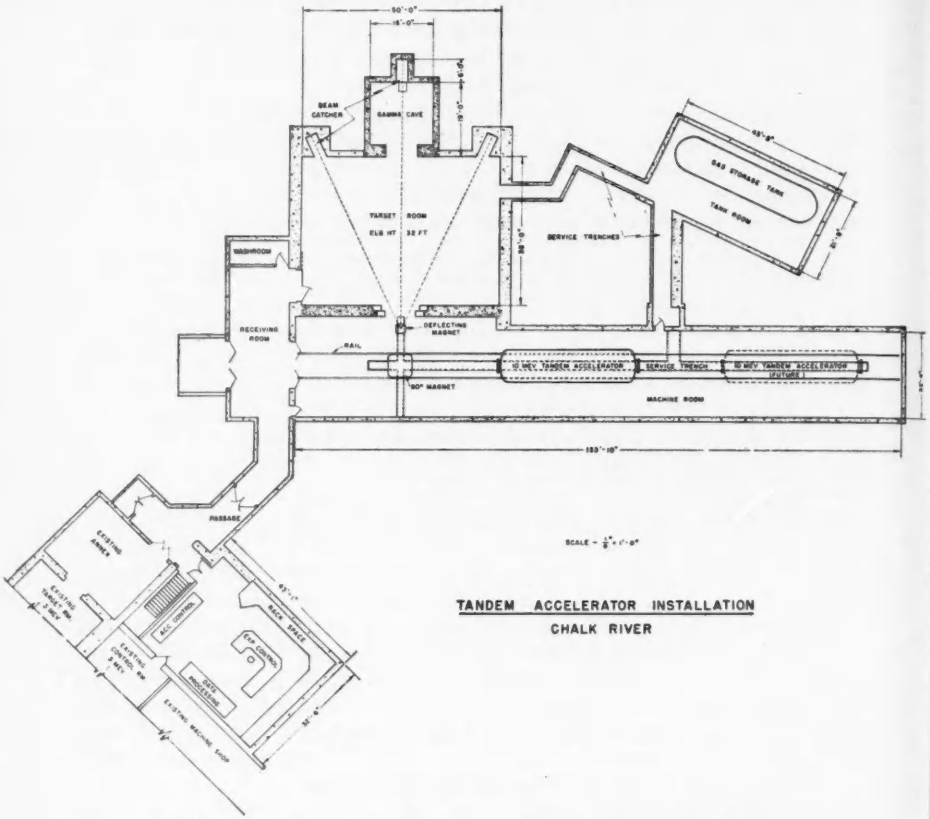

FIG. 1. Plan view of the Chalk River tandem accelerator installation.

used to switch the beam into any one of the three target room beam tubes indicated in the figure. On each tube is a set of magnetic quadrupole lenses capable of producing an image of the beam crossover, occurring at the exit slits of the analyzing magnet, on the target.

It has been found empirically that proper beam optical conditions are obtained when the quadrupole lenses at the output of the machine are adjusted to provide maximum beam transmission through the analyzer magnet and those following are adjusted to give the desired beam profile on the target. In the present work it was found advantageous to adjust the lenses to give a beam spot about 1/8- to 3/16-in. diameter at the target position in the center of the target room rather than to use the line image of the slits.

To monitor the beam profiles and positions, closed-loop television cameras feeding receivers in the accelerator control room are used to view retractable

quartz plates mounted immediately following the exit slits of the analyzer magnet and 4 inches in front of the target. This arrangement has proved invaluable when aligning and focussing the beam and is used whenever a change in beam energy requires readjustment of the focus controls. This was particularly important at high energies where very intense backgrounds are produced if defocussed beam is permitted to strike any material other than the target; activation of the quartz viewer near the target results in significant background radiation and very thin metallic foils coated with a fluorescing compound will be used in future to minimize this background in high-energy experiments.

The beam current incident on the target was measured and integrated using an electrometer – d-c. amplifier circuit (Gingell and Bromley 1958) developed in this laboratory. Focussed proton currents of greater than 1 microampere could be obtained but most of the measurements were carried out with beams of a few tenths of this.

(B) Target and Detector System

The target and detector arrangement is shown in Fig. 2. Targets, either thick enough to stop the proton beam, or if thin, backed by a gold or Ni^{58} beam-

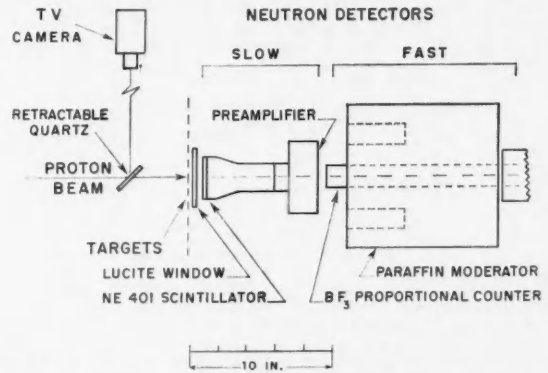

FIG. 2. Schematic representation of the experimental arrangement used in obtaining the neutron-excitation and counter-ratio curves. This figure has been drawn to the scale shown.

stopping plate, were mounted on a slider which permitted the selection of any one of up to 10 targets without opening the vacuum system. Neutrons emerging from the target in the forward direction passed through a 1/4-in. lucite window and were incident on a slow-neutron detector comprising a 3-in. diameter type NE 401, B^{10}- and ZnS-loaded scintillator* optically coupled to a 3-in. Dumont type 6363 photomultiplier. Immediately following this detector on the extrapolated beam axis was mounted a fast-neutron detector; this comprised a modified long counter (Hansen and McKibben 1947), 10 inches in diameter and 10 inches long containing a 1-in. diameter proportional

*Obtained from Nuclear Enterprises Limited, Pembina Highway, Winnipeg, Manitoba.

counter filled to 60-cm pressure with $B^{10}F_3$ isotopically enriched to 99% B^{10}.* The two counters permitted use of the well-known ratio technique (Bonner and Cook 1954) for experimental differentiation between resonant effects and threshold effects in the neutron yield from the target. In many of the cases studied the "slow" counter output alone was adequate to define the threshold.

The operating characteristics of the long counter have been reported previously in connection with studies of the $C^{12}(He^3,n)O^{14}$ reaction (Bromley *et al.* 1957). The characteristics of the NE 401 detector are illustrated in Fig. 3.

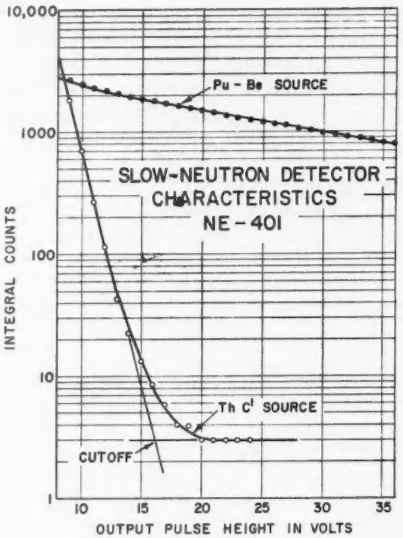

FIG. 3. Characteristics of the NE 401 slow-neutron detector. The pulse height spectra were obtained using calibrated Pu–Be and ThC′ sources mounted on the counter axis. In use as a neutron detector, an integral bias was set at four times the pulse height corresponding to the ThC′ cutoff to discriminate against gamma radiation from the target and environment. This was particularly essential for the $Al^{27}(p,n)Si^{27}$ because of the copious gamma yield, hence electronic add-up from the $Al^{27}(p,\alpha)Mg^{24*}$ and $Al^{27}(p,p')Al^{27*}$ reactions. As noted in the text, the neutron curve extends linearly on this figure to pulse heights $\gtrsim$ 100 volts.

The integral bias curves shown were measured with a 10^5 neutrons/second Pu–Be source mounted 13 inches from the detector which was surrounded by a 3-in. thick paraffin moderator and with a ThC′ source giving a radiation field of about 5 mr/hour of 2.62-Mev gamma radiation at the detector. Similar curves measured with protons incident on an Al target below the $Al^{27}(p,n)Si^{27}$ threshold to give gamma radiation exending to 11 Mev in energy showed experimental cutoff pulse heights (as defined in Fig. 3) roughly twice that for the 2.62-Mev ThC′ radiation.

*We are indebted to Mr. I. L. Fowler for supplying these counters.

Particularly in the case of the neutron threshold measurements on aluminum and nickel targets, very high gamma-radiation backgrounds resulted from proton inelastic scattering reactions. Although the NE 401 detector itself has adequately fast response, the electronic circuitry in use following this detector (double delay line amplifiers, etc.) produced electronic pulse pile-up at the higher gamma counting rates. For this reason an integral bias four times that corresponding to the ThC′ cutoff was used in the present measurements; the neutron spectrum extends linearly on the logarithmic ordinate of Fig. 3 to pulse height $\gtrsim$100 volts. The electronic pile-up, of course, shifts the effective

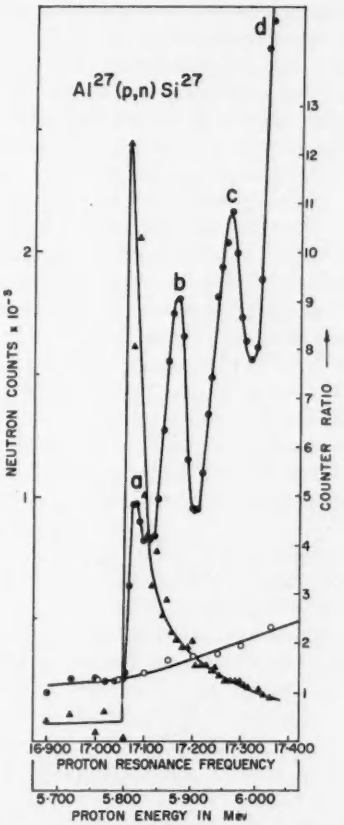

FIG. 4. Thin target slow-neutron excitation and counter-ratio curves for the $Al^{27}(p,n)Si^{27}$ reaction in the region of threshold. The open circles represent the background measured for protons on the gold target backing and the triangles representing the counter ratio were obtained following a point-by-point subtraction of the neutron yield from the backing from that with both target and backing for both slow- and fast-neutron detectors. The letters identify structural features in the excitation curves corresponding to features shown in Fig. 5.

bias point for neutron detection as well. In threshold measurements, however, over a relatively narrow energy range, the gamma-radiation background, hence any such shift, is effectively constant and does not affect the accuracy of these measurements. In the measurement of relative neutron yields from a number of targets, care was taken to keep the beam intensity on target low enough to prevent any significant pile-up. For proton energies in the energy range from 8 to 10 Mev this implies beam intensities in the 1–10 mμa range on thick targets.

Figure 4 illustrates the performance of the ratio technique with these detectors on the $Al^{27}(p,n)Si^{27}$ reaction in the region of the reaction threshold. These data were obtained using a 200 $\mu g/cm^2$ target of aluminum on a thick gold backing; background measurements were carried out in identical geometry using the gold backing alone. By subtracting the background yields point by point from both the "slow" detector results shown and from the "fast" counter data, the "slow" and "fast" yields from the $Al^{27}(p,n)Si^{27}$ reaction alone were determined, and from these in turn were obtained the counter ratios shown in the figure. These data illustrate the excellent discrimination possible between threshold and resonance phenomena using the ratio technique especially in the vicinity of the threshold where the emergent neutrons are of relatively low energy and a stable, pure target is available.

Once the variation of the counter ratio with proton energy has been established it is in principle possible to use a ratio measurement to determine the amount by which the incident proton energy exceeds the threshold value for a given reaction. This application of the ratio technique will be discussed in some detail because it will be used in Section 3(*J*) to obtain the threshold energy of the $Si^{30}(p,n)P^{30}$ reaction which shows marked resonance structure in the neutron yield. The threshold corresponds to an incident proton energy where the reaction cross section is too small to allow detection of the reaction neutrons, in the presence of the inevitable background, with adequate statistical accuracy.

For a given detector arrangement the magnitude of the counter ratio is dependent on the reaction kinematics and geometric effects. Fortunately these are very similar for the $Al^{27}(p,n)Si^{27}$ and $Si^{30}(p,n)P^{30}$ reactions so that the counter-ratio technique may be calibrated using the first of these for use in determining the threshold for the second. The degree of similarity is illustrated by Table I.

TABLE I

Threshold neutron kinematics

$E-E_{th}$, kev		0	3	5	8	12	20	40	100
Neutron energy at 0°, kev	Si^{30}	5.8	16	21	0.1 26	0.9 33	3.7 45	14 72	53 145
	Al^{27}	7.4	19	26	30	0.4 37	2.5 49	11 78	48 150

NOTE: Comparison of neutron energies at 0° from Si^{30} and Al^{27} as a function of excess proton energy above threshold in kiloelectron volts. The neutron cone opens to 90° at 6.2 kev above threshold energy for Si^{30} and at 8 kev above threshold for Al^{27}. At higher proton energies the neutron energy is double value at 0°.

The following discussion of the counter-ratio technique is valid only for proton energies below the threshold for production of the first-excited state of the residual nucleus. In this energy range only a single neutron group is emitted from the target material together with a neutron background from impurities and the target backing. The counter ratio is defined by the relation

$$R = \frac{N_S^0}{N_F^0} = \frac{N_S - B_S}{N_F - B_F}, \tag{2}$$

where the subscripts S and F refer to the slow and fast counters respectively; N^0 is the net count after subtraction of the background B from the total count N. The ratio curve shown in Fig. 4 was obtained by subtracting point by point the background yields as measured with a gold backing identical with that used with the 200 μg/cm^2 Al targets; a small residual normalization ($\sim 5\%$) was required below threshold to compensate for the additional target contaminants which had collected on the original gold backing during previous bombardments.

During the course of these measurements it became apparent that under certain restricted conditions it was possible to avoid the necessity for the detailed background subtractions just described; this applies when sufficiently sharp resonances are present in the (p,n) reaction excitation curve so that narrow energy intervals exist where the quantities R and B in equation 2 remain relatively constant while the neutron yield N varies rapidly. Rearrangement of equation 2 gives

$$N_S = RN_F - (RB_F - B_S) \tag{3}$$

where the term in parentheses may be regarded as constant over the energy interval corresponding to the rising edge of a sharp resonance. In this interval the value of the counter ratio R is given by the slope of a plot of N_S vs. N_F. No determination of the background intensity is required beyond the demonstration that it remains relatively constant over the narrow energy region used. A plot of this type for the $Al^{27}(p,n)Si^{27}$ resonances in the region just above threshold is shown in Fig. 5. The labels a, b, c, and d correspond to those on the four resonances and the threshold as illustrated in Fig. 4. The points obtained from the rising edge of each resonance fall on a straight line whose slope is taken as the value of R at the energy corresponding to the midpoint of the rise. Similarly values at slightly higher energies are obtainable from the trailing edge of each resonance. The value of the counter ratio as a function of energy obtained by this technique with the $Al^{27}(p,n)Si^{27}$ reaction is shown in Fig. 5. This is to be compared with the curve given by detailed background subtractions shown in Fig. 4. The method illustrated in Fig. 5 of course requires the presence of resonances but has the advantage that detailed background measurements, which are sometimes difficult to make if the target compound itself contains a source of background, are not required. Both techniques were used to analyze the $Si^{30}(p,n)P^{30}$ data. Inherently the second technique just described is of lesser precision. In practice it requires measure-

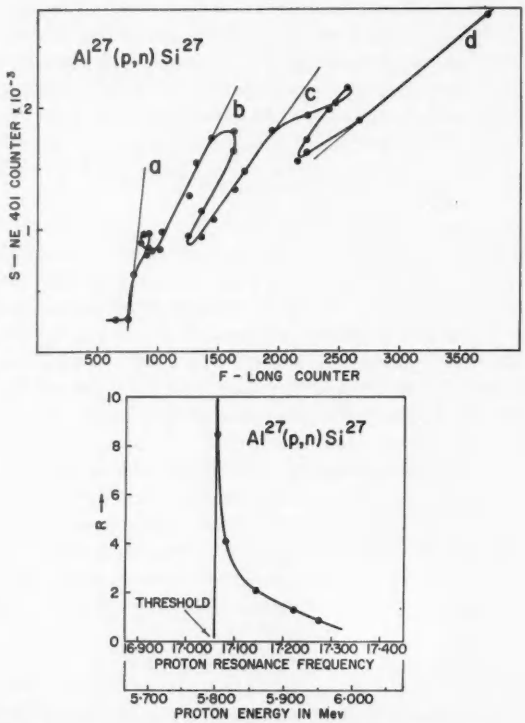

FIG. 5. In the upper part of this figure the slow- vs. fast-neutron detector yields for a thin target of Al^{27} are plotted to obtain an indirect measure of the counter ratio as a function of neutron energy above threshold. The letters identify corresponding structural features of the excitation curves of Fig. 4. The lower part of this figure shows the counter-ratio calibration curve so obtained for the $Al^{27}(p,n)Si^{27}$ reaction.

ments very closely spaced in energy over the structural features of the excitation curve in order to accurately define the slopes of the tangent lines as in Fig. 5. This is of particular importance in the region immediately above threshold where the ratio changes very rapidly; the discrepancies between the ratio values of Figs. 4 and 5 at threshold are clearly attributable to this slope sensitivity.

Perhaps the major utility of this technique lies in its use as a rapid means of displaying data as it is accumulated, in order to identify new threshold phenomena (as reflected by an increase in the slope of the figure). This is particularly true in the case of weak thresholds which might not otherwise be directly observable without performing detailed background subtractions. In the absence of secondary thresholds the slope of the "slow" vs. "fast" plot should decrease monotonically.

(C) Data Handling

The outputs of integral discriminators on both the slow- and fast-neutron channels, together with a digital reading of the resonance frequency from the nuclear resonance probe in the 90°-beam-analyzing magnet field, were applied to transistorized scalers.* An output system† using an electric typewriter and a tape punch in parallel provides a printed and punched paper tape record including (*a*) the run number, (*b*) the date, (*c*) the run duration, (*d*) the integrated beam on target, (*e*) the nuclear resonance frequency, hence beam energy, and (*f*) the contents of up to four scalers with appropriate multipliers all in under 7 seconds. On demand the record includes the output of up to three 100-channel analyzers‡ in addition to their gain and back bias settings.

(D) Targets

Thick targets of high-purity aluminum (99.99%), silicon, electrolytically purified copper, lead, thorium, gold, tungsten, and uranium were cut from metal ingots. Carbon targets were made from high-purity reactor-grade graphite. $Ni^{58}O$ (99.6% Ni^{58}) and $Ni^{60}O$ (99.1% Ni^{60}) targets§ were obtained by sintering the oxide‖ into circular disks (3/8 inch in diameter) of areal density 560 mg/cm². A target of metallic Ni^{58}§, 3/8 inch in diameter and 0.2 g/cm² thick, was used for the threshold measurements. Thick potassium targets were prepared by fusing KOH onto a platinum backing. Targets of red phosphorus on platinum were deposited from a solution in alcohol.

Thin targets of the following materials were used: aluminum foil 200 μg/cm² on gold; isotopic B^{11} (99%) 100 μg/cm² on tantalum;¶ Si^{29} 120 μg/cm² on 0.00025-in. tantalum¶ backed by gold; Si^{30} 120 μg/cm² on 0.00025-in. tantalum¶ backed by gold (CF_2), evaporated onto aluminum; $K^{39}I$ 100 μg/cm² on 0.00025-in. tantalum¶ backed by gold. Thin P_2O_5 targets were prepared by sublimation of P_2O_5 onto gold backings.

(E) Neutron Yields from Thick Targets

Figure 6 presents the results of neutron yield measurements on a number of thick targets using both the NE 401 and the long counter. These were carried out to provide information on the suitability of these materials for use as target backings and in beam collimator assemblies. In addition, these measurements are of value in the design of shielding for use with tandem accelerators. These data were obtained with the detectors just described used in the geometry shown in Fig. 2.

In order to calibrate the long counter, a Pu–Be neutron source standardized at $1.36(+0.05)\times10^5$ neutrons per second was placed in the target geometry.

*Model AEP 918. †Model AEP 2240, AEP 2241, AEP 2245, AEP 2248. ‡Model A 10023.

NOTE: These instruments have been developed by the Electronics Branch, Atomic Energy of Canada Limited, Chalk River, Ontario. We are particularly indebted to Messrs. W. D. Howell and F. S. Goulding for supplying prototype models of several of these circuits for our use.

§Obtained from the Separated Isotopes Division, Oak Ridge National Laboratories, Oak Ridge, Tennessee.

‖We are indebted to Mr. A. Ross for assistance in preparing these sintered targets.

¶Obtained from the Electromagnetic Separator Group, Atomic Energy Research Establishment, Harwell.

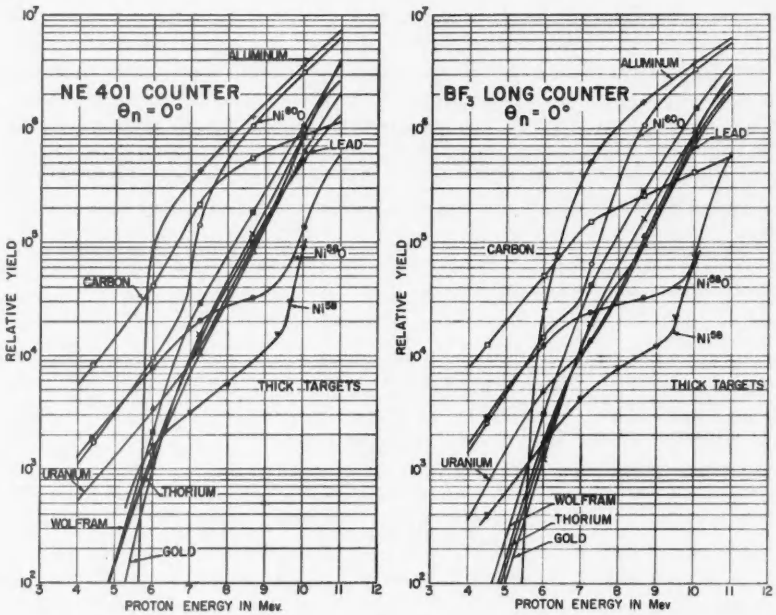

FIG. 6. Relative neutron yields from proton bombardment of the indicated thick targets. In all cases, except where indicated, targets having natural isotopic abundances have been used. Absolute measurements on a thick gold target are discussed in the text; from these and the above figures the absolute yields from other targets may be estimated. Only representative experimental points are shown on these curves for ease in identification.

The number of counts recorded in 10 minutes was 5912. These data provided an absolute calibration which was used to estimate the magnitude of the neutron yields from the thick targets per microcoulomb of beam. No experiments with shadow cones were carried out to determine the contribution from wall scattering since the purpose was to investigate the suitability of beam-stopping materials in the experimental arrangement used and not to attempt absolute yield measurements. However, for a gold target bombarded by 10-Mev protons the result obtained was 3×10^7 neutrons per steradian per microcoulomb of incident proton charge at 0° to the beam. The yields from other materials may be obtained by combining this result with the relative fast-neutron yields shown in Fig. 6.

A number of interesting points are illustrated by this figure. In the case of the high Z targets the yields are all identical within about a factor of 2 and show a roughly exponential increase in neutron yield, with increasing proton energy, of about a factor of 10 per million electron volts of additional proton energy. Uranium is somewhat anomalous in showing increased yield at the low and high ends of the energy range covered. This is presumably from the (p,n) reaction on absorbed O^{18} at low energies and from the proton-induced fission neutron yield at high energies.

Since the thresholds for the $Ni^{60}(p,n)Cu^{60}$ and the $Ni^{58}(p,n)Cu^{58}$ reactions are at 7.018 and 9.480 Mev, respectively, at lower energies the indicated neutron yield from the NiO targets results chiefly from the 0.20% $O^{18}(p,n)F^{18}$ reaction with a threshold energy of 2.58 Mev and to a lesser degree from traces of impurities with low thresholds. The (p,n) reactions on O^{16} and O^{17} have threshold energies of 17.40 and 3.76 Mev, respectively (Ajzenberg-Selove and Lauritsen 1959; Bromley and Rutledge 1958); the O^{17} isotope is present to only 0.04%, however (Nier 1950). Below the Ni^{58} threshold, the neutron yield from a metallic Ni^{58} target is roughly a factor of 5 lower than that from the corresponding oxide targets. This residual yield is presumably from a small amount of oxide contaminant and from other metallic contaminants as in the oxide case. The yield behavior at low energy suggests the presence of medium weight element contaminants.

Below the neutron threshold at 5.800 Mev, proton bombardment of 99.99% aluminum produces very few neutrons. These are presumably from (p,n) reactions on residual impurity nuclides as well as from photoneutron reactions induced by the copious gamma radiation from proton reactions on aluminum; above threshold this yield rises very rapidly as shown. These measurements demonstrate that below 5.80 Mev superpure aluminum constitutes an excellent target-backing material from the viewpoint of neutron yield; for some types of experiments it has the marked disadvantage of very copious gamma-radiation production via the $Al^{27}(p,p',\gamma)$ and $Al^{27}(p,\alpha,\gamma)$ reactions. Neutrons from the carbon target result from the (p,n) reaction on C^{13} (1.1% abundant) with a threshold energy of 3.237 Mev (Bondelid 1958). A target backing of carbon depleted in C^{13} should be excellent since C^{12} (p,n) has a threshold at 19.95 Mev (Ajzenberg-Selove and Lauritsen 1959). Such a backing has not been available although the problems involved in fabricating one are under investigation.

(F) Beam-Energy Stability and Reproducibility

The most suitable threshold for checking the energy stability and reproducibility of the accelerator was found to be that for the $Al^{27}(p,n)Si^{27}$ reaction. It combines a relatively high threshold energy, 5.80 Mev, with a very steeply rising neutron yield as the proton energy is increased above threshold; pure, durable targets are readily obtained. In Fig. 7 are presented results which demonstrate the maximum energy deviations observed for this threshold since the installation of the accelerator at Chalk River. The extreme values indicated in the figure by curves *b* and *c* correspond to deviations of ± 0.006 Mev or ± 1 part in 10^3 in energy away from the mean. Curves *b* and *c* were obtained by using the einzel lenses and injection magnet controls on the accelerator ion source to reduce the beam intensity by factors between 10 and 100 below the maximum obtainable without change in the ion source or charge exchange system parameters. This sensitivity to the ion source lens and injection magnet settings may well reflect the fact that negative ions are produced with different energy from each of the atomic and molecular positive ion beams from the source itself. The negative ions from H^+, HH^+, and HHH^+ normally have

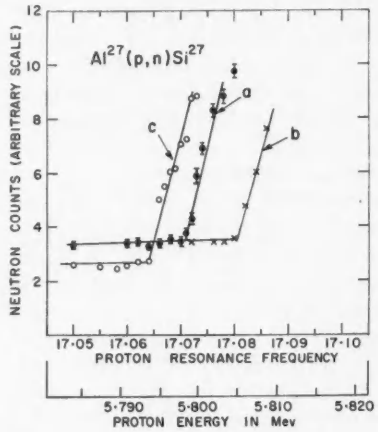

FIG. 7. Threshold measurements on the $Al^{27}(p,n)Si^{27}$ reaction illustrating the maximum apparent threshold shifts corresponding to variation of the ion source beam optical controls.

injection energies to the accelerator of approximately 80, 60, and 53 kev respectively. This maximum energy is variable over some 20 kev depending upon the charge exchange system parameters while the ratio of the three energies remains fixed. The 15° beam selection magnet does not resolve these three components completely. Typical negative ion yields measured from each of the three positive beam components are in the ratio of 1:100:0.15. Under normal operating conditions with this accelerator, the ion source is initially adjusted at the beginning of a 16-hour operation period, the injection magnet and einzel lenses are adjusted to maximize the injected negative ion beam and no further adjustments are made independent of changes in the output energy of the accelerator other than minor ones to correct for minor drifts in the injection magnet field for example. This mode of operation is equivalent to setting a "window" on the peak of the negative ion spectrum corresponding to the HH^+ source output with a fixed injection energy of 60 kev.

When it has been necessary for background or targetry considerations to reduce the beam intensity by large factors, the usual operational technique has involved changing the field of the injection magnet to move this "window" off the dominant peak in the negative ion spectrum. By appropriate adjustment it is of course possible to mix any two of the three beam energy components in an arbitrary intensity ratio; when two energy components are injected for example, it becomes possible for the accelerator to stabilize on one component while transmitting both to the target. In all cases the apparent threshold measured corresponds to the higher-energy beam component.

All threshold measurements reported herein were made with the analyzer magnet entry slit set to 0.150 inch and with the beam focussing such that the beam was balanced between these slit jaws (i.e. equal beam was intercepted by these jaws). The exit slit was set to 0.050 inch. In units of the mean orbit radius

the widths are 0.0045 and 0.0015 respectively. Since the beam was held centered on the input slit as just noted, the exit slit width effectively determines the energy definition of the beam on target. From the geometry of the system alone it might be concluded therefore that the slit setting used would correspond to an energy uncertainty of 1.5 parts in 10^3. This, however, assumes that the beam has negligible lateral extent; this is clearly not justified here. Remote observation of the quartz viewer at these slits indicates a minimum beam width comparable to that of the slit aperture with consequent reduction in the anticipated energy spread, in the beam. Similar measurements on other electrostatic accelerator systems (Kingdon *et al.* 1955) have shown that the maximum energy spread in the beam was at least a factor of 2 smaller than the slit and magnet geometry alone would suggest. An estimate of 5 parts in 10^4 has been included in the assignment of errors to the measured threshold to include this effect of beam energy spread.

Individual measurements, with the ion source controls adjusted for maximum transmission of negative ions (the intensity is still controllable using the parameters of the source itself), have reproduced threshold energies to better than 1 part in 10^4 even when measured before and after disassembly of part of the accelerating column itself.

The results presented in Fig. 7 show that for any given run with fixed ion source conditions over the threshold the energy stability and reproducibility are extremely good; points taken going up through the threshold fall on the same curve as those taken coming down demonstrating that effects due to relative hysteresis between the fluxmeter probe position and beam orbit in the magnet are negligible at least up to the 4-kilogauss value of the $Al^{27}(p,n)Si^{27}$

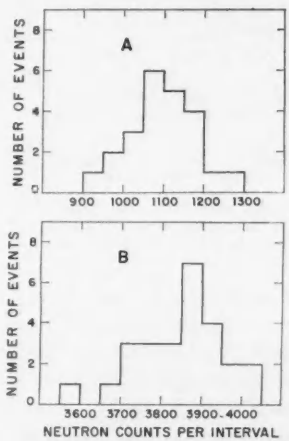

FIG. 8. Histograms showing the variation of the neutron yield from the $Al^{27}(p,n)Si^{27}$ reaction over 1-hour periods with the accelerator, in each case, initially set at selected energies on the rising edge of the thick target threshold yield step (Fig. 4) and without further adjustment of the accelerator controls during the period. The half-widths of these histograms correspond to an energy stability of about 1 part in 10^4 for the proton beam on target.

threshold. The energy stability of the machine over periods of 1 hour or more was examined by taking measurements on the steeply rising part of the yield curve just above threshold and leaving the machine controls untouched except for an occasional manual adjustment. The number of counts per 50 microcoulombs on the target were recorded about every 3 minutes; the hystograms of Fig. 8 were obtained by plotting the number of measurements giving neutron counts in each interval of 50 counts against the number of recorded counts. The full width at half maximum of these distributions, as determined using the neutron counting rate vs. incident energy (or resonance frequency) plot of Fig. 4, is 1 kc/sec in 17,000 or 1 part in 8500 in energy over the test period. These measurements suggest that the 0.5‰ energy uncertainty quoted above is a realistic estimate. An illustration of the energy resolution and stability obtained is given by the measurements on the sharp resonance in the $Si^{30}(p,n)P^{30}$ reaction at 5.205-Mev proton energy shown in Fig. 9; here successive measurements were in some cases made at energy increments of 125 ev.

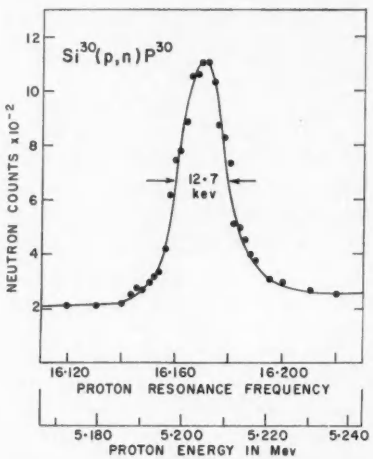

FIG. 9. Detailed neutron-excitation data in the region of the 5.205-Mev resonance in the $Si^{30}(p,n)P^{30}$ reaction illustrating the energy stability available with the tandem accelerator. These measurements were carried out on a 120 $\mu g/cm^2$ target on 0.00025 in. tantalum backed by gold.

In the case of the new reaction thresholds reported herein, the attainable precision was limited by the threshold definition and the cross sections at threshold relative to those for background reactions rather than by the error introduced by the use of the relatively large 0.050-in. slit aperture; consequently it was not considered worth while to reduce this aperture further. In cases where the reaction threshold is sharply defined the attainable precision presumably would be increased with a narrower slit, but with greater operational difficulties in obtaining a given beam current on the target.

(G) Energy Calibrations

The energy of the ion beam incident on the target is defined by the 90° magnetic beam analyzing system; the relation between particle kinetic energy

E and the frequency f of the nuclear resonance fluxmeter which measures the magnetic field is

$$E(1+E/2Mc^2) = kf^2g^2/M, \tag{4}$$

where g is the effective charge of the ion traversing the magnetic field, M is its mass, and E/Mc^2 is the ratio of its kinetic energy to rest mass energy. The calibration parameter k is defined by equation 4; in the present work E is in million electron volts, g in units of the electronic charge, m in atomic mass units, and f in megacycles per second. Measurements reported previously (Gove *et al.* 1958) showed no indication of any variation of k over the range 3 to 14 Mev equivalent proton energy. This corresponds to analyzer magnetic fields from 2.9 to 6.2 kilogauss in which range no magnetic saturation effects are expected to occur. Since all the present measurements lie below 5.4 kilogauss, constancy of k is assumed.

The ground state thresholds for the (p,n) reactions on C^{13} and Cu^{65} were used as calibration points to determine k. They are the most precisely established thresholds above 2 Mev in the energy range readily accessible with the tandem accelerator; the $C^{13}(p,n)N^{13}$ threshold energy has been measured on an absolute scale by Bondelid (1958) using an electrostatic analyzer to be 3.2372 ± 0.0016 Mev and the weighted mean of a number of determinations (Marion and Bonner 1959) of the $Cu^{65}(p,n)Zn^{65}$ threshold energy is 2.1646 ± 0.009 Mev. Measurements made using thick targets of natural isotopic concentration are presented in Figs. 10 and 11. The results of the calibration runs are summarized in Table II. The question of associated errors will be discussed in detail in Section 3(*B*).

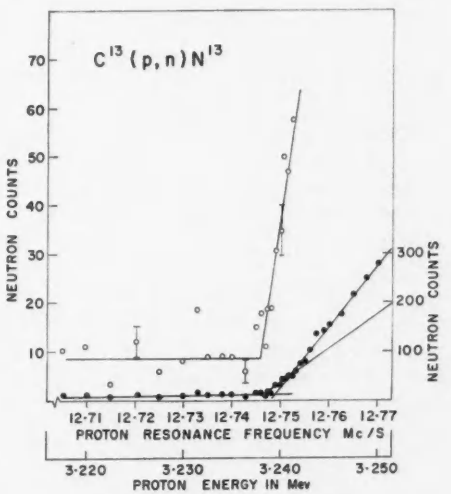

FIG. 10. Slow-neutron excitation data for the reaction $C^{13}(p,n)N^{13}$ on a thick target of superpure pile graphite. The open circles represent the same data plotted on a more expanded ordinate to illustrate the precision with which the threshold frequency is determinable.

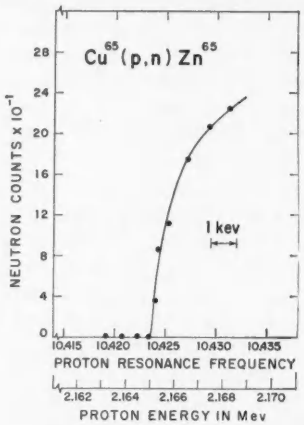

FIG. 11. Slow-neutron excitation curve for proton bombardment of a thick target of electrolytically purified copper with natural isotopic abundances. This figure illustrates the dependence of the yield profile above threshold upon the detailed resonance behavior in the compound system and is opposite in curvature to the profile normally expected.

TABLE II

Calibration reaction data

Run	Reaction	E_{th}, Mev	f, Mc/sec	$k \times 10^{-5}$
1	$C^{13}(p,n)N^{13}$	3.2372±0.0016	12.746±0.006	2011±2
2	$C^{13}(p,n)N^{13}$	3.2372±0.0016	12.738±0.006	2013±2
3	$Cu^{65}(p,n)Zn^{65}$	2.1646±0.0009	10.424±0.005	2010±2

3. RESULTS

(*A*) *General*

Having established the energy calibration of the proton beam analysis system as described in the preceding section, detailed measurements were carried out on neutron yields to establish the threshold energies and hence Q values for the (p,n) reactions on B^{11}, F^{19}, Al^{27}, Si^{30}, P^{31}, Ni^{60}, K^{39}, and Ni^{58}. The first three of these have been measured previously; the measurements reported herein corroborate these earlier measurements. The latter five reactions have not been examined prior to the use of the tandem accelerator; preliminary results on P^{31}, Ni^{60}, and Ni^{58} have been published (Gove *et al.* 1958) following initial measurements with this accelerator.

In cases where neutron background below the threshold under study was negligible, either because of a low threshold energy (e.g. B^{11}) or the absence of either target impurity or backing yields (e.g. Al^{27}), the slow-neutron excitation curve alone was adequate to define the reaction thresholds unambiguously. In other cases where this background was appreciable the counter-ratio technique was used to confirm the identification of the threshold.

The frequency corresponding to the threshold energy was taken in each case as the intercept of the tangent drawn to the slow-neutron yield or counter-

ratio curves, over a 5- to 10-kev energy interval above threshold, with the extrapolated background curve below threshold.

Since the relativistic factor in equation 4 is relatively constant the figures in this paper are plotted effectively against the square root of the incident energy. It has been suggested (Marion 1959*a*) that the greatest precision is obtainable when the reaction thresholds are obtained by extrapolation on a plot of neutron counts versus $(E_{\text{proton}})^{2/3}$. In the cases reported herein the discrepancy between threshold values obtained from these two types of plots is very much less than the quoted errors, consequently it was not considered worth while to reduce the experimental data to the suggested $E^{2/3}$ plot. In measurements with greater precision, i.e. much reduced slit widths etc., this distinction may become much more important.

In the anomalous case of $Si^{30}(p,n)P^{30}$ which will be discussed in detail later such a direct determination of the threshold energy was precluded by the very small cross section at threshold and the counter-ratio calibration technique described above was used. No evidence was found during these measurements for target surface contaminants; the effects of target thickness will be discussed under the $Al^{27}(p,n)Si^{27}$ subheading to follow.

(*B*) *Error Sources*

In evaluating the error associated with each threshold measurement quoted herein, the sources of error considered were those resulting from uncertainties in (*a*) the accelerator energy calibration, (*b*) the energy spread in the beam on target, (*c*) the determination of the magnetic field, i.e. frequency, corresponding to the reaction threshold.

In (*a*), since this calibration is itself based on measurements of reaction thresholds, it is necessary to consider both (*b*) and (*c*) as well as (*d*) the uncertainties in the calibration threshold energies used.

As noted in Table II, the quoted errors in the standard thresholds used are close to 0.5‰; those in the threshold frequencies are also 0.5‰ (1.0‰ in energy). As discussed in Section 2(*F*), an error of 0.5‰ has been assigned to the beam energy on target at a given magnetic field because of the finite slit apertures used and the possibility of a non monoergic beam from the accelerator although this latter situation applies only when the beam was markedly reduced using the ion source optical elements. Such was not the case during the calibration measurements suggesting that the assigned error is a conservative one. Combination of these errors results in an error in the accelerator energy calibration of 1.2‰. In the individual threshold measurements reported herein, the error in energy resulting from the actual threshold frequency determination varies from 0.08‰ in the case of the $B^{11}(p,n)C^{11}$ reaction to 9.8‰ in the case of the $K^{39}(p,n)Ca^{39}$ reaction depending upon the reaction cross section and the ambient backgrounds at the threshold.

Clearly in the case of the $K^{39}(p,n)Ca^{39}$ reaction, for example, this is the dominant error source; in the case of the $B^{11}(p,n)C^{11}$ reaction it is quite negligible.

The error (*b*) corresponding to the finite energy definition on target has been

taken as 0.5‰ for all threshold measurements, as discussed previously. In no case in these measurements was the ion source operated in the extreme conditions corresponding to curves *b* and *c* of Fig. 7, which would correspond to a 1‰ effect.

Table III lists the error contributions for the direct reaction threshold measurements.

TABLE III

Reaction threshold measurement error sources

Reaction	Calibration error, ‰	Energy definition error, ‰	Energy error from threshold frequency, ‰	Total error, ‰
$B^{11}(p,n)C^{11}$	1.2	0.5	0.08	1.3
$F^{19}(p,n)Ne^{19}$			0.14	1.3
$Al^{27}(p,n)Si^{27}$			0.28	1.3
$P^{31}(p,n)S^{31}$			2.8	3.1
$Ni^{60}(p,n)Cu^{60}$			1.6	2.1
$K^{39}(p,n)Cu^{39}$			9.8	9.6
$Ni^{58}(p,n)Cu^{58}$			2.0	2.4

The threshold measurements will be presented in order of ascending energy excepting those on Si^{30}, which will be deferred until the end of this section.

(*C*) $B^{11}(p,n)C^{11}$

Figure 12 presents the yield of slow neutrons from a 100 $\mu g/cm^2$ target of isotopically enriched B^{11} as a function of the bombarding proton energy. The observed threshold frequency of 12.3083±0.0005 Mc/sec corresponds to a threshold energy of 3.019±0.004 Mev.

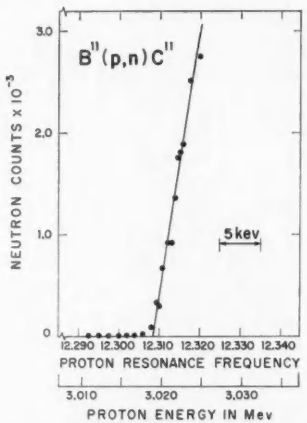

FIG. 12. Slow-neutron excitation curve for the $B^{11}(p,n)C^{11}$ reaction on a 100 $\mu g/cm^2$ target of isotopically enriched B^{11} on 0.020-in. tantalum.

(*D*) $F^{19}(p,n)Ne^{19}$

Figure 13 presents the equivalent data for a thin target of teflon $(CF_2)_n$ evaporated on superpure aluminum. Use of a thick teflon target is precluded by its extremely high resistivity which results in high charge, hence potential, build-up at the target spot. This repelling potential has been observed to shift

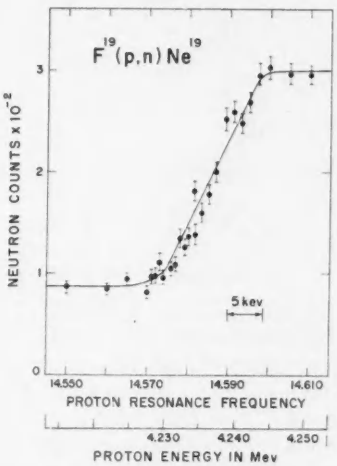

FIG. 13. Slow-neutron excitation curve for proton bombardment of a thin target of teflon $(CF_2)_n$ evaporated onto a superpure aluminum backing.

the apparent threshold by several hundred electron volts. The observed threshold frequency of 14.5725 ± 0.0010 Mc/sec corresponds to a threshold energy of 4.229 ± 0.006 Mev.

(*E*) $Al^{27}(p,n)Si^{27}$

Figure 14 presents the slow-neutron yield curves for both a 200 $\mu g/cm^2$ Al target on gold and for a thick target of superpure Al. No previous measurements are available using a thin Al target. As illustrated in this figure, extrapolation of the thick target yield curve from more than ~ 10 kev above threshold leads to an apparent threshold too high by ~ 2 kev. It should be noted, however, that such extrapolation from thick target yield data does not necessarily lead to a threshold value in excess of, or equal to, that from a thin target as has been assumed in the literature (Marion and Bonner 1959). The exact shape of the excitation curve in the energy interval immediately above threshold depends critically upon the resonance behavior in the compound system involved. Extrapolation of the thick target copper data as presented in Fig. 11 for example would lead to too low a value for the threshold if measurements were made at 1-kev intervals and the tangent extrapolated back using only the data for the first 5 kev above threshold.

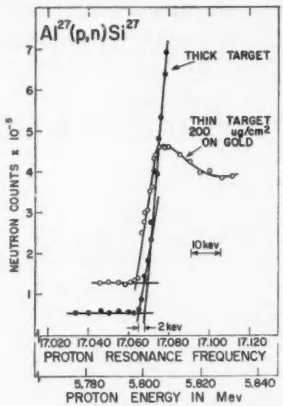

FIG. 14. Thick and thin target excitation curves for the $Al^{27}(p,n)Si^{27}$ reaction. This figure illustrates the characteristic features of the thick and thin target slow-neutron excitation data.

The thin target data of Fig. 14 are consistent with the characteristics of the NE 401 detector; since the efficiency of this detector decreases sharply with increasing neutron energy the apparent yield rises sharply with the reaction yield immediately above threshold and then decreases as the neutron energy increases and the counter efficiency decreases.

The mean threshold frequency of 17.0725 Mc/sec from Fig. 7 corresponds to a threshold energy of 5.800 Mev. From Table III the error in this threshold is ± 8 kev.

(*F*) $P^{31}(p,n)Si^{31}$

Figure 15 shows the slow-neutron excitation and counter-ratio curve for a thin target of P_2O_5 sublimed onto a thick gold backing. The relatively high neutron yield below threshold is attributed to the $O^{18}(p,n)F^{18}$ reaction noted previously.

Measurements using thick targets of red phosphorus were not reproducible, presumably because of deterioration of the target surface under bombardment.

The neutron yield and counter-ratio data are in good accord; the indicated threshold frequency of 18.015 ± 0.025 corresponds to a proton energy of 6.456 ± 0.020 Mev.

(*G*) $Ni^{60}(p,n)Cu^{60}$

Figure 16 shows both the slow-neutron excitation and counter-ratio curves from bombardment of a $Ni^{60}O$ target. The yield below the Ni^{60} threshold is again attributed to the O^{18} component in the oxide target.

The threshold frequency of 18.784 ± 0.015 Mc/sec corresponds to a proton energy of 7.016 ± 0.015 Mev. Because of the large cross section at threshold and hence a marked excitation step, this reaction constitutes a particularly suitable one for calibration use at an energy hitherto inaccessible to precision techniques.

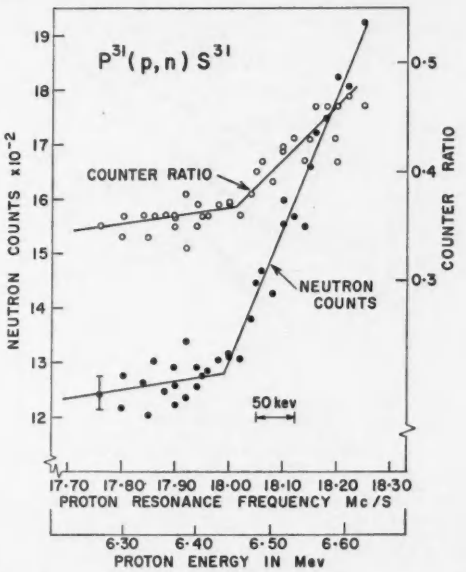

FIG. 15. Slow-neutron excitation and counter-ratio results for proton bombardment of a thin target of P_2O_5 sublimed onto a gold backing.

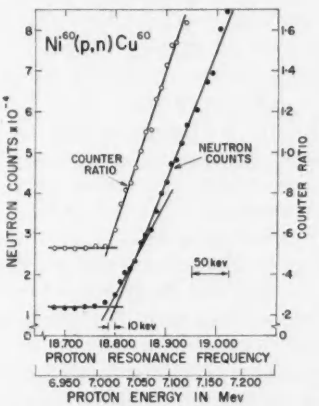

FIG. 16. Slow-neutron excitation and counter-ratio curves for protons on a thick, sintered, target of isotopically enriched Ni^{60} oxide.

(*H*) $K^{39}(p,n)Ca^{39}$

Figure 17 presents the results of measurements on both a thick target of KOH of natural isotopic abundances and a thin target of KI isotopically enriched in K^{39}. In both cases large neutron backgrounds were present below

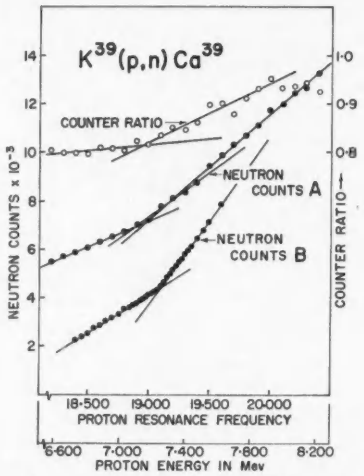

FIG. 17. Slow-neutron excitation and counter-ratio data for the $K^{39}(p,n)Ca^{39}$ reaction. The counter-ratio curve and excitation curve A were measured using a thick target of KOH of normal isotopic abundance; excitation curve B was measured using a 100 $\mu g/cm^2$ target of $K^{39}I$ on 0.00025-in. tantalum backed by a metallic Ni^{58} blank.

the apparent threshold; that using the KOH target results primarily from the (p,n) reaction on the 6.91% abundant (Nier 1950) K^{41} isotope in the target with a calculated threshold energy of 1.25 Mev. The (p,n) reaction on iodine, with a threshold energy of -2.09 Mev (Cameron 1957), contributed the major background below the $K^{39}(p,n)$ threshold; this target was handled only in an inert gas atmosphere prior to bombardment to minimize contamination. The excitation curves for the two targets and the counter-ratio curve for the thick target are in reasonable accord. The mean threshold frequency of 19.065 ± 0.090 Mc/sec corresponds to a proton energy of 7.227 ± 0.070 Mev. The relatively large error attached to this determination reflects the difficulties in obtaining a precisely defined threshold in the presence of a large neutron background. Measurements were extended over a wider range in this case than in the others studied to demonstrate the absence of other neighboring threshold phenomenon which would correspond to the beta decay measurements to be discussed in the following section.

Measurements using metallic potassium targets were not reproducible, again presumably due to target deterioration during bombardment.

(*I*) $Ni^{58}(p,n)Cu^{58}$

Figure 18 presents the results of measurements on an isotopically separated metallic target of Ni^{58}. At this energy extreme care was required in obtaining a precisely defined beam focus on the target since even small amounts of scattered or unfocussed beam striking material other than the Ni^{58} target resulted in copious neutron production. This, together with the relatively

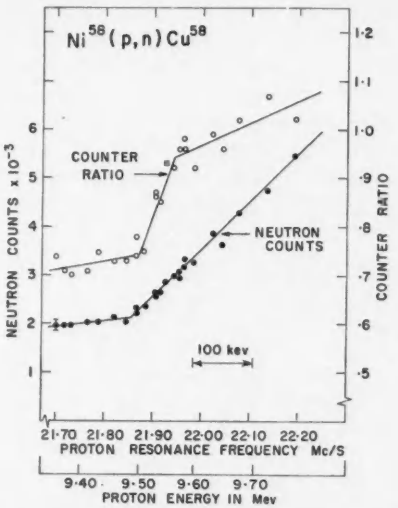

FIG. 18. Slow-neutron excitation and counter-ratio curves for the $Ni^{58}(p,n)Cu^{58}$ reaction on a thick target of isotopically enriched Ni^{58} metal. The discrepancy between the indicated thresholds is characteristic of the effect of the relatively high and somewhat erratic neutron backgrounds encountered at these higher proton energies corresponding to any stray beam components striking other than the target itself.

high background neutron yield from the O^{18} and other heavier target contaminants, limited the precision attainable in earlier measurements (Gove *et al.* 1958) with this accelerator, using sintered NiO targets.

The threshold frequency of 21.850±0.020 Mc/sec corresponds to an incident proton energy of 9.480±0.025 Mev. This is the highest (p,n) threshold measurement measured with this precision to date and as such serves as a convenient calibration reaction, sharing with that on Ni^{60} the advantages of target stability.

(*J*) $Si^{30}(p,n)P^{30}$

Figure 19 presents the results of measurements of the slow-neutron yield from isotopically enriched targets of 30 and 120 $\mu g/cm^2$ areal density of Si^{30} on 0.020- and 0.00025-in. Ta respectively. In the case of the 120 $\mu g/cm^2$ target on Ta, the beam was stopped in a gold blank mounted directly behind the target. In order to obtain the background data, at proton energies below 5.50 Mev, a Si^{29} target (with a calculated (p,n) threshold energy of 5.943 Mev) produced under identical conditions by the Harwell electromagnetic mass separator group, on an identical target backing, was used. It was assumed that this target would have the same contaminants and impurities as that of Si^{30}; the excellent agreement obtained in the regions below and between resonances in the $Si^{30}(p,n)P^{30}$ reaction justify this assumption. Both sets of data have been normalized to the same total beam charge on target. At energies above 5.5 Mev, a dummy target consisting of 0.00025-in. Ta on Au was used for the

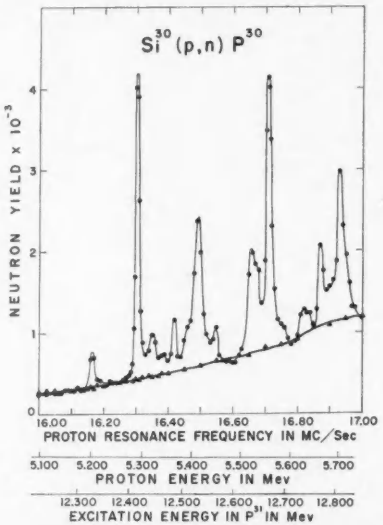

FIG. 19. Slow-neutron excitation curve for the $Si^{30}(p,n)P^{30}$ reaction. The triangular points are the results of background measurements made on identical target backings and under identical conditions with those used for the Si^{30} target. The normalization has been to the same charge delivered by the proton beam. Figure 9 presents the results of detailed measurements on the lowest-energy resonance appearing here.

background; the yield from this target was normalized by 15% to agree with the background measured with the Si^{29} target. This normalization reflects the additional neutron-producing impurities collected by the backing during target preparation.

The very striking features of these data are first the appearance of sharp resonance structure (the resonance at 5.298 ± 0.007 Mev, for example, has a full width at half maximum of 10 kev) at excitations of about 12.5 Mev in the compound nucleus P^{31} and second, the apparent complete absence of broad levels with tails underlying the sharper resonances. The lowest resonance is at an energy of 5.205 ± 0.007 Mev. From the atomic mass data (Kravtsov 1958) the calculated reaction threshold for the $Si^{30}(p,n)P^{30}$ reaction is 5.218 Mev, this would correspond to a threshold in Fig. 19 very close to the lowest energy resonance observed.

In order to examine the possibility that this threshold might lie below this resonance in a region of very low cross section, measurements were also carried out on a thick target of metallic silicon. From the mass data (Kravtsov 1958) the calculated thresholds for the $Si^{28}(p,n)P^{28}$, and $Si^{29}(p,n)P^{29}$ reactions are 15.040 and 5.943 Mev respectively; consequently at proton energies below 5.9 Mev on a natural Si (Si^{28} 92.27%; Si^{29} 4.68%; Si^{30} 3.05%) (Nier 1950) target, only the $Si^{30}(p,n)P^{30}$ reaction is energetically possible. Figure 20 shows the thick target slow-neutron yield and counter ratio in the energy region in

the vicinity of the calculated $Si^{30}(p,n)P^{30}$ threshold. The yield steps observed at 5.20 Mev, both in the slow-neutron yield and in the counter ratio are in excellent accord with the lowest resonance observed in the thin target yield (Fig. 19). The second yield step at 5.30 Mev also showed a similar break in the ratio curve corresponding to the second resonance. The fact that the thick target counter ratio (Fig. 20) at these energies showed sharply defined steps suggested that the resonances were very close to threshold, i.e. the neutron energies at the resonances were too low to be efficiently detected by the fast counter.

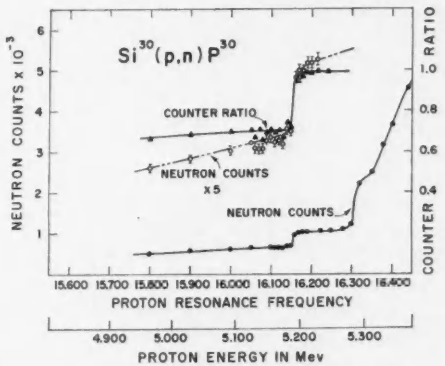

FIG. 20. Thick target neutron excitation and counter-ratio results for the $Si^{30}(p,n)P^{30}$ reaction. The target consisted of a blank of metallic silicon with natural isotopic abundances.

In order to apply the counter-ratio calibration technique described in Section 2(*B*), detailed measurements were carried out on the two lowest resonances, shown in Fig. 19. Typical measurements are shown, for example, in Fig. 21.

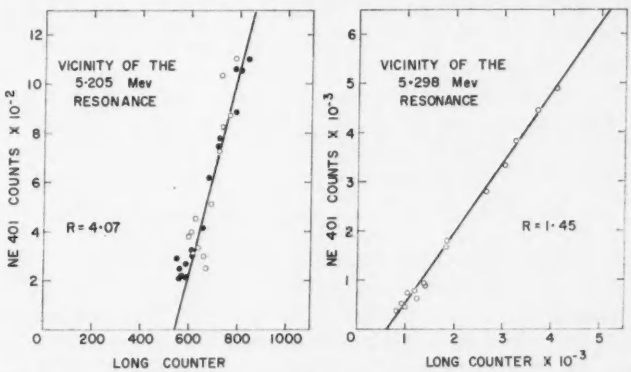
VICINITY OF THE 5·205 Mev RESONANCE
R = 4·07
NE 401 COUNTS x 10-2
LONG COUNTER
VICINITY OF THE 5·298 Mev RESONANCE
R = 1·45
NE 401 COUNTS x 10-3
LONG COUNTER x 10-3

FIG. 21. Slow- vs. fast-neutron detector plots for the two lowest-energy resonances in the $Si^{30}(p,n)P^{30}$ reaction. The slopes of these plots give the effective counter ratio as discussed in the text at these energies.

By subtracting appropriate background yields at the resonance energies from both slow and fast counters, ratios of 3.21 and 1.23 were obtained at 5.205 and 5.298 Mev respectively. When fitted to the $Al^{27}(p,n)Si^{27}$ counter-ratio calibration curve of Fig. 4, an energy interval of 46 kev is indicated between the reaction threshold and the 5.205-Mev resonance.

In order to check this result using the second ratio technique detailed above, which obviates the need for background subtraction, the ratio plots of Fig. 21 were prepared from the detailed yield measurements over these two resonances. Fitting the ratios of 4.07 and 1.45 thus obtained to the corresponding calibration curve of Fig. 22 results in an indicated energy interval of 16 kev between threshold and the first resonance.

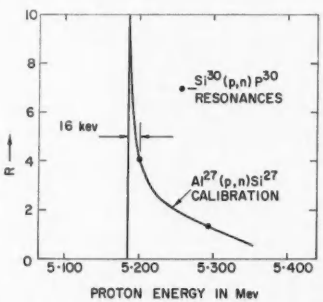

FIG. 22. Indirect determination of the $Si^{30}(p,n)P^{30}$ reaction threshold using the counter-ratio calibration curve for the $Al^{27}(p,n)Si^{27}$ reaction.

Averaging these results leads to a threshold energy for the $Si^{30}(p,n)P^{30}$ reaction of 5.174 ± 0.030 Mev. The quoted 30-kev error includes an estimate of the uncertainty introduced by this indirect measurement of the threshold energy. The sharp resonances in this reaction constitute convenient tests for beam-energy stability and reproducibility as well as calibration points (see Fig. 9).

(*K*) *Summary*

A summary of the information obtained in these measurements is presented in Table IV. The Q values corresponding to the measured threshold energies are obtained using equation 1 and the mass data tabulated by Kravtsov (1958). The positron end-point energy in column 4 is obtained from

$$E_{\beta^+} = |Q| - (1.8049\pm0.0009) \text{ Mev} \tag{5}$$

where a neutron–hydrogen atom mass difference of 0.7830 ± 0.0009 (Kravtsov 1958) Mev has been assumed.

Previously reported measurements of the (p,n) reaction thresholds and of the positron end points are tabulated in columns 5 and 7 for comparison with the present measurements.

Since for each reaction studied the target mass is known with appreciably greater precision than that of the product (Kravtsov 1958), Table V compares

TABLE IV

Summary of neutron threshold measurements

	Present measurements			Previous measurements				
	Threshold energy	Q value	β^+ end point, calculated	Threshold measurements	Ref.	β^+ end-point measurements	Method	Ref.
$B^{11}(p,n)C^{11}$	3.019±0.004	2.766±0.004	0.961±0.004	3.015±0.003	R-1	0.968±0.008	Lens	W-2
$F^{19}(p,n)Ne^{19}$	4.229±0.006	4.016±0.006	2.211±0.006	4.240±0.008	K-2	2.18±0.03	180° defl.	S-1
				4.235±0.005	M-1			
				4.240±0.005	C-1			
$Si^{30}(p,n)P^{30}$	5.174±0.030	5.005±0.030	3.200±0.030			3.24±0.04	180° defl.	G-3
						3.31±0.07	Scint. spect.	H-1
						3.23±0.07	Al absorption	K-3
$Al^{27}(p,n)Si^{27}$	5.800±0.008	5.591±0.008	3.786±0.008	5.792±0.010	K-2	3.74	Cloud ch.	M-3
				5.798±0.005	M-1	3.54±0.10	Cloud ch.	B-1
						3.48±0.10	Scint. spect.	B-2
						3.76±0.08	Scint. spect.	H-1
$P^{31}(p,n)S^{31}$	6.456±0.020	6.253±0.020	4.448±0.020	6.417±0.020	G-2	3.85±0.07	Cloud ch.	W-1
						3.87±0.15	Cloud ch.	E-1
						4.50±0.10	Scint. spect.	H-2
$Ni^{60}(p,n)Cu^{60}$	7.016±0.015	6.900±0.015	5.095±0.015	7.028±0.020	G-2	5.18±0.07*	Scint. spect.	N-1
$K^{39}(p,n)Ca^{39}$	7.227±0.070	7.044±0.070	5.239±0.070			6.10±0.15	Scint. spect.	H-2
						6.7 ±0.5	Al absorption	B-3
						5.490±0.025	Lens	K-1
						5.43±0.06	180° defl.	W-3
$Ni^{58}(p,n)Cu^{58}$	9.480±0.025	9.317±0.025	7.512±0.025	9.459±0.070	G-2	8.2±0.3	Scint. spect.	G-2
						7.4	Scint. spect.	S-2

NOTE:
B-1 Barkas, Creutz, Delsasso, Sutton, and White. 1940. Phys. Rev. **58**, 383.
B-2 Boley and Zaffarano. 1951. Phys. Rev. **84**, 1059.
B-3 Braams and Smith. 1953. Phys. Rev. **90**, 995.
C-1 Chapman and Bichsel. *As quoted by* Marion and Bonner, 1958. University of Maryland Technical Report No. 100 (revised).
E-1 Elliott and King. 1941. Phys. Rev. **60**, 489.
G-1 Gerhart. 1958. Phys. Rev. **109**, 897.
G-2 Gove, Kuehner, Litherland, Almqvist, Bromley, Ferguson, Rose, Bastide, Brooks, and Connor. 1958. Phys. Rev. Letters, **1**.
G-3 Green and Richardson. 1956. Phys. Rev. **101**, 776.
H-1 Hunt and Zaffarano. 1954. United States Atomic Energy Commission Report ISC-469.
H-2 Hunt, Kline, and Zaffarano. 1954. Phys. Rev. **95**, 611A.
K-1 Kistner and Rustad. 1959. Phys. Rev. **112**, 1972.
K-2 Kingdon, Bair, Cohn, and Willard. 1955. Phys. Rev. **99**, 1393.
K-3 Koester. 1954. Naturforsch, **9a**, 104.
M-1 Marion, Bonner, and Cook. 1955. Phys. Rev. **100**, 91.
M-3 McCreary, Kuerti, and Van Voorhis. 1940. Phys. Rev. **57**, 351A.
N-1 Nuusbaum, van Lieshout, Wapstra, Verster, Ten Haaf, Nijgh, and Orustein. 1954. Physica, **20**, 55.
R-1 Richards, Smith, and Browne. 1950. Phys. Rev. **80**, 524.
S-1 Schrank and Richardson. 1952. Phys. Rev. **86**, 248.
S-2 Sutton, Hill, and Sherr. 1959. Bull. Am. Phys. Soc. II, **4**, 278.
W-1 White, Creutz, Delsasso, and Wilson. 1941. Phys. Rev. **59**, 63.
W-2 Wong. 1954. Phys. Rev. **95**, 765.
W-3 Welch and Wallace. 1958. Bull. Am. Phys. Soc. II, **3**, 206.

*The positron decay of Cu^{60} proceeds only to excited states of Ni^{60}; the entry in this table is obtained by summing the appropriate coincident gamma radiation and positron energies and averaging the results for the three major branches. The error quoted is larger than that quoted in ref. N-1 above for the individual branches, because of lack of internal consistency among the energy values obtained.

TABLE V

Summary of mass determinations from neutron threshold measurements

Reaction	Target mass, atomic mass units (Kravtsov)	Residual nucleus mass, atomic mass units		Discrepancy, microatomic mass units
		Experimental	Kravtsov	
$B^{11}(p,n)C^{11}$	11.0128153±56	11.0149454±70	11.0149409±64	+(4.5±9.6)
$F^{19}(p,n)Ne^{19}$	19.0044441±17	19.0079168±64	19.0079312±37	−(14.4±7.4)
$Si^{30}(p,n)P^{30}$	29.9832868±66	29.987822±66	29.987868±5	−(46±82)
$Al^{27}(p,n)Si^{27}$	26.9901117±25	26.9952762±86	26.995293±9	−(17±120)
$P^{31}(p,n)S^{31}$	30.9836125±6	30.989488±23	30.98948±7	+(8±100)
$Ni^{60}(p,n)Cu^{60}$	59.949823±6	59.956393±19	59.956557±30	−(164±36)
$K^{39}(p,n)Ca^{39}$	38.976400±2	38.983125±64	38.98323±80	−(105±102)
$Ni^{58}(p,n)Cu^{58}$	57.953767±7	57.962933±27	—	—

the product masses indicated by the present measurements with those previously quoted. In obtaining the new mass values it has been assumed that

$$1 \text{ atomic mass unit} = 931.143 \pm 0.010 \text{ Mev} \quad \text{(Cohen 1959)}.$$

Column 5 then lists the discrepancy in microatomic mass units between the new product masses thus obtained and those previously quoted.

4. DISCUSSION

(*A*) *General*

The experimental data obtained is summarized and compared with prior results in Tables IV and V. As indicated in these tables there is, in general, quite good agreement with somewhat greater precision available from the (p,n) measurements reported herein.

(*B*) $K^{39}(p,n)Ca^{39}$

The outstanding residual discrepancy is that between the data reported herein leading to a calculated end point for the Ca^{39} positron spectrum of 5.239 ± 0.070 Mev and the most recent direct measurements of this end point yielding 5.490 ± 0.025 (Kistner and Rustad 1959) and 5.43 ± 0.06 Mev (Welch and Wallace 1959) respectively. Although, as noted in the previous section, the precision with which the $K^{39}(p,n)Ca^{39}$ threshold may be determined is significantly less than in all the other cases reported because of the high backgrounds encountered with the available targets, the experimental excitation and ratio curves do not show any evidence of a second discontinuity at an energy corresponding to the β^+-decay measurements as would be the case if the apparent (p,n) threshold reported herein were in reality an excited state threshold in the (p,n) reaction on a target contaminant. This hypothesis of a secondary threshold is also rendered untenable by the fact that within the errors the break occurs at the same point using both KOH and $K^{39}I$ targets. Further work is needed on the $A = 39$ system to remove the present discrepancy between the reaction and beta-spectroscopy measurements.

The decay of Ca^{39} is of particular interest in beta decay since it represents a mirror case where both initial and final nuclides are one nucleon removed from a closed shell. Assuming a half-life value of 0.876 ± 0.012 second (Cline and Chagnon 1959) for the Ca^{39} β^+-decay and the end-point energy of 5.239 ± 0.070 Mev deduced from the (p,n) threshold measurement, an ft value of 3475 ± 200 is obtained using the f value tables prepared by Moszkowski and Jantzen (1955). This is to be compared with the value of 4320 ± 100 as given by Kistner and Rustad (1959).

From an analysis of the available β-decay evidence, Gerhart (1958) has obtained values for the constants A and R in the general expression

$$A = ft\left(\left|\int 1\right|^2 + R\left|\int \sigma\right|^2\right). \tag{4}$$

The results are

$$A = \frac{2\pi^3\hbar^7 \ln 2}{m^5c^4 g_F^2} = 6200\pm120 \text{ seconds},$$

$$R = \left(\frac{g_{GT}}{g_F}\right)^2 = 1.36\pm0.14.$$

From equation (4) and assuming charge independence of nuclear forces, hence $|\int 1| = 1$, and the $ft = 3475\pm200$ value reported herein

$$\left|\int \sigma\right|^2 = \left\{\frac{A}{ft} - \left|\int 1\right|^2\right\} \cdot \frac{1}{R} = 0.58\pm0.05.$$

The value of $|\int \sigma|^2$ calculated for the configuration appropriate to the observed magnetic moment of Ca^{39}, i.e. from interpolation between the Schmidt limits, is 0.39 (Winther and Kofoed-Hansen 1953) whereas the extreme single-particle value uncorrected is 0.60. The relatively close agreement between the $|\int \sigma|^2$ value obtained from the (p,n) threshold measurement and the extreme single-particle value is certainly surprising. The beta-decay data, on the other hand, yield a value of 0.38 ± 0.05 in excellent agreement with the interpolated predictions.

(*C*) $Ni^{58}(p,n)Cu^{58}$

On the basis of a systematic analysis of the odd–odd $N = Z$ nuclei Moszkowski and Peaslee (1954) identify the Cu^{58} positron decay as belonging to the $0^+ \rightarrow 0^+$ pure Fermi class including O^{14}, Al^{26}, Cl^{34}, and K^{38}. The *ft* values for these transitions (Gerhart 1958) are 3103 ± 62, 3092 ± 52, 3110 ± 103, and 3140 ± 400; the excellent internal agreement displayed here has been interpreted in detail by Gerhart (1958) to imply a Fierz constant of 0.00 ± 0.12 for the pure Fermi decay processes.

The Cu^{58} decay half-life has been measured as 3.30 ± 0.10 (Gerhart 1959) and 3.04 seconds (Martin and Breckon 1952). From the systematics of the odd–odd $N = Z$ nuclide series this lifetime is anomalously long and suggests the possibility that the observed decay proceeds from an isomeric state in Cu^{58}. Martin and Breckon (1952) have reported preliminary observation of a 0.14-second activity superposed on the pronounced 3-second yield lending support to such an hypothesis.

Assuming the calculated β^+ end point of 7.512 ± 0.025 Mev corresponding to the (p,n) threshold data reported herein, *ft* values of 2478 and 58,400 are found (Moszkowski and Jantzen 1955) corresponding to half-lives of 0.14 and 3.30 seconds respectively. No error is quoted for the 0.14-second half-life determination (Martin and Breckon 1952); a value of ~ 0.175 second would bring the *ft* value for this transition to the average of the four $0^+ \rightarrow 0^+$ decays quoted above and this may well be encompassed in the experimental error in this measurement. It is clear that a re-examination of the Cu^{58} β^+ decay is indicated to establish with precision the half-life for the 0^+ to 0^+ transition as well as to identify the transition having the 3.3-second half-life.

Sutton, Hill, and Sherr (1959) have examined the branching of the Cu^{58}, 3.3-second positron activity, and find an 80% branch with an end point of 7.4 Mev to the ground state of Ni^{58}. No error is quoted for this end-point value. The isomeric state hypothesis just advanced for this activity would require that the end point of the ground state branch should be greater than 7.512 ± 0.025 Mev. This may be within the experimental accuracy of the above measurements.

(*D*) $Si^{30}(p,n)P^{30}$

As shown in Table III, quite acceptable agreement is obtained between the measured β^+ end points and that corresponding to the (p,n) threshold reported herein. From the systematics of the odd–odd $N = Z$ nuclides it might be expected that the ground state of P^{30} should have an assignment 0^+, $T = 1$ with a low-lying 1^+, $T = 0$ level at an excitation of, at most, a few hundred kiloelectron volts. The present measurements do not preclude the existence of a closely spaced doublet of levels close to the ground state of P^{30}. Evidence from the measurements on the $Si^{29}(p,\gamma)P^{30}$ capture radiation (Broude *et al.* 1956; Wilkinson 1956) suggests a $T = 1$ assignment for the 685-kev level in P^{30}; if this is indeed the lowest $T = 1$ level, the energy spacing between it and the ground state is much larger than the systematics would suggest and presumably reflects a depression of the $T = 0$ level as a result of interaction with one or more higher 1^+, $T = 0$ levels (Kerman 1956).

As noted previously, the striking features of the $Si^{30}(p,n)P^{30}$ excitation data of Fig. 20 are the existence of narrow resonances with relatively large level spacing, and the almost complete absence of broad levels with tails overlapping the narrow resonances to give a "background" cross section both at threshold and between these narrow resonances. Such a "background" is clearly evident in the $Al^{27}(p,n)Si^{27}$ data of Fig. 4.

In considering the relative paucity of narrow compound system levels involved in the $Si^{30}(p,n)P^{30}$ reaction it should be noted that for an assignment of 1^+ to the P^{30} ground state, only compound states with assignments $1/2^+$, $3/2^+$, $1/2^-$, $3/2^-$, and $5/2^-$ are involved if centrifugal barrier effects are assumed to limit the outgoing low-energy neutrons to only *S* and *P* waves. A priori it might have been anticipated that narrow resonance structure at this excitation in the compound system would correspond to high angular momentum states. This is clearly not the case in this instance; in the $Al^{27}(p,n)Si^{27}$ reaction, albeit at somewhat higher excitation, where similar criteria allow $J_{comp} \leq 4$, no comparable isolated resonance structure is observed. It should be noted, however, that since the target used corresponded to an energy loss of about 5-kev for 5-Mev protons, the cross-section contribution from broad levels would be relatively small, i.e. the experimental situation would be expected to emphasize narrow resonance structure in the yield.

Although much more detailed study is required to elucidate the level density situation here, it is of interest to note that the most recent level density formulations due to Cameron (1958; 1959) predict a level spacing, averaged over the allowed *J* values, of about 100 ev, in this region of mass and excitation.

Experimentally the observed average spacing over the interval concerned is 34 kev; other evidence which suggests that the theoretical estimates of level spacings are too small by at least an order of magnitude has been obtained in studies on (p,α) reactions in the nuclear d-shell (Clarke *et al.* 1959).

There is a suggestion in the data of Fig. 20 of a periodicity in the resonance intensity envelope of roughly 120 kev.

From a study of the $Al^{27}(\alpha,n)P^{30}$ reaction, Katman and Williamson (1959) have determined a value for the threshold for observation of the P^{30} decay positrons of 3.056 ± 0.0005 Mev. Because of a high yield of background neutrons from the $C^{13}(\alpha,n)$ reaction on a carbon target contaminant, neutrons from the $Al^{27}(\alpha,n)P^{30}$ reaction were detected only at resonances and no reliable neutron production threshold data was obtained. The $(p,n)Q$ value which would correspond to this positron threshold is given by

$$\begin{aligned} |Q_{pn}| &= |Q|_{\alpha n} + M_{Al^{27}} - M_{Si^{30}} + M_{He^4} - M_{H^1} \\ &= 5.436\pm0.009 \text{ Mev} \end{aligned}$$

using the Kravtsov (1958) mass values. This is to be compared with the value of 5.005 ± 0.030 found here.

(E) Neutron Yields

The neutron yield data of Fig. 6 has been discussed in some detail in Section 1(*D*). Although the break in the effective yield curve for oxygen (from the $Ni^{58}O$ target below 9.480 Mev) at about 7 Mev might be attributed to the onset of the competing $O^{18}(p,d)O^{17}$ reaction with a threshold energy of 6.20 Mev (Ajzenberg-Selove and Lauritsen 1959), no such explanation is available for the similar behavior of the carbon curve. It is perhaps worth noting that at the corresponding excitations of 14.5 and 14.2 Mev respectively in the compound nuclides F^{19} and N^{14}, a $2S$ single-particle strength function behavior is expected (Vogt 1959). The yield curve breaks observed here may then result from the energy dependence of the S wave penetrability as has been investigated by Porter (1957) for the case of a manganese target.

5. SUMMARY

This study of a number of (p,n) reactions near threshold has served to calibrate the energy scale of the tandem accelerator beam-handling system. A number of new calibration points, e.g. the $Ni^{60}(p,n)$ and $Ni^{58}(p,n)$ thresholds at 7.016 ± 0.015 and 9.480 ± 0.025 Mev respectively and the sharp resonances at 5.205 and 5.298 Mev in the $Si^{30}(p,n)P^{30}$ reaction, have been located for future use in this energy range. A number of the problems involved in precision neutron measurements in this energy range have been investigated, e.g. target-backing materials, beam focus conditions, and target contaminants.

The (p,n) threshold data, in general, is in satisfactory agreement with the positron decay data; the $K^{39}(p,n)Ca^{39}$ threshold is in disagreement with the positron data however. Measurements on the $Ni^{58}(p,n)Cu^{58}$ reaction suggest that the 0.14-second activity observed by Breckon and Martin (1952) is in fact the ground state de-excitation of Cu^{58}, rather than the dominant 3.3-second

activity which has received detailed study and which may well be that from an isomeric state in Cu^{58}. A half-life of approximately 0.175 second, which may well be within the experimental uncertainty, would result in an *ft* value for the Cu^{58} decay of 3100 as found for other $0^+ \rightarrow 0^+$ pure Fermi decays in O^{14}, Al^{26}, Cl^{34}, and K^{38}.

Surprisingly sharp resonance structure has been observed in the neutron-excitation curves corresponding to compound system excitations in the range from 12 to 17 Mev. The narrow widths observed cannot be attributed solely to high angular momentum states; the average level spacings observed are greater than those predicted by current level density formalism.

The counter-ratio technique has been extended for use where marked resonance structure is present in the excitation curves but where the threshold falls between resonances and is therefore not directly observable.

Thick target neutron yields have been measured on a variety of elements and compounds throughout the periodic table as a function of incident proton energy in the range from 4 to 10 Mev. Away from the reaction threshold and above the barrier for the target in question, the neutron yield is essentially independent of the target material and is very roughly one neutron per 10^6 incident protons in the 10-Mev region. These data are of interest in the design of accelerator shielding and in the selection of target backings, collimators, etc. for experimental use in this energy range.

ACKNOWLEDGMENTS

We are indebted to Dr. D. M. Robinson for permission to use the facilities of the High Voltage Engineering Corporation laboratories in Burlington, for the initial preliminary measurements with this accelerator, and to Drs. R. J. Connor, A. J. Gale, P. H. Rose, and their colleagues at H.V.E.C. for their collaboration in these initial measurements.

We would also express our appreciation to Mr. P. Ashbaugh and his staff for efficient operation of a new and unique accelerator, to Mr. C. E. L. Gingell and his colleagues for their invaluable assistance with the experimental apparatus, and to Mr. W. Woytowich for the preparation of many of the targets used.

REFERENCES

AJZENBERG-SELOVE, F. and LAURITSEN, T. 1959. Nuclear Physics, **11**, 1.
BONDELID, P. O. 1959. *As quoted by* Marion and Bonner (1959).
BONNER, T. W. and COOK, C. F. 1954. Phys. Rev. **96**, 122.
BROMLEY, D. A. and BRUNER, J. 1954. U.S. Atomic Energy Commission Document NYO-3823.
BROMLEY, D. A., ALMQVIST, E., GOVE, H. E., LITHERLAND, A. E., PAUL, E. B., and FERGUSON, A. J. 1957. Phys. Rev. **105**, 957.
BROMLEY, D. A. and RUTLEDGE, A. R. 1958. Nuclear reaction *Q* values, Chalk River Report CRP-789 (unpublished).
BROUDE, C., GREEN, L. L., SINGH, J. J., and WILLMOTT, J. C. 1956. Phys. Rev. **101**, 1052.
CAMERON, A. G. W. 1957. Can. J. Phys. **35**, 1021; Chalk River Report CRP-690 (unpublished).
——— 1958. Can. J. Phys. **36**, 1040.
——— 1959. Can. J. Phys. **37**, 244.
CLARKE, R. L., ALMQVIST, E., and PAUL, E. B. 1959. To be published.
CLINE, J. E. and CHAGNON, P. R. 1958. Bull Am. Phys. Soc. II, **3**, 206.
COHEN, E. R. 1959. Methods of experimental physics, Vol. I, *edited by* I. Estermann (Academic Press, Inc., New York), Chap. 2.

GERHART, J. B. 1958. Phys. Rev. **109**, 897.
——— 1959. Unpublished measurements.
GIBBON, J. H. and MACKLIN, R. L. To be published.
GINGELL, C. E. L. and BROMLEY, D. A. Unpublished.
GOVE, H. E., KUEHNER, J. A., LITHERLAND, A. E., ALMQVIST, E., BROMLEY, D. A., FERGUSON, A. J., ROSE, P. H., BASTIDE, R., BROOKS, N., and CONNOR, R. J. 1958. Phys. Rev. Letters, **1**, 251.
HANSEN, A. O. and MCKIBBEN, J. L. 1947. Phys. Rev. **72**, 673.
KATMAN, T. S. and WILLIAMSON, R. M. 1959. Bull Am. Phys. Soc. II, **4**, 286.
KERMAN, A. K. 1956. Kgl. Danske Videnskab. Selskab, Mat.-fys. Medd. **30**, No. 15.
KISTNER, O. C. and RUSTAD, B. M. 1959. Phys. Rev. **112**, 1972.
KRAVTSOV, V. A. 1958. Uspekhi Fiz. Nauk, **65** (3), 451.
LANGSDORF, A. S., MONAHAN, J. E., and REARDON, W. A. 1954. Argonne National Laboratory Report, ANL-5219 (unpublished).
LITHERLAND, A. E. and GOVE, H. E. 1959. To be published.
MARION, J. B. and BONNER, T. W. 1959. Fast neutron physics, *edited by* J. B. Marion and J. L. Fowler (Academic Press, Inc., New York), Chap. 5 (to be published).
MARION, J. B. 1959*a*. Private communication.
MARTIN, W. M. and BRECKON, S. W. 1952. Can. J. Phys. **30**, 643.
MOSZKOWSKI, S. A. and JANTZEN, K. M. 1955. University of California Radiation Laboratory Technical Report No. 10-26-55 (unpublished).
MOSZKOWSKI, S. A. and PEASLEE, D. C. 1954. Phys. Rev. **93**, 455.
NIER, A. O. 1950. Phys. Rev. **77**, 789.
PORTER, C. E. 1958. Size resonances in nuclei, Los Alamos Report No. LAMS-2182 (unpublished).
SUTTON, D. C., HILL, H. A., and SHERR, R. 1959. Bull. Am. Phys. Soc. II, **4**, 278.
VOGT, E. 1959. Private communication.
WELCH, J. A. and WALLACE, R. 1958. Bull. Am. Phys. Soc. II, **3**, 206.
WILKINSON, D. H. 1956. Phil. Mag. **1**, 1031.
WINTHER, A. and KOFOED-HANSEN, O. 1953. Kgl. Danske Videnskab. Selskab, Mat.-fys. Medd. **27**, No. 14.

NOTES

L'INFLUENCE DU DÉVELOPPEMENT SUR LA STRUCTURE DES TRAJECTOIRES ET SUR LE VOILE DANS LES ÉMULSIONS À GRAINS FINS

I. Ahmad* et J. Demers

INTRODUCTION

Quand une particule chargée traverse une émulsion ionographique elle rend développables quelques uns des cristaux de bromure d'argent rencontrés sur son passage. Ces cristaux apparaissent sous l'action du révélateur, et l'on sait très bien que l'action prolongée du révélateur sur les trajectoires des particules chargées peut en modifier l'apparence: (1) le diamètre des grains augmente, (2) le nombre de paquets diminue, (3) les grains deviennent plus noirs, (4) il y a augmentation du voile dans l'émulsion.

Jusqu'à maintenant peu de travaux ont été faits sur ce sujet, et les données numériques montrant le rapport qui existe entre le temps de développement et les effets produits nous manquent (voir Alvial 1954; Bermond et Scherer 1958; Bermond 1959; Ahmad 1958; Ahmad et Demers 1959). Nous avons donc étudié systématiquement ces phénomènes.

MANIPULATIONS

Pour cela nous avons préparé des plaques d'émulsion ionographique à grains fins (formule No 19) à laquelle nous avons ajouté une petite quantité de chlorure de sodium (formule No 21). Ces émulsions ont été préparées suivant la méthode employée par M. le Professeur Pierre Demers (voir Demers 1958; Demers et Demers 1958, 1959).

Ces plaques ont été irradiées par les rayons α du thorium de 7 Mev et par des neutrons de 14 Mev qui ont donné des protons de recul.

Pour le développement nous avons utilisé un révélateur à la chlorohydroquinone préparé suivant la formule employée au laboratoire et à une température d'environ 0° C: 45 g chlorohydroquinone; 30 g Na_2SO_3; 32.5 g KOH, 8 g KBr; eau q.s. 1 l. Diluer à 1:4 pour l'usage.

Pour obtenir différents temps de développement sur une même plaque, ce que nous considérons comme nécessaire, nous avons imaginé le dispositif suivant. Nos plaques sont placées verticalement en ajoutant périodiquement dans le vase une certaine quantité de révélateur, à intervalles donnés, augmentant ainsi à chaque addition le niveau du révélateur jusqu'à ce que la plaque soit entièrement recouverte. Si on a noté le temps à chaque addition on pourra ainsi connaître le temps pendant lequel chaque partie de la plaque a été en contact avec le révélateur.

*Boursier du plan de Colombo. Adresse actuelle: Département de Physique, Government College, Lahore, Pakistan.

Les temps de développement suivants furent choisis: 1, 2, 4, 5, 10, 20, 30, 40, 50, 60, 90, 120, 150 et 180 minutes.

On a étudié visuellement et photométriquement seulement les 30 derniers μ des traces α. Les traces des protons n'ont pas été utilisées.

Pour compter les grains du voile nous avons utilisé un quadrillage de 8×10 mm placé dans l'oculaire. Oculaire ×12.5; objectif ×90 O.N. 1.3 à immersion d'huile.

RÉSULTATS

La figure 1 montre la variation des diamètres des grains avec la durée du développement, t. Il y a une courbe pour les grains isolés dans les traces et une courbe pour les grains du voile.

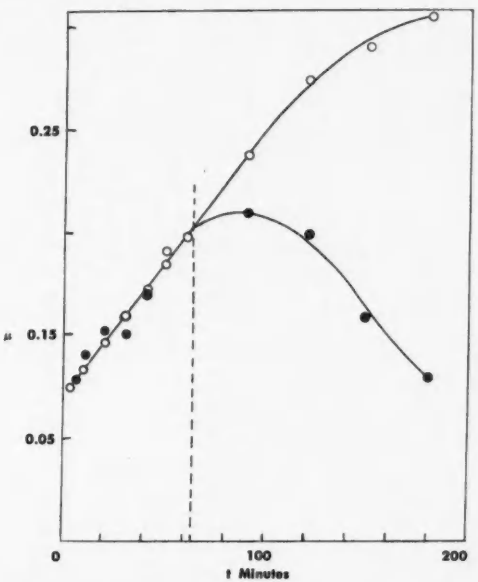

FIG. 1. Variation des diamètres des grains avec la durée du développement, t. ○ grains isolés dans les traces, ● grains du voile. Chaque point résulte de la mesure d'environ 30 grains.

Des traces faibles et pâles apparaissent déjà après un développement de 4 ou 5 minutes.

Au commencement, les grains isolés dans les traces et les grains du voile ont des grandeurs égales. Après un développement de 1 heure, il y a du voile très fin, par conséquent le diamètre moyen des grains du voile est devenu plus petit. D'autre part la grandeur des grains dans les traces continue d'augmenter mais pas linéairement.

La figure 2 montre la croissance du voile avec la durée du développement. La pente de la courbe augmente rapidement avec t. Il y a très peu de voile

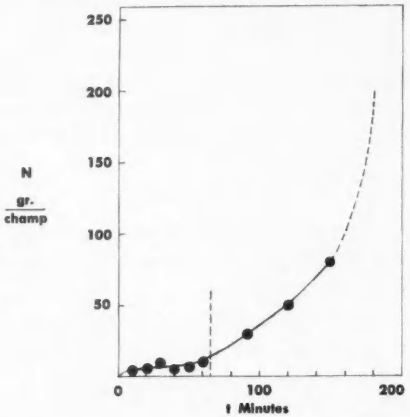

FIG. 2. Croissance du voile avec la durée du développement. Chaque point résulte du comptage de cinq champs (quadrillages de 8×10 mm).

pour t inférieur à 45–60 minutes. Pour $t > 1$ heure, il y a beaucoup de voile très fin. Il semble qu'il existe deux types de voile: le voile qui est produit par le révélateur en même temps que les grains des traces, et un autre voile formé de grains très fins, qui manifeste sa présence dans les courbes à partir de 60 minutes.

La figure 3 montre la diminution du nombre des lacunes avec la durée du développement. Il y a une diminution brusque au commencement, puis la diminution des lacunes suit une loi presque linéaire.

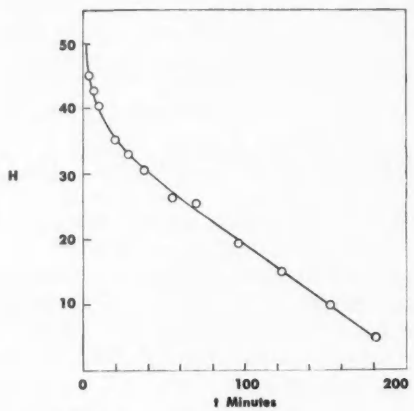

FIG. 3. Diminution du nombre des lacunes par 30 μ avec la durée du développement.

La figure 4 montre la variation du pourcentage des grains isolés dans les paquets, avec la durée du développement. Ici aussi la diminution est très brusque au commencement. D'après les figures 3 et 4 on remarque que, avec le développement, il y a un remplissage rapide des lacunes qui disparaissent entre deux grains isolés, lacunes que l'on pouvait voir dans les traces faibles au commencement du développement.

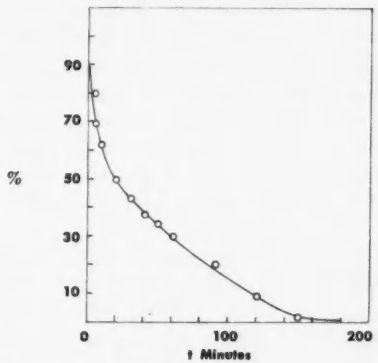

FIG. 4. Variation du pourcentage des grains isolés dans les paquets, avec la durée du développement.

La figure 5 montre les changements de l'absorption déterminée avec un photomètre à fente étroite dans les segments des 10 derniers μ pour des particules α à différentes durées de développement. Pour 20 minutes les traces sont très pâles, et il est difficile d'en faire une bonne mise au point sur la fente du photomultiplicateur. Le changement de l'opacité des traces

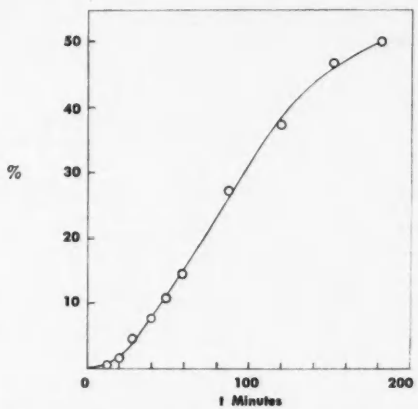

FIG. 5. Changements de l'absorption dans les segments des 10 derniers μ pour des particules α à différentes durées de développement.

devient très rapide ensuite entre les limites de 40 minutes et 80 minutes de développement, le diamètre des grains est doublé, mais leur noircissement est décuplé.

CONCLUSIONS

En somme dans ce premier travail nous avons obtenu quelques résultats précis:

(1) Les grains exposés sont affectés par le révélateur immédiatement et leur diamètre augmente relativement plus vite que dans le cas des grains non exposés qui sont aussi développables après un développement énergique.

(2) Si on développe les plaques pendant longtemps, dans l'espoir de voir les traces au minimum, on n'augmente pas beaucoup le diamètre des grains mais on réduit fortement la visibilité des traces parce que le voile augmente beaucoup plus rapidement. Ainsi les traces des basses énergies seront complètement saturées. La meilleure visibilité des traces est obtenue après un développement moyen.

(3) Après un certain temps de développement, quand les traces sont clairement visibles, le changement dans le noircissement des grains est beaucoup plus rapide que celui du diamètre des grains, de sorte que l'opacité des grains augmente sans que le diamètre visuel paraisse augmenter.

Nous remercions le Professeur Pierre Demers pour son aide et son encouragement dans ce travail. Nous remercions l'administration du Plan de Colombo au Pakistan et au Canada, et le Conseil National des Recherches pour leur aide financière.

AHMAD, I. 1958. Thèse de doctorat, Université de Montréal, Montréal, Qué.
AHMAD, I. et DEMERS, J. 1959. Ann. Acfas (sous presse).
ALVIAL, C. G. 1954. Nuovo cimento, **12**, 351.
BERMOND, J. 1959. Phot. Corp. II (sous presse, Les Presses universitaires de Montréal).
BERMOND, J. et SCHERER, M. 1958. Phot. Corp. I, 375.
DEMERS, P. 1958. Ionographie (Les Presses Universitaires de Montréal).
DEMERS, J. et DEMERS, P. 1958. Ann. Acfas, 24.
——— 1959. Phot. Corp. II (sous presse).

REÇU LE 7 JUILLET 1959.
DÉPARTEMENT DE PHYSIQUE,
UNIVERSITÉ DE MONTRÉAL,
MONTRÉAL, QUÉ.

DRIFT MOBILITY OF ELECTRONS IN ATOMIC HYDROGEN*

MAHENDRA SINGH SODHA† AND YATENDRA PAL VARSHNI‡

Considering the scattering of electrons by neutral hydrogen atoms to be spherical, Erginsoy (1950) has shown that the time of relaxation τ is given by

$$\frac{1}{\tau} = N_n v Q_0, \tag{1}$$

*Work supported by Armour Research Foundation, Chicago, Illinois, U.S.A.
†Armour Research Foundation, Chicago 16, Illinois, U.S.A.
‡Physics Department, Allahabad University, Allahabad, U.P., India.

where N_n is the number of hydrogen atoms per unit volume,
v is the velocity of the electron,
and Q_0 is the zero order partial cross section.

If we introduce two new symbols,

$$y = h\nu/2\pi q^2 = (2\pi m v/h)a_0 \tag{2}$$

and

$$Q_0' = Q_0/a_0^2, \tag{3}$$

where $a_0 = h^2/4\pi^2 mq^2$ is the first Bohr radius of bound electron,
h is Planck's constant,
q is the electronic charge,
and m the electronic mass,

we can express eq. (1) as

$$\tau = c/y\, Q_0', \tag{4}$$

where

$$c = 8\pi^3 q^2 m^2/N_n h^3.$$

Erginsoy (1950) noticed that for slow electrons ($y < 0.5$)

$$yQ_0' \sim 20$$

and hence

$$\tau = c/20.$$

It has been found that the expression

$$Q_0' = 10^5/(344+2440y+7200y^3) \tag{5}$$

adequately represents the variation of Q_0' with y, theoretically and numerically obtained by Massey and Moiseiwitsch (1951). The fit is illustrated in Table I. The last column also indicates the limits of validity of Erginsoy's approximation.

TABLE I

Fit of equation (7)

	Q_0'		
y	Theor.	Calc. eq. 7	yQ_0'
0.1	168	168	16.8
.15	138	136.1	20.7
.2	112	112.4	22.4
.3	77.6	78.7	23.28
.4	55.0	56.12	22.0
.5	41.3	40.58	20.65
.6	30.2	29.73	18.12
.8	17.5	16.71	14.0
1.0	10.5	10.02	10.5
1.2	6.55	6.36	7.86
1.5	3.54	3.53	5.31
2.0	1.55	1.59	3.1

If we introduce a dimensionless variable

$$x = (m/2k_0T)^{\frac{1}{2}}v, \tag{6}$$

we obtain

$$y = (h/2\pi q^2)(2k_0T/m)^{\frac{1}{2}}x = 2.5166\times10^{-3}T^{\frac{1}{2}}x = \lambda x, \tag{7}$$

where k_0 is the Boltzmann constant, and T the temperature of the gas.

Now eqs. (4) and (5) give

$$\tau = c\{7200\lambda^2x^2+2440+(344/\lambda x)\}\times10^{-5}. \tag{8}$$

The velocity distribution of electrons in weak electric fields is essentially Maxwellian given by

$$N(x)dx = Ax^2e^{-x^2}dx. \tag{9}$$

The drift mobility is given by

$$\mu = \frac{q}{m}\cdot\frac{\langle\tau x^2\rangle}{\langle x^2\rangle}. \tag{10}$$

From eqs. (8), (9), and (10) we obtain

$$\mu_N = \frac{8}{3}\pi^{-1/2}\frac{qc}{m}\left[7200\lambda^2\int_0^\infty x^6e^{-x^2}dx+2440\int_0^\infty x^4e^{-x^2}dx+\frac{344}{\lambda}\int_0^\infty x^3e^{-x^2}dx\right] \tag{11}$$

$$= \frac{10^{19}}{N_n}\{9.812257+2.1002\times10^5+8.851\times10^6T^{-1/2}\}.$$

It is seen that at high temperatures μ_N varies almost linearly with T. Table I also shows the product yQ_0'. It will be observed that up to $y = 0.5$ Erginsoy's relation $yQ_0' \simeq 20$ is a good approximation.

The scattering due to ions and other electrons can be taken into account by the approximate relation

$$\mu^{-1} = \mu_N^{-1}+\mu_{I,E}^{-1}$$

where $\mu_{I,E}$ is the mobility due to scattering by ions and other electrons, discussed by Sodha and Varshni (1958).

At high temperatures, contributions due to inelastic collisions of electrons with H atoms need also be taken into account. However, this will be a minor improvement because theoretical results (Massey 1956) show that the cross section for excitation of the 2*s* state of hydrogen is much smaller than the elastic cross section at the same energy.

ACKNOWLEDGMENTS

One of the authors (M. S. Sodha) is grateful to Dr. L. Reiffel and Dr. J. J. Brophy for kind encouragement.

ERGINSOY, C. 1950. Phys. Rev. **79**, 1013.
MASSEY, H. S. W. and MOISEIWITSCH, B. L. 1951. Proc. Roy. Soc. (London), A, **205**, 483.
MASSEY, H. S. W. 1956. Revs. Modern Phys. **28**, 199.
SODHA, M. S. and VARSHNI, Y. P. 1958. Phys. Rev. **111**, 1203.

RECEIVED JULY 16, 1959.
ARMOUR RESEARCH FOUNDATION OF THE
ILLINOIS INSTITUTE OF TECHNOLOGY,
CHICAGO, ILLINOIS.

CELLULAR GROWTH IN TIN ALLOYS

T. S. PLASKETT AND W. C. WINEGARD*

Tiller *et al.* (1953), from a theoretical treatment of the distribution of solute ahead of a plane solid–liquid interface, predicted that cellular growth should occur when the following relationship was satisfied:

$$G/R = -\frac{mC_0}{D}\left(\frac{1-k_0}{k_0}\right), \tag{1}$$

where G is the temperature gradient in the liquid ahead of a solid–liquid interface,

R is the rate of growth,
C_0 is the solute concentration,
D is the diffusion coefficient in the liquid,
m is the slope of the liquidus line,
and k_0 is the distribution coefficient.

The validity of the equation was established for face-centered cubic lead alloys by Tiller and Rutter (1956). The present investigation was undertaken to determine whether the equation predicted the onset of cellular growth for alloy systems with a solvent material other than face-centered cubic lead. Walton *et al.* (1955) found the equation to hold for lead in tin alloys, but these experiments alone were not considered sufficient to establish the effect of crystal structure. It was also desired to determine whether the equation applied when k_0 was greater than unity.

The alloys investigated were made from zone-refined tin with additions of lead, bismuth, or antimony. The k_0 and m values for each solute in tin were obtained from published phase diagrams and are listed in Table I.

TABLE I

Alloying element in tin	k_0	m, °C/at.%
Pb	0.1	−3.5
Bi	0.2	−2.2
Sb	3.0	2.1

*Department of Metallurgical Engineering, University of Toronto, Toronto, Ontario.

The onset of cellular growth was determined by observing the decanted solid–liquid interface of samples of various concentrations grown over a range of G/R ratios. The criterion used to indicate the onset of cellular growth was the first visible appearance of a pox-like structure on the interface. This is the same condition used by Tiller and Rutter (1956) and Walton *et al.* (1955). The concentrations used ranged from 0.005 to 0.020 at. %, and the G/R ratios varied from 200 to 5000° C sec/cm².

By using the experimental values of G, R, and C_0 for the onset of cellular growth, a value of D was calculated from equation 1. The values for D obtained in this manner are in reasonably good agreement with the values of D obtained by liquid diffusion measurements as seen from Table II. In fact, no better agreement should be expected, since it is difficult to determine accurate values of k_0 and m at low concentrations, and the liquid diffusion coefficients are experimentally difficult to determine even by standard methods.

TABLE II

Alloying element in tin	Diffusion coefficient, cm²/sec	
	Calculated from equation 1	Previously reported*
Pb	9×10^{-5}	2.3×10^{-5}
Bi	8×10^{-5}	0.9×10^{-5}
Sb	2×10^{-5}	2.0×10^{-5}

*References: Pb, Jost (1952); Bi and Sb, Niwa *et al.* (1957).

It is considered that these results justify the use of the equation for any metal system regardless of the solvent crystallography. It is of particular interest to note that the relationship applies for a system with a k_0 value greater than unity.

With respect to systems with a k_0 greater than unity, Rutter and Chalmers (1953) in the first comprehensive paper on cell formation suggested that the solute distribution should be reversed from the k_0 less than unity case.

Experimental evidence has been obtained to justify the above prediction. Figure 1 shows a cellular interface for a k_0 greater than unity-type alloy, i.e., antimony in tin. The fine lines shown in the figure were caused by drawing a camel hair brush across the interface. The one coarse straight line was produced by placing the edge of a razor blade on the interface. From these lines, it is evident that the centers of the cells are projections as in the case of k_0 less than unity. For this profile to have a stable configuration and conform with the temperature gradients, the center must melt at a higher temperature than the boundary. For a system where k_0 is greater than unity, i.e., where additions of solute raise the liquidus temperature, the cell projections must be less pure than the cell walls. In other words, the cell walls contain the pure material which is opposite to the k_0 less than unity case.

PLATE I

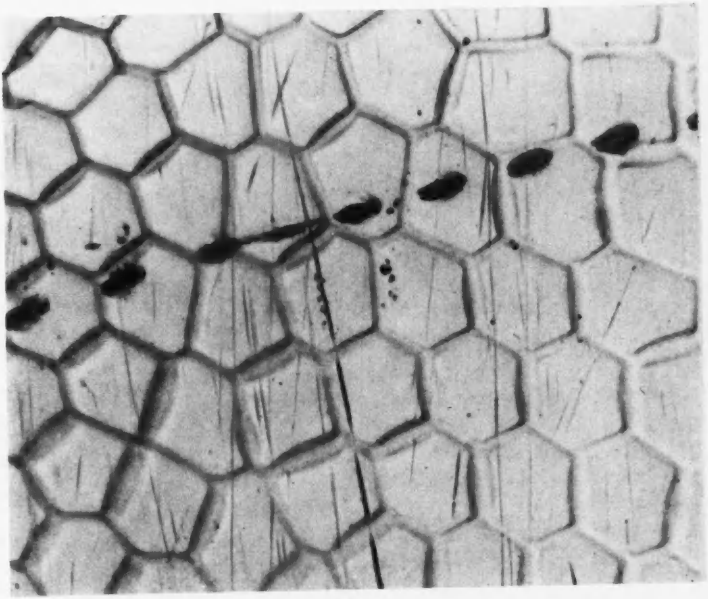

FIG. 1.

This work was supported by the Defence Research Board Grant 9535-01 and the University of Toronto.

JOST, J. 1952. Diffusion (Academic Press, Inc., New York), p. 479.
NIWA, K., SHIMOJI, M., KADO, S., WATANABE, Y., and YOKOKAWA, T. 1957. Trans. Am. Inst. Mining Met. Engrs. **207**, 96.
RUTTER, J. W. and CHALMERS, B. 1953. Can. J. Phys. **31**, 15.
TILLER, W. A., JACKSON, K. A., RUTTER, J. W., and CHALMERS, B. 1953. Acta Met. **1**, 428.
TILLER, W. A. and RUTTER, J. W. 1956. Can. J. Phys. **34**, 96.
WALTON, D., TILLER, W. A., RUTTER, J. W., and WINEGARD, W. C. 1955. Trans. Am. Inst. Mining Met. Engrs. **203**, 1023.

RECEIVED AUGUST 10, 1959.
DEPARTMENT OF METALLURGICAL ENGINEERING,
UNIVERSITY OF TORONTO,
TORONTO, ONTARIO.

RELAXATION TIME AND MULTIPLE PUMPING EFFECTS IN MASERS*

A. SZABO

INTRODUCTION

A major disadvantage of present solid state masers is the requirement of operation at very low temperatures. The problem of increasing the operating temperature is twofold:

1. Pump relaxation times must be long enough so that saturation can be achieved with a reasonable amount of pump power.

2. Since the population difference contributing to maser action is inversely proportional to temperature, some means must be found to enhance this difference independently of temperature. This can be done by (i) increasing the ratio of pump-to-signal frequency, (ii) multiple pumping, and (iii) achieving large relaxation time ratios between certain of the transitions involved. The application of (ii) recently has resulted (Ditchfield and Forrester 1958) in maser operation at temperatures ($\sim$60° K) well above the usual liquid helium operating range.

In this note, we propose to examine maser operation under points (ii) and (iii) mentioned above. In particular a comparison will be made of systems (singly and multiply pumped) in which all relaxation times are equal, and those in which one specific relaxation time is much smaller than the others. The concept of an idler temperature will be introduced, and the effect on the latter temperature of shortening certain relaxation times and of multiple pumping will be discussed in relation to maser operation.

THREE-LEVEL MASER

Consider a three-level system where the transition $1 \leftrightarrow 3$ is saturated by radiation of frequency ν_p, the signal frequency ν_s corresponding to the transition $1 \leftrightarrow 2$. A figure of merit for the system acting as an amplifier is the

*Issued as N.R.C. No. 5425.

difference in populations between 2 and 1. An analysis similar to that of Schulz-DuBois *et al.* (1959) readily gives

$$(1) \qquad n_2-n_1 = \frac{Nh\nu_1}{3kT}\left(\frac{R_{32}-\nu_s/\nu_1}{1+R_{32}}\right), \qquad R_{32} = \frac{\tau_{21}}{\tau_{32}}$$

where N is the total population; ν_1 is the idler frequency, $\nu_1 = \nu_p - \nu_s$; τ_{21}, τ_{32} are the signal and idler relaxation times respectively; T is the absolute bath temperature; h is Planck's constant and k is Boltzmann's constant. In the derivation of the above equation and succeeding ones, relationships like $\tau_{21}/\tau_{12} = \exp(-h\nu_s/kT)$ are used, thus implicitly assuming that these relaxation time ratios remain the same under pumped conditions as at equilibrium. Also we assume all $h\nu$'s $\ll kT$. In terms of the idler temperature T_1 defined by $n_3/n_2 = \exp(-h\nu_1/kT_1)$, an alternate expression for n_2-n_1 is

$$(2) \qquad n_2-n_1 = \frac{Nh\nu_1}{3kT_1}.$$

From this equation it is seen that, in order to make n_2-n_1 large, one possibility is to make T_1 small. The other possibilities of making N or ν_1 large will not be considered here except to say that in practice N cannot be advantageously increased much above a certain point (Bogle and Symmons 1959). Comparing equations (2) and (1) it is evident that the lowest possible temperature for T_1 is bath temperature which occurs for $R_{32} \to \infty$. This result is, of course, to be expected since decreasing τ_{32} implies making better heat contact between the idler transition and lattice, or alternately, increasing τ_{21} lengthens the time of contact between the two, again forcing the idler to bath temperature.

MULTIPLE PUMPING

Another method of "cooling the idler" is by pumping between one of the idler levels and an additional level. The principle (Geusic *et al.* 1959) is illustrated in the energy level – population diagram shown in Fig. 1 and its application to a three-level maser is shown in Fig. 2. This method of pumping may be termed pull–pull pumping in analogy to the push–pull scheme described by Makhov *et al.* (1958). The other obvious variation would be push–push pumping (Meyer 1958) where the signal transition occurs between levels 3 and 4 and pumping is done at transitions $1 \leftrightarrow 2$ and $2 \leftrightarrow 4$.

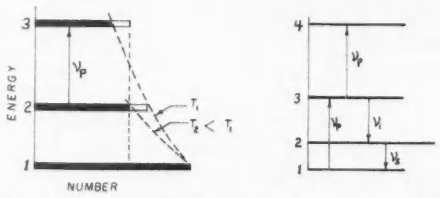

FIG. 1 (left). Cooling of transition $1 \leftrightarrow 2$ by pumping transition $2 \leftrightarrow 3$. T_1 is the bath temperature.

FIG. 2 (right). Application of the cooling principle shown in Fig. 1 to the three-level maser.

Analyzing the situation shown in Fig. 2, the rate equation for level 2 can be written

$$\frac{dn_2}{dt} = -n_2(\omega_{21}+\omega_{23}+\omega_{24})+n_1\omega_{12}+n_3\omega_{32}+n_4\omega_{42} \tag{3}$$

where $\omega_{ij} = 1/\tau_{ij}$.

Under saturation conditions $n_1 = n_3 = n_4$, whence we obtain from (3), and the condition $\sum_i n_i = N$,

$$n_2-n_1 = \frac{Nh\nu_1}{4kT}\left[\frac{R_{32}+2R_{42}+(\nu_s/\nu_1)(R_{42}-1)}{1+R_{32}+R_{42}}\right] \tag{4}$$

where

$$R_{j2} = \frac{\tau_{21}}{\tau_{j2}} \ (j = 3, 4).$$

Comparing the two situations (a) all R's = 1, and (b) $R_{32} \to \infty$, i.e. signal to idler relaxation time ratio large, we observe that n_2-n_1 is the same in either case, namely

$$n_2-n_1 = \frac{Nh\nu_1}{4kT} \text{ for all } R\text{'s} = 1 \text{ or } R_{32} \to \infty. \tag{5}$$

A way of interpreting this result is that the additional pumping between levels 3 and 4 cools the idler to bath temperature, and thus short-circuiting the idler to the bath by making $R_{32} \to \infty$ has no further effect on n_2-n_1. The relaxation time which can be advantageously decreased is τ_{42}. In the limit of $R_{42} \to \infty$ we get from (4)

$$n_2-n_1 = \frac{Nh\nu_1}{4kT}[2+(\nu_s/\nu_1)]. \tag{6}$$

A simple extension of the results to m levels shows that, in general, n_2-n_1 is largest for R_{m2} large.

To summarize the results, a comparison of maser operation under various pumping and relaxation time ratio conditions is given in Table I. Two relaxation time conditions are considered: (i) all relaxation times equal and (ii) the relaxation times optimized to give the largest n_2-n_1, i.e. $R_{m2} \to \infty$. As noted in column three, the parameter being compared is the bath temperature. N, ν_1, ν_s/ν_1, and n_2-n_1 are common for all cases. In particular we have chosen $\nu_s/\nu_1 = \frac{1}{2}$ and n_2-n_1 to be that calculated for a (typical) three-level maser operating under the conditions: (i) all relaxation times equal and (ii) $T = 4.2°$K (method of operation 1(a) in Table I). The results of the calculations for the normalized n_2-n_1 are summarized in the second column. To illustrate the effect of multiple pumping and the relaxation times on "idler cooling", the corresponding idler temperatures are also listed.

As an illustration of the results we find, for example (3(b)(i) of Table I), that a maser which has $m = 8$ and $R_{82} \to \infty$ can operate at 51.9° K and yield the same n_2-n_1 (or gain–bandwidth product) as a three-level maser

TABLE I

Comparison of single- and multiple-pumped masers for various relaxation time ratios

Method of operation	$(kT/Nh\nu_i)(n_2-n_1)$	$\nu_s/\nu_i = \frac{1}{2}$	
		Bath temperature for n_2-n_1 equivalent to 1(*a*) at 4.2° K, °K	Idler temperature, °K
1. Three-level			
(*a*) All relaxation times equal	$1/6[1-(\nu_s/\nu_i)]$	4.2	16.8
(*b*) $R_{32} \to \infty$	1/3	16.8	16.8
2. Four-level (pull–pull pumping)			
(*a*) All relaxation times equal	1/4	12.6	12.6
(*b*) $R_{42} \to \infty$	$1/4[2+(\nu_s/\nu_i)]$	31.5	12.6
3. *m*-Level ((*m*-2) fold–pull pumping)			
(*a*) All relaxation times equal			
(i) $m = 8$*	$1/8[3+(2\nu_s/\nu_i)]$	25.3	6.3
(ii) $m \to \infty$	$[1+(\nu_s/\nu_i)]$	75.6	0
(*b*) $R_{m2} \to \infty$			
(i) $m = 8$*	$1/8[6+(5\nu_s/\nu_i)]$	51.9	6.3
(ii) $m = 1500$, $\nu_i = 6000$ Mc		300	~0

*Largest known number of low-lying spin levels.

which has equal relaxation times and operates at 4.2° K, the pump and signal frequencies and the total spin population N being the same in both cases. It is apparent, however, that equivalent room temperature operation cannot be obtained except for unrealistic values of m. In general, similar results are obtained for the push–push and push–pull pumping schemes.

MASER OPERATION WITH LOW-FREQUENCY PUMPING

An examination of equation (4) shows that if $\tau_{21} \ll \tau_{32}, \tau_{42}$, then n_2-n_1 becomes negative, i.e. n_4-n_2 becomes positive if levels 1, 3, and 4 are saturated. Thus, under these conditions, maser operation can occur at frequency $\nu_p+\nu_i$ with pumping at a lower frequency ν_p. In the limit of $\tau_{21} \to 0$, we have $R_{32} \to 0$, $R_{42} \to 0$ so that

$$n_4-n_2 = \frac{Nh\nu_s}{4kT}. \tag{7}$$

In general, for m levels, the ratio of operating frequency to pump frequency increases with m; however, the population difference or efficiency of frequency multiplication decreases as $1/m$.

CONCLUSION

It is concluded that optimization of relaxation times combined with multiple pumping cannot by itself extend the operation of masers past the liquid nitrogen range and still result in performance comparable to that presently attainable at liquid helium temperatures with three-level masers. The only remaining possibility appears to be that of increasing the pump-to-signal frequency ratio.

A possible scheme of maser operation with pump frequency less than the signal frequency has been indicated for systems of four or more levels if certain relaxation time ratios are favorable. To achieve this operation, a rather high degree of control over the relaxation times is necessary. In practice, the impurity and self-doping schemes investigated by Scovil *et al.* (1957) and Schulz-DuBois *et al.* (1959) have been shown to result in a reduction of relaxation times of particular transitions by factors as large as 10. At present, however, such techniques are limited to a few materials and then only applicable under very special conditions. Presumably these restrictions will diminish as the cataloguing of host crystals along with their acceptable impurities continues, and a better understanding of the fundamental factors which control relaxation processes evolves.

Bogle, G. S. and Symmons, H. F. 1959. Australian J. Phys. **12**, 1.
Ditchfield, C. R. and Forrester, P. A. 1958. Phys. Rev. Letters, **1**, 448.
Geusic, J. E., Schulz-DuBois, E. O., De Grasse, R. W., and Scovil, H. E. 1959. J. Appl. Phys. **30**, 1113.
Makhov, G., Kikuchi, C., Lambe, J., and Terhune, R. W. 1958. Phys. Rev. **109**, 1399.
Meyer, J. W. 1958. M.I.T. Report M37-32.
Schulz-DuBois, E. O., Scovil, H. E. D., and De Grasse, R. W. 1959. B.S.T.J. **38**, 335.
Scovil, H. E. D., Feher, G., and Seidel, H. 1957. Phys. Rev. **105**, 762.

Received July 27, 1959.
Division of Radio and Electrical Engineering,
National Research Council,
Ottawa, Canada.

LETTERS TO THE EDITOR

Under this heading brief reports of important discoveries in physics may be published. These reports should not exceed 600 words and, for any issue, should be submitted not later than six weeks previous to the first day of the month of issue. No proof will be sent to the authors.

Frequency Measurement of Standard Frequency Transmissions[1, 2]

Measurements are made at Ottawa, Canada, using N.R.C. caesium-beam frequency resonator as reference standard (with an assumed frequency of 9 192 631 770 c.p.s.). Frequency deviations from nominal are quoted in parts per 10^{10}. A negative sign indicates that the frequency is below nominal.

Date, September 1959	MSF, 60 kc/s	GBR, 16 kc/s		KK2XEI, 60 kc/s
		5-hour average*	24-hour average	
1	−179	−176	−177	−84
2	−175	−174	−175	−83
3	−173	−177	−177	−83
4	N.M.	−174	−176	−84
5	−174	−181	−176	N.M.
6	−177	−180	−178	N.M.
7	−174	−177	−176	N.M.
8	−179	−175	−178	−83
9	−180	−176	−177	−82
10	−177	−180	−179	−80
11	−186	−175	−179	−85
12	−179	−179	−174	N.M.
13	N.M.	−181	N.M.	N.M.
14	−166	N.M.	N.M.	−81
15	−175	−178	N.M.	−80
16	−170	−172	N.M.	−82
17	−172	N.M.	N.M.	N.M.
18	−173	−182	N.M.	N.M.
19	−173	−175	−177	N.M.
20	−182	−180	−176	N.M.
21	−175	−172	−173	−79
22	−166	−176	−174	−77
23	−169	−170	−170	−76
24	−168	−166	−169	−79
25	−172	−170	−170	−78
26	−172	−162	−164	N.M.
27	−164	−169	−162	N.M.
28	−162	−168	−167	−82
29	−167	−166	−166	N.M.
30	−164	−169	−165	N.M.
Midmonthly mean	−173	−174	−173	−81
Midmonthly mean of WWV	−106			

NOTE: N.M. no measurement.
*Time of observations: 01.00 to 04.30 and 11.30 to 13.00 U.T.

RECEIVED OCTOBER 13, 1959.
DIVISION OF APPLIED PHYSICS,
NATIONAL RESEARCH COUNCIL,
OTTAWA, CANADA.

S. N. KALRA

[1]Issued as N.R.C. No. 5446.
[2]Cf. Kalra, S. N. 1959. Can. J. Phys. 37, 1328.

Comment on the Paper "The scattering of electromagnetic waves by a corrugated sheet" by T. B. A. Senior*

In a recent paper, Senior (1959*a*) has evaluated by the method of physical optics the scattering of a normally incident plane wave by a perfectly conducting sheet having sinusoidal corrugations. His procedure was to represent the scattered field by an infinite Kirchhoff-type integral containing the assumed physical optics current distribution on the sheet (i.e., twice the tangential component of the incident magnetic field), and then to manipulate this integral via a number of intricate steps (involving asymptotic evaluations of certain auxiliary integrals) into a form exhibiting the scattered field as a spectrum of plane wave modes. The amplitudes A_m of the scattered plane waves are expressed in terms of an integral extending over one period of the corrugations only. The derivation of this integral expression for A_m, in the course of which the assumed current distribution is employed at the outset, constitutes a main feature of Senior's paper.

It should be pointed out that Senior's formula for A_m could have been deduced at once from results available in the theory of infinite gratings (Twersky 1956, pp. 330–345, eqs. 23 and 24). Alternatively, and more directly, the expression can be derived from a simple waveguide procedure which is recalled briefly. Consider the planar array of identical cylindrical obstacles shown in Fig. 1(*a*), separated by a distance *d* along the *y* axis. Each obstacle is assumed to be perfectly conducting, has infinite extent along the *x* direction, and possesses reflection symmetry about a central plane perpendicular to the *y* axis. The array is illuminated by an incident plane electromagnetic wave whose electric or magnetic vector is parallel to the *x* axis (i.e., the problem is two-dimensional and independent of the *x* co-ordinate). In view of the periodicity of the grating, the scattered field is represented in terms of a complete set of "grating modes" which satisfy on the symmetry planes shown by dashed lines in Fig. 1(*a*) the necessary periodicity conditions. The grating problem is thereby reduced to the equivalent waveguide problem shown in Fig. 1(*b*), in which the symmetry planes constitute the "waveguide walls" whereon the boundary conditions are of the "periodic" type. Because of the above equivalence, the grating problem can be regarded as a scattering problem in a multimode waveguide wherein

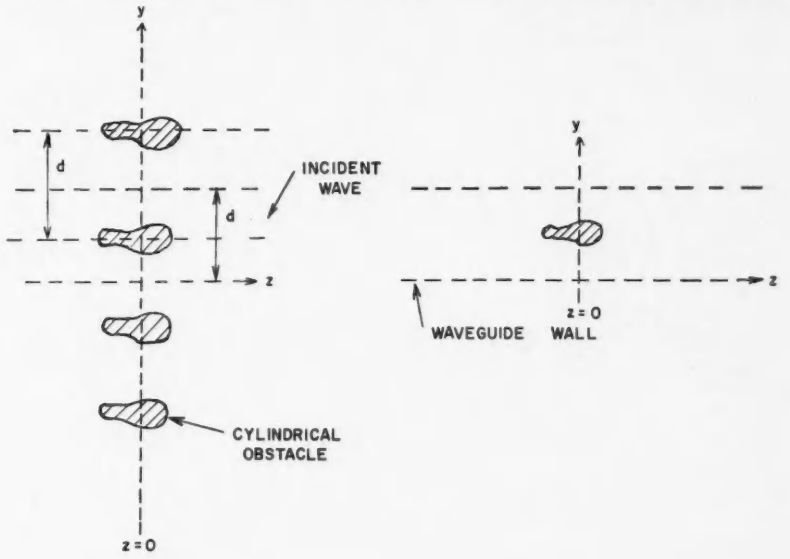

FIG. 1. Equivalent configurations: (*a*) infinite array of cylinders, (*b*) waveguide problem.

*Can. J. Phys. **37**, 787 (1959).

the possible grating modes propagating away from the grating constitute the propagating modes, while the "surface waves" in the grating constitute the non-propagating modes. If the incident plane wave has its magnetic vector directed along the x axis and impinges normally on the grating, the waveguide walls can be replaced by perfect conductors and the analogy with a conventional waveguide problem becomes complete. For simplicity, only this case is considered below.

Let $\mathscr{E}_i^{(\pm)}(\mathbf{r})$ denote the vector electric field in the empty waveguide in Fig. 1(b) associated with the ith mode travelling in the $\pm z$ direction. The $\mathscr{E}_i$ functions are so normalized as to correspond to waves with unit voltage amplitude. If a wave $\mathscr{E}_0^{(-)}(\mathbf{r})$ originating at $z = \infty$ is incident upon the obstacle, the total field $\mathbf{E}(\mathbf{r})$ in the waveguide is given by (Marcuvitz and Schwinger 1951, eq. 3.34) (note: the incident wave is the *TEM* mode in parallel plate waveguide)

$$\mathbf{E}(\mathbf{r}) = \mathscr{E}_0^{(-)}(\mathbf{r}) - \int_S \boldsymbol{Z}(\mathbf{r}, \mathbf{r}') \cdot \mathbf{J}(\mathbf{r}')\, dS', \tag{1}$$

where S is the obstacle surface, $\mathbf{J}$ the induced surface current, and $\boldsymbol{Z}$ the dyadic Green's function:†

$$\boldsymbol{Z}(\mathbf{r}, \mathbf{r}') = \begin{cases} \displaystyle\sum_{i=0}^{\infty} \frac{Z_i}{2} \mathscr{E}_i^{(+)}(\mathbf{r}) \mathscr{E}_i^{(-)}(\mathbf{r}'), & z > z' \\ \displaystyle\sum_{i=0}^{\infty} \frac{Z_i}{2} \mathscr{E}_i^{(-)}(\mathbf{r}) \mathscr{E}_i^{(+)}(\mathbf{r}'), & z < z'. \end{cases} \tag{2}$$

Z_i denotes the characteristic impedance of the ith mode. The induced current $\mathbf{J}$ is specified implicitly by the integral equation obtained from (1) upon letting $\mathbf{n} \times \mathbf{E}(\mathbf{r}) = 0$, $\mathbf{r}$ on S, where $\mathbf{n}$ is the unit vector normal to S. Upon substituting (2) into (1), one obtains for the field anywhere to the right of the obstacle:

$$\mathbf{E}(\mathbf{r}) = \mathscr{E}_0^{(-)}(\mathbf{r}) + \sum_{i=0}^{\infty} S_{i0}\, \mathscr{E}_i^{(+)}(\mathbf{r}), \tag{3}$$

$$S_{i0} = -\frac{1}{2} Z_i \int_S \mathscr{E}_i^{(-)}(\mathbf{r}') \cdot \mathbf{J}(\mathbf{r}')\, dS'. \tag{3a}$$

The scattering coefficient S_{i0} represents directly the amplitude of the ith mode scattered wave. Analogous expressions exist for the field to the left of the obstacle, or in the obstacle region. The S_{i0} coefficients as represented in (3a) are directly proportional to Senior's desired A_m, the proportionality factor depending on the normalization of the mode functions.

Returning now to the problem of the corrugated sheet, we note that the obstacle in this case has the form of a sinusoid; because of the symmetry about the central plane, the basic wave-

†The representation in (2) requires that the transverse mode functions $(\mathbf{z}_0 \times \mathscr{E}_i^{(\pm)}) \times \mathbf{z}_0$ are real, where $\mathbf{z}_0$ is a unit vector along the z direction. This choice can always be made for a conventional waveguide bounded by perfectly conducting walls. If the mode functions are complex, as for the case of arbitrary direction of incidence depicted in Fig. 1 (see Marcuvitz (1951, pp. 88–89) for the form of the mode functions), the dyadic Green's function can be shown to be represented more generally as

$$\boldsymbol{Z}(\mathbf{r}, \mathbf{r}') = \begin{cases} \displaystyle\sum_{i=1}^{N} \frac{Z_i}{2} \mathscr{E}_i^{(+)}(\mathbf{r}) \mathscr{E}_i^{(+)*}(\mathbf{r}') + \sum_i{}' \frac{Z_i}{2} \mathscr{E}_i^{(+)}(\mathbf{r}) \mathscr{E}_i^{(-)*}(\mathbf{r}'), & z > z' \\ \displaystyle\sum_{i=1}^{N} \frac{Z_i}{2} \mathscr{E}_i^{(-)}(\mathbf{r}) \mathscr{E}_i^{(-)*}(\mathbf{r}') + \sum_i{}' \frac{Z_i}{2} \mathscr{E}_i^{(-)}(\mathbf{r}) \mathscr{E}_i^{(+)*}(\mathbf{r}'), & z < z'. \end{cases} \tag{2a}$$

The first sum in (2a) extends over the modes propagating away from the grating (N such modes, numbered $i = 1 \ldots N$, are assumed to exist), while the second sum $\sum_i{}'$ extends over all non-propagating modes. The asterisk* denotes the complex conjugate. The scattering coefficients S_{ij}, where $\mathscr{E}_j^{(-)}(\mathbf{r})$ denotes the incident wave, are obtained as above. If the transverse mode functions are real, one finds that $\mathscr{E}_i^{(+)} = \mathscr{E}_i^{(-)*}$ for the propagating modes and $\mathscr{E}_i^{(\pm)} = \mathscr{E}_i^{(\pm)*}$ for the non-propagating modes, so that (2a) reduces to (2).

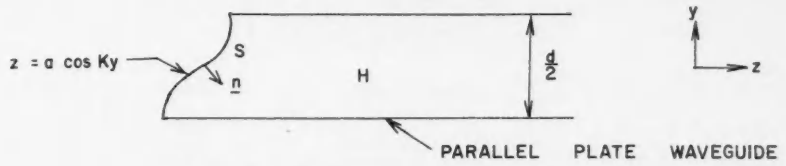

FIG. 2. Equivalent waveguide problem for corrugated sheet.

guide can, for normal incidence, be further reduced to that in Fig. 2. Upon substituting the appropriate parallel plate mode function $\mathscr{E}_i^{(-)}$ into (3*a*) (Marcuvitz 1951) and employing the assumed physical optics current distribution, one obtains directly Senior's eq. (17), save for a direction cosine under the integrand, the omission of which has been rectified by Senior (1959*b*).

MARCUVITZ, N. 1951. Waveguide handbook (McGraw-Hill Book Co., Inc., New York), pp. 62–65.
MARCUVITZ, N. and SCHWINGER, J. 1951. J. Appl. Phys. **22** (6), 806.
SENIOR, T. B. A. 1959*a*. Can. J. Phys. **37**, 787.
——— 1959*b*. Can. J. Phys. **37**, 1572.
TWERSKY, V. 1956. IRE Trans. PGAP, **AP-4**, 330.

RECEIVED OCTOBER 1, 1959.
L. B. FELSEN
MICROWAVE RESEARCH INSTITUTE,
POLYTECHNIC INSTITUTE OF BROOKLYN,
NEW YORK, N.Y.

The Valence State of Metallic Lead

From considerations of atomic diameters it has long been concluded (Hume-Rothery 1936) that lead is divalent rather than quadrivalent in the solid metallic state, and this conclusion is consistent with the chemical evidence of the stability of the divalent state in lead. This view has recently been questioned by Pearson (1958) on the basis of the results of measurements of electrical resistance and thermoelectric force of dilute solutions of cadmium, indium, tin, and bismuth in lead. These experiments show that tin produces the least, and cadmium the greatest, effect on the electrical properties concerned, from which it is argued that lead is tetravalent rather than divalent.

Consideration suggests that the argument of Pearson is open to criticism. If metallic lead is divalent, the $(6s)^2$ subgroup of electrons forms atomic bound states, and the shared electrons which give rise to the conductivity will be in states derived from the $(6p)$ states of the free atoms, or from hybrids of these and higher states. Such electrons will not necessarily resemble the predominantly *s*-like (or sp-hybridized) electrons in cadmium, and the relatively large effect produced by cadmium can be understood. Further, since tin gives rise to divalent compounds, and to a metallic form (white tin) in which the interatomic distances are greater than in silver, there is no reason why tin should not dissolve in lead so that the $(5s)^2$ subgroup of the tin atom is an atomic state like the $(6s)^2$ subgroup of the lead atom. It is suggested, therefore, that the data presented by Pearson need not disturb the conclusion that lead is divalent in the metallic crystal. It may be noted that this view closely resembles that recently advanced by Cohen and Heine (1958), according to whom the relatively large difference between the $(6s)$ and $(6p)$ levels in the free atoms of lead prevents the (sp^3) hybridization which underlies the diamond type of structure, and so prevents lead from crystallizing in this structure.

COHEN, M. and HEINE, V. 1958. Advances in Physics, **7**, 395.
HUME-ROTHERY, W. 1936. The structure of metals and alloys (The Institute of Metals, London).
PEARSON, W. B. 1958. Can. J. Phys. **36**, 631.

RECEIVED OCTOBER 26, 1959.
W. HUME-ROTHERY
DEPARTMENT OF METALLURGY,
UNIVERSITY OF OXFORD,
OXFORD, ENGLAND.

CONTENTS OF VOLUME 37

Ahmad, I. and **Demers, J.** L'influence du développement sur la structure des trajectoires et sur le voile dans les émulsions à grains fins, 1548.
Almqvist, E. See Bromley, D. A., 1514.
Aziz, R. A. and **Baird, D. C.** The superconducting transition in polycrystalline tin, 937.
Baerg, A. P., Bartholomew, R. M., Brown, F., Katz, L., and **Kowalski, S. B.** *With an appendix by* **Dyson, P. M., Kennedy, J. M.,** and **Vogt, E.** The angular distribution of photofission fragments, 1418.
Bailey, H. See Romanowski, M., 896.
Baird, D. C. Fluctuations in the intermediate state of superconducting tantalum, 129.
See also, Aziz, R. A., 937.
Baird, K. M. and **Smith, D. S.** Kr 86 and Hg 198 wavelength standards, 832.
Barrie, R. Negative and oscillatory longitudinal magnetoresistance, 893.
Bartholomew, G. A. See Litherland, A. E., 53; Campion, P. J., 377; Baerg, A. P., 1418.
Batchelor, R. See Bromley, D. A., 1514.
Bell, R. E. See Sosniak, J., 1.
Berry, R. J. The temperature–time dependence of the triple point of water, 1230.
Betts, D. D. Solid harmonics as basis functions for cubic crystals, 350.
Bickmore, R. W. See Shanks, H. E., 263.
Bingel, W. A. Extension of Davydov's theory of molecular crystals to vibronic transitions, 680.
Blackmore, W. R. A thermistor hypsometer, 1331.
Ebulliometry and the determination of the molecular weights of polymers. Part III. Considerations on thermistor Wheatstone bridges, 1365.
Bland, J. A. The thermal expansion of cubic barium titanate ($BaTiO_3$) from 350° C to 1050° C, 417.
Bloom, M. See Rocard, J. M., 522; Oppenheim, I., 1324.
Blum, L. and **Cohan, N. V.** Orbital following in tetrahedral molecules, 1002.
Boswell, F. W. C. The effect of deformation on the internal friction of iron measured at the carbon peak position, 1474.
Bourret, R. Particle equations from non-associative algebras, 183.
Autocorrelation of quantum-mechanical wave functions, 1062.
Bowsher, J. M. On "plastic" waves in solids, 1017.
Bradford, H. M., Fraser, D. M., Langstroth, G. F. O., and **MacDonald, A. D.** Electrical breakdown in xenon and krypton at ultrahigh frequencies, 1166.
Bratina, W. J. Investigation of deformation processes in Armco iron by means of internal friction at megacycle frequencies, 579.
Bromley, D. A., Ferguson, A. J., Gove, H. E., Kuehner, J. A., Litherland, A. E., Almqvist, E., and **Batchelor, R.** Studies of (p,n) reactions in the proton energy range from 2 to 10 Mev, 1514.
Brown, F. See Baerg, A. P., 1418.
Brysk, H., Hiatt, R. E., Weston, V. H., and **Siegel, K. M.** The nose-on radar cross sections of finite cones, 675.
Burgess, R. E. Statistical theory of avalanche breakdown in silicon, 730.
Cameron, A. G. W. Spin dependence of nuclear level spacings, 244.
Multiple neutron capture in the Mike fusion explosion, 322.
Campion, P. J., Knowles, J. W., Manning, G., and **Bartholomew, G. A.** Gamma radiation from the $U^{238}(n,\gamma)U^{239}$ reaction, 377.
Carmichael, C. M. and **Misener, A. D.** On maintaining an object at a uniform temperature, 890.
Carroll, P. K. The C–X system of N_2^+, 880.
Chambers, Ll. G. Solution of the Hund gravitational equations, 433.
The Hund gravitational equations and geons, 1008.
Chopra, K. L. and **Hutchison, T. S.** Study of phase propagation in superconducting aluminum by ultrasonic attenuation measurements, 614.
Ultrasonic attenuation in superconducting and normal mercury, 1100.
Cohan, N. V. See Blum, L., 1002.
Conda, A. M. See Wait, J. R., 1384.
Covington, A. E. and **Harvey, G. A.** Resolving power of three antenna patterns derived from the same aperture, 1216.
Daniels, J. M. An isotope effect in antiferromagnetism at low temperatures, 75.
Daniels, J. M. and **LeBlanc, M. A. R.** Nuclear orientation of cobalt-60 in antiferromagnetic $Co(NH_4)_2(SO_4)_2 \cdot 6H_2O$, 82.
Some observations on nuclear alignment in cobalt metal, 1321.
Das, S. C. On the general plane problem of plasticity and its geophysical significance, 63.

Davison, B. Multilayer problems in the multigroup spherical harmonics method, 1482.
Demers, J. See Ahmad, I., 1548; Fujii, E., 1465.
Demers, P. See Fujii, E., 1465.
DeMille, G. R., Kavanagh, T. M., Moore, R. B., Weaver, R. S., and **White, W.** Rotational states of even–even nuclei, 1036.
Dixon, R. N. The 0–0 and 1–0 bands of the $A(^3\Pi_i)$–$X(^3\Sigma^-)$ system of NH, 1171.
Dosso, H. W. See Singh, P. P., 1055.
Dowling, J. M. and **Stoicheff, B. P.** High resolution Raman spectroscopy of gases. XII. Rotational spectra of C_2H_4 and C_2D_4 and the structure of the ethylene molecule, 703.
Dunn, A. F. Determination of the unit of capacitance, 35.
Duwalo, G. and **Jacobs, J. A.** Effects of a liquid core on the propagation of seismic waves, 109.
Dyson, P. M. See Baerg, A. P., 1418.
Eastwood, T. A. See Millar, C. H., 1126.
Eastwood, T. A. and **Roy, J. C.** The occurrence of $(n, 3n)$ reactions in a nuclear reactor, 815.
Evans, J. E., Kinsey, B. B., and **Whitmore, B. G.** Measurement of the energies of nuclear states excited by inelastic neutron scattering, and a search for electric monopole transitions in Pb, 396.
Ewan, G. T., Geiger, J. S., Graham, R. L., and **MacKenzie, D. R.** The *K–LL* Auger spectrum of $_{94}Pu^{239}$, 174.
Felsen, L. P. Comment on the paper "The scattering of electromagnetic waves by a corrugated sheet" by T. B. A. Senior, 1563.
Fenton, A. G., McCracken, K. G., Rose, D. C., and **Wilson, B. G.** Transient decreases in cosmic ray intensity during the period October 1956 to January 1958, 569.
The onset times of Forbush-type cosmic ray intensity decreases, 970.
Ferguson, A. J. See Bromley, D. A., 1514.
Ferguson, A. J. and **Gove, H. E.** Analysis of two interfering 1/2+ levels in the disintegration of C^{14} by protons, 660.
Fickel, H. R. and **Tomlinson, R. H.** Thermal neutron absorption cross section of Xe^{135}, 531.
The cumulative fission yields of light mass fragments in the thermal neutron fission of Pu^{239}, 916.
The cumulative fission yields of 21 heavy mass nuclides produced in the thermal fission of Pu^{239}, 926.
Fink, H. J. Quasi-persistent currents in rings composed of superconducting and non-superconducting regions, 474.
The destruction of superconductivity in tantalum wires by a current, 485.
A new absolute noise thermometer at low temperatures, 1397.
Firth, D. R. Exchange reaction of 90-Mev protons on deuterons, 1074.
Foster, J. S. Notes on a photograph of the Stark effect, 1202.
Fraser, D. M. See Bradford, H. M., 1166.
Freistadt, H. Poisson brackets in field theory, 5.
Froese, C. On the calculation of the velocity of sound in sea water, 775.
Fujii, E., Fujii, H., Demers, J., and **Demers, P.** Nouvelles émulsions ionographiques à l'alcool polyvinylique, 1465.
Fujii, H. See Fujii, E., 1465.
Geiger, J. D. See Ewan, G. T., 174.
Geiger, K. W. Absolute standardization of radioactive neutron sources. II. The use of the $F^{19}(\alpha,n)Na^{22}$ reaction, 550.
Geiger, K. W. and **Whyte, G. N.** Absolute standardization of radioactive neutron sources. I. Activation of manganese bath, 256.
Gerson, N. C. and **Gossard, W. H.** Noise trains, 1061.
Glass, D. G. See Kavadas, A., 690.
Gossard, W. H. See Gerson, N. C., 1061.
Gove, H. E. See Litherland, A. E., 53; Ferguson, A. J., 660; Bromley, D. A., 1514.
Graham, R. L. See Ewan, G. T., 174.
Green, R. M. See McNeill, K. G., 528, 683.
Griffiths, G. M. See Singh, P. P., 866, 1055.
Griffiths, G. M., Singh, P. P., Ssu, Y. I., and **Warren, J. B.** A simple gamma-ray insensitive fast-neutron counter, 858.
Guptill, E. W. See Lawrence, D. J., 1069.
Gush, H. P. See Kiss, Z. J., 362.
Haering, R. R. Note on the motion of electrons and holes in perturbed lattices, 47.
Impurity molecule-ions and impurity molecules, 384.
Luminescence and conductivity induced by field ionization of traps, 1374.
Hall, G. Ionization loss by cosmic-ray mu-mesons in argon, 189.
Hanes, G. R. Limiting precision in optical interferometry, 1283.
Hart, J. F. and **Worsley, B. H.** Approximate wave functions of Pb^{+++} by the method of self-consistent field without exchange, 983.
Hartz, T. R. Radio star scintillations and ionospheric disturbances, 1137.

Harvey, G. A. See Covington, A. E., 1216.
Haslam, R. N. H. See Roalsvig, J. P., 499, 607, 722.
Hay, D. R. and **Poaps, G. E.** Prolonged signal fade-out on a short microwave path, 313.
Frontal perturbation of a tropospheric scatter path, 1272.
Hay, H. J. and **Warren, J. B.** The photodisintegration of neon, 1153.
Hedgcock, F. T. The effect of concentration of the magnetic susceptibility of trapped electrons and holes in semiconductors, 381.
Herzberg, G. and **Howe, L. L.** The Lyman bands of molecular hydrogen, 636.
Herzberg, G. and **Moore, H. R.** The spectrum of Li^+, 1293.
Hiatt, R. E. See Brysk, H., 675.
Hobson, J. P. First adsorbed layer of helium at 4.2° K, 300.
First adsorbed layer of nitrogen on pyrex at 77.4° K, 1105.
Holmes, E. L. and **Winegard, W. C.** Normal grain growth in zone-refined high-purity metals, 496.
Comparisons between free energies of activation for grain growth, grain-boundary self-diffusion, and liquid self-diffusion, 899.
Howe, L. L. See Herzberg, G., 636.
Howlett, L. E. Announcement on the international yard and pound, 84.
Hume-Rothery, W. The valence state of metallic lead, 1565.
Hutchison, T. S. See Chopra, K. L., 614, 1100.
Jacobs, J. A. See Duwalo, G., 109.
Johns, M. W. See King, W. J., 755.
Johns, M. W. and **MacArthur, J. D.** Zero spin of the 1265-kev state in Pt^{194}, 1205.
Judek, B. Experiments on processing and mounting of nuclear emulsions, 102.
Kaempffer, F. A. On the possible existence of a derivative coupling in quantum electrodynamics, 1339.
Kaiser, R. On the theory of the spectrophone, 1499.
Kalra, S. N. Frequency measurement of standard frequency transmissions against caesium beam resonator standard, 1328.
Frequency measurement of standard frequency transmissions, 1562.
Kalra, S. N., Pattenson, C. F., and **Thomson, M. M.** Canadian standard of frequency, 10.
Katz, L. Betatron energy calibration, 1455.
See also Parsons, R. W., 809; Baerg, A. P., 1418; King, H., 1357.
Katzman, J. The sun as a source of cosmic rays of intermediate energies, 1207.
Kavadas, A. and **Glass, D. G.** Polarization of radar echoes from aurora, 690.
Kavanagh, T. M. See DeMille, G. R., 1036.
Kennedy, J. M. See Baerg, A. P., 1418.
Keys, J. E. and **Primich, R. I.** The nose on radar cross sections of conducting right circular cones, 521.
King, H. and **Katz, L.** Fine structure in the $O^{16}(\gamma,n)O^{15}$ yield curve, 1357.
King, W. J. and **Johns, M. W.** Spins of excited states of Os^{188}, 755.
Kinsey, B. B. See Evans, J. E., 396.
Kirkaldy, J. S. Diffusion in multicomponent metallic systems. IV. A general theorem for construction of multicomponent solutions from solutions of the binary diffusion equation, 30.
Crystal growth and the thermodynamics of irreversible processes, 739.
Kiss, Z. J. See van Kranendonk, J., 1187.
Kiss, Z. J., Gush, H. P., and **Welsh, H. L.** The pressure-induced rotational absorption spectrum of hydrogen. I. A study of the absorption intensities, 362.
Kiss, Z. J. and **Welsh, H. L.** The pressure-induced rotational absorption spectrum of hydrogen, 1249.
Kleman, B. and **Uhler, U.** A $^6\Sigma$–$^6\Sigma$ transition in CrH, 537.
Knowles, J. W. A high resolution flat crystal spectrometer for neutron capture γ-ray studies, 203.
See also Campion, P. J., 377.
Kowalski, S. B. See Baerg, A. P., 1418.
van Kranendonk, J. and **Kiss, Z. J.** Theory of the pressure-induced rotational spectrum of hydrogen, 1187.
Kuehner, J. A. See Bromley, D. A., 1514.
Langleben, M. P. Some physical properties of sea ice. II, 1438.
Langstroth, G. F. O. See Bradford, H. M., 1166.
Laubitz, M. J. Thermal conductivity of powders, 798.
Design of gradientless furnaces, 1114.
Lawrence, D. J., Stewart, A. T., and **Guptill, E. W.** Thermal conductivity of solid argon at 80° K, 1069.
LeBlanc, M. A. R. See Daniels, J. M., 82, 1321.
Leech, J. W. Irreversible thermodynamics and kinetic theory in the derivation of thermoelectric relations, 1044.
Anharmonic forces and the Einstein model of a crystal, 1067.
Litherland, A. E. See Bromley, D. A., 1514.

Litherland, A. E., Paul, E. B., Bartholomew, G. A., and **Gove, H. E.** Some properties of the 2.23-Mev excited state of P^{31}, 53.
Little, E. M. See Pounder, E. R., 443.
Little, W. A. The transport of heat between dissimilar solids at low temperatures, 334.
Loh, S. C. On toroidal functions, 619.
The calculation of the electric potential and the capacity of a tore by means of toroidal functions, 698.
MacArthur, J. D. See Johns, M. W., 1205.
McCracken, K. G. See Fenton, A. G., 569, 970.
McDiarmid, I. B. Low energy proton flux at sea level, 79.
MacDonald, A. D. See Bradford, H. M., 1166.
McIntosh, B. A. An experimental study of interception noise in electron streams at microwave frequencies, 285.
McKenzie, D. J. See Roalsvig, J. P., 607.
MacKenzie, D. R. See Ewan, G. T., 174.
McLaren, E. H. Intercomparison of 11 resistance thermometers at the ice, steam, tin, cadmium, and zinc points, 422.
McNeill, K. G. See Storey, R. S., 1072.
McNeill, K. G. and **Green, R. M.** The effective half-lives of Cs and I in the body, 528.
Measurements with a whole body counter, 683.
Manchester, F. D. The specific heat of rubidium between 1.2 and 4.2° K, 525.
A cryostat for measuring specific heats between 1 and 4.2° K using a mechanical thermal switch, 989.
Manning, G. See Campion, P. J., 377.
Maradudin, A. A. See Weiss, G. H., 965.
Maradudin, A. A. and **Weiss, G. H.** A method for evaluating lattice sums, 170.
March R. H. and **Stewart, A. T.** Momentum distribution of annihilating electron–positron pairs in LiF, 1076.
Mathews, P. M. Atmospheric effects on cosmic ray intensity at sea level, 85.
Millar, C. H., Eastwood, T. A., and **Roy, J. C.** The decay of Bi^{208}, 1126.
Millar, R. F. Radiation and reception properties of a wide slot in a parallel-plate transmission line: I, 144.
Radiation and reception properties of a wide slot in a parallel-plate transmission line: II, 160.
Misener, A. D. See Carmichael, C. M., 890.
Moore, H. R. See Herzberg, G., 1293.
Moore, R. B. See DeMille, G. R., 1036.
Morris, D. See Mungall, A. G., 1349.
Mungall, A. G. and **Morris, D.** Surface wave propagation over a sand-covered conducting plane, 1349.
Newton, T. D. On the spherical oscillator nucleus, 944.
Niven, C. D. A proposed mechanism for ice friction, 247.
The change of resistance of hydrophilic films subjected to constant voltage, 438.
Oppenheim, I. and **Bloom, M.** Nuclear spin relaxation in low-temperature liquids, 1324.
Parsons, R. W. The photodisintegration of manganese and rhodium, 1344.
Parsons, R. W. and **Katz, L.** The photodisintegration of tantalum, 809.
Paskievici, W. Principe d'une analyse des courbes expérimentales composées: Application à la mesure de la densité des grains dans les traces fortement ionisées dans les émulsions nucléaires, 1314.
Pattenson, C. F. See Kalra, S. N., 10.
Paul, D. A. L. Possible chemical reaction of orthopositronium with oxygen, 1059.
Paul, E. B. See Litherland, A. E., 53.
Plaskett, T. S. and **Winegard, W. C.** Cellular growth in tin alloys, 1555.
Poaps, G. E. See Hay, D. R., 313, 1272.
Pounder, E. R. and **Little, E. M.** Some physical properties of sea ice. I, 443.
Prasad, S. Corner-driven coupled square loop antennas, 1407.
Primich, R. I. See Keys, J. E., 521.
Rao, M. S. Size of irregularities in the E region of the ionosphere, 557.
Rastogi, R. G. Magnetic control on the variations of critical frequency of the F_2 layer of the ionosphere, 874.
Redhead, P. A. The magnetron gauge: A cold-cathode vacuum gauge, 1260.
Roalsvig, J. P. and **Haslam, R. N. H.** Absolute β-counting in a proportional flow-counter, 499.
Roalsvig, J. P., Haslam, R. N. H., and **McKenzie, D. J.** Photoneutron cross section of Ni^{58}, 607.
Roalsvig, J. P., Haslam, R. N. H., Skarsgard, L. D., and **Wuschke, E. E.** Photo alpha reactions in silver, 722.
Robinson, L. B. See Rocard, J. M., 522.
Rocard, J. M., Bloom, M., and **Robinson, L. B.** Nuclear magnetic resonance in lead-containing compounds, 522.

Romanowski, M. and **Bailey, R.** Suggested modifications to a method for the determination of the absolute ampere, 896.
Rose, D. C. See Fenton, A. G., 569, 970.
Rosen, S. P. A spherical wave expansion for double β-decay, 780.
Roy, J. C. Evidence for neutrons with an energy of 20.3 Mev in the NRX reactor, 827.
See also Eastwood, T. A., 815; Millar, C. H., 1126.
Roy, J. C. and **Roy, L. P.** Radioactive decay of Au^{200}, 385.
Effective and thermal neutron capture cross section and resonance capture integral of Pr-143, 907.
Roy, L. P. See Roy, J. C., 385, 907.
Scheidegger, A. E. On the theory of flow of underground fluids in compressible strata, 276.
Senior, T. B. A. The scattering of electromagnetic waves by a corrugated sheet, 787.
Seth, K. K. A note on s-wave average neutron cross sections, 1199.
Shanks, H. E. and **Bickmore, R. W.** Four-dimensional electromagnetic radiators, 263.
Sharp, R. T. Self and external meson fields, 515.
Siegel, K. M. See Brysk, H., 675.
Singh, N. L. Rotational analysis of the β bands of phosphorus monoxide, 136.
Singh, P. P. See Griffiths, G. M., 858.
Singh, P. P., Dosso, H. W., and **Griffiths, G. M.** The energies and relative pair production cross sections for Zn^{65} and Na^{22} gamma rays, 1055.
Singh, P. P., Griffiths, G. M., Ssu, Y. I., and **Warren, J. B.** The neutron yield from heavy ice targets bombarded with protons below the $D(p, n)2p$ threshold, 866.
Skarsgard, L. D. See Roalsvig, J. P., 722.
Smith, A. W. The impedance, rectification, and electroluminescence of anodic oxide films on aluminum, 591.
Smith, D. S. See Baird, K. M., 832.
Smith, R. W. The grey tin $\rightleftharpoons$ white tin transition in tin–mercury alloys, 1079.
Sodha, M. S. Spectral distribution of bremsstrahlung from an ionized gas, 1380.
Sodha, M. S. and **Varshni, Y. P.** Drift mobility of electrons in atomic hydrogen, 1552.
Sosniak, J. and **Bell, R. E.** Genetic measurement of the half life of Bi^{207}, 1.
Ssu, Y. I. See Griffiths, G. M., 858; Singh, P. P., 866.
Stewart, A. T. See Lawrence, D. J., 1069; March, R. H., 1076.
Stoicheff, B. P. See Dowling, J. M., 703.
Storey, R. S. and **McNeill, K. G.** The decay of Mg^{23}, 1072.
Sueoka, S. The theory of the photonuclear reaction using the independent particle model of the nucleus, 232.
Swarup, P. Paramagnetic resonance line shapes, 848.
Szabo, A. Relaxation time and multiple pumping effects in masers, 1557.
Thomson, M. M. See Kalra, S. N., 10.
Tiller, W. A. The function of constitutional supercooling in crystal growth, 1204.
Tomlinson, R. H. See Fickel, H. R., 531, 916, 926.
Uhler, U. See Kleman, B., 537.
Varshni, Y. P. See Sodha, M. S., 1552.
Vogt, E. See Baerg, A. P., 1418.
Wait, J. R. Radiation from a small loop immersed in a semi-infinite conducting medium, 672.
Wait, J. R. and **Conda, A. M.** On the diffraction of electromagnetic pulses by curved conducting surfaces, 1384.
Warren, J. B. See Griffiths, G. M., 858; Singh, P. P., 866; Hay, H. J., 1153.
Weaver, R. S. See DeMille, G. R., 1036.
Weiss, G. H. See Maradudin, A. A., 170.
Weiss, G. H. and **Maradudin, A. A.** On an asymptotic expansion occurring in the evaluation of a lattice sum, 965.
Welsh, H. L. See Kiss, Z. J., 362, 1249.
Weston, V. H. See Brysk, H., 675.
White, W. See DeMille, G. R., 1036.
Whitmore, B. G. See Evans, J. E., 396.
Whyte, G. N. See Geiger, K. W., 256.
Williams, R. L. Modification of PbS noise spectra by radiation, 841.
Williams, R. W. Heavy-liquid bubble chambers, 1085.
Wilson, B. G. A study of μ-mesons incident at large zenith angles, 19.
See also Fenton, A. G., 569, 970.
Winegard, W. C. See Holmes, E. L., 496, 899; Plaskett, T. S., 1555.
Wong, J. Y. A note of the scattering of a plane electromagnetic wave by a small, thin-walled, cylindrical dielectric tube, 77.
Woodside, W. Water vapor permeability of porous media, 413.
Worsley, B. H. Scattering factors for some of the heavier atoms, 967.
See also Hart, J. F., 983.
Wuschke, E. E. See Roalsvig, J. P., 722.

CORRECTIONS

Volume 37, 1959

Page 434. On page 434, line 11, "and if there is no creation of matter," should read "and if the density is constant,".

Page 787. The following correction was submitted by T. B. A. Senior concerning his paper "The scattering of electromagnetic waves by a corrugated sheet".

I am indebted to Professor L. B. Felsen for pointing out an error in my paper of the above title. In writing down the expression for the field as an integral over the physical optics current, a factor $1/(\mathbf{n}\cdot\mathbf{y}) = \sqrt{\{1+(aK\sin Kx)^2\}}$ was omitted from the numerator of the integrand. This now cancels out a corresponding factor from the denominator of equation (8) and from all the subsequent equations in which the factor occurred. Apart from this change the analysis is correct as it stands.

The new expression for the modal amplitudes is

$$A_m = \frac{1}{2\pi}\int_{-\pi}^{\pi}\left\{1+\frac{mK}{\sqrt{\{k^2-(mK)^2\}}}aK\sin x\right\}\exp(-imx-i\mu_m\cos x)dx$$

(cf. equation (17)), which can be evaluated to give

$$A_m = (-i)^m\frac{k}{\sqrt{\{k^2-(mK)^2\}}}J_m(\mu_m).$$

This is similar to the results obtained by other approximate methods for treating the corrugated sheet.

Page 1056. On page 1056, line 20, "0.1%" should read "1%".

Page 1061. On page 1061, paragraph 4, "500 Mc/s spectrograph" should read "500 kc/s spectrograph" and "5000 Mc/sec^2" should read "5000 kc/sec^2".

NOTES TO CONTRIBUTORS

Canadian Journal of Physics

MANUSCRIPTS

General.—Manuscripts, in English or French, should be typewritten, double spaced, on paper $8\frac{1}{2}\times11$ in. **The original and one copy are to be submitted.** Tables and captions for the figures should be placed at the end of the manuscript. Every sheet of the manuscript should be numbered. Style, arrangement, spelling, and abbreviations should conform to the usage of recent numbers of this journal. Greek letters or unusual signs should be written plainly or explained by marginal notes. Characters to be set in boldface type should be indicated by a wavy line below each character. Superscripts and subscripts must be legible and carefully placed. Manuscripts and illustrations should be carefully checked before they are submitted. Authors will be charged for unnecessary deviations from the usual format and for changes made in the proof that are considered excessive or unnecessary.

Abstract.—An abstract of not more than about 200 words, indicating the scope of the work and the principal findings, is required, except in Notes.

References.—References should be listed **alphabetically by authors' names,** unnumbered, and typed after the text. The form of the citations should be that used in current issues of this journal; in references to papers in periodicals, titles should not be given and only initial page numbers are required. The names of periodicals should be abbreviated in the form given in the most recent *List of Periodicals Abstracted by Chemical Abstracts.* All citations should be checked with the original articles and each one referred to in the text by the authors' names and the year.

Tables.—Tables should be numbered in roman numerals and each table referred to in the text. Titles should always be given but should be brief; column headings should be brief and descriptive matter in the tables confined to a minimum. Vertical rules should not be used. Numerous small tables should be avoided.

ILLUSTRATIONS

General.—All figures (including each figure of the plates) should be numbered consecutively from 1 up, in arabic numerals, and each figure referred to in the text. The author's name, title of the paper, and figure number should be written in the lower left corner of the sheets on which the illustrations appear. Captions should not be written on the illustrations.

Line drawings.—Drawings should be carefully made with India ink on white drawing paper, blue tracing linen, or co-ordinate paper ruled in blue only; any co-ordinate lines that are to appear in the reproduction should be ruled in black ink. Paper ruled in green, yellow, or red should not be used. All lines must be of sufficient thickness to reproduce well. Decimal points, periods, and stippled dots must be solid black circles large enough to be reduced if necessary. Letters and numerals should be neatly made, preferably with a stencil (**do NOT use typewriting**) and be of such size that the smallest lettering will be not less than 1 mm high when the figure is reduced to a suitable size. Many drawings are made too large; originals should not be more than 2 or 3 times the size of the desired reproduction. Whenever possible two or more drawings should be grouped to reduce the number of cuts required. In such groups of drawings, or in large drawings, full use of the space available should be made; the ratio of height to width should conform to that of a journal page ($4\frac{3}{4}\times7\frac{1}{2}$ in.), but allowance must be made for the captions. **The original drawings and one set of clear copies (e.g. small photographs) are to be submitted.**

Photographs.—Prints should be made on glossy paper, with strong contrasts. They should be trimmed so that essential features only are shown and mounted carefully, with rubber cement, on white cardboard, with no space between those arranged in groups. In mounting, full use of the space available should be made. **Photographs are to be submitted in duplicate;** if they are to be reproduced in groups one set should be mounted, the duplicate set unmounted.

REPRINTS

A total of 50 reprints of each paper, without covers, are supplied free. Additional reprints, with or without covers, may be purchased at the time of publication.

Charges for reprints are based on the number of printed pages, which may be calculated approximately by multiplying by 0.6 the number of manuscript pages (double-spaced typewritten sheets, $8\frac{1}{2}\times11$ in.) and including the space occupied by illustrations. Prices and instructions for ordering reprints are sent out with the galley proof.

Contents

W. R. Blackmore—A thermistor hypsometer - - - - - - - - - - 1331

F. A. Kaempffer—On the possible existence of a derivative coupling in quantum electrodynamics - 1339

R. W. Parsons—The photodisintegration of manganese and rhodium - - 1344

A. G. Mungall and D. Morris—Surface wave propagation over a sand-covered conducting plane - - - - - - - - - - - - - - - - - - 1349

H. King and L. Katz—Fine structure in the $O^{16}(\gamma,n)O^{15}$ yield curve - - 1357

W. R. Blackmore—Ebulliometry and the determination of the molecular weights of polymers. Part III. Considerations on thermistor Wheatstone bridges - 1365

Rudolph R. Haering—Luminescence and conductivity induced by field ionization of traps - - - - - - - - - - - - - - - - - - - 1374

Mahendra Singh Sodha—Spectral distribution of bremsstrahlung from an ionized gas - 1380

James R. Wait and Alyce M. Conda—On the diffraction of electromagnetic pulses by curved conducting surfaces - - - - - - - - - - - 1384

H. J. Fink—A new absolute noise thermometer at low temperatures - - - 1397

Sheila Prasad—Corner-driven coupled square loop antennas - - - - - 1407

A. P. Baerg, R. M. Bartholomew, F. Brown, L. Katz, and S. B. Kowalski. With an appendix by P. M. Dyson, J. M. Kennedy, and E. Vogt—The angular distribution of photofission fragments - - - - - - - - - - - 1418

M. P. Langleben—Some physical properties of sea ice. II - - - - - - 1438

L. Katz—Betatron energy calibration - - - - - - - - - - - 1455

Etsuo Fujii, Hideko Fujii, Joseph Demers, and Pierre Demers—Nouvelles émulsions ionographiques à l'alcool polyvinylique - - - - - - - - 1465

F. W. C. Boswell—The effect of deformation on the internal friction of iron measured at the carbon peak position - - - - - - - - - - 1474

B. Davison—Multilayer problems in the multigroup spherical harmonics method - 1482

R. Kaiser—On the theory of the spectrophone - - - - - - - - - - 1499

D. A. Bromley, A. J. Ferguson, H. E. Gove, J. A. Kuechner, A. E. Litherland, E. Almquist, and R. Batchelor—Studies of (p,n) reactions in the proton energy range from 2 to 10 Mev - - - - - - - - - - - - - - 1514

Notes:

I. Ahmad and J. Demers—L'influence du développement sur la structure des trajectoires et sur le voile dans les émulsions à grains fins - - 1548

Mahendra Singh Sodha and Yatendra Pal Varshni—Drift mobility of electrons in atomic hydrogen - - - - - - - - - - - - - - - 1552

T. S. Plaskett and W. C. Winegard—Cellular growth in tin alloys - - - 1555

A. Szabo—Relaxation time and multiple pumping effects in masers - - - 1557

Letters to the Editor:

S. N. Kalra—Frequency measurement of standard frequency transmissions 1562

L. P. Felsen—Comment on the paper "The scattering of electromagnetic waves by a corrugated sheet" by T. B. A. Senior - - - - - - - 1563

W. Hume-Rothery—The valence state of metallic lead - - - - - - 1565

Contents of Volume 37 - - - - - - - - - - - - - - - - - - - 1567

Printed in Canada *by* University of Toronto Press